Mechanisms Governing Mechanical Performance in Material Extrusion Additive Manufacturing

by

Maryam SHOKROLLAHI

MANUSCRIPT-BASED THESIS PRESENTED TO
ÉCOLE DE TECHNOLOGIE SUPÉRIEURE
IN PARTIAL FULFILLMENT FOR THE DEGREE OF
DOCTOR OF PHILOSOPHY

Ph.D.

MONTRÉAL, MARCH 16TH, 2026

ÉCOLE DE TECHNOLOGIE SUPÉRIEURE
UNIVERSITÉ DU QUÉBEC

BOARD OF EXAMINERS

THIS THESIS HAS BEEN EVALUATED

BY THE FOLLOWING BOARD OF EXAMINERS

Mr. Ilyass Tabiai, Thesis supervisor
Department of Mechanical Engineering, École de technologie supérieure

Ms. Martine Dubé, Thesis Co-Supervisor
Department of Mechanical Engineering, École de technologie supérieure

Mr. Simon Joncas, Chair, Board of Examiners
Department of Systems Engineering, École de technologie supérieure

Mr. Lucas Hof, Member of the Jury
Department of Mechanical Engineering, École de technologie supérieure

Mr. Andy Gleadall, External Examiner
School of Mechanical, Electrical and Manufacturing Engineering, Loughborough University

THIS THESIS WAS PRESENTED AND DEFENDED

IN THE PRESENCE OF A BOARD OF EXAMINERS AND THE PUBLIC

ON FEBRUARY 19TH, 2026

AT ÉCOLE DE TECHNOLOGIE SUPÉRIEURE

ACKNOWLEDGEMENTS

I would like to express my sincere gratitude to my supervisors, Prof. Ilyass Tabiai and Prof. Martine Dubé, for their guidance, trust, and continued support throughout these years. I am grateful for the opportunities they offered me and for the many lessons I gained under their supervision, both academic and non-academic. I feel truly fortunate to have been their student, as their mentorship shaped not only my research but also my perspective on learning, growth, and perseverance beyond academia.

I would also like to thank the members of my jury, Prof. Lucas Hof and Prof. Andy Gleadall, for agreeing to review this work and for the time and care they devoted to its evaluation. I am equally grateful to Prof. Simon Joncas for agreeing to serve as the jury president and for his guidance throughout this process.

I would like to sincerely thank Prof. Arthur Levy and the Laboratoire de Thermique et Énergie de Nantes (LTEN) for hosting me during my internship at the Université de Nantes. It was a wonderful opportunity that enriched my knowledge and experience, and I deeply appreciated their generosity, guidance, and the welcoming environment they provided throughout my stay.

I feel very fortunate to have worked alongside outstanding postdoctoral researchers during my PhD. I would like to sincerely thank Dr. Adam Smith, Dr. Olivier Lampron, Dr. Mélanie Girard, and Dr. Jacques Lengaigne for their valuable discussions, support, and generosity with their time and expertise. Their help greatly enriched my research experience.

I am also grateful to my friends and colleagues at the Polymer and Composite Engineering Laboratory (LIPEC) for making this journey truly memorable. The welcoming and friendly atmosphere of the lab created an inspiring environment in which to work. In particular, I would like to thank Romain, Sare, Carl-Olivier, Stéphane, André, Daria, and all other office members who are not mentioned here but who, in one way or another, helped make these years both productive and enjoyable.

I would like to acknowledge the support of the technical staff at ÉTS, whose expertise and dedication were essential to this work. I am especially thankful to Mr. Joël Grignon, without whom many of the experimental prints would not have been possible; his constant availability, patience, and support made a significant difference. I also thank Mr. Serge Plamondon for his assistance with mechanical testing, and Mr. Nabil Mazeghrane for his invaluable help with orders, deliveries, logistics, and laboratory equipment.

I gratefully acknowledge the financial support provided by the Natural Sciences and Engineering Research Council of Canada (NSERC) and the Research Center for High Performance Polymer and Composite Systems (CREPEC).

Finally, my deepest thanks go to my loved ones. To my partner, Hamed, for his unconditional support, patience, and encouragement throughout these PhD years. His presence, understanding, and belief in me carried me through both the challenging and rewarding moments of this journey. I am also profoundly grateful to my parents, Elaheh and Masoum, for their unwavering support, sacrifices, and constant encouragement throughout my education and life. Everything I have achieved is built on their love and trust.

Declaration of AI Use

During the preparation of this thesis, ChatGPT (OpenAI) and Gemini (Google) were used to verify grammar and improve readability. The author reviewed and edited the content as necessary and takes full responsibility for the final text.

Mécanismes gouvernant les performances mécaniques en fabrication additive par extrusion de matière

Maryam SHOKROLLAHI

RÉSUMÉ

La fabrication additive polymère par extrusion de matière (MEAM) représente la classe de technologies de fabrication additive la plus largement utilisée, offrant des matériaux polyvalents et abordables, un large éventail d'imprimantes, une facilité de mise en œuvre et une bonne évolutivité. Malgré ces avantages, son adoption dans des applications à hautes performances reste limitée, principalement en raison des difficultés à prédire et à contrôler les propriétés des pièces finales. Ces défis persistent malgré d'importants efforts de recherche, en partie à cause du grand nombre de paramètres de procédé ajustables et d'une compréhension encore incomplète des mécanismes par lesquels ces paramètres influencent les performances des pièces.

Cette thèse explore plusieurs mécanismes encore peu étudiés, qui sont influencés par les paramètres de procédé et jouent un rôle déterminant dans les propriétés des pièces. Les contributions incluent une analyse approfondie du procédé d'extrusion et de ses effets sur les propriétés morphologiques, microstructurales et mécaniques des extrudats, qui constituent les éléments fondamentaux des pièces imprimées. Des mécanismes supplémentaires liés à l'adhésion intercouche sont également examinés. En particulier, les encoches d'interface formées naturellement aux jonctions entre extrudats sont identifiées comme une source majeure d'anisotropie, tant pour les impressions à petite qu'à grande échelle. Une méthodologie est développée afin de dissocier les effets de la qualité de l'adhésion intercouche de ceux induits par ces encoches, et les champs de déformation résultants sont quantifiés expérimentalement pour différentes caractéristiques d'encoches.

Par ailleurs, l'étude aborde le contact interfacial selon une approche distincte de celles généralement adoptées dans la littérature. Le développement du contact est souvent considéré comme une augmentation de la largeur de liaison, les zones liées étant supposées être en contact complet. Cependant, des microvides sont observés à l'interface, et leur prévalence varie fortement en fonction des conditions de procédé. Des mesures in situ de la pression de contact, combinées à des caractérisations thermiques, rhéologiques et de rugosité de surface, sont réalisées afin de tester expérimentalement les modèles existants de contact intime issus de procédés analogues et d'évaluer leur validité dans le contexte du MEAM.

Enfin, l'interaction entre les effets des encoches d'interface et la qualité de l'adhésion intercouche est démontrée, montrant que l'influence relative de chaque mécanisme sur les propriétés mécaniques finales dépend fortement de la présence et de l'ampleur des autres mécanismes. Ces résultats permettent une compréhension plus complète des relations procédé–structure–propriété en MEAM polymère et offrent des indications pour une prédiction et un contrôle plus fiables des performances des pièces imprimées.

Mots-clés: Fabrication additive par extrusion de matière, Paramètres de procédé, Propriétés mécaniques

Mechanisms Governing Mechanical Performance in Material Extrusion Additive Manufacturing

Maryam SHOKROLLAHI

ABSTRACT

Polymer-based material extrusion additive manufacturing (MEAM) represents the most widely used class of AM technologies, offering versatile and affordable materials, a broad range of printer options, ease of processing, and scalability. Despite these advantages, its adoption in high-performance applications remains limited, largely due to challenges in predicting and controlling the properties of final parts. These challenges persist despite extensive research efforts, in part because of the large number of tunable process parameters and an incomplete understanding of the mechanisms through which they influence part performance. This thesis investigates several less-explored mechanisms that are affected by process parameters and play a critical role in determining part properties. The contributions include an in-depth analysis of the extrusion process and its effects on the morphological, microstructural, and mechanical properties of extrudates, which serve as the fundamental building blocks of printed parts. Additional mechanisms related to interlayer bonding are also examined. In particular, interface notches formed naturally at the junctions of extrudates are identified as a primary source of anisotropy in both small- and large-scale prints. A methodology is developed to decouple the effects of interface bonding quality from the impact of these notches, and the resulting strain fields are quantified experimentally for notches of varying characteristics.

Furthermore, the study explores interlayer contact from a perspective distinct from prior approaches in the literature. Contact development is often considered as an increase in bond width, with bonded regions assumed to be in full contact. However, microvoids are observed at the interface, and their prevalence varies significantly with processing conditions. In-situ contact pressure measurements, combined with thermal, rheological, and surface roughness characterization, are performed to experimentally test existing intimate contact models from similar processes and assess their validity for MEAM.

Finally, the interplay between interface notch effects and bonding quality is demonstrated, showing that the relative influence of each mechanism on the final mechanical properties depends strongly on the presence and magnitude of the other mechanisms. These findings provide a more comprehensive understanding of the process–structure–property relationships in polymer MEAM and offer guidance for more reliable prediction and control of part performance.

Keywords: Material extrusion additive manufacturing, Process parameters, Mechanical properties

TABLE OF CONTENTS

LIST OF TABLES

LIST OF FIGURES

LIST OF ABBREVIATIONS

ABS	Acrylonitrile Butadiene Styrene
AM	Additive Manufacturing
ASTM	American Society for Testing and Materials
CAD	Computer-Aided Design
CAGR	Compound Annual Growth Rate
CF	Carbon Fibre
CFRC	Continuous Fibre-Reinforced Composite
CNC	Computer Numerical Control
CT	Computed Tomography
DCB	Double Cantilever Beam
DIC	Digital Image Correlation
DIW	Direct Ink Writing
DSC	Differential Scanning Calorimetry
ESPI	Electronic Speckle Pattern Interferometry
FDM	Fused Deposition Modelling
FEA	Finite Element Analysis
FFF	Fused Filament Fabrication
FGF	Fused Granular Fabrication
HIPS	High-Impact Polystyrene

ISO	International Organization for Standardization
MEAM	Material Extrusion Additive Manufacturing
MFI	Melt Flow Index
PA	Polyamide
PC	Polycarbonate
PCHIP	Piecewise Cubic Hermite Interpolating Polynomial
PE	Polyethylene
PEEK	Polyether Ether Ketone
PEI	Polyetherimide
PET	Polyethylene Terephthalate
PETG	Polyethylene Terephthalate Glycol
PLA	Polylactic Acid
PMMA	Polymethyl Methacrylate
POM	Polarized Optical Microscopy
PP	Polypropylene
PPS	Polyphenylene Sulfide
SEM	Scanning Electron Microscopy
SENB	Single Edge-Notched Bending

LIST OF SYMBOLS AND UNITS OF MEASUREMENTS

a	Notch depth (mm)
a_0	Initial length of surface asperity in Lee-Springer model (μm)
b_0	Initial width of surface asperity in Lee-Springer model (μm)
D_h	Degree of healing
$D_{extrudate}$	Extrudate diameter (mm)
D_{nozzle}	Nozzle diameter (mm)
D_{ic}	Degree of intimate contact
E	Elastic modulus (MPa)
E_a	Activation energy (kJ/mol)
H	Layer height (mm)
K	Pre-exponential factor (Pa·s)
K_ϵ	Strain concentration factor
$K_{\epsilon-notch}$	Strain concentration factor at the notch
n	Power-law index
P	Contact Pressure (MPa)
Q	Volumetric flow rate (mm^3/s)
r	Notch root radius (μm)
R	Universal gas constant (J/(mol·K))
R_a	Arithmetic mean surface roughness (μm)

R_c	Roughness parameter
R_q	Root mean square surface roughness (μm)
S^{rd}	Spatial resolution of displacement (mm)
$S^{r\epsilon}$	Spatial resolution of strain (mm)
t	Time (s)
t_c	Contact time (s)
T	Temperature (°C)
T_g	Glass transition temperature (°C)
T_m	Melting temperature (°C)
t_R	Reptation time (s)
t_w	Welding time (s)
W	Nominal extrudate width or Layer width (mm)
W_{bond}	Bond width (mm)
w_0	Initial spacing between asperities in Lee-Springer model (μm)
X_c	Degree of crystallinity (%)
γ	Surface tension (N/m)
$\dot{\gamma}$	Shear rate (s^{-1})
ϵ_{yy}	Strain in y-direction (mm/mm)
$\epsilon_{yy\text{-}n}$	Nominal strain in y-direction (mm/mm)
$\epsilon_{yy\text{-}n\text{-}failure}$	Nominal strain in y-direction before failure (mm/mm)

θ	Notch angle (°)
μ	Viscosity (Pa·s)
σ	Stress (MPa)
σ_{VM}	Von Mises stress (MPa)
τ_c	Capillary time (s)

INTRODUCTION

0.1 Research Background

Additive manufacturing (AM) encompasses a broad range of processes that fabricate components through the controlled, incremental addition of material, in contrast to conventional subtractive or formative methods. By constructing parts layer by layer, AM enables geometrical complexity far beyond what is typically achievable with traditional manufacturing techniques. While AM spans multiple material classes, including metals, ceramics, and polymers, polymer-based technologies remain the most extensively employed and are projected to exceed a market value of USD 36 billion by 2031 (Meticulous Market Research Pvt Ltd, 2024).

Among polymer AM techniques, material extrusion additive manufacturing (MEAM), which encompasses fused filament fabrication (FFF) and fused granular fabrication (FGF), has emerged as one of the most accessible and rapidly developing categories (Maguire, Pottackal, Saadi, Rahman & Ajayan, 2021). In addition to advantages in material availability and printer cost, thermoplastic MEAM offers ease of use compared to other AM methods and potential sustainability benefits through reduced waste and recyclability (Zander, Gillan, Burckhard & Gardea, 2019). Recent advancements have extended MEAM from small desktop systems to large-format platforms capable of producing metre-scale components, mould tooling, architectural structures, and industrial fixtures (Goh, Wong, Tan, Seet & Nai, 2024).

These advancements, including improvements in extrusion hardware, pellet-fed systems, and toolpath strategies, have enhanced the reliability, precision, and scalability of polymer-based MEAM. As the technology continues to progress in terms of scale, speed, and material capability, its applications are expected to expand across sectors such as aerospace, automotive, construction, and biomedical engineering (Tientcheu, Djouda, Bouaziz & Lacazedieu, 2024).

0.2 Problem Statement and Objectives

Despite the rapid growth and expanding industrial interest in polymer-based MEAM, significant challenges continue to limit its broader implementation, particularly for high-performance applications. Achieving a successful print remains nontrivial for certain geometries, as print quality is highly sensitive to several processing parameters. Additionally, MEAM parts generally exhibit reduced dimensional accuracy and poorer surface resolution compared to components produced through conventional polymer-processing techniques (Tao, Fu & Zhong, 2025). Most critically, the mechanical properties of MEAM components are inherently anisotropic and often inferior to those of their bulk counterparts, restricting the technique's adoption largely to prototyping and non-structural applications (Spiller, Berto & Razavi, 2022).

At present, no reliable predictive or optimization tools exist that can consistently relate printing parameters to final part performance across different materials, geometries, and process conditions. Current practice, therefore, relies heavily on trial-and-error parameter tuning, which is inefficient and offers limited scientific insight. A major barrier to developing such tools is the incomplete understanding of the mechanisms through which printing parameters influence the behaviour of printed parts. These mechanisms may represent one of the missing links between process settings and part performance, and clarifying them is essential for advancing modelling and optimization efforts.

While the full challenge is broad, this thesis contributes to addressing it by examining some of the less-studied mechanisms influenced by process parameters that govern mechanical behaviour in MEAM parts, with the aim of strengthening the fundamental understanding needed for more reliable prediction, control, and future optimization of the process.

0.3 Outline

This thesis is structured as follows. Chapter 1 presents an overview of the academic literature relevant to polymer-based MEAM and identifies areas where further investigation is required. Chapter 2 outlines the specific objectives of the thesis and describes how each subsequent chapter contributes to them. Chapters 3 through 6 present the main research findings. The thesis then concludes with a Conclusions section, which summarizes the key contributions of this work, followed by a Recommendations section outlining directions for future research.

CHAPTER 1

LITERATURE REVIEW

1.1 Material Extrusion Additive Manufacturing

Defined by ISO/ASTM 52900 as one of the seven core AM categories, MEAM involves the selective extrusion of material through a nozzle to construct parts layer by layer. The technology has since evolved into a versatile platform capable of processing a diverse range of feedstocks. Although polymer extrusion represents the dominant form, several variants have emerged to accommodate pastes, inks, hydrogels, ceramics, and metal–polymer mixtures (G. Rocha, Saiz, S. Tirichenko & García-Tuñón, 2020; Oleff, Küster, Stonis & Overmeyer, 2021).

Extrusion of pastes and inks, most commonly implemented through direct ink writing (DIW), enables the deposition of viscoelastic or particle-laden formulations. DIW is widely used for architected materials, soft robotics, energy devices, and electronic structures (Yang *et al.*, 2021). Robocasting represents a ceramic-focused branch of DIW, relying on concentrated ceramic slurries that are deposited and later sintered to achieve fully dense components (Lamnini *et al.*, 2022). Extrusion-based bioprinting extends the approach to cell-laden hydrogels and bioinks, allowing the fabrication of tissue-engineered constructs under mild processing conditions (Li & Cui, 2021; Jeon, Park, Moon & Yang, 2025). MEAM has also been adapted for metal and ceramic composites through bound metal/ceramic extrusion routes, in which powder-loaded polymer filaments are printed and subsequently debound and sintered (Gonzalez-Gutierrez *et al.*, 2018; Rane & Strano, 2019).

While these variants are increasingly explored for specialized applications, polymer-based MEAM remains predominant due to the relative ease of processing polymers compared to metals or ceramics, the lower processing temperatures required, and the broad range of available materials, ranging from commodity plastics to engineering-grade thermoplastics. In addition, polymer extrusion is highly accessible, with printers available across a wide range of costs, materials readily obtainable, and minimal post-processing required. These factors

have established polymer extrusion as a preferred method for both rapid prototyping and the fabrication of selected functional components (Maguire *et al.*, 2021; Verbeeten & Lorenzo-Bañuelos, 2022). The following sections focus specifically on polymer-based MEAM processes, including filament-fed and pellet-fed systems.

1.1.1 Fused filament fabrication

FFF, often commercially known as fused deposition modelling (FDM), is the most widely adopted method within the MEAM family and remains the most common 3D printing process worldwide (Grand View Research, 2024). In this process, illustrated schematically in Figure 1.1(a), a thermoplastic filament is fed through a heated nozzle and deposited layer by layer to build a three-dimensional object. The material strand deposited by the nozzle, referred to as the extrudate, serves as a fundamental building block of the printed part. The nozzle moves in the horizontal X–Y plane to trace each layer, while the build platform or print head shifts vertically to initiate subsequent layers.

Owing to its simplicity, low equipment cost, and compatibility with a broad range of thermoplastic materials, FFF is extensively used for rapid prototyping, concept modelling, small-batch production of tooling and fixtures, consumer-grade parts, and, in some cases, end-use components across sectors such as automotive, healthcare, and education (Buj-Corral, Tejo-Otero & Fenollosa-Artés, 2021; Krishnanand & Taufik, 2021). From a market perspective, the FFF equipment market was valued at approximately USD 2.9 billion in 2024 and is projected to reach around USD 7.8 billion by 2033, corresponding to a compound annual growth rate (CAGR) of roughly 11.5% over the period 2025–2033 (DataHorizzon Research, 2024).

1.1.2 Fused granular fabrication

FGF operates on a concept similar to filament-based MEAM, but uses thermoplastic pellets as feedstock, which are directly melted or softened and extruded through a screw-based system, as schematically shown in Figure 1.1(b) (Sun, Rizvi, Bellehumeur & Gu, 2008). The screw

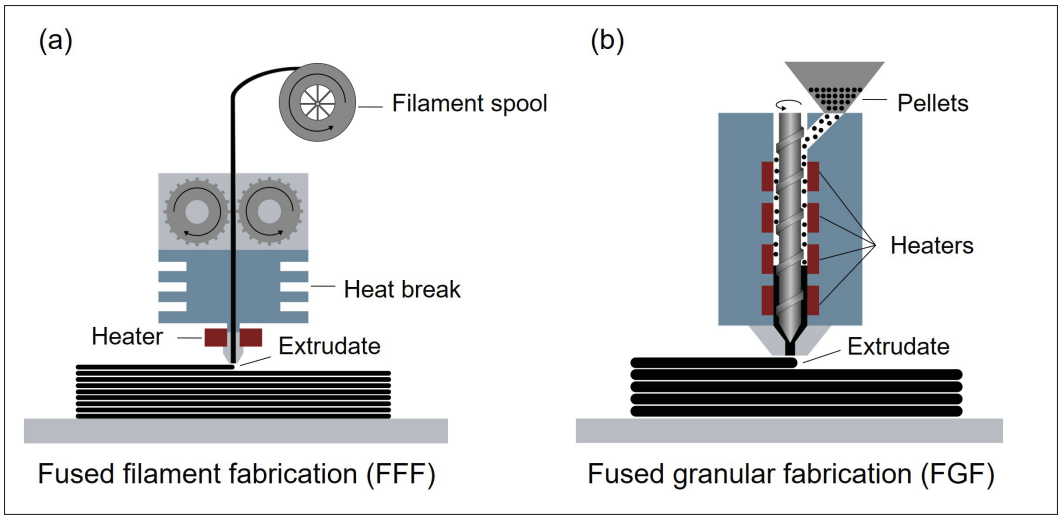

Figure 1.1 Schematic representation of polymer-based MEAM processes: (a) FFF, where a thermoplastic filament is fed through a heated nozzle and deposited layer by layer; and (b) FGF, which employs a screw-based extruder to melt and deposit thermoplastic pellets for larger-scale part production

mechanism enables higher throughput and the production of medium-to-large-scale components, reaching sizes up to several metres, which would be challenging with filament-based systems (Penumakala, Santo & Thomas, 2020; Pignatelli & Percoco, 2022). FGF offers advantages such as lower material cost, wider material selection, improved scalability, and the ability to process regrind or compounded materials for recycling (Goh *et al.*, 2024; Patel & Taufik, 2022). This makes it suitable for large-format additive manufacturing, moulds and tooling, structural prototypes, furniture, marine components, and architectural elements. Trade-offs include coarser surface finish and larger machine footprints compared to FFF. By moving from filament to pellet feedstock, FGF extends polymer MEAM to applications requiring larger parts, higher deposition rates, and enhanced material efficiency.

1.1.3 Materials

FFF and FGF processes encompass a broad range of thermoplastic feedstocks, from virgin polymers to reinforced and recycled formulations. The choice of material plays a critical role

in determining processability, mechanical performance, and the final application of printed components (Leśniowski, Stawiarski & Barski, 2025).

Thermoplastics used in FFF and FGF can be broadly classified as amorphous or semi-crystalline, with the main difference in printing behaviour being the tendency to warp. Amorphous polymers such as polyethylene terephthalate glycol (PETG), acrylonitrile butadiene styrene (ABS), polycarbonate (PC), polymethyl methacrylate (PMMA), and polyetherimide (PEI) exhibit relatively low shrinkage and more uniform cooling, making them easier to print with stable dimensional accuracy. In contrast, semi-crystalline polymers such as polyethylene (PE), polypropylene (PP), polyamide (PA, e.g., nylon), and polyether ether ketone (PEEK) are more prone to warpage (Rane & Strano, 2019; Zerriouh *et al.*, 2025). This is because the formation of crystalline regions during cooling introduces additional shrinkage and internal stresses between layers, making the printing process more challenging. Semi-crystalline polymers may also develop uneven temperature gradients during cooling, which can further increase the risk of delamination and dimensional distortion (Zerriouh *et al.*, 2025; Turner & Gold, 2015).

To extend the capabilities of FFF and FGF, polymer matrices are frequently reinforced with fibres, particles, or functional fillers. Short fibre–reinforced composites (e.g., carbon or glass fibres) improve stiffness and dimensional stability, while continuous fibre composites achieve higher specific strength, making them suitable for structural and aerospace applications (Billah, Lorenzana, Martinez, Wicker & Espalin, 2020; Sam-Daliri *et al.*, 2023; Ding *et al.*, 2023).

Particulate and nanofillers, such as carbon black, graphene, or ceramic particles, are incorporated to tailor electrical, thermal, or wear properties. These filled systems extend these techniques beyond prototyping, enabling functional parts with application-specific performance (Vidakis *et al.*, 2021b; Arif *et al.*, 2020). However, the inclusion of such additives increases the complexity of the process, influencing melt flow behaviour, thermal gradients, and interlayer bonding mechanisms that ultimately govern the printed part's properties (Hassanifard & Behdinan, 2024; Gao *et al.*, 2021; Bernagozzi, Battegazzore, Arrigo & Frache, 2023).

In parallel, sustainability concerns have driven growing interest in recycled and bio-based materials. Recycled polymers such as PLA, PET, and PP are increasingly reprocessed into filaments or pellets for use in both FFF and FGF systems. Likewise, bio-based polymers derived from renewable sources offer pathways to reduce the environmental footprint of these methods (Toth, Slezák, Bocz & Ronkay, 2024). Despite these advantages, recycled materials often exhibit reduced molecular weight and thermal stability, requiring careful processing or blending strategies to maintain print quality and mechanical integrity (Zander *et al.*, 2019).

1.1.4 Limitations of FFF/FGF processes

While thermoplastics dominate the 3D printing plastic market (Pulidindi & Ahuja, 2024), polymer-based MEAM techniques account for a relatively small share of the parts produced by commercial additive manufacturing services. This suggests that for functional or high-performance parts, other AM methods are generally preferred because they offer superior performance (Sher, 2024a).

The factors that limit part performance in FFF and FGF stem from the inherent characteristics of layer-by-layer material deposition. Key challenges include maintaining dimensional accuracy, achieving consistent mechanical properties, and reliably predicting the final behaviour of printed components. The following subsections discuss these aspects in detail.

1.1.4.1 Dimensional accuracy

Dimensional accuracy is one of the performance indicators in MEAM, reflecting how closely the printed geometry matches the intended design. The achievable resolution strongly depends on the extrusion system and scale. In FFF, the typical resolution ranges between 100 and 400 µm, limited primarily by nozzle diameter and layer height, while FGF systems, designed for large-scale fabrication, generally achieve coarser resolutions of about 1–5 mm due to higher flow rates and larger nozzle sizes (JuggerBot 3D, 2023).

Several factors contribute to dimensional inaccuracy in these processes. One is warpage, caused by thermal contraction and residual stresses during cooling, which can lead to distortion or curling of printed parts (Zerriouh *et al.*, 2025). Another important factor is die swell, referring to the expansion of the molten polymer as it exits the nozzle due to the elastic recovery of stretched polymer chains. This phenomenon increases the extrudate diameter beyond its nominal value, altering bead width and layer geometry (Smith *et al.*, 2024). Flow inconsistencies, arising from uncalibrated extrusion rates, variations in melt viscosity, or fluctuations in screw speed, further compound the problem—particularly in FGF systems where pressure and temperature fluctuations are more pronounced (Fontana, Giubilini, Arrigo, Malucelli & Minetola, 2022). In addition, the inherent shape of the extrudates leads to a rippled or ridged surface texture, as adjacent strands and layers do not form a perfectly smooth interface. This surface roughness is intrinsic to the layer-by-layer nature of the process (Sun, Mazur & Cheng, 2023).

A range of strategies is employed to minimize these deviations. Process optimization, including fine-tuning of extrusion temperature, speed, and layer height, helps reduce surface ridges, limit thermal distortion, and improve extrudate uniformity. Flow calibration tools and real-time monitoring systems can compensate for die swell and ensure consistent material flow (Sun *et al.*, 2023; Bouzaglou, Golan & Lachman, 2023; Oleff *et al.*, 2021). To improve final surface quality, post-processing techniques are often applied. In large-scale FGF parts, surface machining or milling is commonly used to restore dimensional accuracy. In small-scale FFF components, vapour polishing, in which the surface is briefly exposed to a solvent vapour that softens and smooths the outer polymer layer, can significantly reduce roughness and enhance the surface finish (Castro-Casado, 2021).

Overall, achieving high dimensional accuracy in FFF and FGF remains a balance between process control, material behaviour, and post-processing, particularly as part size and material complexity increase.

1.1.4.2 Mechanical performance

Inferior mechanical performance represents one of the primary limitations of parts produced by MEAM. Mechanical performance in this study is specifically defined by the part's ability to withstand external loads, characterized by its tensile strength, stiffness, and toughness. Compared to conventionally manufactured polymers, such as those produced by injection or compression moulding, MEAM components generally exhibit lower overall mechanical performance (Spiller *et al.*, 2022; Priyanka, Kumar, Reddy & Tadepalli, 2021; Cuan-Urquizo *et al.*, 2019). These parts also display pronounced anisotropy, with higher strength in the longitudinal direction (0°), where the extrudates are aligned with the applied load. In contrast, the transverse direction (90°), where the load is perpendicular to the extrudate orientation, exhibits significantly weaker properties (Ghorbani, Koirala, Shen & Tehrani, 2022; Jeon *et al.*, 2025).

Numerous studies (e.g., Khan, Joshi & Deshmukh, 2022; N. Turner, Strong & A. Gold, 2014; Cuan-Urquizo *et al.*, 2019; Popescu, Zapciu, Amza, Baciu & Marinescu, 2018; Bartolai, Simpson & Xie, 2018) have sought to establish relationships between printing parameters and final part quality, as well as to identify the underlying mechanisms responsible for this performance gap. These efforts, along with a detailed discussion of the factors governing the mechanical response of printed parts, are further explored in the following sections.

1.2 Impact of Printing Parameters on Mechanical Performance

A substantial body of research has investigated the influence of printing parameters on the mechanical performance of MEAM parts. These parameters can be broadly classified into process parameters, which include layer height, extrusion width, printing speed, and nozzle and build platform temperatures, and structural parameters, such as infill pattern, infill density, and part orientation. While structural parameters often have a strong effect on mechanical properties, the present work focuses on process parameters as they govern the thermal, rheological, and interlayer conditions that ultimately determine how closely a printed part can approach bulk material behaviour .

Several comprehensive reviews have attempted to identify consistent trends and draw general conclusions regarding the influence of process parameters on the mechanical performance of printed parts (Bouzaglou *et al.*, 2023; Gao, Xu, Xu, Tang & Liu, 2022; Khan *et al.*, 2022; Doshi, Mahale, Kumar Singh & Deshmukh, 2022; Bakhtiari, Aamir & Tolouei-Rad, 2023; Popescu *et al.*, 2018; Jaisingh Sheoran & Kumar, 2020; Tientcheu *et al.*, 2024). Despite extensive research, conclusions in the literature remain inconsistent. Reported trends often conflict; as an example, while some studies find that greater layer height increases strength (Pan, Huang, Guo & Liu, 2016; Torres, Cotelo, Karl & Gordon, 2015), others report the opposite (Kuznetsov, Solonin, Urzhumtsev, Schilling & Tavitov, 2018).

Such discrepancies indicate that directly linking individual printing parameters to mechanical performance oversimplifies the problem. The mechanical behaviour of MEAM parts is likely governed by the complex and interdependent relationships among multiple parameters. As a result, determining optimal printing parameters for a given geometry and material still largely relies on trial-and-error experimentation rather than systematic prediction. Recognizing these limitations, the present review focuses on the fundamental mechanisms that govern the mechanical response of printed parts, rather than considering only the influence of process parameters. Examining existing studies from this mechanistic perspective helps to clarify how processing conditions influence material behaviour and contribute to the final properties of MEAM components, providing a more coherent understanding of their mechanical performance.

1.3 Contributors to the Mechanical Performance

Four main mechanisms have been identified through which process parameters can influence the mechanical performance of printed parts. These mechanisms are schematically illustrated in Figure 1.2. The first mechanism relates to the properties of the extrudates themselves, which form the basic structural units of the part. The next two mechanisms are associated with the shape of the extrudates. The first refers to macrovoids that form between adjacent extrudates due to their typically oval cross-section, while the second involves sharp grooves at extrudate junctions, which act as stress concentrators and are referred to as interface notches. The final

and most extensively studied mechanism is the interlayer bonding quality between successive extrudates. Each of these mechanisms, and the ways in which the literature has examined them, is discussed in detail in the following sections.

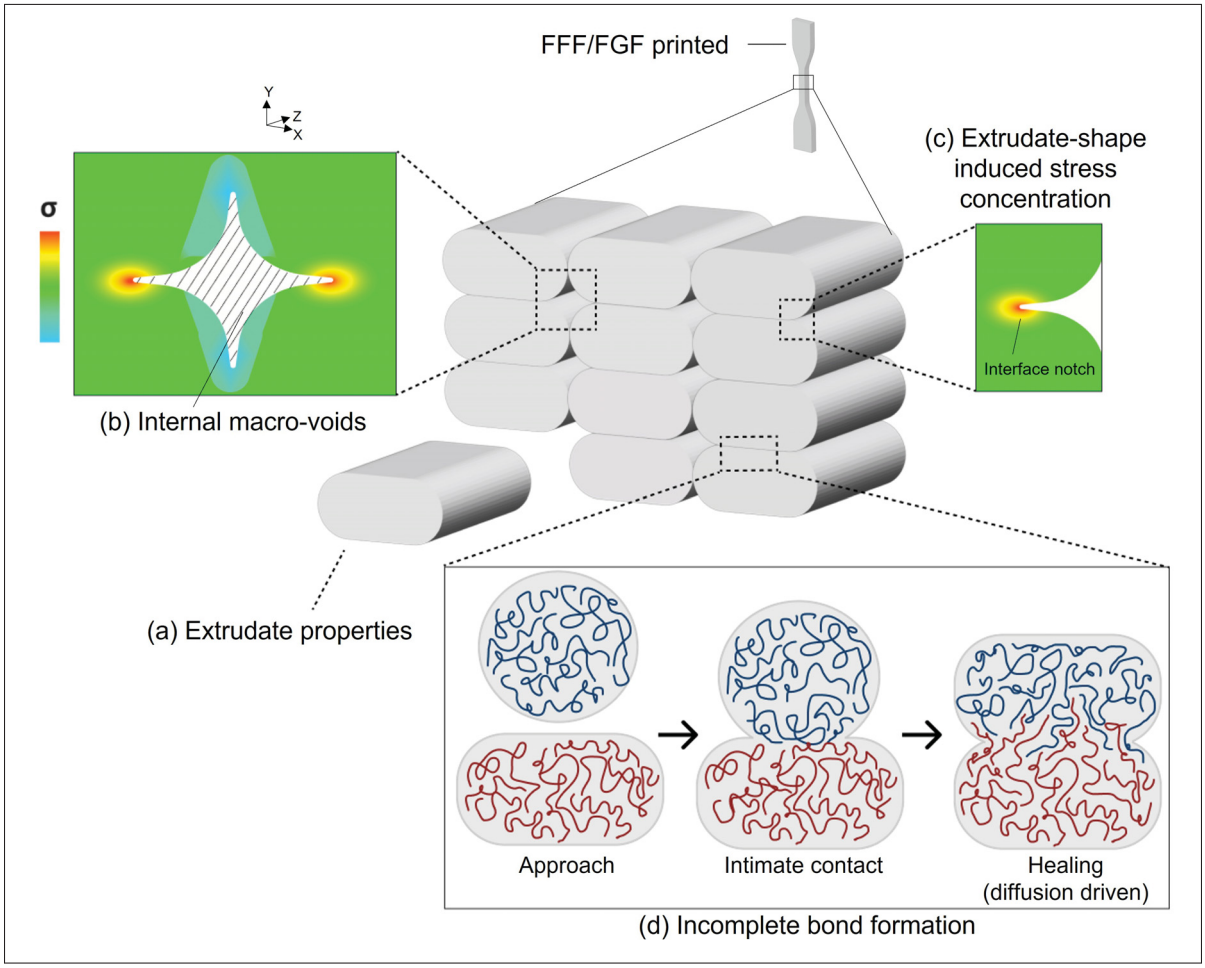

Figure 1.2 Schematic illustration of the four main mechanisms influencing the mechanical performance of MEAM parts: (a) Intrinsic properties of individual extrudates, (b) Macrovoids between adjacent extrudates arising from their oval cross-section, (c) Sharp grooves at extrudate junctions acting as interface notches, and (d) Interlayer bonding quality between successive extrudates

1.3.1 Extrudate properties

Extrudates constitute the basic structural units of printed parts, and their intrinsic properties play a crucial role in determining the overall mechanical performance, particularly in regions where the load is primarily borne along the extrudate direction. The properties of individual extrudates are largely governed by the extrusion process and the subsequent cooling conditions. These factors influence key physical attributes such as the degree of crystallinity, surface quality, geometric stability, and the presence of residual stresses. Variations in these characteristics can significantly affect the mechanical response and reliability of the final printed component.

While the testing approach is similar, it is important to differentiate between the characterization of the feedstock filament and that of the extrudate formed during printing. The feedstock filament is generally produced through screw extrusion, followed by stretching and quenching (Dey, Roan Eagle & Yodo, 2021), whereas during FFF, it undergoes rapid remelting, extrusion through a narrow nozzle, and deposition on the previous layer. Although the mechanical behaviour of feedstock filaments has been widely studied (Rodrigues *et al.*, 2023), only a limited number of works have examined how the FFF extrusion process itself modifies the extrudate properties.

Priyanka et al. investigated the tensile properties of PLA extrudates printed with a 0.4 mm nozzle as a function of gauge length (5, 10, and 15 cm). They reported reduced tensile strength and reliability in longer samples due to the increased probability of defects along the gauge section (Priyanka *et al.*, 2021). Barrasa et al. examined the effects of extrusion temperature and test strain rate on PLA extrudates, finding that higher extrusion temperatures (190 °C versus 180 °C) generally enhanced tensile strength. The study also demonstrated that natural aging at room temperature for up to 100 days significantly increased mechanical properties, with the elastic modulus rising from 2.4 GPa in one-day-old samples to 4 GPa after full aging, and the yield strength increasing from 40 MPa to 62 MPa. Aging conditions were identified that accelerate the attainment of maximum mechanical performance (Orellana Barrasa, Ferrández-Montero, Ferrari & Pastor, 2021; Orellana-Barrasa, Tarancón & Pastor, 2023). In a subsequent study, Barrasa et al. investigated the incorporation of magnesium particles into PLA. The addition of

magnesium increased crystallinity and slightly raised porosity and density, but no improvement in tensile strength was observed, as the particles primarily acted as crack nucleation sites rather than barriers to crack propagation (Orellana-Barrasa, Ferrández-Montero, Boccaccini, Ferrari & Pastor, 2022a).

For high-performance polymers, Comelli et al. investigated the effect of extrusion conditions on PEEK extrudates. The study showed that strong molecular orientation in the feedstock filament can persist after extrusion, as the relatively short heating time in FFF process is insufficient to erase the filament's initial microstructure, including crystallinity (Comelli, Davies, van der Pol & Ghita, 2022).

A key consideration in the extrusion process is the flow behaviour of the extrudate. Higher flow rates are often sought to increase printing speed; however, they can also affect extrudate morphology by inducing flow instabilities. Balani et al. reported that increasing the extrusion speed promotes such instabilities in PLA extrudates (Bakrani Balani, Chabert, Nassiet & Cantarel, 2019). On the other hand, Geng et al. demonstrated that very low extrusion speeds of PEEK can also lead to defects, as shown in Figure 1.3, where insufficient melt pressure produces surface irregularities such as cavities and bubbles. Images (a) to (d) compare open-air and deposited extrudates printed at low and high speeds, with their magnified views shown in images (e) to (h). In both cases, the low-speed samples exhibit more pronounced defects, highlighting the critical role of adequate melt pressure in maintaining extrudate quality (Geng *et al.*, 2019).

Domenech et al. investigated flow instabilities at different extrusion rates for PP of varying molecular weights. As shown in Figure 1.4, typical extrusion instabilities, known as melt fracture, are observed for the high molecular weight material at all extrusion speeds, with the period of the instability increasing as the flow rate rises. For the medium molecular weight material, melt fracture appears only at higher flow rates, while lower molecular weight grades remain largely stable across the range of tested speeds. These instabilities are attributed to the high shear stress experienced by the polymer melt at the capillary wall of the printing nozzle (Domenech *et al.*, 2025).

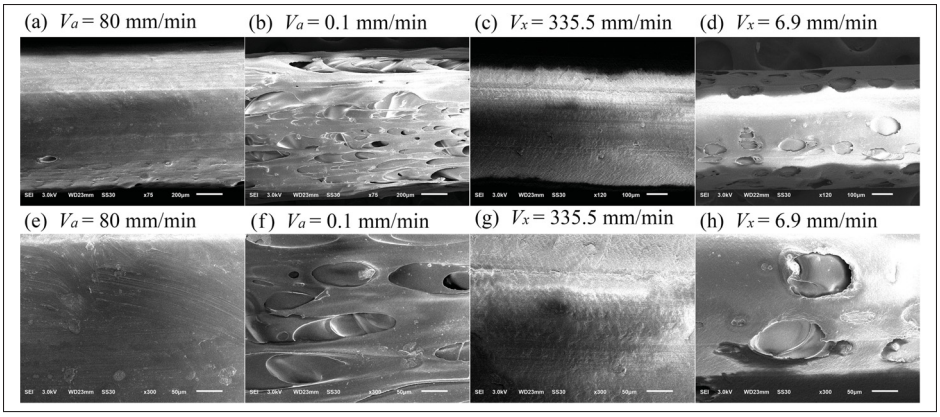

Figure 1.3 Surface morphology of PEEK extrudates at different speeds. (a) and (b) show open-air extrudates at low and high speeds, while (c) and (d) show deposited extrudates. (e) to (h) present magnified views of the corresponding images. Low-speed samples exhibit more pronounced defects, such as cavities and bubbles, due to insufficient melt pressure
Taken from Geng et al. (2019, p. 266)

The extrusion process also influences die swell. Heller et al. developed a computational model of polymer melt flow and extrudate swell and showed that swelling alters the orientation of short carbon fibres, reducing axial alignment, decreasing the axial modulus, and increasing the radial modulus (Heller, Smith & Jack, 2016). Smith et al. demonstrated that extrudate swell affects the overlap between printed filaments, where higher swell increases raster contact, reduces the presence of air gaps, and can improve mechanical performance (Smith *et al.*, 2024).

However, in the study conducted by Domenech et al., the authors reported a different behaviour. Although substantial die swell was observed at the nozzle exit in open air extrusion, the printed extrudates did not exhibit the dimensional changes commonly reported in the literature. Cross-sectional measurements and the evolution of extrudate geometry along the print path showed that die swell had very little influence on the final dimensions of the deposited filaments. The authors suggested that, under the confined flow conditions of FFF, the primary role of die swell could be related to interlayer adhesion and polymer chain orientation rather than to changes in geometric accuracy (Domenech *et al.*, 2025).

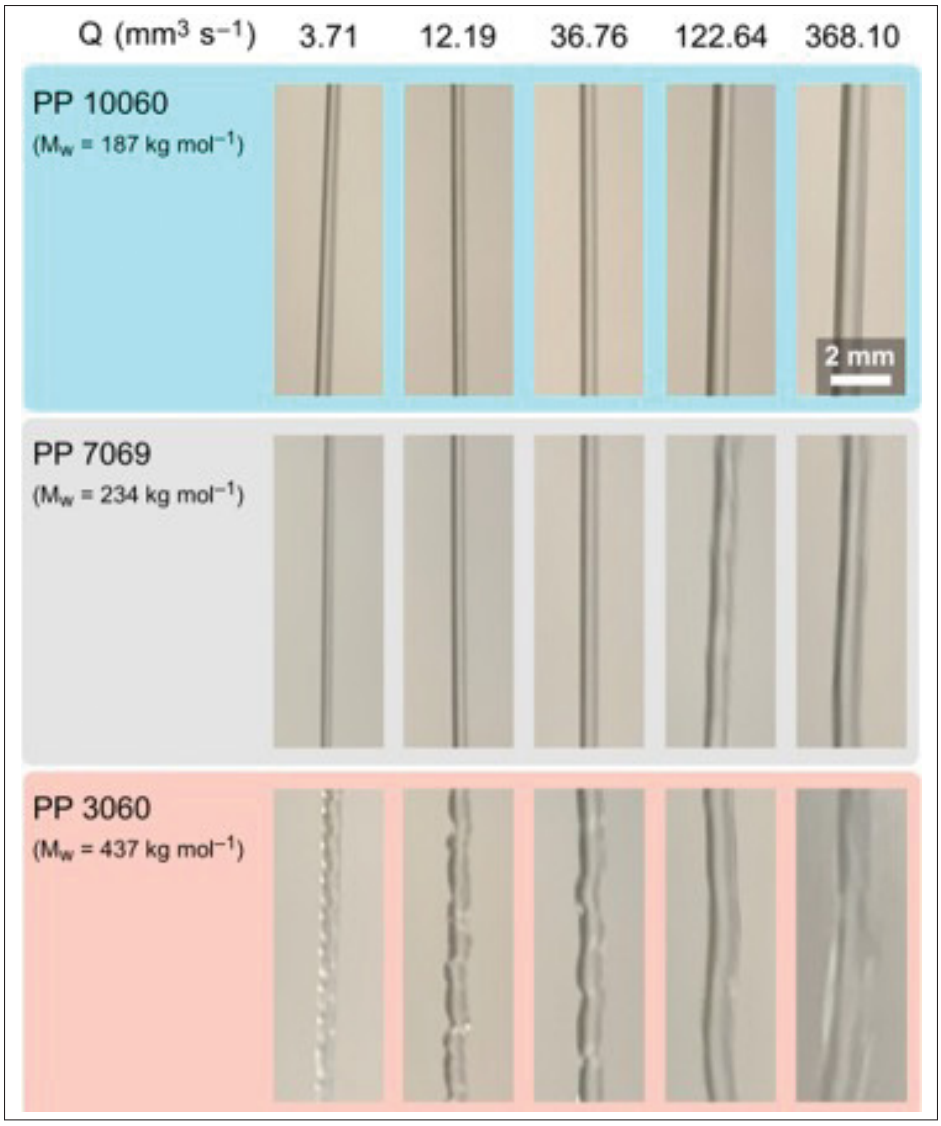

Figure 1.4 Extrusion flow instabilities in PP extrudates of different molecular weights at varying extrusion speeds. High molecular weight material exhibits melt fracture at all speeds, with the instability period increasing with flow rate. Medium molecular weight shows melt fracture only at high speeds, while low molecular weight remains largely stable
Taken from Domenech et al. (2025, p. 11393)

The interaction between extrudates in multi-extrudate and film configurations was studied by Patterson et al., who investigated single extrudates, series of extrudates, and thin printed films, with a focus on dimensional accuracy and the scalability of tensile performance. The authors

found that a printed series of extrudates exhibited greater strength than the sum of individual extrudates, suggesting that interactions between extrudates and their interfaces enhance energy dissipation and overall toughness (Patterson, Chadha, Jasiuk & Allison, 2023).

These studies highlight that extrudate properties are determined by a combination of material characteristics and extrusion conditions. While feedstock properties set the initial baseline, the extrusion process and subsequent interactions among extrudates can significantly modify the final performance. Understanding these effects is crucial for optimizing mechanical behaviour and reliability in MEAM-printed parts.

1.3.2 Extrudate geometry effects

The influence of the deposited extrudate on part performance can be attributed to two primary mechanisms. As shown in Figure 1.2(b), the first involves macrovoids that form between deposited extrudates, resulting from their inability to completely fill the gaps due to their inherent geometry. The second mechanism, illustrated in Figure 1.2(c), concerns geometric features at the junctions of bonded extrudates, referred to as interface notches. The following sections review the existing literature on each of these effects.

1.3.2.1 Macrovoids

Voids are widely recognized as a major cause of reduced mechanical performance and a significant source of anisotropy due to their typically non-uniform distribution in MEAM parts (Sun *et al.*, 2023; Zhang, Hu & Qin, 2025c; Eiliat & Urbanic, 2018; Jeon *et al.*, 2025). It should be noted that these process-induced voids must be distinguished from intentionally designed porosity, such as sparse infill, which serves functional purposes (Sun *et al.*, 2023; Yu *et al.*, 2023)

As shown in Figure 1.5, four main void types typically arise due to extrudate geometry and toolpath constraints (Sun *et al.*, 2023). (a) Macrovoids between extrudates (inter-track voids) form because the extrudates do not tessellate perfectly, leaving triangular or diamond-shaped gaps. These voids often represent the largest fraction of total porosity and have the greatest

impact on mechanical performance. (b) Layer underfill voids occur when adjacent extrudates fail to meet properly, often due to part geometries that are not exact multiples of the track width or limitations in slicer pathing. (c) Intra-extrudate voids, or intra-track voids, are smaller voids within individual extrudates, typically originating from thermal gradients, localized shrinkage, binder loss in metal MEAM, or fibre presence in composite filaments (Zhang *et al.*, 2025a; Spiller *et al.*, 2022). They are usually less detrimental but can still affect strength. (d) Surface Voids occur when curved surfaces are approximated by discrete layers, producing small gaps or stair-stepping effects. These mainly influence dimensional accuracy and surface quality, although they may introduce stress concentrators in structural regions (Zhang *et al.*, 2025a; Sun *et al.*, 2023).

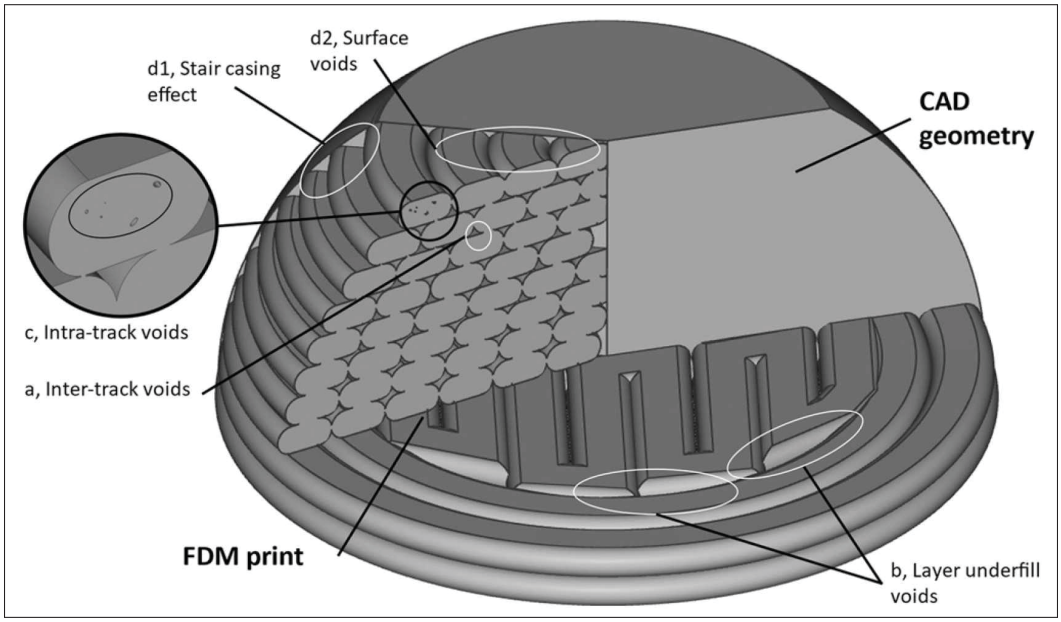

Figure 1.5 Schematic representation of the four main void types in MEAM parts. (a) Macrovoids (inter-track) form between extrudates, creating triangular or diamond-shaped gaps that strongly affect mechanical performance. (b) Layer underfill voids occur when adjacent extrudates fail to contact. (c) Intra-extrudate (intra-track) voids arise within individual extrudates due to thermal gradients, shrinkage, or material-specific effects. (d) Surface voids result from layer-wise approximation of curved surfaces, affecting dimensional accuracy and surface quality, and potentially introducing stress concentrators
Taken from Sun et al. (2023, p. 103463)

Kumar et al. reported that reducing void content from 3.79% to 1.91% increased tensile strength by 21.6% for ABS and 41.9% for carbon fibre–reinforced ABS (CF/ABS), and flexural strength by 16.1% for ABS and 12.1% for CF/ABS (Kumar *et al.*, 2021). Similarly, Joen et al. observed improvements of up to 103% and 143% in ultimate tensile strength in the longitudinal and transverse directions, respectively, following void reduction for carbon fibre-reinforced plastic parts (Jeon *et al.*, 2025). Mohseni et al. further highlighted that the influence of voids is particularly pronounced in complex geometries: minimizing voids in a non-linear end-use component led to a threefold improvement in mechanical response, compared to only a 1.5-fold increase for a simple linear dogbone sample (Mohseni, Suresh, Wille, Yarlagadda & Little, 2025). Some sources even suggest that eliminating voids entirely can yield near-isotropic properties, emphasizing the critical role of void control in achieving reliable, high-performance MEAM parts (Ghorbani *et al.*, 2022; Bond3D, 2025).

Void content in MEAM parts can be quantified using numerical or experimental approaches. Numerical methods offer rapid analysis and predictive capability by estimating void density from process parameters such as bead width, raster angle, and layer height. These models enable evaluation of the influence of printing conditions but rely on idealized assumptions about extrudate geometry and deposition (Eiliat & Urbanic, 2018; Jin, He, Xue & Fu, 2015). Experimental methods provide more accurate and direct measurements, although they are limited by resolution, speed, and cost. Common techniques include cross-sectional imaging obtained through cutting or freeze-fracture, followed by digital, optical, or SEM inspection (Ghorbani *et al.*, 2022; Wang, Xie, Weng, Senthil & Wu, 2016; Sun, Mazur & Cheng, 2025). Non-destructive methods such as computed tomography (CT) and radiography (Wang, Zhao, Fuh & Lee, 2019) allow characterization of void size, shape, and spatial distribution. Simpler techniques, including Archimedes' principle, can also be used to estimate total void volume fraction when high-resolution imaging is not required (Heidari-Rarani, Rafiee-Afarani & Zahedi, 2019).

Several strategies have been explored to reduce void formation in MEAM. Among these, pre-printing approaches focus on optimizing the printing setup and toolpath. For example, Mohseni

et al. demonstrated that adjusting the toolpath enhances extrudate placement (Mohseni *et al.*, 2025), while Eiliat et al. developed a mathematical model to optimize extrudate width, extrudate angle, and overlap percentage, thereby minimizing void area within each layer (Eiliat & Urbanic, 2018). Sun et al. proposed an interlaced deposition strategy in which each layer is printed in two alternating passes, specifically targeting inter-extrudate voids and achieving reductions in porosity of up to 65.5% (Sun *et al.*, 2025). Process parameter optimization, such as adjusting printing temperature and layer height, can also reduce void content (Akhoundi & Behravesh, 2019; Ghorbani *et al.*, 2022; Torres *et al.*, 2015). Feedstock modifications have also been investigated, including the incorporation of expandable microspheres that expand during post-processing to fill residual void space (Wang *et al.*, 2016; Zhang *et al.*, 2025c).

In addition to pre-printing strategies, in-situ techniques have been developed to reduce void formation during MEAM. Thermal methods, such as a heated build platform or localized pre-deposition heating with a laser, enhance material bonding and improve flow into voided regions (Han *et al.*, 2025; Torres *et al.*, 2015; Wach, Wolszczak & Adamus-Wlodarczyk, 2018). Ultrasonic vibration applied during printing can also lower polymer viscosity and promote material flow (Li *et al.*, 2018; Wu *et al.*, 2022). Ravoori et al. introduced an in-situ nozzle-integrated compression rolling technique, achieving a tenfold reduction in void formation along with increases of up to 154% in ultimate tensile strength and 495% in material toughness (Ravoori *et al.*, 2021). Krishnanand et al. developed an innovative in-situ pellet-filament co-extrusion system that addresses poor surface finish caused by the staircase effect. By combining two materials with different melt flow indices (MFI), the higher-MFI material flows into and fills staircase gaps and voids during printing, improving both surface quality and mechanical performance (Krishnanand, Singh, Singh & Shrivastava, 2025).

Post-processing techniques offer additional ways to reduce void content in MEAM parts. Thermal annealing promotes polymer reflow, decreasing porosity and improving surface finish, though excessive heating may affect dimensional accuracy. Chemical treatments, such as acetone etching for ABS (Castro-Casado, 2021), or laser polishing (Chai *et al.*, 2018), help reduce surface voids. Mechanical approaches, including ultrasonic treatment to apply pressure and vibration (Li *et al.*,

2018) and hydrostatic compression through a fluid medium (Jeon *et al.*, 2025), have also been shown to effectively reduce void content and enhance mechanical performance.

Although various strategies exist to mitigate voids in MEAM parts, a comprehensive understanding of void formation, their geometry, and predictive tools to anticipate voids at different scales is still lacking (Sun *et al.*, 2023). Addressing these gaps is essential for fully controlling part quality and mechanical performance.

1.3.2.2 Interface notches

While macrovoids have been extensively studied, the local phenomena at naturally formed interface notches have received less attention. As schematically illustrated in Figure 1.2(c), the sharp groove where two filaments join resembles a notch and can act as a stress or strain concentration region, potentially leading to premature failure. These notches can occur on the surface of the printed part or within internal voids.

Allum et al. highlighted the significance of these features in printed PLA with single-extrudate geometries. The study showed that isotropic strength could be achieved in both transverse and longitudinal directions, although toughness and strain at break were lower in the transverse samples, attributed to the presence of interface notches. Finite element analysis (FEA), using an elastic–perfectly plastic material model, was conducted to examine the evolution of strain localization after yielding and to illustrate how interface-notch geometry drives the reduced toughness observed experimentally (Allum, Moetazedian, Gleadall & Silberschmidt, 2020c). The corresponding FEA strain-field results are shown in Figure 1.6. Introducing the same notch geometry into longitudinal samples resulted in isotropic behaviour, indicating that interface notches are a primary cause of anisotropy and that the bonding area exhibits the properties of bulk material. Moetazedian et al. also proposed that full bond strength is attainable across a wide range of printing conditions (Moetazedian, Allum, Gleadall & Silberschmidt, 2023).

Kundurthi et al. demonstrated that interface notches could reduce the effective transverse strength by up to 40%. Notch depth and notch root radius were identified as critical geometric factors

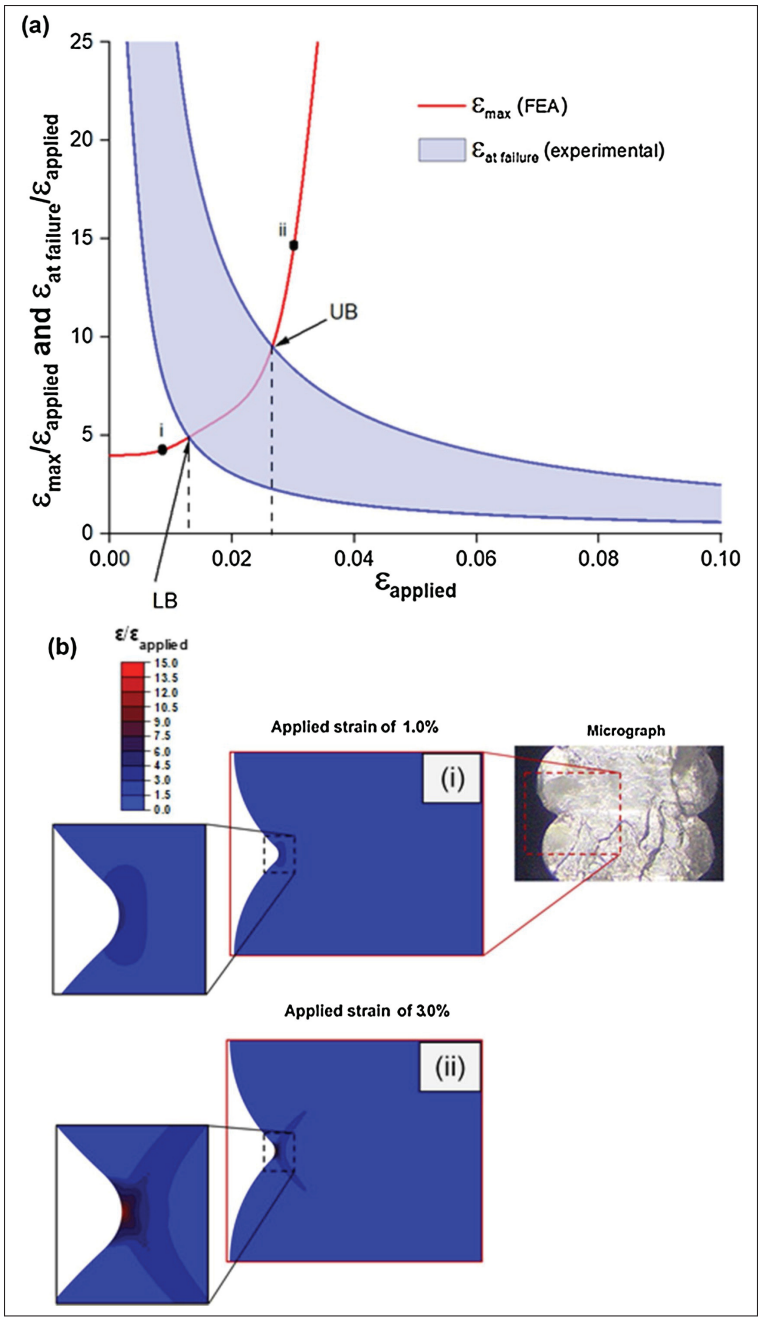

Figure 1.6 FEA results illustrating strain localization around an interface notch in single-extrudate PLA using an elastic–perfectly plastic material model. (a) Evolution of strain concentration as a function of applied strain, indicating the onset of post-yield strain localization. (b) Corresponding strain-field distributions at increasing applied strain levels, showing the development of localized deformation around the interface notch

Taken from Allum et al. (2020, p. 101297)

influencing the stress concentration factor. Parametric meso-scale FEA, shown in Figure 1.7, was used to derive a predictive relationship for the stress concentration factor, which increases with larger notch depth and smaller notch root radius (Kundurthi, Tran, Chen, Mapkar & Haq, 2023).

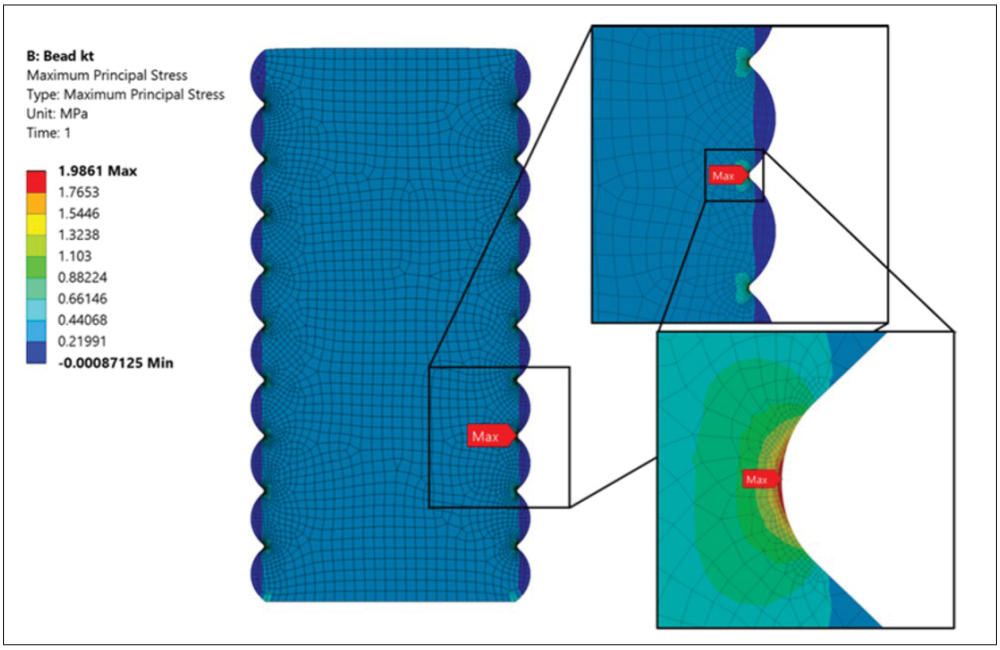

Figure 1.7 FEA of the stress field across a stack of layers using a linear elastic isotropic material model. The simulation shows the maximum principal stress field and highlights the influence of notch depth and root radius on the stress concentration factor
Taken from Kundurthi et al. (2023, p. 1438)

Park et al. investigated the influence of external notches on transverse tensile samples, showing that the notches act as stress concentrators, leading to random fracture locations and high variability in tensile strength measurements. By removing the notches via optimized laser cutting, fractures occurred consistently within the gauge section, yielding more reliable and reproducible tensile results (Park *et al.*, 2022). Ghorbani et al. used micromechanical numerical modelling to show that local stress fields in the transverse direction depend on extrudate shape and void geometry, although the mechanisms driving these variations are not yet fully understood (Ghorbani *et al.*, 2022). In a subsequent study, the authors used finite element simulations on representative volume elements to examine inter-extrudate voids and confirmed that these voids

act as stress concentrators, particularly reducing transverse stiffness and promoting extrudate debonding and layer delamination. The study also quantified how layer height, layer width, and overlap affect void size and local stress concentrations at extrudate interfaces (Gonabadi, Zamani Miandashti & Oila, 2025; Ghorbani *et al.*, 2022).

Similar conclusions have been reported in 3D-printed cementitious materials. He et al. examined interface notches in 3D-printed cement paste, characterizing notch depth and angle to assess their effect on interlayer strength. Tensile failure was found to initiate at these notches, reducing part strength, and numerical simulations further linked printing parameters to interlayer strength through the resulting notch geometry (He, Chow & Li, 2020).

These studies highlight the critical role of interface notches as localized stress concentrators in MEAM parts. Despite increasing evidence of their significance, the relationship between process parameters and the mechanisms governing notch formation remains unclear. Emerging evidence suggests that interface notches are not fixed geometric outcomes but can be systematically influenced and potentially minimized through optimized processing conditions.

1.3.3 Interlayer bonding

Interlayer bonding has been extensively studied in polymer-based MEAM, as it is widely recognized as one of the primary factors governing the mechanical performance and anisotropy of printed parts. The prevailing consensus is that rapid cooling during deposition limits the time and temperature available for polymer chain mobility, resulting in weaker bonds between adjacent layers (Penumakala *et al.*, 2020; Dey *et al.*, 2021; Khan *et al.*, 2022). Many studies describe interlayer bonding as a multi-step process. As illustrated in Figure 1.2 (d), it typically involves three key stages: the approach of the newly deposited extrudate toward the previously solidified one, the formation of intimate contact at their interface, and the subsequent interdiffusion (or healing) of polymer chains across that interface (Coogan & Kazmer, 2017b; Xu *et al.*, 2025; Bellehumeur, Li, Sun & Gu, 2004). Extensive work has focused on quantifying both intimate contact and healing, and these concepts have been used to formulate metrics such as degree of

bonding to assess interlayer performance. These two mechanisms will be discussed in more detail in the following sections.

1.3.3.1 Intimate contact development

Several studies have identified interlayer contact formation as a primary factor governing the ultimate bond strength between adjacent layers. In these studies, Intimate contact is quantified through the bond width that develops at the interface between two neighbouring extrudates. The extent of this contact determines how effectively load can be transferred across layers and establishes the foundation upon which subsequent healing and polymer interdiffusion can occur (Abbott, Tandon, Bradford, Koerner & Baur, 2018; Tronvoll, Welo & Elverum, 2018; Hart *et al.*, 2018; Bartolai *et al.*, 2018; Coogan & Kazmer, 2020; Zhang *et al.*, 2025a).

The development of intimate contact during printing has been examined and quantified through different modelling approaches. Several studies attribute contact formation primarily to capillary-driven wetting and coalescence between adjacent extrudates (Lepoivre, Levy, Boyard, Gaudefroy & Sobotka, 2021; Bellehumeur *et al.*, 2004; Sun *et al.*, 2008; Yin, Lu, Fu, Huang & Zheng, 2018). To describe this process, extrudates have often been idealized as spheres, where the decrease in necking angle between the two extrudates is taken as a measure of contact growth. The rate of this geometric evolution, and thus the progression of coalescence, is governed by the balance between surface-tension forces and viscous dissipation (Coogan & Kazmer, 2020; Lepoivre *et al.*, 2021). This modelling approach originates from the classical wetting model introduced by Pokluda et al. (Pokluda, Bellehumeur & Vlachopoulos, 1997), which considers the coalescence of two molten spheres in the absence of external forces. Building on this framework, Lepoivre et al. adapted the geometry from spheres to cylinders to better represent printed filaments and emphasized the importance of incorporating temperature-dependent surface tension to more accurately capture intimate-contact evolution (Lepoivre *et al.*, 2021).

An alternative perspective emphasizes that high cooling rates in typical FFF processes rapidly increase the polymer viscosity, limiting the contribution of capillary-driven wetting to con-

tact formation (Gao *et al.*, 2021; Coogan & Kazmer, 2019). In this view, pressure-driven contact development dominates. Coogan and Kazmer compared both mechanisms and concluded that pressure-induced intimate contact is the primary driver of contact development (Coogan & Kazmer, 2020).

This framework draws on the traditional intimate contact theory for composites originally proposed by Dara and Loos. In this model, surface asperities are idealized as non-uniform rectangles that deform under applied pressure and elevated temperature, progressively eliminating interfacial gaps. Contact is considered complete when the surfaces fully conform with no remaining voids at the interface (Loos & Dara, 1987). Lee and Springer later introduced a simplified asperity model using uniform rectangular features (Lee & Springer, 1987), as shown in Figure 1.8(a). In this modelling approach, described by Equation 1.1, the degree of intimate contact (D_{ic}) is determined by the surface roughness of the bonding interfaces, characterized by the parameters a_0, b_0 and w_0 shown in Figure 1.8 (b), as well as by the applied pressure (P) and the temperature-dependent evolution of Newtonian viscosity (μ).

$$D_{\mathrm{ic}}(t) = \left[\frac{1}{1 + \frac{w_0}{b_0}} \left(1 + 5 \left(1 + \frac{w_0}{b_0} \right) \left(\frac{a_0}{b_0} \right)^2 \int_0^{t_c} \frac{P}{\mu(T)}\, dt \right) \right]^{1/5} \tag{1.1}$$

When adapted to FFF, the model shifts focus from assessing the true extent of interfacial contact through the elimination of voids, as typically done in composite welding, to describing the evolution of the *apparent* contact area between bonding extrudates during deposition. As illustrated in Figure 1.9, each deposited extrudate is treated as a single asperity undergoing squeeze flow under its own weight and the applied deposition pressure. Greater deformation increases the bond width, resulting in a higher degree of intimate contact, calculated by the ratio of bond width (W_{bond}) to the nominal extrudate width (W) (Zhang *et al.*, 2025c; Coogan & Kazmer, 2019; Xu *et al.*, 2025).

Some studies have attempted to experimentally validate this model for FFF, although quantifying pressure remains challenging. Coogan and Kazmer measured pressure using a transducer

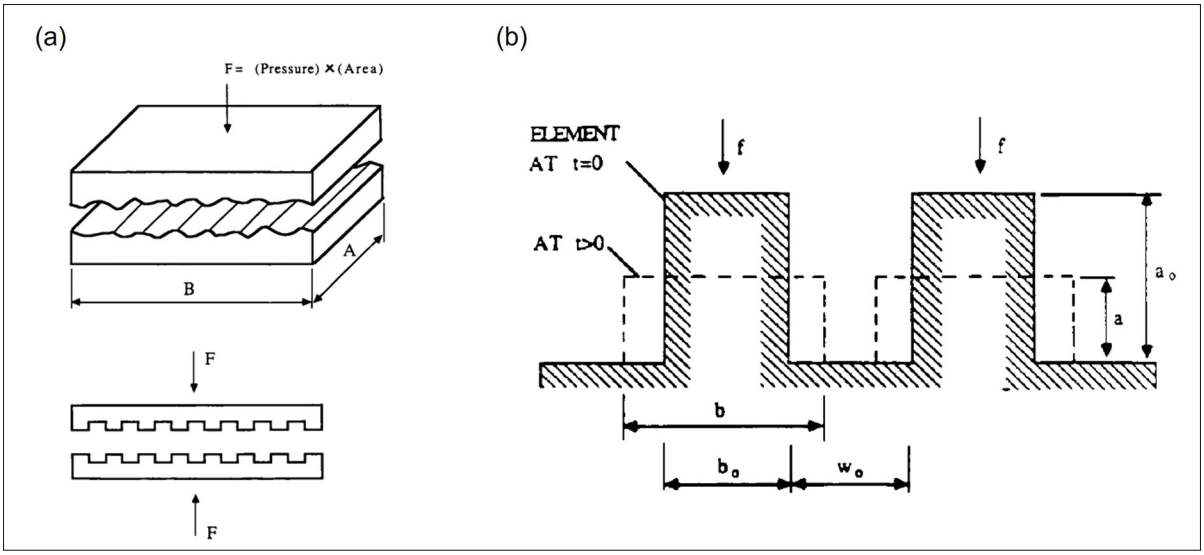

Figure 1.8 (a) Schematic of two plies being welded under elevated temperature and pressure, following the modelling approach of Lee and Springer, which represents surface asperities as identical rectangular features. (b) Surface roughness parameters of the rectangles, where a_0 is the initial length, b_0 the initial width, and w_0 the initial spacing between repeating rectangles
Taken from Lee & Springer, (1987, p. 017)

embedded within the nozzle, as illustrated in Figure 1.10. By subtracting the open-extrusion pressure from the in-print pressure, they obtained the effective exit pressure, which ranged from 0.012 MPa to 0.60 MPa and was used to estimate the contact pressure at the interface (Coogan & Kazmer, 2018).

Zhang et al. employed a force sensor beneath the build plate and estimated interface pressure by dividing the measured force by the extrudate cross-section (Zhang *et al.*, 2025a). Xu et al. used finite element simulations of the deposition process to determine the pressure distribution at the interface (Xu *et al.*, 2025).

In these studies, viscosity is obtained from rheological characterization and incorporated through temperature-dependent models, while surface roughness features are often treated as fitting parameters. The predicted degree of intimate contact is then compared with the measured ratio of bond width to extrudate width, with good agreement typically reported.

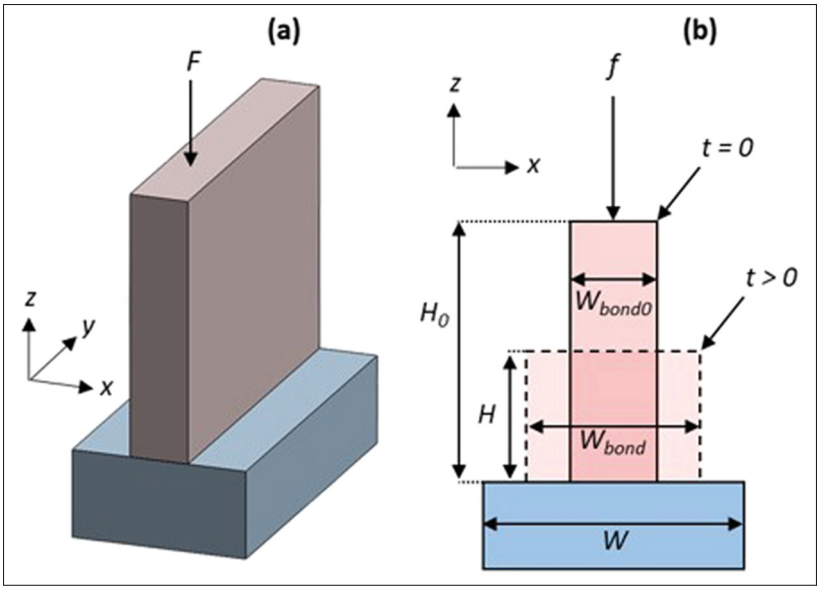

Figure 1.9 Adaptation of the Lee–Springer model for MEAM, where the deposited extrudate is modelled as a single asperity undergoing squeeze flow. Increased deformation leads to a larger bond width (W_{bond}) relative to the nominal extrudate width (W), enhancing interlayer contact
Taken from Coogan & Kazmer (2019, p. 1122)

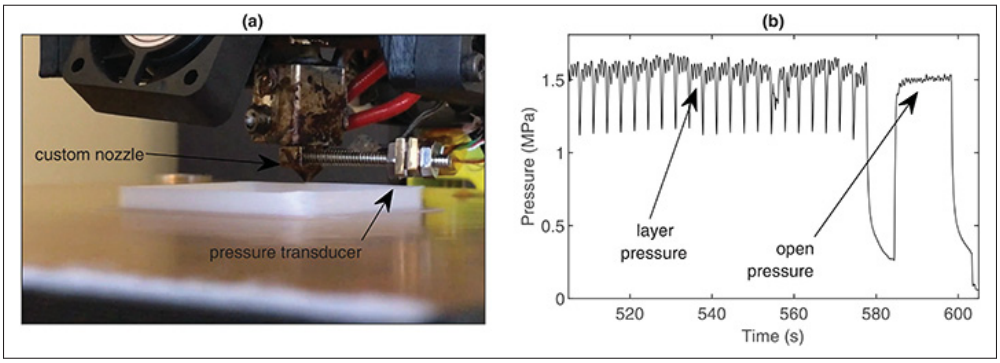

Figure 1.10 (a) Pressure measurement setup showing the transducer embedded within the nozzle to capture in-print pressure. (b) The last 100 seconds of the recorded pressure data, used to estimate the contact pressure by subtracting the open-extrusion baseline
Taken from Coogan & Kazmer (2018, p. 141)

In addition to modelling approaches, interpretations of increased contact vary across the literature. Some studies argue that increased contact directly enhances interlayer bonding, leading to stronger printed parts (Coogan & Kazmer, 2020; Zhang *et al.*, 2025a; Xu *et al.*, 2025). Others suggest that its primary benefit is the reduction of macrovoids between extrudates; by more effectively filling these gaps, the material exhibits improved overall performance independent of any increase in interfacial bonding strength (Han *et al.*, 2025; Torres *et al.*, 2015; Wach *et al.*, 2018).

1.3.3.2 Interface healing

At the moment the two surfaces come into contact, polymer chains begin to diffuse across the interface. This process is described by Wool's healing model (Wool & O'Connor, 1981)and de Gennes' reptation theory (de Gennes, 1971). According to this framework, which has been successfully used to explain many polymer welding phenomena, interfacial strength increases in proportion to the extent of chain diffusion. This model has also been effectively applied to describe bonding in the MEAM process. As illustrated in Figure 1.11, this theory assumes that polymer chains are entangled within a tube-like region that restricts their motion so that they cannot cross one another. Chain movement is therefore limited to forward and backward motion along the tube. When two polymer surfaces come into contact and begin to bond, chain ends near the interface disengage from their original tubes and form minor chains. Mechanical properties at the interface develop progressively as these minor chains interpenetrate across the boundary. At the reptation time (t_R), the minor chains have completely left their initial entanglements and fully diffused across the interface. Beyond this point, the molecular configuration becomes indistinguishable from the bulk, and the interface is considered fully healed. At high molecular weight, the chains are sufficiently long that full entanglement, and thus maximum strength, is reached earlier at the welding time (t_w), which is shorter than the reptation time.

The nonisothermal local degree of healing evolution with time is defined as:

$$D_h(t) = \left[\int_0^t \frac{1}{t_w(T)}\, dt \right]^{1/4} \tag{1.2}$$

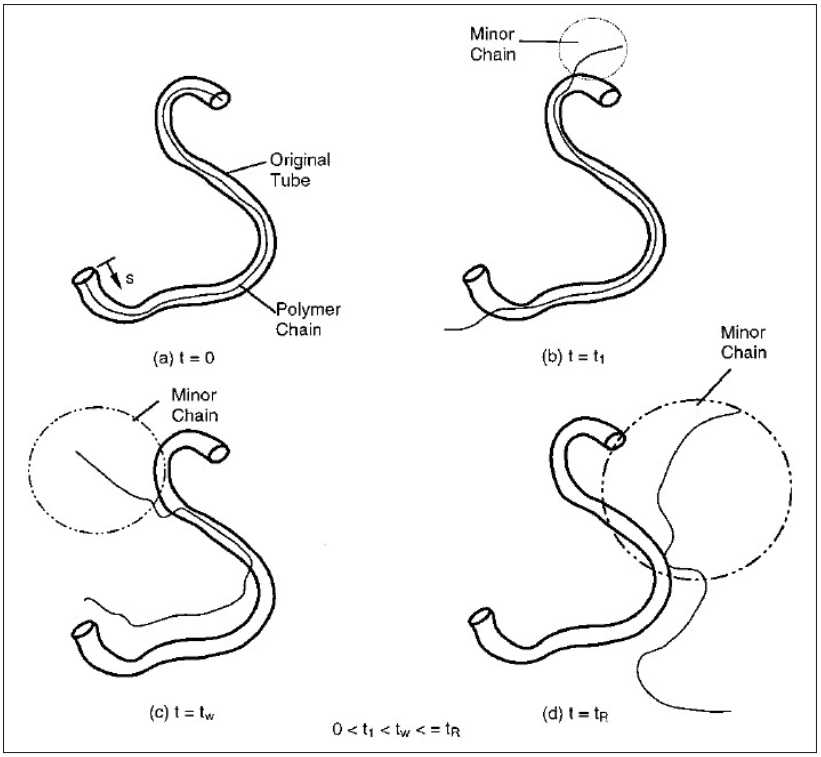

Figure 1.11 Schematic of polymer chain motion in reptation theory. Chains begin confined within tube-like regions; over time, chain ends move along the tube to form minor chains that progressively grow. At the reptation time, these minor chains reach their maximum length and the original chain has fully relaxed from its initial conformation
Taken from Yang & Pitchumani, (2002, p. 3213)

This equation is widely used to estimate the degree of healing in MEAM and predict the resulting mechanical strength (Coogan & Kazmer, 2017a; Zhang *et al.*, 2025c; Coasey, Hart, Wetzel, Edwards & Mackay, 2020; Lacambra-Andreu, Morelle, Maazouz, Chenal & Lamnawar, 2023). In this framework, any factor that enhances interlayer healing is expected to improve part performance, with heat transfer playing a key role. To achieve this, efforts have focused on reducing the cooling rate at the interface between a newly deposited extrudate and the underlying layer. Common strategies include the use of a heated chamber to slow the cooling of deposited material, in-situ laser heating of the underlying layer immediately before deposition of the next

extrudate, and other techniques such as ultrasonic vibration to promote better bonding (Han *et al.*, 2025; Han, Tofangchi, Deshpande, Zhang & Hsu, 2019; Li *et al.*, 2018).

Other factors can also influence polymer chain diffusion at the interface. In semi-crystalline polymers, crystallization can begin shortly after deposition, complicating the analysis of diffusion. Early crystal formation at the bonding region may hinder chain mobility and reduce the degree of healing (Domenech *et al.*, 2024). On the other hand, it has been reported that if sufficient chain diffusion occurs prior to crystallization, the subsequent growth of crystalline structures across the interface enhances bond strength by forcing the crack to follow a circuitous path around the spherulites (Barocio, Brenken, Favaloro & Pipes, 2022). Additives, such as fibres, can further affect the bonding behaviour and interlayer strength (Brenken, Barocio, Favaloro, Kunc & Pipes, 2018).

1.4 Assessment of Mechanical Behaviour–Mechanism Relationships

Mechanical properties of printed parts under varying process parameters have been extensively studied using a range of mechanical characterization methods. In some of these works, the observed behaviour has been linked to underlying mechanisms, and used to develop predictive models informed by these mechanistic insights. Mechanical characterization methods include tensile and compression tests, bending and torsion (e.g., three-point bending and twist loading), dynamic mechanical analysis, mode I fracture tests (mainly double cantilever beam and compact tension), fatigue and cyclic loading, as well as impact testing (Cuan-Urquizo *et al.*, 2019).

The underlying mechanisms investigated primarily include interdiffusion of polymer chains at interfaces, development of contact between extrudates, void content, extrudate geometry (including interface notches), and crystallization in semi-crystalline polymers.

For example, Faes et al. performed tensile tests on multilayer printed ABS samples in the transverse direction and reported improved mechanical properties when the layer time was reduced. They interpreted bonding as a thermally driven process involving contact, wetting, and diffusion of polymer chains, all of which are enhanced at lower cooling times. They also

observed that stronger interlayer bonds produced a more rugged fracture surface, as shown in Figure 1.12, with residues from the previous layer visible at the break, whereas weaker bonds resulted in a smoother interlayer fracture surface (Faes, Ferraris & Moens, 2016). Qi et al. took a similar approach with multilayer printed long-chain polyamide 12 (PA12) samples in the transverse direction and observed that higher nozzle temperatures improved bond strength by prolonging the time the polymer remains above glass transition temperature (T_g), thereby enhancing molecular diffusion. They also found that increasing the build platform temperature exerted an annealing effect, raising crystallinity in the extrudates and increasing strength in longitudinal samples (Qi *et al.*, 2021).

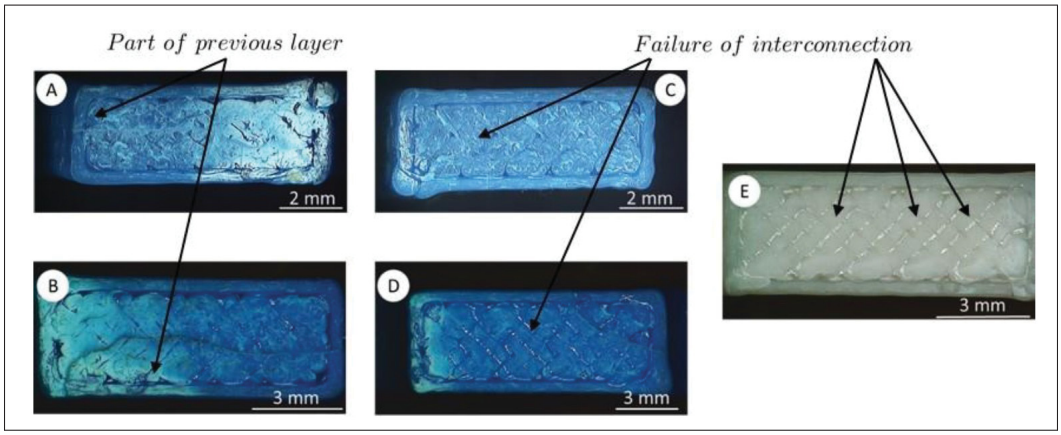

Figure 1.12 Fracture surfaces of multilayer ABS samples illustrating the effect of interlayer bonding: stronger bonds produce a rugged surface with residues from the previous layer, while weaker bonds result in a smoother interlayer fracture
Taken from Faes et al., (2016, p.748)

Zhou modelled the combined effects of contact formation and molecular diffusion to predict bond strength in transverse PLA samples. Using Gibbs free energy theory to describe diffusion and incorporating printing parameters through a process factor, the model showed good agreement with experimental tensile results (Zhou *et al.*, 2021) .

Barocio et al. developed a phenomenological model for carbon fibre reinforced polyphenylene sulphide (CF-PPS) composites that couples polymer reptation with crystallization kinetics to predict bond strength. They demonstrated that maintaining elevated interface temperatures

allows sufficient molecular diffusion before crystallization occurs, resulting in strong, interlocked bonds. Validation using double cantilever beam (DCB) fracture tests showed good agreement between the model and experimental strain energy release rates (Barocio *et al.*, 2022).

Waly et al. investigated crack propagation in printed PMMA parts using single edge-notched bending (SENB) tests. As shown in Figure 1.13, they identified two distinct fracture modes: crack deflection along the interface or penetration into subsequent layers. They determined that weak interlayer bonding promotes deflection, while stronger bonding resulting from reduced porosity and enhanced chain diffusion at higher nozzle temperatures enables the crack to penetrate the bulk material (Waly, Petersmann & Arbeiter, 2023). In a similar approach, Domenech et al. performed lap-shear tests on PP samples cut from printed stacks. Strength and failure mode (cohesive or adhesive) were linked to interlayer bonding, governed by chain interdiffusion, contact width between extrudates, and crystallization kinetics. Optimal conditions occur when crystallization time exceeds coalescence time, allowing maximum bonding before solidification. Stronger bonding results in higher strength and adhesive failure resembling the bulk material (Domenech *et al.*, 2024).

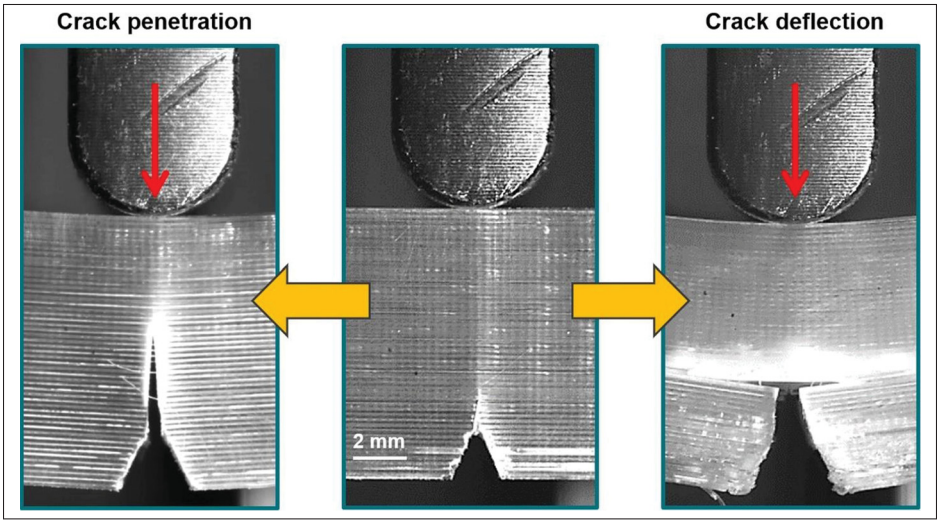

Figure 1.13 Fracture behaviour of PMMA showing crack deflection along weak interfaces and penetration into subsequent layers under stronger interlayer bonding conditions
Taken from Waly et al., (2023, p. 104032)

Coasey et al. performed SENB tests on printed ABS to validate the interface-healing model. They developed an analytical solution for the temperature profile, confirmed by infrared thermography, and applied it to their non-isothermal healing model. The results showed that higher nozzle temperatures increase the degree of healing and improve physical contact, leading to higher interlayer fracture toughness (Coasey *et al.*, 2020).

Vaes et al. performed mode III torsional fracture tests on pre-cracked single-layer PA walls printed under varying conditions. While their healing model correctly predicted increased bond strength with higher nozzle temperatures, it failed to capture the effect of build plate temperature. Contrary to expectations, higher plate temperatures reduced bond strength. Under these conditions, larger and more perfect spherulites were observed, and it was hypothesized that they caused chain disentanglement and a lower density of tie chains, making the interface brittle and weak (Vaes, Coppens, Goderis, Zoetelief & Van Puyvelde, 2021).

Ghorbani et al. identified voids and their geometry as the primary mechanism driving anisotropy in printed parts. They tested ABS tensile samples printed in transverse and longitudinal directions with varying void content and void shapes. Nearly isotropic properties were obtained when voids were minimized or eliminated (Ghorbani *et al.*, 2022).

Coogan and Kazmer developed a model combining interface healing with pressure-driven intimate contact to predict interlayer strength, validated through tensile testing of high-impact polystyrene (HIPS) samples. They found that incomplete interlayer contact was prevalent across most processing conditions, while insufficient diffusion occurred only at low temperatures, highlighting that achieving full contact is more difficult than achieving complete diffusion (Coogan & Kazmer, 2020). Similarly, Zhang et al. emphasized the importance of pressure-driven contact formation in printing continuous fibre-reinforced composites. They showed that increased printing pressure enhanced bond width, improved impregnation within fibre bundles, and promoted chain diffusion at the interface, all contributing to superior mechanical properties (Zhang *et al.*, 2025a). Xu et al. used contact pressure results from process simulations of different nozzle geometries to estimate the degree of intimate contact in PLA, which was

then coupled with a healing model to predict interlayer bonding. The model predictions were compared with tensile test results, indicating that the square nozzle geometry, which generated higher contact pressures, leads to improved bonding strength (Xu *et al.*, 2025).

Table 1.1 summarizes these studies, highlighting the mechanical testing methods used and the mechanisms considered in analyzing mechanical performance.

Table 1.1 Summary of studies on mechanical testing methods and mechanisms

Study	**Material**	**Testing Method**	**Mechanisms-Behaviour Relationship**
Faes *et al.*, 2016	ABS	Uniaxial tensile testing on multilayer printed sample	Reduced layer time improved thermally driven mechanisms (contact, wetting, and diffusion of polymer chains), resulting in better bonding and higher transversal strength
Qi *et al.*, 2021	PA12	Uniaxial tensile testing on multilayer printed sample	Higher nozzle temperature enhances chain diffusion, improving bonding and transverse strength. Higher platform temperature increases crystallinity, boosting longitudinal strength.
Zhou *et al.*, 2021	PLA	Uniaxial tensile testing on multilayer printed sample	Diffusion was described using Gibbs free energy theory, with printing parameters incorporated via a process factor.
Barocio *et al.*, 2022	CF-PPS	DCB test on multilayer samples. A thin film was inserted between layers during printing to initiate the crack	Diffusion model coupled with crystallization kinetics. Elevated interface temperatures allow sufficient molecular diffusion before crystallization, enhancing bond strength.

Study	Material	Testing Method	Mechanisms-Behaviour Relationship
Waly *et al.*, 2023	PMMA	SENB on multi-layer samples, performed in a 3-point bending arrangement	Higher nozzle temperatures reduce viscosity, which improves interlayer contact, thereby minimizing voids and enhancing polymer chain diffusion.
Domenech *et al.*, 2024	PP	Lap shear on single extrudate samples	Higher nozzle temperature enhances molecular diffusion before crystallization, while lower layer height increases contact pressure. These effects strengthen interlayer bonding and lead to cohesive failure.
Coasey *et al.*, 2020	ABS	SENB test on multi-layer samples with cracks initiated by inserted tape	Higher nozzle temperature reduces viscosity, increases molecular diffusion, and promotes greater physical contact area, resulting in a significant improvement in fracture toughness.
Ghorbani *et al.*, 2022	ABS	Uniaxial tensile testing on multilayer printed sample	Increasing the extrusion multiplier reduces void content, and void-free samples exhibit nearly isotropic mechanical properties.
Vaes *et al.*, 2021	PA	Mode III torsional fracture tests on pre-cracked single-layer walls	Diffusion model correctly predicted increased bond strength at higher nozzle temperatures. Model failed to predict decreased bond strength at higher platform temperatures, likely due to the effect of interfacial crystallization.

Study	Material	Testing Method	Mechanisms-Behaviour Relationship
Coogan & Kazmer (2020)	HIPS	Uniaxial tensile testing on single extrudate samples	Diffusion model is coupled with pressure-driven intimate contact. Strength loss is primarily attributed to insufficient interlayer contact under most processing conditions.
Zhang *et al.*, 2025a	CFRC	Uniaxial tensile testing on multi-layer printed sample	Lower layer heights enhanced bond width, improved impregnation within fibre bundles, and promoted chain diffusion at the interface resulting in higher strength
Xu *et al.*, 2025	PLA	Uniaxial tensile testing on multi-layer printed sample	Diffusion model coupled with pressure-driven intimate contact model Square nozzle produces a wider, more sustained pressure distribution, resulting in higher bond strength
Allum *et al.*, 2020c	PLA	Uniaxial tensile testing on single extrudate samples	Interface notches are the primary source of anisotropy and full bond strength is observed for a wide range of process parameters
Kundurthi *et al.*, 2023)	PEEK	Uniaxial tensile testing on single extrudate samples	Empirical model was developed to predict the stress concentration factor as a function of notch depth and root radius. Lower layer height was shown to produce smaller interface notch depths, resulting in reduced stress concentrations and therefore less strength reduction.

1.5 Research Gaps

The review presented herein details the state-of-the-art in identifying the process-related mechanisms that impact the mechanical performance of polymer-based MEAM parts. Gaps in the literature have been identified and are discussed below.

Despite extensive process modelling efforts, the underlying mechanisms governing property development are not yet well established. Many studies consider only a subset of the relevant factors, and even in works considering multiple mechanisms, the relative contribution of each remains unclear, as their effects are difficult to decouple. Better understanding these mechanisms and their contribution to part performance could be the missing link for predictive tools and process optimization for this technology.

A notable gap concerns the properties of the extrudates themselves, which serve as the fundamental building blocks of printed parts. Limited attention has been given to how processing conditions influence extrudate properties and the mechanisms through which these changes occur. More specifically, the effect of extrusion rate, which is a key parameter given the increasing interest in high-throughput printing, on the mechanical properties of extrudates has not been investigated. Furthermore, it remains unknown whether the process-parameter dependency of extrudate-level mechanical behaviour is transferred to the part scale.

Another understudied contributor is the shape of the extrudates and the interfacial notches formed at the junctions of adjacent extrudates. Although a few studies have examined the effects of these notches, the relationship between process conditions and notch geometry remains unresolved, and their influence in large-scale printing has not been investigated. In addition, the limited strain-field predictions available from finite-element simulations have not yet been verified experimentally, which is an important requirement for advancing and validating predictive models.

With respect to interlayer bonding, the widely accepted assumption of full contact at the bonding interface has not been verified, and the potential presence of microvoids in this region

has not been examined, despite their likely impact on bond quality and overall mechanical performance. Prior works have largely focused on polymer-chain interdiffusion and geometric measures of contact formation, which is the ratio of bond width to extrudate width. In addition, while recent studies emphasize the role of pressure-driven intimate contact and a few methods for measuring contact pressure have been proposed, the effect of process parameters on the development of contact pressure has not been systematically investigated.

Finally, rigorous experimental methodologies to quantify the interdependent effects of co-occurring mechanisms on mechanical performance have not been established. While distinct factors like interface notches and interlayer bonding are recognized, their combined influence has not been systematically quantified for an arbitrary polymer. Consequently, the interactions between these factors remain poorly understood, and the extent to which one mechanism modulates the effects of another has not been investigated. Establishing this experimental foundation is essential to move beyond isolated studies toward a comprehensive, multi-mechanism understanding of part quality.

CHAPTER 2

THESIS OBJECTIVES AND STRUCTURE

2.1 Thesis Objectives

Currently, a significant challenge in polymer-based MEAM is the lack of reliable tools to optimize or predict mechanical properties based on process parameters. This stems from an incomplete understanding of the complex controlling mechanisms that link manufacturing settings to final part performance. Consequently, this thesis addresses the following research question: To what extent do less-studied mechanisms, specifically intrinsic extrudate properties, interfacial microvoids, and their interaction with geometric notches, govern the mechanical response and anisotropy of printed parts?

It is hypothesized that the performance gap in MEAM is driven by a nonlinear interplay between these multiscale mechanisms, and that isolating these effects is essential for developing the fundamental understanding required for future predictive modelling.

Based on these gaps and the increasing use of polymer-based MEAM across multiple industries, the general objective of this thesis is to investigate and elucidate the less-studied mechanisms that govern the mechanical performance of MEAM parts. The specific objectives are:

1. Determine how extrusion conditions affect the morphology, microstructure, and mechanical properties of extrudates and if these properties transfer to the parts they form.

2. Quantify the role of interfacial notches in stress concentration and strength reduction in both small-scale and large-scale material-extrusion printing.

3. Examine the presence of microvoids at the bonding area and understand their formation mechanisms.

4. Evaluate the interaction between bonding quality and interface notches and their coupled effect on mechanical performance.

2.2 Methodology and Structural Overview of Chapters 3 to 6

To achieve the defined objectives, this research employs an experimental framework focused on decoupling co-occurring mechanisms at the mesoscale. The methodology utilizes a strategy of using single-extrudate-thick samples to isolate interfacial and material behaviour from the geometric effects of the extrudate. By simplifying the geometry, the specific impact of process parameters on the bonding area and the individual extrudates can be quantified. The structural relationship between these experimental stages and the resulting manuscripts is detailed below:

Chapter 3 presents a journal paper investigating how extrusion conditions affect the morphology, microstructure, and mechanical properties of both individual extrudates and the resulting printed parts. By comparing single extrudates to multi-layer specimens, this chapter establishes whether intrinsic properties, influenced by the extrusion rate, transfer to the macro-scale structure.

Chapter 4, the second journal paper, focuses on the role of interface notches in the strength reduction of parts printed at both small (FFF) and large (FGF) scales. A machining method is used to remove the notches, enabling an independent evaluation of interlayer bonding and interface notch effects. DIC is employed to provide experimental quantification of the strain fields induced by these notches under different printing conditions, supplemented by design guidelines obtained through FEA.

Chapter 5, composed of a third journal paper, presents a methodology for the visualization of interfacial microvoids using high-resolution micro-computed tomography (Micro-CT) and polarized optical microscopy (POM). This study includes in-situ measurements of contact pressure to experimentally verify the applicability of the Lee-Springer intimate contact model in describing void formation and bonding evolution under various printing parameters.

Chapter 6, the final journal paper, evaluates the combined effects of interface notches and bonding quality on the mechanical performance of printed components. Layer height was strategically varied to print single-extrudate-thick walls, providing a range of notch severity and bonding quality. Samples were extracted from both surface-machined and non-machined walls printed at different layer heights to investigate the combined effects of notch severity and bonding quality on tensile properties.

CHAPTER 3

EXTRUDATE-LEVEL ANALYSIS OF THERMOPLASTIC PROPERTIES IN MATERIAL EXTRUSION ADDITIVE MANUFACTURING

Maryam Shokrollahi[1] , Olivier Lampron [1] , Martine Dubé[1,2] , Ilyass Tabiai [1,2]

[1] Department of Mechanical Engineering, École de technologie supérieure, Montréal, Canada

[2] CREPEC, Research Center for High Performance Polymer and Composite Systems, Mechanical Engineering Department, McGill University, Montréal, Canada

Paper submitted to *Progress in Additive Manufacturing*, January 2026

3.1 Abstract

Polymer-based material extrusion additive manufacturing techniques, including Fused Filament Fabrication (FFF) and Fused Granular Fabrication (FGF), are rapidly expanding across multiple industries. These processes build parts layer by layer by depositing thermoplastic extrudates through a heated nozzle. However, their wider adoption for high-performance applications remains limited due to challenges in predicting mechanical properties and the generally reduced performance of printed parts. These challenges are typically attributed to insufficient interlayer bonding and meso-scale effects related to extrudate geometry. However, the influence of process conditions on the intrinsic properties of the extrudates, which are the fundamental building units of printed parts, has received limited attention. In this study, polylactic acid (PLA) was extruded at different rates and examined at both extrudate and printed levels. Tensile testing showed that increasing the extrusion rate did not affect ultimate tensile strength or stiffness but caused substantial reduction in ductility and an ~85% and ~60% loss in toughness for extrudates and printed samples, respectively. Digital image correlation revealed more uniform strain distribution and delayed failure in low-rate samples, whereas high-rate samples exhibited early strain localization. Differential scanning calorimetry and structured light profilometry demonstrated that higher extrusion rates increased crystallinity in both extrudate and printed samples, and increased surface roughness in extrudates only. Notably, the effect on these

properties is non-proportional, with substantial changes occurring only beyond a threshold. These results demonstrate that extrusion rate markedly influences extrudate properties, with direct consequences for printed part performance, highlighting that process optimization should account for extrudate-level behaviour in FFF and FGF.

3.2 Introduction

Fused filament fabrication (FFF) and fused granular fabrication (FGF) are manufacturing processes belonging to the material extrusion additive manufacturing (MEAM) family. In these processes, a thermoplastic feedstock is fed into a heated nozzle that extrudes a softened material, depositing it layer by layer to form three-dimensional parts. Although highly popular due to their accessibility and versatility, polymer-based MEAM techniques remain predominantly limited to prototyping and tooling applications, with only a few examples in structural or critical components (Pignatelli & Percoco, 2022; van de Werken *et al.*, 2020; Wickramasinghe, Do & Tran, 2020). This limitation mainly arises from the complex and difficult-to-predict mechanical behaviour of printed parts (Cuan-Urquizo *et al.*, 2019; Lampron, Therriault & Lévesque, 2023; Rivet, Dialami, Cervera & Chiumenti, 2024). Industrial surveys have identified achieving the desired reliability and quality as the primary concern among users of additive manufacturing technologies (Stratasys, 2020; Protolabs, 2024).

A large body of literature has examined the relationship between process parameters and the resulting macroscopic mechanical properties of printed parts (see Sultana, Rahman, Wang, Ahmed & Xiaohu, 2024; Vălean, Baban, Rajak & Linul, 2024; Lendvai, Fekete, Rigotti & Pegoretti, 2025 as recent examples, and Syrlybayev *et al.*, 2021; Bouzaglou *et al.*, 2023 for review studies). Parametric studies and design-of-experiment methodologies are frequently used to identify optimal parameter sets for given performance targets. However, the FFF process features a large number of process variables, such as extrusion and chamber temperature, extrusion speed, bead aspect ratio, and infill density, to name a few, that interact in complex ways. These parameters influence the resulting mechanical properties through multiple meso-scale mechanisms occurring during fabrication, such as interlayer polymer chain diffusion (Bartolai *et al.*, 2018),

bead geometry and pore formation (Sun *et al.*, 2025; Shokrollahi, Smith, Levy, Dubé & Tabiai, 2025), degree of crystallinity (Doyle, García-Molleja, Fernández-Blázquez & González, 2025), and residual stress development (Issametova *et al.*, 2024). As a result, isolating the effects of individual parameters is particularly challenging, even on simple geometries such as so-called *dogbone samples* or three-point bending samples, due to the strong coupling between the underlying mechanisms.

To address this complexity, the use of single-extrudate-thick samples, also called single-wall in the literature, has gained popularity in recent years, as they allow decoupling the intrinsic behaviour of the printed material from structural effects related to infill patterns and inter-extrudate porosity. For instance, Seppala et al. employed trouser tear (mode III) tests on single-extrudate-thick samples to investigate the effects of print speed and extrusion temperature on interfacial tear resistance (Seppala, Hoon Han, Hillgartner, Davis & Migler, 2017). Gilmer et al. used single-extrudate-thick samples to validate models predicting the interlayer welding and the residual-stress-induced warping in FFF polyetherimide parts (Gilmer *et al.*, 2021). Allum et al. and Shokrollahi et al. used single-extrudate-thick samples to study the influence of process parameters on the notch-like defects formed at bead interfaces and their impact on the out-of-plane strength of FFF structures (Shokrollahi *et al.*, 2025; Allum *et al.*, 2020c; Allum *et al.*, 2023).

Nevertheless, the fundamental structural unit of FFF parts remains the extrudates. Compared to single-extrudate-thick samples, studying a single extrudate enables the decoupling of the material's intrinsic mechanical behaviour from additional mesostructural effects such as bead-to-bead interface geometry and incomplete interfacial healing. Several studies have examined how printing parameters affect die swell, part accuracy, and fibre or molecular alignment at the extrudate level (Heller *et al.*, 2016; Bakrani Balani *et al.*, 2019; Geng *et al.*, 2019; Domenech *et al.*, 2025), but very few investigations have addressed the influence of FFF extrusion parameters on the mechanical properties of the extrudate itself. Although it is well known that conventional polymer manufacturing processes can induce anisotropic material properties through mechanisms such as preferential molecular orientation and residual stress

(Thakkar, Broutman & Kalpakjian, 1980; Senden, Peters, Govaert & Van Dommelen, 2013), the mechanical response of individual extrudates remains largely underexplored.

The work of (Rodrigues *et al.*, 2023) provides a comprehensive review of single-extrudate testing in the FFF literature. Although the methodology is similar, it is essential to distinguish between characterizing the feedstock filament prior to the FFF process and characterizing the extrudate produced during FFF. The feedstock filament is typically produced by screw extrusion, stretched, and quenched in a coolant, often water (Dey *et al.*, 2021). During FFF, however, this filament is reheated well above its melting temperature, forced by axial compression through a narrow nozzle, and deposited without quenching. While several studies have employed single-filament tests to assess feedstock mechanical behaviour, only a limited number have examined how the FFF extrusion process itself affects the mechanical properties of the extrudate.

Given the scarcity of studies on testing FFF extrudates, we present here a concise review of the available literature. In (Priyanka *et al.*, 2021), the tensile modulus, tensile strength, and toughness of extruded polylactic acid (PLA) filaments were investigated as a function of sample length using single-extrudate tensile testing. A Weibull statistical analysis revealed a size effect, whereby longer samples, having a higher volume and thus a greater probability of defects, exhibited lower strength. In (Orellana Barrasa *et al.*, 2021), the effect of extrusion temperature, test strain rate, and polymer ageing on the yield strength and elastic modulus of PLA extrudates was characterized using single-extrudate testing. Extrudates fabricated at 180 °C were found to have a strength about 17% lower than those extruded at 190 °C. However, ageing the extrudates in a dry and protected environment from direct solar radiation for 100 days significantly increased the yield strength and elastic modulus, compensating for the initially lower strength observed for lower extrusion temperature. In related studies (Orellana-Barrasa, Tarancón & Pastor, 2022b; Orellana-Barrasa *et al.*, 2022a), single extrudate tensile testing was used to identify optimal ageing parameters and to characterize the mechanical properties of magnesium-filled PLA. However, the influence of the extrusion parameters on the extrudate mechanical behaviour was not studied. In (Comelli *et al.*, 2022), the effect of FFF extrusion conditions on the tensile behaviour of polyetheretherketone (PEEK) 450G extrudates produced

from feedstock filaments with different crystalline structures was examined. The strength, strain at break, and tensile modulus were characterized through single-extrudate testing as functions of the feedstock microstructure, extrusion temperature, and extrusion speed. It was found that, although the FFF extrusion process exhibited a normalization effect, strong molecular orientation and crystallinity in the feedstock filament could remain in the extrudate and influence its mechanical properties. The process parameters themselves were not found to significantly affect the extrudate properties, which was attributed to the fast-crystallizing nature of PEEK 450G, potentially erasing microstructural effects induced during extrusion. In (Patterson *et al.*, 2023), the tensile behaviour of acrylonitrile butadiene styrene (ABS), polycarbonate (PC), and PLA single freely fabricated extrudates, single deposited extrudates, a series of extrudates, and thin printed films was studied under constant process conditions. The analysis focused on the dimensional accuracy and on the scalability of the tensile behaviour from the single extrudate to multiple-fibre and film geometries, revealing that printed series of N extrudates exhibited greater strength than the sum of the strength of N individual extrudates.

From this review, it can be observed that although (Orellana Barrasa *et al.*, 2021; Orellana-Barrasa *et al.*, 2022b) demonstrated that the tensile modulus and strength of PLA extrudate could be tuned through extrusion temperature and ageing time, the effect of the FFF process parameters on the toughness of the extrudate has only been studied for fast-crystallizing PEEK 450G. Moreover, the effect of extrusion speed, a key parameter considering the increasing interest in high-throughput FFF (Kantaros, Katsantoni, Ganetsos & Petrescu, 2025), on the mechanical properties of the extrudate has received little attention. Finally, whether the process-parameter dependency of the extrudate's mechanical behaviour can be transferred and observed at the part scale has not been investigated to date.

In this work, we explore the influence of extrusion rate on FFF part performance, selecting PLA for its prevalence in printing and ease of processing. To this end, the tensile modulus, ultimate strength, and toughness of single extrudates and single-extrudate-thick printed samples are evaluated for three levels of extrusion speed and two test rates. Strain during testing is measured using image tracking and digital image correlation (DIC) on the printed samples,

while offline die swell measurements assess the stretching induced by extrusion. Differential scanning calorimetry (DSC) characterizes the microstructure, and structured light profilometry quantifies the surface roughness of extrudates and printed parts. This approach enables an assessment of how extrusion parameters influence both the intrinsic properties of the extrudates and the performance of printed structures, providing insight into the mechanisms linking process conditions, microstructure, and mechanical behaviour.

3.3 Methodology

3.3.1 Material

The feedstock material used in this study was PolyLite™ LW-PLA, supplied by Polymaker, provided as a 1.75 mm-diameter filament spool. According to the manufacturer's datasheet, the material exhibits a tensile modulus of 1688.5 ± 80.8 MPa, a tensile strength of 24.4 ± 0.3 MPa, and an elongation at break of 8.8 ± 0.3 %, all measured in the X–Y direction following the ISO 527 and GB/T 1040 standards. The glass transition temperature (T_g) and melting temperature (T_m) determined by differential scanning calorimetry (DSC) at a heating rate of 10 °C min^{-1} were 59 °C and 150 °C, respectively.

3.3.2 Sample preparation

Samples were prepared in the form of both extrudates and printed parts. The following sections describe the fabrication process for each.

3.3.2.1 Extrudate fabrication

The filament spool was dried at 55 ℃ for at least 8 hours prior to use. Figure 3.1 illustrates the extrudate fabrication and the printed single-extrudate thick box from which samples were extracted. A 1 mm nozzle and a Sprite direct drive extruder on an Ender printer were used to produce extrudates of approximately 90 cm length at three extrusion rates (6, 12, and 24 mm^3/s)

and a constant temperature of 205 °C, which falls within the manufacturer's recommended range for PLA and ensures stable, consistent extrusion across all rates. As shown in Figure 3.1(a), the extrudate was guided through a tube to minimize sagging and diameter variations. The extrudate temperature at the nozzle exit was monitored at high flow rates to confirm that it remained consistent with the set extrusion temperature. A set of extrudates fabricated at 24 mm^3/s was subsequently annealed at 60 ℃ (above T_g) for two hours to investigate the effect of potential stress relaxation due to chain alignment induced during extrusion. Table 3.1 summarizes all sample sets along with their corresponding fabrication and testing details.

Table 3.1 Sample sets along with their corresponding manufacturing details

Sample	**Type**	**Extrusion rate (mm^3/s)**	**Annealed**
EXT-E6-NA	Extrudate	6	No
EXT-E12-NA	Extrudate	12	No
EXT-E24-NA	Extrudate	24	No
EXT-E24-A	Extrudate	24	Yes
PR-E12-NA	Printed	12	No
PR-E24-NA	Printed	24	No

3.3.2.2 Printing

Hollow, single-extrudate-thick boxes were printed according to the parameters summarized in Table 3.2. Similar to the extrudate fabrication, the extrusion temperature was set to 205 ℃, and the printing speed was adjusted to match the corresponding extrusion rates of 12 and 24 mm^3/s, reflecting the fact that higher print speeds require higher material flow. The printed boxes were subsequently cut along the corners, and ASTM D638 (ASTM International, 2014) Type IV tensile samples were extracted along the 0° direction from the resulting sheets using a die cut.

Table 3.2 Printing parameters used for the single-extrudate-thick box

Parameter	Value
Extrusion temperature (°C)	205
Layer height (mm)	0.5
Layer width (mm)	1
Print speed (mm/s)	24, 48
Bed temperature (°C)	25

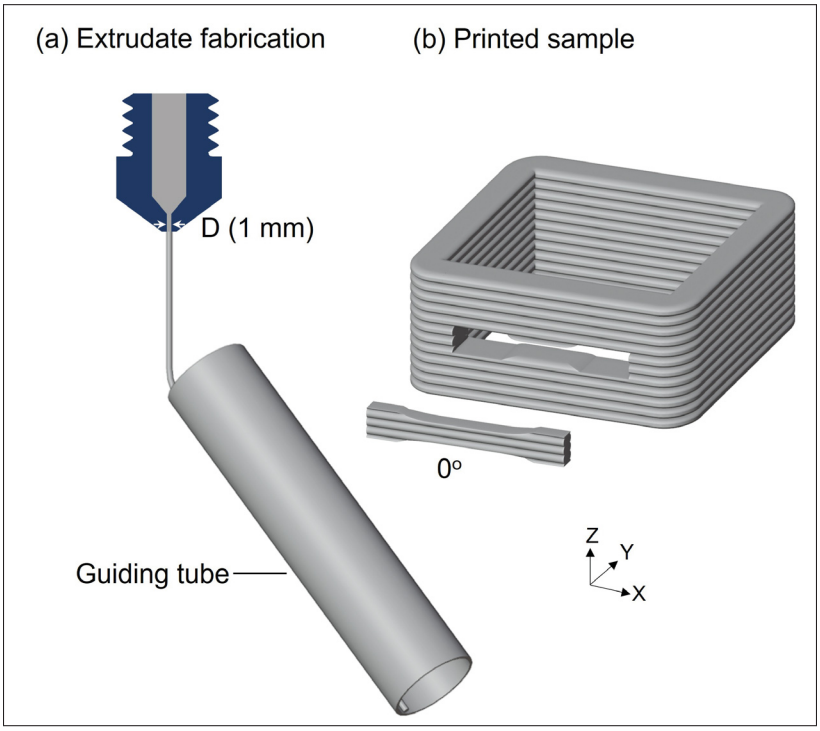

Figure 3.1 Schematic illustration of the samples produced using a 1 mm nozzle: (a) Extrudate fabrication, and (b) A hollow, single-extrudate-thick box from which tensile samples were extracted along the 0° direction

3.3.3 Offline die swell characterization

Cross-sectional cuts were obtained at a minimum of six locations along each extrudate, with spacing between locations of approximately 10 cm. The sections were mounted, polished, and analyzed by optical microscopy, and the diameters measured at each location were averaged to obtain a representative value.

3.3.4 Surface roughness characterization

Surface profiles of the extrudates and printed samples were acquired using a Keyence VR-5200 digital microscope in high-resolution mode. The system employs structured white light projection to capture the surface topography, generating detailed 3D data by analyzing the deformation of the projected patterns. Quantitative roughness measurements were performed over a 5 mm scan length at five different locations on each sample, and the results were averaged.

3.3.5 Differential scanning calorimetry (DSC)

Thermal analysis was performed using a DSC 2500 (TA Instruments). Samples were extracted from the extrudates and printed parts, each weighing approximately 6 ± 1 mg. The samples were heated from room temperature to 200 ℃ at a constant heating rate of 10 ℃/min in a nitrogen atmosphere.

3.3.6 Tensile testing and DIC

3.3.6.1 Extrudates

To evaluate the tensile properties, each fabricated extrudate was tested using Capstan grips (Model G1092, Mark-10 Corporation, Copiague, USA) with a diameter of 92.9 mm. Figure 3.2 illustrates the experimental setup used for extrudate tensile testing. The gauge length was defined as the distance between the centres of the two bollards and was kept constant at 165 mm, following the recommendation of (Rodrigues *et al.*, 2023). Tests were conducted at two strain

rates of 0.02 min^{-1} and 0.04 min^{-1}. The higher rate of 0.04 min^{-1} was selected based on the literature recommendation, while the lower rate of 0.02 min^{-1} was used to assess whether slower deformation would allow the material to exhibit phenomena associated with flow-induced molecular orientation. For each condition, six extrudates with a length of 90 cm were tested. Tensile testing was performed using an MTS universal testing machine equipped with a 500 N load cell. Data were recorded at a frequency of 10 Hz. The extrudate diameter within the gauge length was measured at three locations and averaged. The nominal stress values were determined by dividing the load by the average initial cross-sectional area within the gauge section. Strain was obtained by tracking two reference markers placed along the gauge length using the TrackMate plugin in ImageJ software, allowing for synchronization of mechanical and optical data. The stiffness was calculated from the slope of the stress-strain curve within 0.1% and 0.5% of strain. Toughness was calculated in accordance with ASTM D882 (ASTM International, 2018) as the area under the force–displacement curve divided by the sample volume, where the volume was taken as the initial cross-sectional area multiplied by the initial gauge length. This approach accounts for localized plastic deformation occurring at multiple locations along the extrudate after yielding.

3.3.6.2 Printed samples

Dogbone samples were tested using an MTS Alliance RF/200 testing machine equipped with a 500 N load cell. Prior to testing, a speckle pattern suitable for DIC analysis was applied. A uniform white acrylic paint layer (Vallejo Game Colour) was first airbrushed onto the sample surface using a 0.2 mm nozzle, followed by the application of dispersed black speckles to create the required contrast. Image acquisition was performed using a monochrome Grasshopper 3-51SM5M camera, positioned to capture the full field of view during tensile testing. The image acquisition rate and other DIC parameters are summarized in Table 3.3. Stress values were calculated by dividing the measured load by the cross-sectional area, which was determined using ImageJ from images of the sample cross-sections. Strain measurements were obtained using the virtual extensometer tool in the VIC-2D software (Correlated Solutions), which calculates the

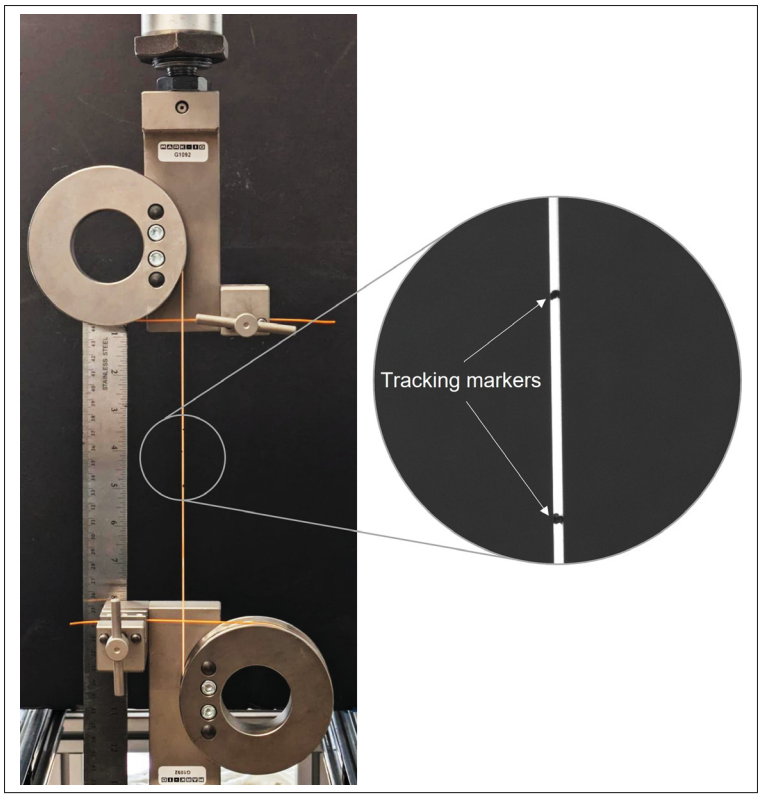

Figure 3.2 Experimental setup for tensile testing of the extrudates. Tracking markers at the gauge length were used to measure strain

average strain between two defined points along the gauge length. This value was reported as the nominal strain. A total of six samples were tested for each set.

Table 3.3 Imaging and DIC analysis parameters

Parameter	**Value**
FPS	0.5
Scale (px/μm)	17.3
Subset (px $\times$ px)	9
Step (px)	1
Correlation type	Direct
Strain variation (%)	0.02

3.4 Results

3.4.1 Offline die swell measurements

Figure 3.3(a) presents the swell ratio of the fabricated extrudates at different extrusion rates. The results show that the extent of die swell increases with increasing extrusion rate. This effect becomes more pronounced at higher flow rates; while the swell ratio increases by approximately 13% from EXT-E6-NA to EXT-E12-NA, it further rises by 25% from EXT-E12-NA to EXT-E24-NA. For the highest rate, the extrudate diameter is approximately 1.6 times larger than the nozzle diameter. Moreover, the extrudate geometry appears more stable at this condition, as indicated by the smaller standard deviation measured for EXT-E24-NA. Figure 3.3(b) presents the area expansion ratio of the printed extrudate, calculated as the ratio between the measured cross-sectional area and the nominal area, where the latter is taken as a rectangle defined by the nominal layer height and layer width. Measurements were performed on at least five cross sections and averaged. The results indicate that the cross-sectional area remains unchanged with extrusion rate, demonstrating that swelling is significantly reduced, if not suppressed, when the extrudate is deposited onto the previously printed layer rather than extruded freely into open air.

3.4.2 Crystallinity analysis

Figure 3.4(a) and (b) present the DSC results of the fabricated extrudates, printed samples, and the filament spool. The extrudates and printed samples exhibit a similar thermal behaviour characterized by three main transitions: the onset of the glass transition around 57 °C accompanied by an enthalpy relaxation peak, a cold crystallization peak near 95 °C, and a melting peak at approximately 163 °C. For the extrudates, increasing the extrusion rate to 24 mm^3/s results in a reduction in both the enthalpy relaxation and cold crystallization peaks. Additionally, EXT-E6-NA and EXT-E12-NA exhibit a small shoulder just before the melting peak, which disappears in samples produced at higher extrusion rates.

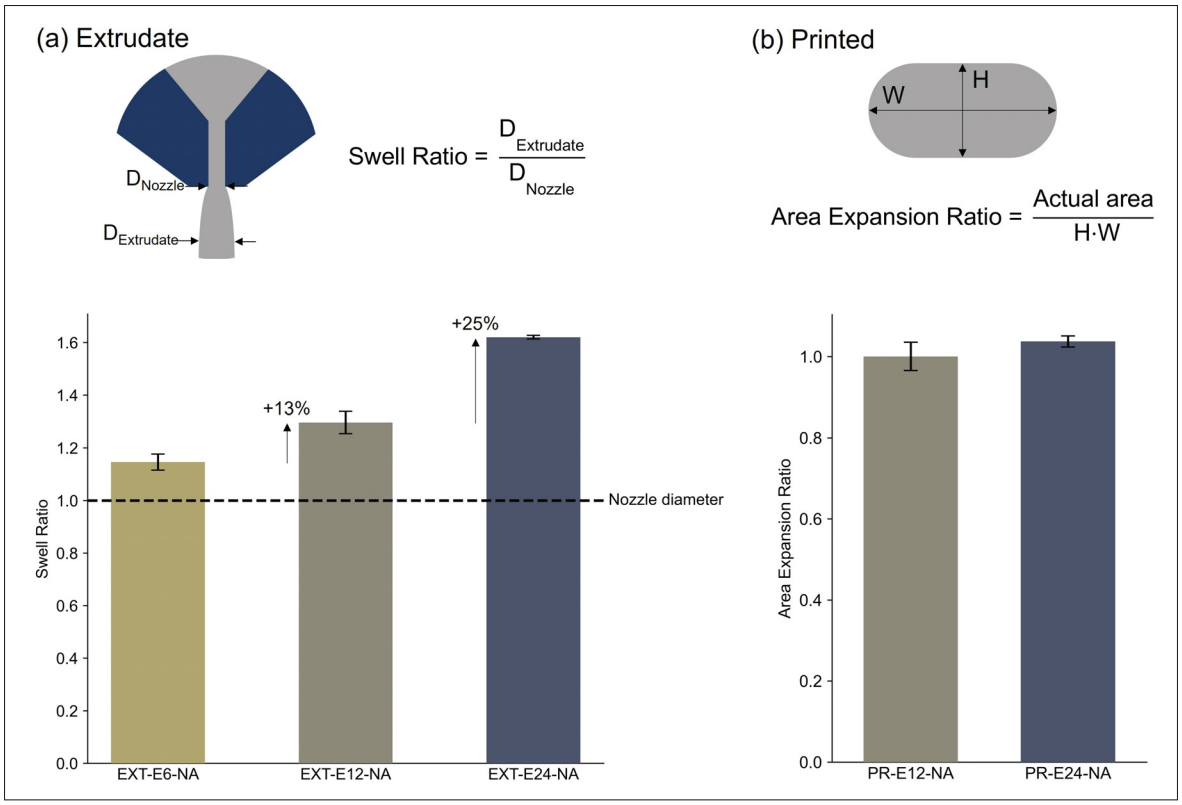

Figure 3.3 (a) Swell ratio of fabricated extrudates at different extrusion rates. Swelling increases with extrusion rate, rising by 13% from EXT-E6-NA to EXT-E12-NA and by 25% from EXT-E12-NA to EXT-E24-NA; at the highest rate, the extrudate diameter reaches about 1.6 times the nozzle diameter with improved stability. (b) Area expansion ratio of deposited extrudates, averaged over at least five cross sections. The nominal area is estimated by the nominal layer height (H) and layer width (W). Unlike open-air extrusion, the cross-sectional area remains unchanged with extrusion rate, indicating suppression of die swell upon deposition

Annealing produces only a minor shift of the cold crystallization peak toward lower temperatures. The printed samples display a similar thermal response, with negligible variation across the different extrusion rates. The filament spool does not exhibit a clear enthalpy relaxation or cold crystallization peak, although a minor exothermic peak is observed at the onset of the melting peak.

Table 3.4 presents the values extracted from the DSC curves. As shown, the glass transition temperature (T_g) and enthalpy relaxation remain nearly constant across all samples. The degree

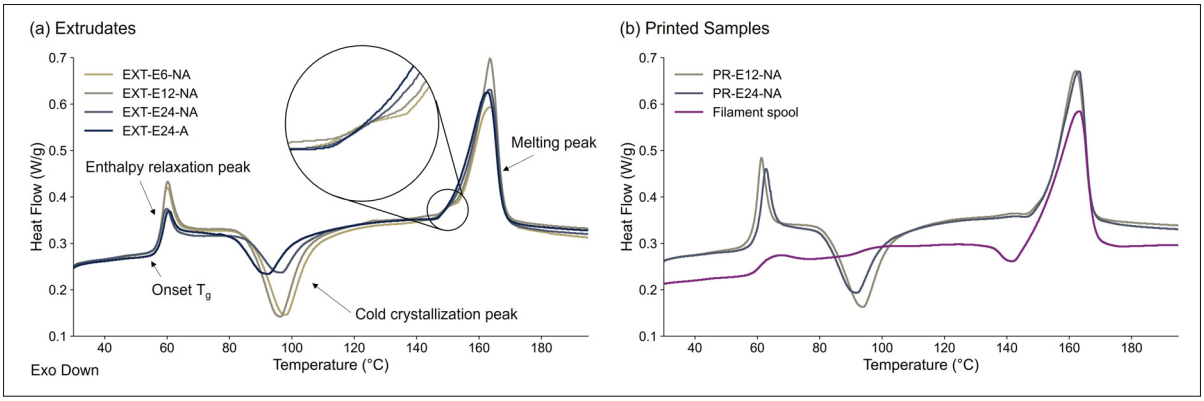

Figure 3.4 DSC thermograms of (a) extrudates and (b) printed samples and the filament spool. Extrudates and printed samples exhibit a glass transition around 57 °C with an enthalpy relaxation peak, followed by cold crystallization near 95 °C and melting around 163 °C. The enthalpy relaxation and cold crystallization peaks decrease with increasing extrusion rate, while annealing slightly shifts the crystallization peak to lower temperatures. Printed samples show similar behaviour across extrusion rates, while the filament spool does not exhibit a clear enthalpy relaxation or cold crystallization peak

of crystallinity was calculated using the melting and cold crystallization enthalpies, with the cold crystallization enthalpy subtracted from the melting enthalpy and divided by the enthalpy of fusion for a 100% crystalline PLA (93 kJ/mol) (Matos *et al.*, 2019; Coppola, Cappetti, Di Maio, Scarfato & Incarnato, 2018). Compared with the higher extrusion rate samples, the degree of crystallinity decreases by approximately 70% from EXT-E24-NA to EXT-E6-NA and EXT-E12-NA for the extrudates. Annealing does not significantly alter the crystallinity of EXT-E24-NA. A similar trend is observed for the printed samples, with PR-E24-NA showing higher crystallinity than PR-E12-NA. The filament spool exhibits a crystallinity of approximately 20%, which is higher than that of both the extrudates and the printed samples.

Table 3.4 Parameters extracted from the DSC curves

Sample	T_g (°C)	**Enthalpy relaxation (J/g)**	**Cold crystallization enthalpy (J/g)**	**Melting enthalpy (J/g)**	X_c (%)
EXT-E6-NA	57.2	3.1	14.5	16.8	2.5

Sample	T_g (°C)	Enthalpy relaxation (J/g)	Cold crystallization enthalpy (J/g)	Melting enthalpy (J/g)	X_c (%)
EXT-E12-NA	57.3	3.4	14.2	17.2	3.2
EXT-E24-NA	56.8	2.2	6.7	17.8	11.9
EXT-E24-A	57.8	2.0	6.6	18.1	12.0
PR-E12-NA	57.9	3.8	14.0	16.4	2.6
PR-E24-NA	59.4	3.2	10.5	18.5	8.6
Filament spool	59.8	–	–	19.0	20.0

3.4.3 Surface roughness characterization

Figure 3.5(a), (b), and (c) show the surface roughness profiles of the extrudates produced at different extrusion rates. EXT-E6-NA and EXT-E12-NA exhibit smooth and similar surface profiles, whereas EXT-E24-NA shows noticeably higher roughness with periodic surface corrugations, indicative of extrusion instabilities at high flow rates. The dashed line on the EXT-E6-NA sample marks the path along which the arithmetic mean surface roughness, R_a, was calculated, representing the average deviation of the surface from the mean line, based on five measurements from different locations. The R_a results, shown in Figure 3.5(d), confirm these observations, with EXT-E24-NA showing significantly higher roughness than the lower-rate samples.

To assess whether the same effect is observed in the printed parts, the surface profiles of the printed samples are shown in Figure 3.6. Both the images and the R_a values indicate that the surface roughness is similar across these samples, suggesting that the higher extrusion rate does not significantly affect the printed surface quality.

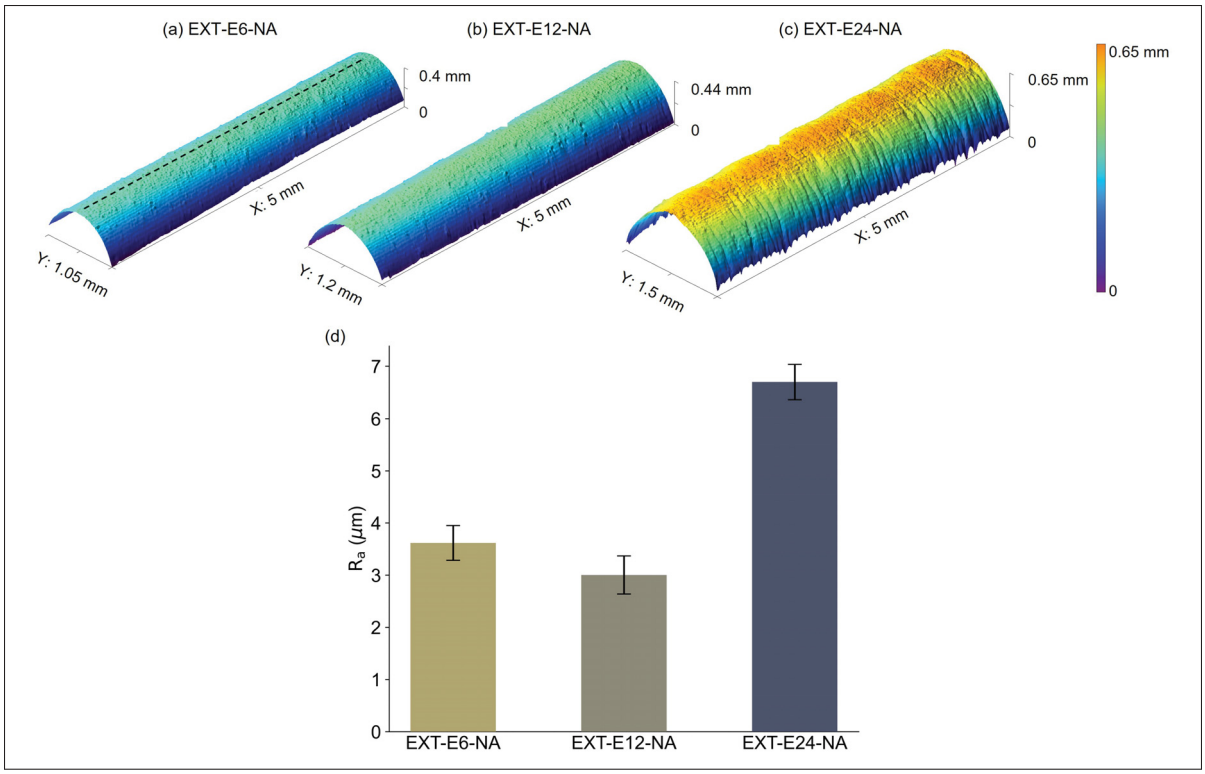

Figure 3.5 Surface roughness profiles of extrudates at different extrusion rates. EXT-E6-NA and EXT-E12-NA show smooth, similar surfaces, whereas EXT-E24-NA exhibits higher roughness with periodic corrugations, indicative of extrusion instabilities. The dashed line in (a) marks the path used to calculate the arithmetic mean roughness, R_a, shown in (d)

3.4.4 Tensile properties

3.4.4.1 Extrudates

Figure 3.7(a) and (b) show the stress–strain curves of one representative extrudate from each set tested at strain rates of 0.02 min^{-1} and 0.04 min^{-1}, respectively. The strain data are truncated at 7% to better illustrate the elastic region, the onset of plastic deformation, and the subsequent elongation. Experimental stress–strain data were smoothed using the Gaussian Process Regressor tool available in Scikit-learn (Pedregosa *et al.*, 2011), which provides a mean curve and 95% confidence interval to highlight the overall trend and variability in the measurements. As shown, the extrudates exhibit an initial linear elastic response, followed by yielding and a subsequent

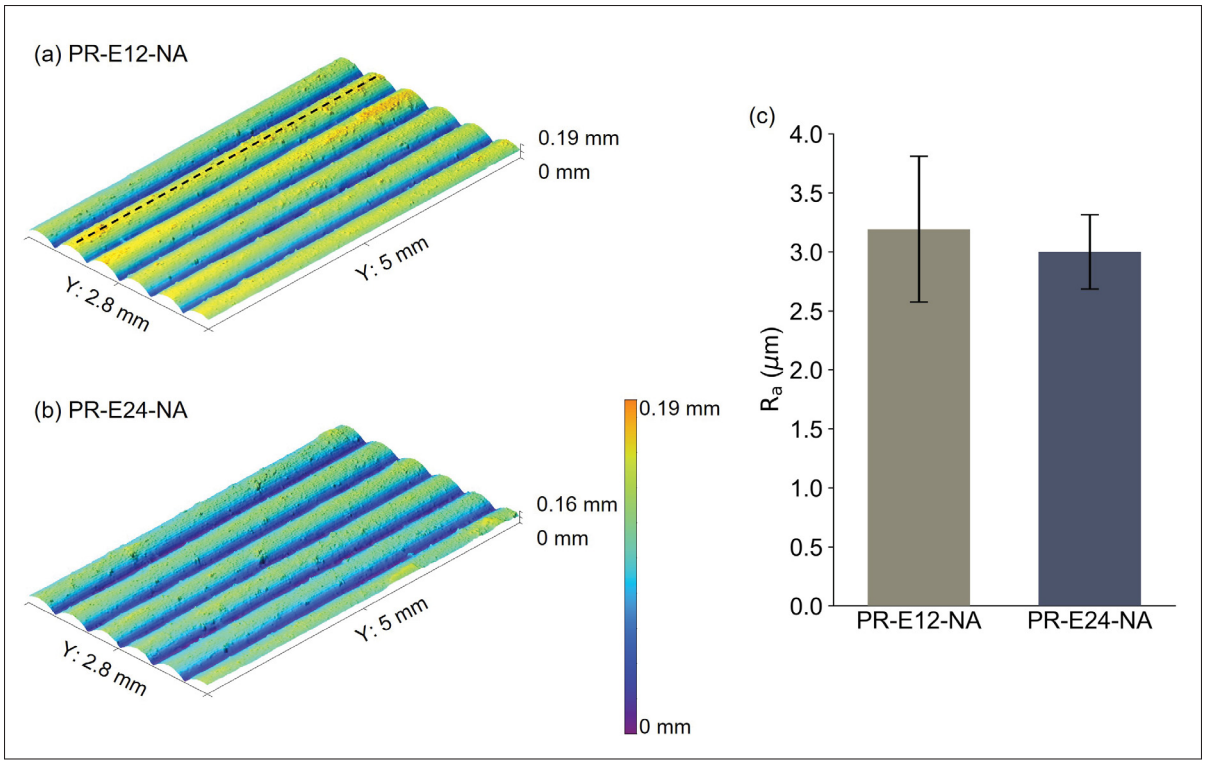

Figure 3.6 Surface profiles of printed samples at different extrusion rates. (a) PR-E12-NA and (b) PR-E24-NA, with the dashed line indicating the path along which R_a was measured. (c) R_a values, showing similar surface roughness for both samples

drop in stress after reaching the maximum load. The stress then remains nearly constant until fracture. Regardless of strain rate, the EXT-E24 samples failed earlier than those extruded at lower rates. Moreover, annealing did not noticeably alter the overall stress–strain behaviour. A detailed comparison of the mechanical properties, including ultimate stress, stiffness, and toughness, is presented in Figure 3.8. Figure 3.8(a) and (b) show that ultimate stress and stiffness values do not vary significantly with extrusion rate, and strain rate has minimal influence on these properties. In contrast, toughness is approximately 85% lower for EXT-E24-NA and EXT-E24-A, indicating reduced ductility for extrudates fabricated at higher extrusion rates. This trend is consistent across both strain rates, with these samples failing more rapidly than those extruded at lower rates. It should be noted that annealing had no significant effect, as EXT-E24-NA and EXT-E24-A exhibited similar values for all properties. Overall, variability in the results was higher at the 0.04 min^{-1} strain rate.

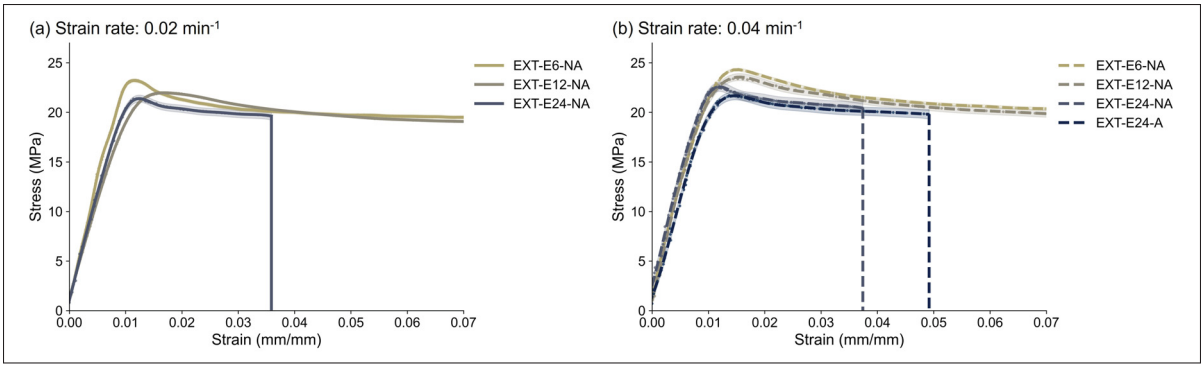

Figure 3.7 Stress–strain curves of representative extrudates tested at strain rates of (a) 0.02 min^{-1} and (b) 0.04 min^{-1}. Data are truncated at 7% strain. Stress–strain data were smoothed using Gaussian Process Regression with 95% confidence intervals. Round markers represent measurements, lines represent the mean curve, and the translucent area around each curve represents the 95% confidence interval. All samples exhibit an initial elastic response followed by plastic deformation and a stress plateau until fracture. EXT-E24 samples showed markedly lower ductility than those extruded at lower rates, while annealing appeared to have no noticeable effect on the behaviour

3.4.4.2 Printed samples

Figure 3.9(a) and (b) show the stress–strain curves and corresponding DIC analyses for representative samples of PR-E12-NA and PR-E24-NA, respectively. The DIC results are presented at different deformation stages, corresponding to various strain levels. The stress–strain data were truncated at 4% strain to better illustrate the sample behaviour prior to plastic deformation. In both cases, the stress reaches a maximum value and then drops to a certain level, where it plateaus until failure, with the plateau occurring at a higher level for PR-E24-NA.

The DIC results reveal that the strain in PR-E12-NA is more uniformly distributed along the gauge length at each deformation stage. In contrast, PR-E24-NA exhibits strain localization along horizontal bands, which ultimately leads to premature failure. The more uniform strain distribution in PR-E12-NA allows the sample to sustain greater elongation before fracture.

Figure 3.10 presents the tensile properties of PR-E12-NA and PR-E24-NA samples. Similar to the extrudate results, both stiffness and ultimate strength show no significant differences, while the toughness is markedly lower, about 60%, for PR-E24-NA.

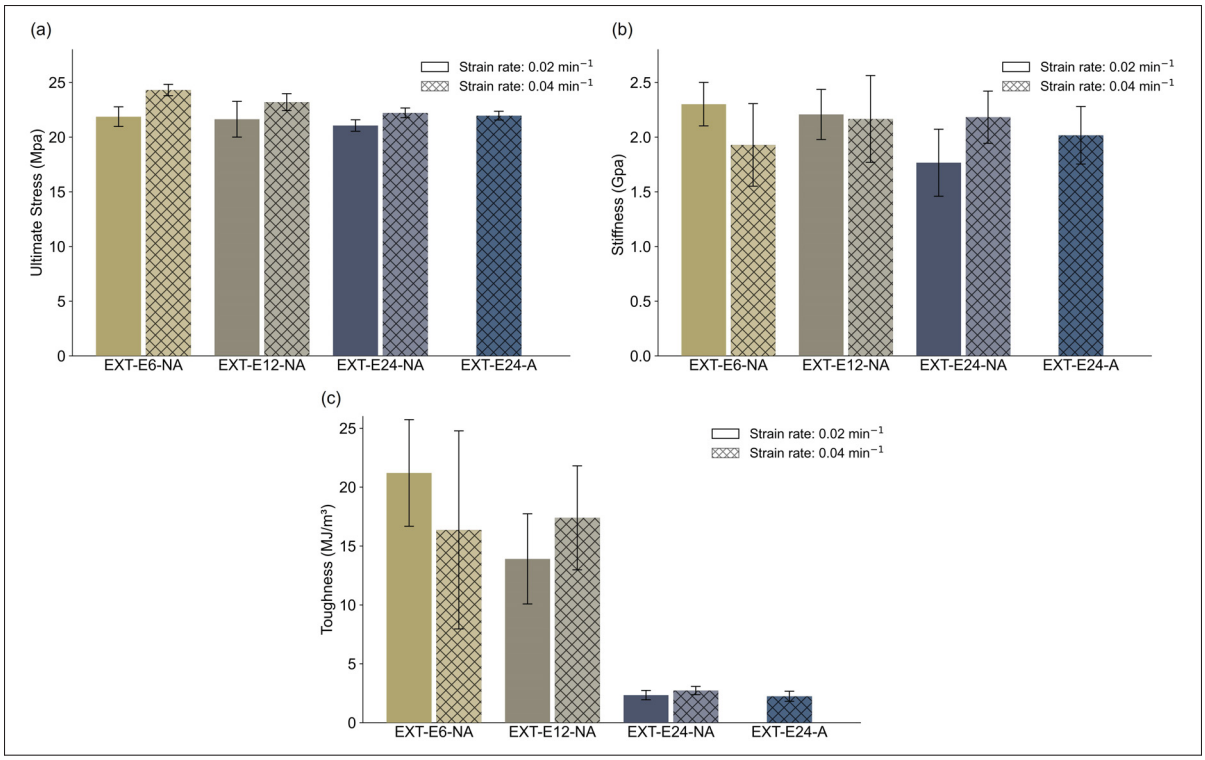

Figure 3.8 Tensile properties of extrudates at two strain rates: (a) Ultimate stress, (b) Stiffness, and (c) Toughness. While ultimate stress and stiffness show little variation with extrusion rate and testing strain rate, toughness is significantly reduced for EXT-E24 samples. Annealing had no noticeable effect on tensile properties

3.4.5 Damage mechanisms

Figure 3.11 shows representative failed samples from each set of extrudates and printed parts. Stress whitening is observed in all samples, indicating localized plastic deformation. In EXT-E24-NA, whitening is concentrated along distinct bands oriented perpendicular to the loading direction, reflecting strain localization. In contrast, EXT-E6-NA and EXT-E12-NA display a more uniform distribution of whitening across the gauge section, consistent with homogeneous deformation and higher ductility. A similar behaviour is observed in the printed samples, which aligns with the strain patterns revealed by DIC in Figure 3.9.

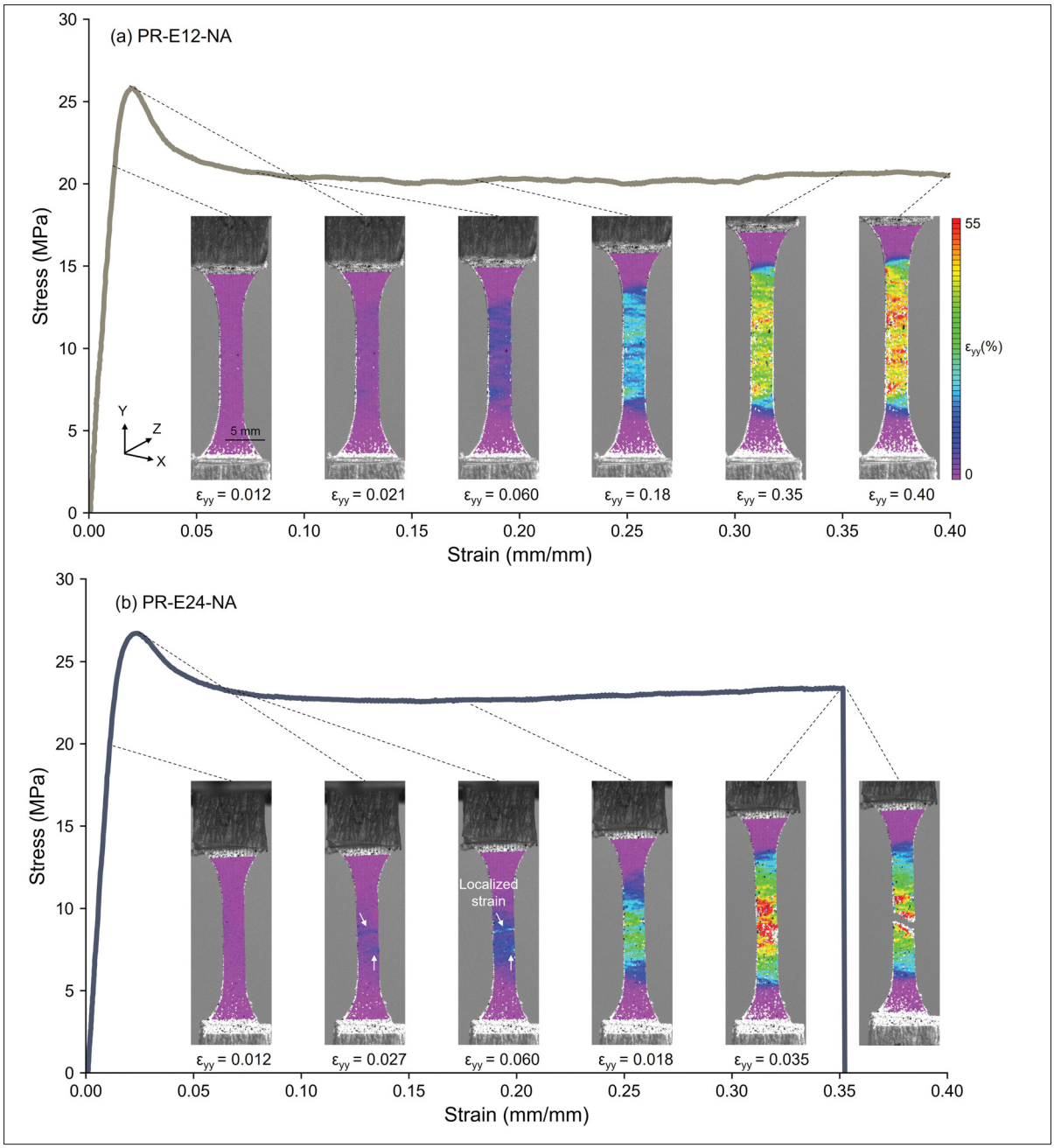

Figure 3.9 Stress–strain curves and corresponding DIC strain maps for (a) PR-E12-NA and (b) PR-E24-NA at selected deformation stages. PR-E12-NA shows more uniform strain distribution, while PR-E24-NA exhibits strain localization leading to earlier failure

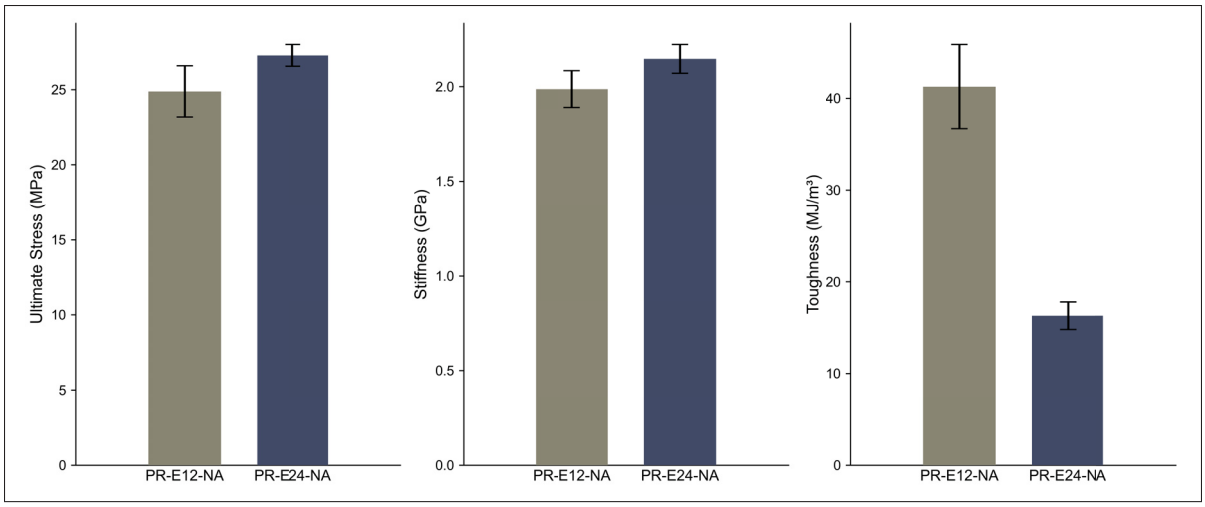

Figure 3.10 Tensile properties of PR-E12-NA and PR-E24-NA samples. Stiffness and ultimate strength are similar, while toughness is significantly lower for PR-E24-NA

3.5 Discussion

3.5.1 Tensile behaviour of extrudates

Toughness was calculated using the grip separation strain as proposed by ASTM D882, which corresponds to the grip displacement over the gauge length. However, it was observed during the experiments that the extrudate segment between the grips and bollards was under load, meaning that evaluating the toughness through the stress and strain over the gauge length is potentially an overestimation of the toughness. It should also be noted that failure occurred at the bollards for a majority of extrudates, where stress concentration can take place due to the curvature and the contact pressure with the bollards, further inducing a measurement error in the reported material strength and toughness. Although the testing methodology followed the recommendations of (Rodrigues *et al.*, 2023), these observations suggest that further improvements in sample geometry or testing setup may be necessary to more accurately capture the intrinsic tensile behaviour of the extrudates.

The observation of similar stiffness and ultimate tensile stress across different extrusion conditions suggests that the elastic behaviour of the material is not significantly affected by extrusion rate.

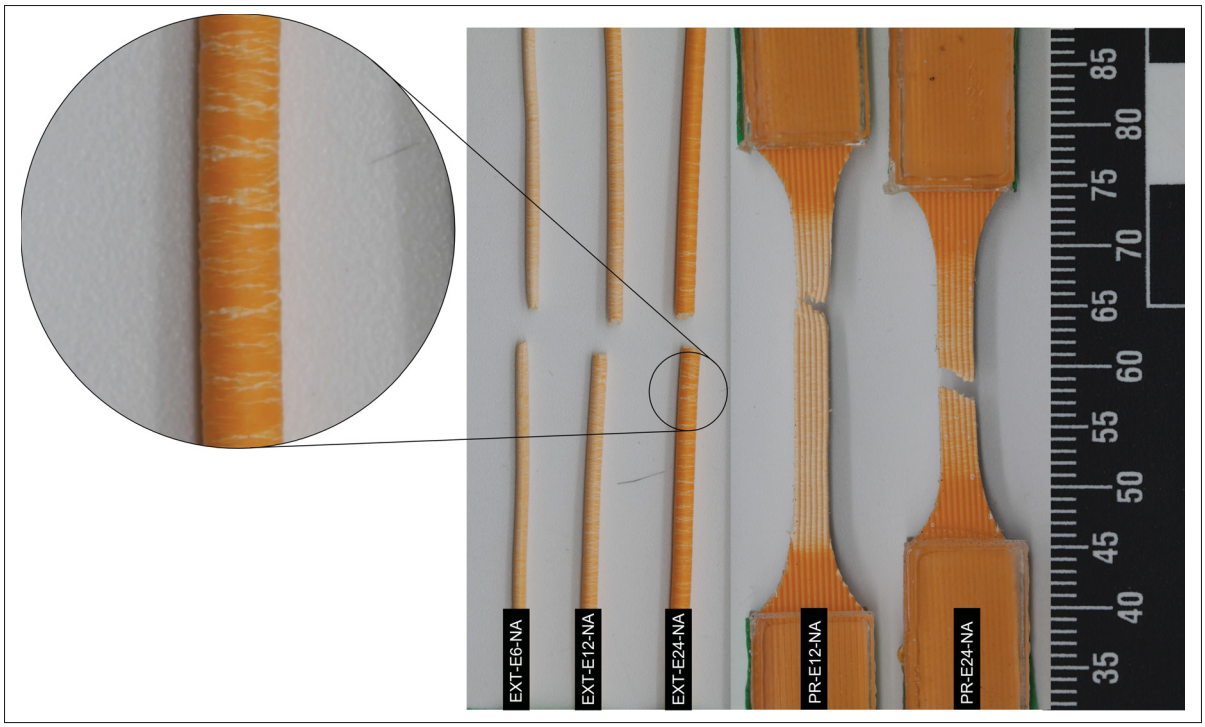

Figure 3.11 Representative failed samples of extrudates and printed parts. Stress whitening indicates localized plastic deformation, with EXT-E24-NA showing strain localization along bands, while EXT-E6-NA and EXT-E12-NA exhibit more uniform deformation. Similar trends are observed in printed samples

High extrusion rate samples exhibit a significant reduction in toughness, with extrudates showing an approximately 85% decrease, compared to around 60% for printed samples. This reduction may be explained by two main hypotheses. First, these samples exhibit a higher degree of crystallinity, which will be examined in detail in the following section. Second, higher extrusion rates may promote greater surface roughness in the extrudate samples, which could further contribute to the reduction in toughness. As shown in Figure 3.11, the rough surface features develop into deeper grooves under tensile load, visible as whitened lines, which likely act as high-strain locations initiating failure. This effect can explain the more pronounced reduction in toughness observed for extrudates, whereas the printed samples show less variation in surface roughness.

3.5.2 Morphology and microstructural analysis

The observed increase in swell ratio with extrusion rate is consistent with previous findings in the literature (Heller *et al.*, 2016; Smith *et al.*, 2024; De Rosa, Tammaro & D'Avino, 2023; Colon, Kazmer, Peterson & Seppala, 2023). For the printed samples, the cross-sectional area of the extrudate remained essentially unchanged across extrusion rates, which agrees with observations of (Domenech *et al.*, 2025; Geng *et al.*, 2019). In confined FFF flow conditions, the limited space between the nozzle and the previously deposited extrudate can restrict die swell, indicating that its effect on print dimensions is minimal. Instead, die swell under these conditions is more likely to influence interlayer adhesion through unrelaxed polymer chains.

Surface roughness exhibits a similar trend. An extrusion rate of 24 mm^3/s produces a noticeably rough and corrugated surface on the freely fabricates extrudates, whereas this effect is largely suppressed in the printed samples. This difference may be attributed to the faster cooling during printing or to the distinct deposition conditions in printing, where the material is extruded onto a pre-existing layer rather than into open air.

Higher extrusion rate samples, both extrudates and printed parts, exhibited increased crystallinity, which may result from shear-induced crystallization due to elevated shear rates inside the nozzle. Another contributing factor could be partial preservation of the feedstock filament's microstructure, as noted by (Comelli *et al.*, 2022). At higher extrusion rates, the polymer resides in the hot nozzle for a shorter period of time, potentially retaining some chain orientation and conserving more of the feedstock's original crystallinity. This higher degree of crystallinity can lead to reduced toughness, as also reported by (Hart, Dunn & Wetzel, 2020). Differences in crystallinity between extrudates and printed samples can be attributed to their cooling behaviour. Extrudates, with a larger cross-section and therefore greater thermal mass, cool relatively slowly in open air. In contrast, printed extrudates, with a smaller cross-section, cool more rapidly, and heat conduction into the underlying layer further accelerates their cooling. Faster cooling during printing may limit crystallization. Annealing was performed to relax polymer chains in the amorphous region without significantly altering crystallinity. DSC results showed a slight

decrease in cold crystallization, likely due to chain relaxation. The absence of significant changes in tensile behaviour after annealing suggests that differences in ductility are not governed by the amorphous regions, and that the extrusion process likely does not induce substantial chain orientation within these regions.

3.6 Conclusion

In this study, the impact of extrusion rate on the properties of FFF extrudates was investigated. Tensile testing showed that extrudates produced at higher extrusion rates exhibited a significant reduction in toughness, to approximately 85% of the low-rate samples, while the ultimate tensile strength and stiffness remained largely unaffected. DSC revealed that low extrusion rate extrudates displayed roughly 70% lower crystallinity compared with high-rate extrudates. High extrusion rate extrudates also exhibited increased swell ratios and greater surface roughness.

While the increases in swell ratio and surface roughness seen in the free extrudates were largely suppressed in printed samples, similar trends in mechanical performance were observed when the extrudates were printed as single-extrudate hollow boxes using the same extrusion parameters. Digital image correlation on printed samples highlighted differences in strain distribution: low extrusion rate samples showed more uniform strain throughout the part, while high extrusion rate samples exhibited localized strain concentrations and early onset of surface damage, indicating lower effective deformation before failure.

These findings suggest that the loss of toughness in PLA at high extrusion rates may be linked to increased crystallinity at higher flow rates, with increased surface roughness potentially further reducing ductility by promoting earlier strain localization. The results demonstrate that variations in extrusion parameters can substantially affect extrudate properties and the mechanical behaviour of printed parts, emphasizing the importance of considering extrudate-level properties in the design and optimization of FFF and FGF processes. In particular, increasing print speed to enhance productivity may lead to more brittle parts, highlighting the need for careful process

selection. Alternative strategies, such as optimized extruder or nozzle design, could help mitigate this effect and improve the performance and reliability of additive-manufactured components.

CHAPTER 4

REASSESSING ANISOTROPY IN 3D PRINTED STRUCTURES: THE ROLE OF EXTRUDATE GEOMETRY VS INTERFACE BONDING

Maryam Shokrollahi[1] , Adam W. Smith [1] , Arthur Levy[2] , Martine Dubé[1,3] , Ilyass Tabiai [1,3]

[1] Department of Mechanical Engineering, École de technologie supérieure, Montréal, Canada

[2] Nantes Université, CNRS, Laboratoire de thermique et énergie de Nantes, LTeN, UMR 6607, F-44000 Nantes, France

[3] CREPEC, Research Center for High Performance Polymer and Composite Systems, Mechanical Engineering Department, McGill University, Montréal, Canada

Paper published in *Journal of Manufacturing Processes*, September 2025

4.1 Abstract

Mechanical performance of 3D-printed parts produced through fused filament fabrication (FFF) and fused granular fabrication (FGF) is governed by interface bond quality and extrudate geometry. This study investigates these factors in polyethylene terephthalate glycol (PETG) parts printed at small (FFF) and large (FGF) scales, subjected to tensile testing along extrudate and transverse directions. Anisotropy in 3D-printed parts arises from incomplete interface bonding and formation of periodic ridges (interface notches) between extrudates. A machining method is used to remove the notches, enabling independent evaluation of these mechanisms. Results show that interface notches reduce part strength, with tensile strength decreasing by 28% in small-scale and 70% in large-scale samples. Digital image correlation (DIC) quantifies strain fields induced by the notches during loading, showing that the strain concentration factor (K_ε) decreases with smaller layer heights. Mesoscale finite element analysis (FEA), validated by DIC, confirms the experimental findings and highlights the critical influence of notch root radius in K_ε. Once interface notches are eliminated, isotropic properties are achieved, demonstrating full bond strength. These findings emphasize the primary role of extrudate geometry in anisotropy and

premature failure, guiding optimization of printing parameters and the design of next-generation 3D printing equipment aimed at mitigating these issues.

4.2 Introduction

The global Additive Manufacturing (AM) market, valued at over $20 billion in 2023, is projected to grow at an annual rate of 23% through 2030 (Grand View Research, 2024). Originally used primarily for prototyping, AM has evolved into a key player in consumer goods production, with nearly 37 million 3D-printed parts produced in 2023—a 23% increase from 2022. Polymer AM services dominate this sector, while metal-based technologies continue to show steady growth. Among polymer AM techniques, polymer extrusion ranks third, showing a 25.3% growth and reaching 833,000 parts produced in 2023 (Sher, 2024a). However, its further adoption is hindered by limited mechanical properties of the printed parts.

Polymer extrusion-based additive manufacturing includes fused filament fabrication (FFF) and fused granular fabrication (FGF), both of which involve extruding material through a heated nozzle onto a platform to construct components layer by layer. FFF uses pre-fabricated filaments with relatively high tolerancing, to print small-to-medium sized (few centimetres to a meter) components with intricate geometries (Patel & Taufik, 2022; Penumakala *et al.*, 2020). FGF systems, on the other hand, feature a screw mechanism that allows for the direct extrusion of polymer pellets to produce medium-to-large scale (up to several meters) components (Pignatelli & Percoco, 2022; Woern & Pearce, 2018).

Despite their rapid adoption, polymer extrusion methods have seen limited use in high-quality applications due to inferior mechanical performance. However, polymers have shown promise in conventional manufacturing for lightweight, acceptable-performance components such as aerospace brackets and mounts (PlasticsToday Staff, 2015). If anisotropy and mechanical property challenges in FFF can be addressed, it could become a transformative, cost-effective, and scalable solution for producing lightweight components across various sizes without significant cost increases. In large-scale polymer AM, the use of FGF remains limited to certain

applications for similar reasons as FFF. For instance, in the wind turbine industry, FGF has the potential to replace traditional composite manufacturing by meeting required mechanical demands (Zarzoor, Jaber & Shandookh, 2024). FGF would offer production by reducing costs for moulds, shortening production times, and minimizing material waste and energy consumption—effectively addressing the growing demand for sustainable and eco-friendly manufacturing solutions.

Unlocking such applications requires a deeper understanding of the strength reduction mechanisms in FFF/FGF parts. Two principal mechanisms have been identified as the possible root causes of the inferior mechanical performance of these parts: the first involves the bond formation between consecutive layers of material. Figure 4.1(a) schematically represents the healing process at the polymer chain level. Development of intimate contact of the interface coupled with sufficient molecular diffusion is needed to ensure a bonded interface with properties like those of the bulk material. However, with both of these processes being highly temperature-dependent and the rapid cooling of the extrudate during additive manufacturing, achieving a fully formed bond is often hindered (Deshpande, Ravi, Kusel, Churchwell & Hsu, 2019; Gao *et al.*, 2021; Kishore *et al.*, 2017; Patadiya, Dave & Rajpurohit, 2020; Ravi, Deshpande & Hsu, 2016; Tronvoll, Vedvik, Elverum & Welo, 2019).

The second mechanism, as shown in Figures 4.1(b) and 4.1(c), involves the geometry of the extrudate, which typically has a rounded rectangular shape. This results in a ridge effect on the surface of the printed part, as illustrated in Figure 4.1(b), and large internal macrovoids, shown in Figure 4.1(c) The resulting macrovoids are a significant contributor to the strength decrease observed in FFF and FGF parts. Many studies have reported an increase in mechanical properties by reducing the void content in printed parts (Al-Maharma, Patil & Markert, 2020; Kechagias & Zaoutsos, 2024; Pourali & Peterson, 2021; Rodriguez, Thomas & Renaud, 2000; Tao *et al.*, 2021). Additionally, stress concentration occurs at the ridges formed between adjacent extrudates (referred to as interface notches) when subjected to loads perpendicular to the print direction, as schematically shown in Figure 4.1(c) (Allum *et al.*, 2020c; Ghorbani *et al.*,

2022). This second mechanism, distinct from molecular bonding, points to the need for deeper investigation of geometric effects, which persists even when bonding is optimized.

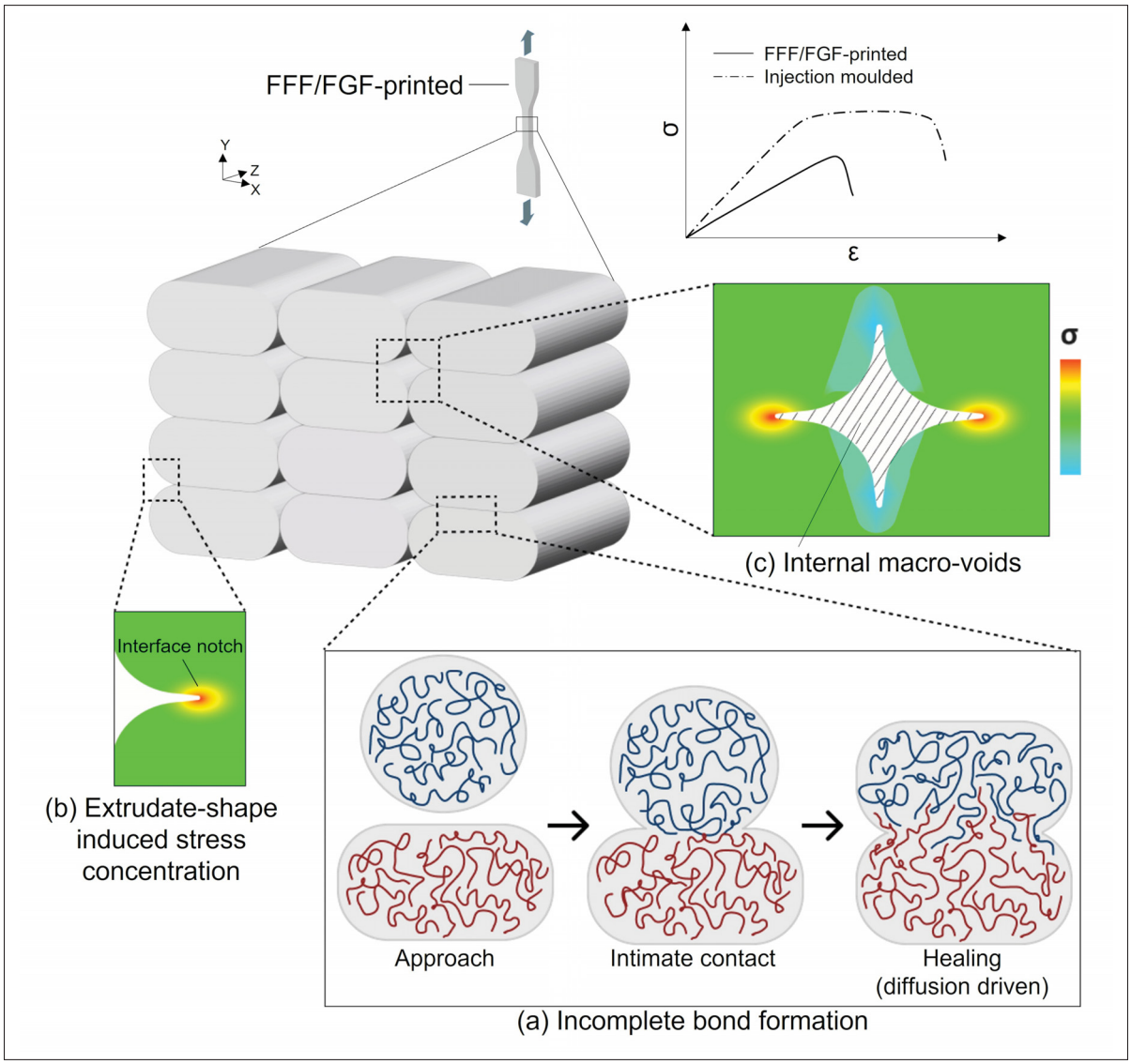

Figure 4.1 Schematic of the main strength reduction mechanisms in FFF/FGF printed parts: (a) Fast cooling of the extrudates prevents the complete interdiffusion of the polymer chains at the interface. (b) Interface notches act as stress concentration areas. (c) Porous mesostructure is also a result of the oval shape geometry of the extrudate

While earlier literature largely attributed mechanical weakness to insufficient interlayer bonding, more recent studies have demonstrated that bond strengths approaching bulk values can be

achieved—across a wide range of printing conditions—when the actual contact area between filaments is considered, rather than the nominal sample width measured by callipers (Allum, Moetazedian, Gleadall & Silberschmidt, 2021; Moetazedian *et al.*, 2023). Although such studies reported near-isotropic tensile strength, significant anisotropy remained in deformation behaviour. Further evidence comes from the work of Allum et al., where notches were deliberately introduced into compression-moulded thermoset samples to replicate the geometric features found in printed parts. Remarkably, these modified moulded samples exhibited mechanical performance—including tensile strength and damage mechanisms—closely resembling that of printed samples (Allum, Gleadall & Silberschmidt, 2020a). These findings suggest that interlayer bonding may not be the sole or dominant factor in strength reduction; instead, the microscale ridges and voids formed between adjacent extrudates appear to play a critical role (Allum *et al.*, 2023; Lin *et al.*, 2022, 2024).

Studies on the failure mechanisms of FFF/FGF printed parts often focus on the role of mesoscale characteristics in their structure. Mesoscale here refers to features at the level of individual extrudates (Conway & Pataky, 2019; Lingua, Piccirelli, Therriault & Lévesque, 2022; Webbe Kerekes, Lim, Joe & Yun, 2019). Lingua et al. identified mesostructure-related local phenomena that lead to interface failure in FFF-printed ABS samples with different layup orientations. Distinctive mesoscale damage mechanisms were identified using microstereoscopic digital image correlation (DIC) to obtain local strain distribution (Lingua *et al.*, 2022). Kerekes et al. (Webbe Kerekes *et al.*, 2019) investigated the progressive failure mechanisms in FFF-printed samples with varying infill densities and layer heights. They found that failure was initiated by strain concentrations at voids formed during the printing process, primarily at the intersections between extrudates. DIC results demonstrated localized strain at these premature voids, which increased in size as the load increased. The damage further progressed through the necking and tearing of extrudates and the nucleation of voids between them. Additionally, a stress-whitening effect, indicated by a change in colour to a whitish tone in the tensioned area, was observed following necking. This effect is attributed to the formation of crazes, i.e., microvoids resulting

from chain scission under tension, which scatter light and lead to a colour change (Bhardwaj, Henein & Wolfe, 2022; Farahani, Bagheri & Marouf, 2023).

Despite these findings on mesostructured features, less attention has been given to the localized phenomena at the extrudate scale induced by its shape. Allum et al. (Allum *et al.*, 2020a; Allum, Gleadall & Silberschmidt, 2020b) explored this aspect by using single-extrudate thick tensile samples to focus on the local strain fields around extrudate shape characteristics. They investigated the impact of interface notches on PLA's tensile properties and found that transverse samples failed at lower strain, while strength remained unchanged. FEA modelling suggested that after yielding, stress plateaued while strain kept increasing, leading to rapid strain concentration and premature failure. Ghorbani et al. (Ghorbani *et al.*, 2022) reported that anisotropy in tensile properties decreases as the void content reduces. They performed micromechanical numerical modelling to examine the local effects of extrudate shape characteristics in various void geometries. The results revealed different stress fields in transverse direction for distinct void geometries, but the underlying reasons for these variations in stress remain unclear. In a recent study by Kundurthi et al. (Kundurthi *et al.*, 2023), single extrudate thick dogbone samples were tested as-printed and after surface polishing in the transverse direction. The results highlighted that significant strength reduction in the as-printed samples is attributed to the interface notch characteristics that act as stress concentrators. Two parameters affecting the stress concentration factor at the notches were identified as the notch depth, and the radius at the notch root normalized by the layer height. Based on their obtained empirical equation, the theoretical stress concentration factor increases with a larger notch depth and smaller notch root radius. He et al. (He *et al.*, 2020) characterized the interface notches by the notch depth and notch angle in 3D printed cement paste to investigate its effect on the interface strength. They reported that tensile failure initiated at the notches, significantly reducing the strength.

Understanding how notch characteristics evolve under different print conditions is essential for improving mechanical performance in material extrusion processes. Moetazedian et al. (Moetazedian *et al.*, 2023) demonstrated that lower print speeds result in more acute notch angles, leading to higher stress concentrations, while extrusion temperature and layer time appear to

have limited influence. Layer height, on the other hand, has been shown to significantly affect the extrudate shape and, consequently, the formation of interface notches (Balta & Altınkaynak, 2022). However, the precise relationship between process parameters and the mechanisms governing notch formation remains unclear. Emerging evidence suggests that interface notches are not fixed geometric outcomes but can be systematically tuned through processing conditions. This highlights the need for experimental validation, particularly when scaling up to larger structures where process control is more difficult.

Although previous studies have demonstrated the significant impact of interface notches on mechanical properties through mechanical testing and FEA, they have largely focused on tensile strength recovery and have not fully examined whether other key properties, such as strain at failure or necking behaviour, could be similarly recovered. Moreover, experimental quantification of strain fields around the notches—and, consequently, the validation of FEA models—remains lacking.

This study aims to address these gaps. Polyethylene terephthalate glycol (PETG), an amorphous polymer known for its durability, high chemical resistance, and ductility, was selected for this study due to its cost-effectiveness and ease of printing compared to other materials with similar performance (Özen, Abali, Völlmecke, Gerstel & Auhl, 2021a; Özen, Auhl, Völlmecke, Kiendl & Abali, 2021b; Srinivasan, Ruban, Deepanraj, Bhuvanesh & Bhuvanesh, 2020; Valvez, Silva & Reis, 2022). The effects of interface notch characteristics on the tensile behaviour of FFF and FGF printed samples have been explored. By decoupling the influence of interface notches from interface bond quality, the study provides a clearer understanding of how notch severity affects mechanical performance, without altering the microstructure of the printed part. FEA is employed to complement and validate the experimental results, specifically focusing on strain field distribution at the notch root. Experiments were conducted at different print conditions to compare the extent of strength reduction caused by notch characteristics, providing new insights into the relationship between print conditions and mechanical performance.

4.3 Materials and Methods

4.3.1 Materials

PETG pellets were obtained from 3DXTech Advanced Materials, featuring a density of 1.24 g/cm^3, a glass transition temperature of 80 °C measured by differential scanning calorimetry (DSC), and a tensile strength of 45 MPa according to ISO 527 (obtained from the material's datasheet).

4.3.2 Sample preparation

Two types of samples were printed: small-scale samples using FFF and large-scale samples using FGF. The following section describes the process for each.

4.3.2.1 Small-scale samples

- **Feedstock preparation: filaments**

The filament needed to print FFF samples was manufactured using PETG pellets and a Filament Maker Composer 450/350 (from 3devo). This machine is equipped with a single-screw extruder and four distinct heating zones, along with two fans serving as a cooling system. Additionally, it incorporates two rollers for extrudate pulling, an optical sensor with a 43 μm precision for measuring extrudate diameter, and a spooling system. Extrusion parameters for each extrudate were determined to maintain consistency in extrudate diameter (1.75 mm). The temperature settings for the four heating zones were as follows: 190 °C, 210 °C, 220 °C, and 230 °C.

- **Printing**

Single-extrudate walls measuring 8 cm in length and 7 cm in height (140 layers in total) were printed using the COGIT AM printer manufactured by the COGIT Composites company. This printer is equipped with a heated chamber with three heating zones, along with laminar and

circular air flow systems, ensuring a uniform chamber temperature distribution. Table 4.1 shows the printing parameters used during FFF printing.

Table 4.1 Small-scale printing parameters

Print temperature (°C)	**Nozzle diameter (mm)**	**Print speed mm/s**	**Layer height (mm)**	**Chamber temperature (°C)**	**Bed temperature (°C)**
220	1	15	0.5	25	44

- **Interface notch removal: sanding**

To eliminate the influence of interface notches, they were removed from the surface. As shown in Figure 4.2, the printed walls were initially attached to a flat surface using double-sided tape. Subsequently, one side of the wall was coated with a layer of paint and was sequentially sanded using an automatic polisher with sandpapers of 80, 120, 240, 400, 600, 800, 1000, 1500, 2000, 2500, and 3000 grit. The sanding process was continued until the paint was fully removed to ensure all surface features were eliminated. Debris and particles were removed from both the sandpaper and the wall surface using an air compressor. The process was repeated for the opposite side of the wall. Thickness measurements were taken before sanding, after sanding one side, and after sanding both sides by measuring 10 uniformly spaced points on the wall surface using a micrometre. Table 4.2 displays the measurements for a representative wall. The surface characteristics of the walls before and after the sanding process were captured using a LEXT4100 laser confocal microscope. Process parameters included a Z-stack with a Z-stack range of 900 μm and a Z-stack spacing of 10 μm and image corrections for improved quality. As shown in Figure 4.2, the inspection ensures that all surface features are removed, resulting in a R_a value of 45 μm.

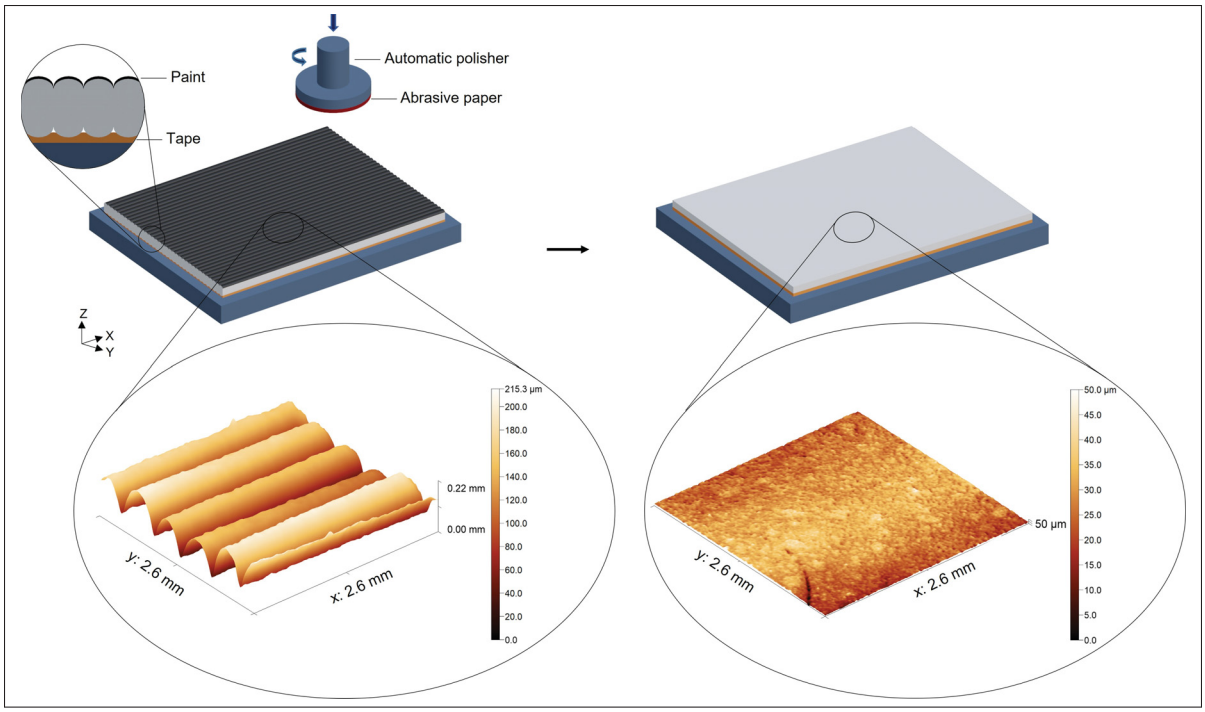

Figure 4.2 Schematic illustration of the sanding process: a layer of paint is applied on one side of the wall, which is affixed to a flat metallic surface. The wall surface is then sanded using an automatic polisher until the paint is completely removed. The same process is repeated for the other side of the wall, resulting in a final thickness variation of less than 5%. Confocal laser scanning microscopy images of a representative wall before and after sanding show that all peaks and grooves are removed, with a Ra value of 45 μm

Table 4.2 Thickness measurements of a representative small-scale wall. Measurements were taken at 10 uniformly spaced points on the wall surface using a micrometre. A relatively uniform thickness is achieved by sanding both sides of the wall

Initial thickness (mm)	**Thickness after sanding one side (mm)**	**Final thickness (mm)**	**Number of measurements**
1.407 ± 0.052	1.181 ± 0.033	0.619 ± 0.015	10

- **Dogbone extraction**

A cutting die was then employed to extract samples from the sanded walls following the ASTM D638 Type V geometry. Three different sets of samples were obtained according to the schematic depicted in Figure 4.4. The two 90° sets compare properties with and without surface characteristics, while the 0° set serves as a baseline for comparison with properties along the extrudate direction. Due to the thinness of the samples (0.5–0.7 mm), two tabs were attached to the ends of each sample to prevent failure at the grips during mechanical testing.

Large-scale samples Large-scale printing was performed because the larger extrudates make it easier to quantify the strain field around the interface notches. Additionally, this approach allows for a comparison with other studies that have focused on desktop-sized parts.

- **Printing**

An AM Flexbot 3D printer produced by the CEAD company was used for large-scale printing (Figure 4.3). The robot extruder features a base unit controlling temperature, extrusion speed, and automatic material transport. The printer processes various thermoplastic pellets, including fibre-reinforced ones. Additionally, it features a pellet dryer and a specialized print bed with diversion plugs to enhance workflow efficiency. PETG pellets were used to print one-extrudate thick walls measuring 50 cm in length and 30 cm in height (67 layers in total), based on the parameters shown in Table 4.3.

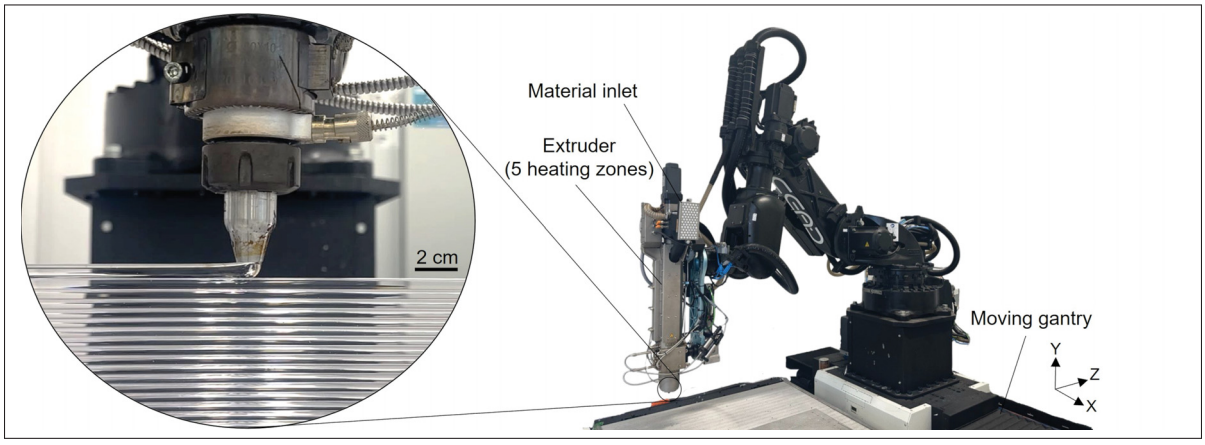

Figure 4.3 The robot extruder used for large-scale printing. The zoomed-in view shows the wall being printed

Table 4.3 Large-scale printing parameters

Extrusion temperature (°C)	**Nozzle diameter (mm)**	**Layer time (s)**	**Layer height (mm)**	**Bed temperature (°C)**
190-215	12	125	3, 4.5	25

- **Sample manufacturing & interface notch: machining**

To prepare tensile samples for mechanical testing, machining was carried out using CNC milling. Approximately 4 mm was machined from each side of the wall to fully remove the surface feature. Table 4.4 summarizes the machining parameters employed during the process, ensuring consistency and reproducibility in sample preparation. ASTM D638 Type III samples were chosen according to the thickness range of the walls. Similar to small-scale sets, samples were machined at 90° and 0° of the extrudate orientation from machined and non-machined walls, according to Figure 4.4.

Table 4.4 Machining parameters for surface removal and sample extraction

Operation	**Tool**	**Feed rate (mm/min)**	**Spindle speed (RPM)**	**Depth of cut (mm)**
Profiling	Endmill 1/4 Niagara (Seco) A345 #17003141	2540	12000	1.524
Rough facing	Facemill Walter 2" F4042.UB.051.Z06.11, inserts: ADHT1204PER-G88 WK10	3632	5730	1.27

Operation	Tool	Feed rate (mm/min)	Spindle speed (RPM)	Depth of cut (mm)
Finish facing	Facemill Walter 2" F4042.UB.051.Z06.11, inserts: ADHT1204PER-G88 WK10	3632	5730	0.762

Table 4.5 summarizes all samples studied in this work at both scales. In the sample codes, S and L denote small and large sizes, 90 and 0 indicate the extrudate direction with respect to the mechanical loading direction, and NM and M represent non-machined or machined samples, respectively. The final number corresponds to the layer height in millimetres.

Table 4.5 Samples' codes with different manufacturing methods, extrudate direction, and surface removal conditions

Sample	Fabrication method	Sample length (mm)	Extrudate direction with respect to tensile direction (°)	Surface removal	Layer height (mm)
S-90-NM-0.5	FFF	63.5	90	No	0.5
S-90-M-0.5	FFF	63.5	90	Yes	0.5
S-0-NM-0.5	FFF	63.5	0	No	0.5
L-90-NM-4.5	FGF	246	90	No	4.5
L-90-NM-3	FGF	246	90	No	3
L-90-M-4.5	FGF	246	90	Yes	4.5
L-0-NM-4.5	FGF	246	0	No	4.5

4.3.2.2 Temperature control experiment

A temperature control experiment was conducted and detailed in Appendix II to ensure that the material's properties are not affected by the heat generated during surface removal (sanding and

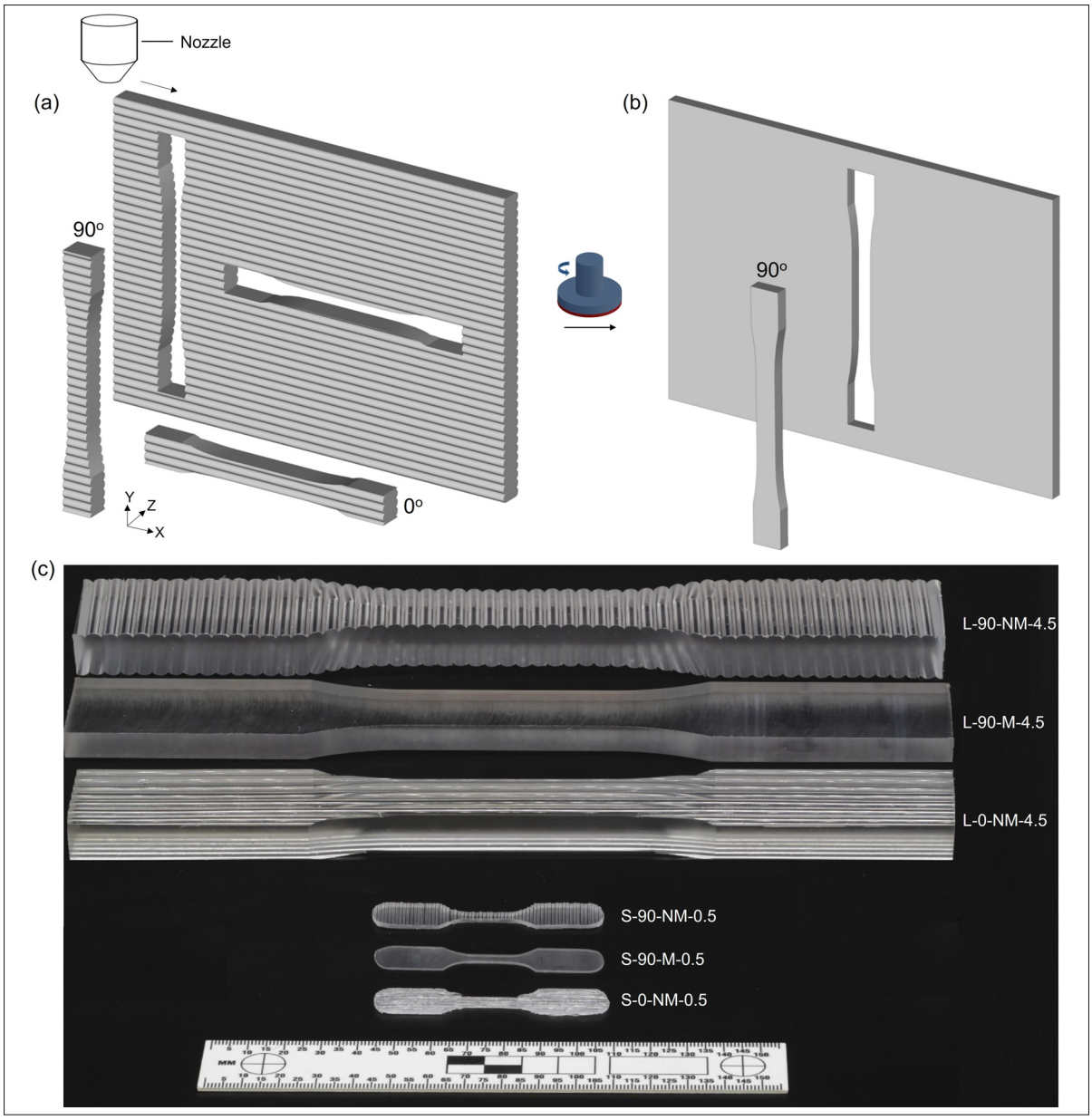

Figure 4.4 Schematic illustration of the three sets of samples extracted from a wall (a) With interface notches and (b) After surface machining. (c) Large- and small-scale samples

machining). The temperature variation in both surface removal methods was maintained below T_g, ensuring that the material properties remained unaffected by the surface removal process.

4.3.2.3 Compression moulding process

Bulk material properties were obtained using compression moulding to fabricate tensile samples. PETG pellets were first dried at 60 °C for 4 hours to remove moisture. The material was then moulded in a heated steel mould shaped according to ASTM D638 Type IV geometry, using a two-step process. In the first step, the mould was heated to 210 °C and a low pressure of 0.8 MPa was applied for 5 minutes to melt the material and allow trapped air to escape. This was followed by a consolidation step under 10 MPa pressure. The mould was cooled to room temperature under pressure to solidify the polymer and reduce residual stresses.

4.3.2.4 Microscopy

Cross-sections of the printed walls at both scales were observed under a microscope prior to the surface machining process. The cut surfaces were polished sequentially with sandpapers of 600, 800, 1200, and 2000 grit to obtain a smooth surface for the optical observations. The observations were performed using a Clemex microscope, and the images were analyzed using ImageJ software to characterize the interface notches, specifically the notch angle, notch depth, and notch root radius.

4.4 Tensile testing

The tensile properties of the samples were determined using an MTS Alliance RF/200 machine equipped with a 200 kN load cell for large-scale samples and a 500 N load cell for small-scale and compression-moulded samples. The samples were pre-conditioned at 60 °C for 8 hours before testing. The experiments were performed at a strain rate of 1 min^{-1} under room environmental conditions. A mechanical extensometer was utilized to measure the sample strain during the test for large-scale samples, while digital image correlation (DIC) was employed for strain measurement of all small-scale samples. For the DIC analysis, the virtual extensometer tool featured in VIC2D software (provided by Correlated Solutions) was used to calculate the average strain value between the two selected points in the gauge length, which is then reported as

the nominal strain value. Six and eight samples per set were tested at small and large scales, respectively. The number of samples reflects the maximum extractable from each printed wall, and both exceed the ASTM D638 minimum of five, ensuring reliable tensile properties assessment. For the compression-moulded set, five samples were tested after excluding those affected by trapped bubbles during the moulding process.

4.4.0.1 Digital image correlation

Sample preparation and setup

A layer of white acrylic colour paint (Vallejo Game Colour) was initially applied to the samples using an airbrush equipped with a 0.5 mm nozzle. Subsequently, a speckle pattern was achieved using a 0.2 mm nozzle to disperse black dots on the white background.

The imaging setup utilized a monochrome Grasshopper 3-51SM5M camera carefully positioned for full-field capture during tensile testing. The picture acquisition frequency (frame rate per second) for each set is reported in Table 4.6.

Software parameters

DIC analysis was performed using the commercial software package VIC2D. The smallest subset size was chosen to capture the interfaces accurately, ensuring at least three subsets per layer. Table 4.6 lists the selected subset sizes and the main DIC parameters for each test, including subset size, step size, and correlation type. Step size refers to the spacing between analyzed points. A subset of 2 means every second pixel is tracked, with untracked pixel displacements interpolated. Lagrangian strains were calculated using a 15-pixel filter size. The spatial resolution of displacement measurements (S_{rd}), defined as the distance between independent displacement measurements, is equivalent to the subset size. The spatial resolution of strain measurements ($S_{r\varepsilon}$), or the effective strain gauge length, was computed as: Step × (Strain Filter – 1) + Subset (Schaefer, Guglhoer, Sause & Drechsler, 2017). The speckle pattern and software parameters were optimized to achieve a minimal σ parameter, which represents the standard deviation

of the displacement error, keeping it below 0.03 for all sets to ensure low uncertainty. Noise assessment was conducted by capturing multiple images of an unloaded sample to obtain the resulting displacement and strain variations. The imaging and DIC analysis parameters are summarized in Table 4.6. The selected subset size and spatial resolution provide a sufficient number of independent measurement points per layer, ensuring the capture of detailed strain distributions. Specifically, each layer comprises approximately 3–4 independent measurement points (0.5 mm divided by 0.170 mm in small scale and 4.5 mm divided by 1.45 mm in large scale), which is adequate to distinguish strain variations both within individual extrudates and the strain concentration at the interfaces between extrudates. However, high strain gradients cannot be captured, which is important when comparing to FEA results due to the finer spatial resolution of FEA compared to DIC.

Table 4.6 Imaging and DIC analysis parameters

Sample	**FPS**	**Scale (px/ um)**	**Subset (px × px)**	**Step (px)**	**Corr. type**	**S^{rd} (mm)**	**S^{re} (mm)**	**Disp. var. (mm)**	**Strain var. (%)**
S-90-NM-0.5	3	17.3	9	1	Direct	0.156	0.170	6×10^{-3}	0.04
S-90-M-0.5	3	17.3	9	1	Direct	0.156	0.170	6×10^{-3}	0.04
S-0-NM-0.5	3	17.3	9	1	Direct	0.156	0.170	6×10^{-3}	0.04
L-90-NM-4.5	14	56.8	25	2	Direct	1.422	1.450	2×10^{-4}	0.02
L-90-NM-4.5 Side view	50	27.4	19	2	Direct	0.507	0.521	10^{-5}	0.002

Sample	FPS	Scale (px/ um)	Subset (px × px)	Step (px)	Corr. type	S^{rd} (mm)	S^{re} (mm)	Disp. var. (mm)	Strain var. (%)
L-90-NM-3 Side view	50	27.4	19	2	Direct	0.507	0.521	10^{-5}	0.002
L-90-M-4.5	14	56.8	25	2	Direct	1.422	1.450	2×10^{-4}	0.02
L-0-NM-4.5	14	56.8	25	2	Direct	1.422	1.450	2×10^{-4}	0.02

4.4.0.2 High-speed camera

High-speed camera imaging was used to capture the failure moment of the L-90-NM-4.5 sample in order to determine where the damage initiates and how it propagates. The fracture was captured using a Chronos High-Speed Camera. A high-density LED light source was positioned behind the sample's region of interest, and the video was recorded at 24,038 FPS with a resolution of 640×96 pixels.

4.4.1 Finite element analysis

A two-dimensional (2D) plane-strain quasi-static mechanical model was developed in COMSOL to evaluate strain concentration around a representative notch in the YZ plane (shown in Figure 4.14). The Y-direction corresponds to the tensile loading direction, following the coordinate system of the printing process. The plane strain condition was imposed, assuming negligible out-of-plane (X-axis) strain in the thickness direction. The notch geometry, including notch depth, angle, and root radius, was constructed based on experimental measurements. A quadratic interpolation for the displacement field was used. The triangular mesh was refined and verified

through convergence analysis, particularly around the notch where high strain gradients were expected. The generated geometry was subjected to a prescribed displacement at the top boundary representing the experimental condition. Symmetry was imposed on the left boundary corresponding to the symmetry plane. Perfect slip was imposed on the bottom boundary. The material was modelled as linear, elastic, and isotropic. The elastic modulus and Poisson's ratio were set to 2150 MPa and 0.4, respectively, as determined from tensile testing and DIC results of PETG samples.

4.5 Results

4.5.1 Tensile testing

The stress-strain curves for representative samples from the S-90-NM-0.5 and L-90-NM-4.5 sets are presented in Figure 4.5. In these samples, the interface notches are present, and the load applied is perpendicular to the extrudate direction. DIC results are also shown at different stages, corresponding to various levels of nominal strain. Nominal stress values were calculated by dividing the load values by the cross-sectional area at the bond width. Nominal strain ($\varepsilon_{yy\text{-n}}$) values are obtained through DIC using a virtual extensometer along the entire gauge length.

For the small-scale sample S-90-NM-0.5, the drop after the ultimate stress is not abrupt as shown in Figure 4.5(a), indicating that the sample underwent some plastic deformation before complete failure. At stage 2 (strain at failure, $\varepsilon_{yy\text{-n-failure}}$), the sample begins to plastically deform at the interfaces with the highest strain levels. The sample eventually breaks at these points, with the crack propagating from the edges of the sample.

The stress-strain curve for L-90-NM-4.5 indicates a brittle fracture with no plastic deformation prior to fracture. Similar to S-90-NM-0.5, the DIC results show concentrated strain at interfaces. However, all interfaces experience similar levels of strain up to the failure point, unlike S-90-NM-0.5, where plastic deformation occurs at the interfaces with the highest strain levels. This

indicates a better robustness of the large FGF process: the smaller FFF process results in more variable strain fields from interface to interface.

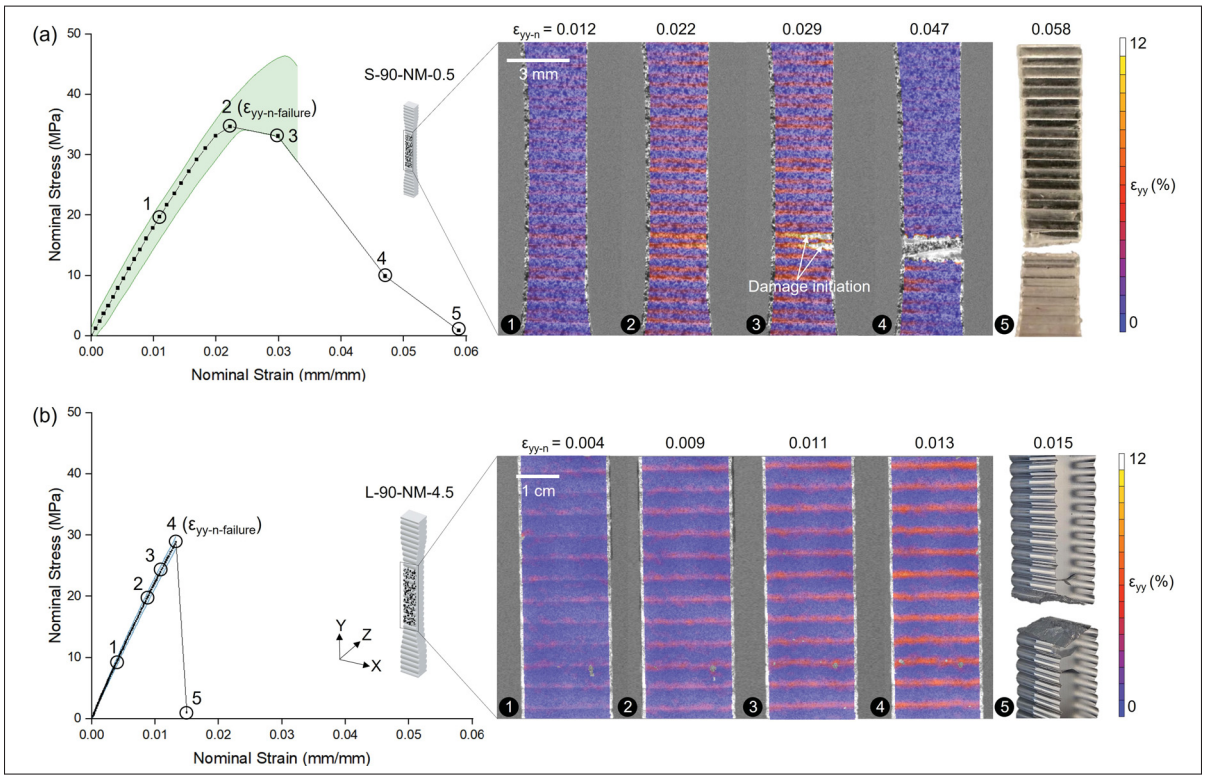

Figure 4.5 Stress-strain curve and DIC analysis of (a) S-90-NM-0.5 and (b) L-90-NM-4.5 at various stages. In S-90-NM-0.5, the strain is concentrated at the interfaces, with the concentration being more pronounced at some interfaces. The sample begins to plastically deform and ultimately fails in these regions. L-90-NM-4.5 shows a brittle failure at considerably low strain values. The brittle behaviour observed in these samples is attributed to the premature growth of the crack due to the strain concentration at the interface notches naturally formed during printing. Error bands indicate the range between the maximum and minimum data points from six tested samples

Figure 4.6 presents the results for 90°-machined and 0° samples in both scales. A noticeable shift in the sample's behaviour is observed upon surface machining: the brittle behaviour observed in Figure 4.5(a) with non-machined samples turns into a ductile deformation for S-90-M-0.5, as shown in Figure 4.6(a). Interfaces are not visible on DIC analysis, with the strain being uniformly distributed prior to yielding. A yielded band of higher strain is visible at an angled

direction, originating from two different locations. Subsequently, the yielded region extends throughout the entire length of the gauge length, reaching a nominal strain of over 100 %.

Similar behaviour is observed for S-0-NM-0.5, as shown in Figure 4.6(b), indicating that isotropic behaviour is achieved after removing surface roughness. For S-0-NM-0.5, the cross-sectional area was determined using the ImageJ software from an image of the sample's cross-section. The stress-strain data was truncated in both cases to better illustrate the sample behaviour before necking. Figure 4.6(c) shows that, similar to small-scale samples, the behaviour of the large-scale sample changes after surface machining.

The toughness values, measured by the area under the curve, are 0.2 MPa for L-90-NM-4.5 and 12.9 MPa for L-90-M-4.5. This indicates a shift from brittle to ductile behaviour upon the removal of interface notches. L-90-M-4.5 begins to yield at an angled direction, and the yielded region expands until the whitening effect occurs, coinciding with the second drop in the stress-strain curve. The sample ultimately fractures at the whitened area, which is also observed in L-0-NM-4.5 samples, as shown in Figure 4.6(d).

Figure 4.7 shows the strain profiles along the centre line in the Y-direction at $\varepsilon_{yy\text{-n-failure}}$ for both large- and small-scale samples, before and after the removal of interface notches. In non-machined samples (S-90-NM-0.5 and L-90-NM-4.5), strain concentration at the interfaces is observed. While the high strain level is reproduced from interface to interface for L-90-NM-4.5, it varies in S-90-NM-0.5. The high strain region deviates from the interface line around the two interfaces with the maximum strain values due to plastic deformation. After removing the interface notches, the strain distribution becomes nearly uniform, with no visible effect of the interface.

4.5.1.1 Effect of interface notches at small- and large-scale

Figure 4.8 presents the ultimate stress values for the three sample sets: small-scale (S-90-NM-0.5, S-90-M-0.5) and large-scale (L-90-NM-4.5, L-90-M-4.5, L-0-NM-4.5). In the small-scale samples, removing the interface notches increases the ultimate stress by an average of 28%,

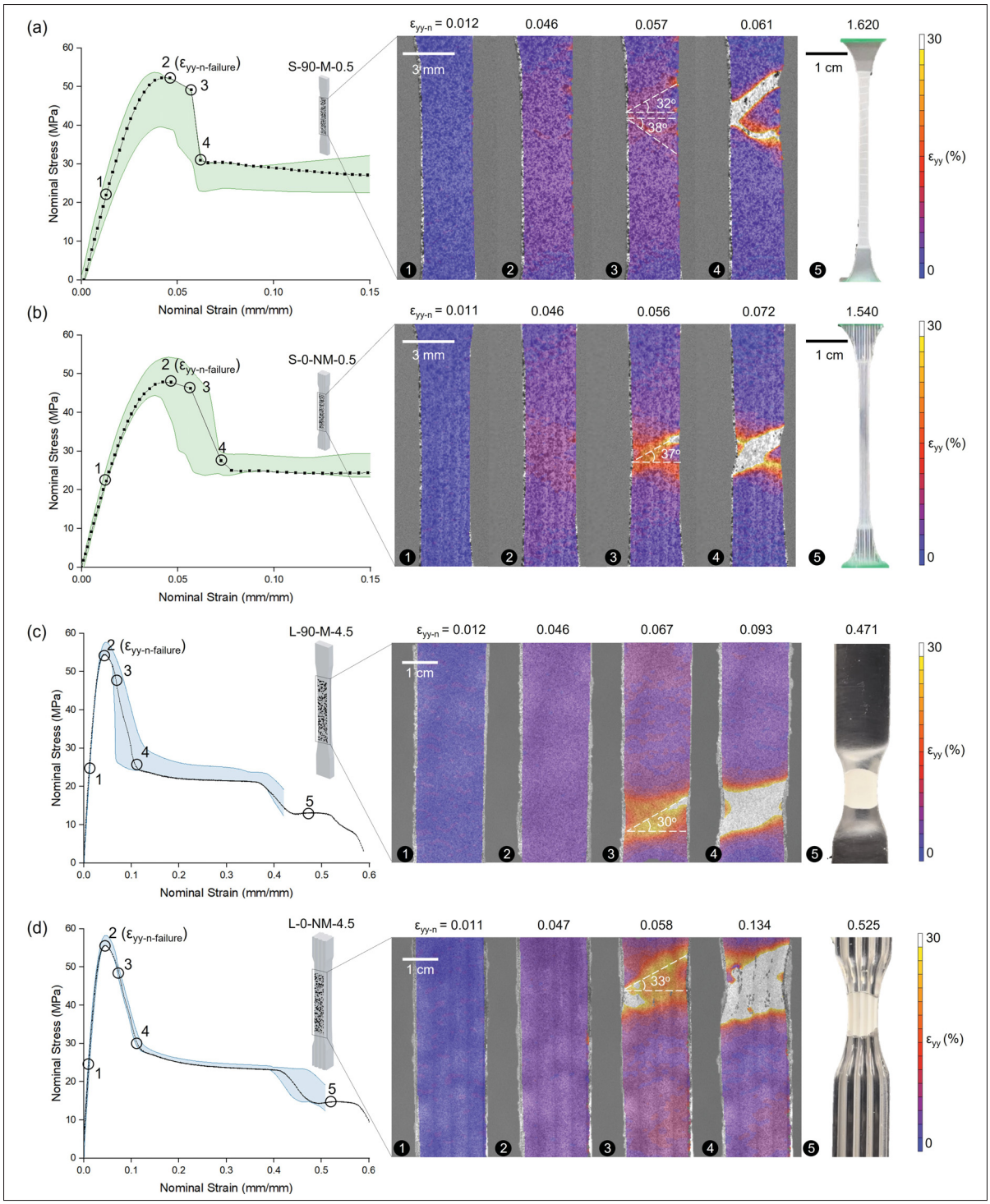

Figure 4.6 Stress-strain curve and DIC analysis of (a) S-90-M-0.5, (b) S-0-NM-0.5, (c) L-90-M-4.5 and (d) L-0-NM-4.5 at various stages. Samples show considerably high elongation at break after surface machining. Damage is initiated with a 45-degree angle yielding followed by extensive necking along the entire gauge length, typical of a bulk polymer behaviour. Necking is followed by whitening in large-scale samples. Error bands indicate the range between the maximum and minimum data points from six tested samples

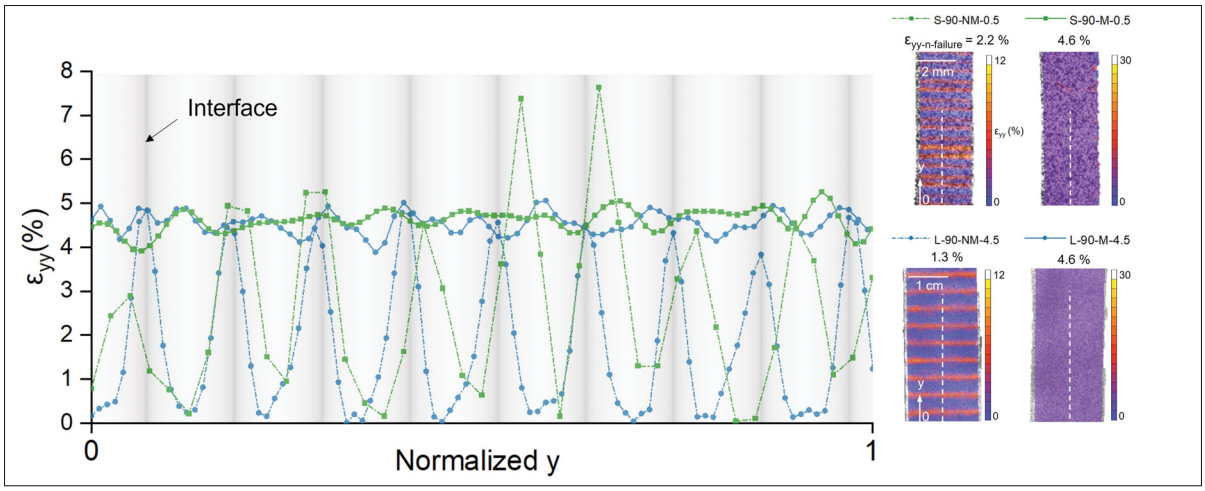

Figure 4.7 Strain values along the dashed line in S-90-NM-0.5, S-90-M-0.5, L-90-NM-4.5, and L-90-M-4.5. The y-axis data on the graph is normalized by dividing the values by the length of the dashed line. Strain concentration at the interfaces is evident in non-machined samples. While the strain levels at the interfaces remain consistent for L-90-NM-4.5, they vary and deviate from the interface line in S-90-NM-0.5 due to plastic deformation. Uniform distribution of strain is observed in machined samples

confirming that these notches act as strain concentrators, reducing both strength and ductility. Additionally, identical strength in S-90-M-0.5 and S-0-NM-0.5 indicates that the strength reduction transversely to the extrudate is solely due to this strain concentration effect and not to poor interface bonding. The results here suggest that under these printing conditions, it is possible to achieve a fully healed interface. Comparing the obtained properties of the large-scale samples shows that a significant recovery is achieved, with a 70% increase after surface machining. The resulting values closely approach those of the bulk samples prepared by compression moulding. Similar to the small scale, the same ultimate stress is obtained for L-90-M-4.5 and L-0-NM-4.5, which shows that healing is achieved during printing.

The different extent of recovery after surface machining in small- and large-scale samples is attributed to the strain concentration effect induced by the interface notches. Table 7 presents the notch geometric characterization parameters, including notch angle (θ), notch depth (a), and notch root radius (r), as schematically shown in Figure 4.8. The measurement procedures from

micrographs are detailed in Appendix III. The cross-sectional view of S-90-NM-0.5 shows a U-notch with a curved root, while L-90-NM-4.5 displays a V-notch at the interface. Unlike the small-scale samples, the notch root in the large-scale samples is significantly sharper, which could lead to higher strain concentration.

Table 4.7 Notch geometric characteristics at small and large scales

	Notch angle, θ (°)	**Notch depth, a (mm)**	**Root radius, r (μm)**	**Number of measurements**
Small-scale	36 ± 7	0.17 ± 0.02	6 ± 1	16
Large-scale	26 ± 3	1.36 ± 0.04	-	8

The high-speed camera images captured at the fracture moment of L-90-NM-4.5 are presented in Figure 4.9. At t_1, crack initiation is observed at one of the interface notches. In the next captured frame (t_2), this crack propagates through the sample's thickness. Multiple high-strain regions lead to simultaneous damage initiation at several opposite positions, resulting in the observation of two additional cracks at t_2. The cracks propagate in different directions, indicating that the interfaces are not the preferred crack propagation paths. By t_3, the sample begins to detach at the initial crack location, ultimately splitting into several parts due to damage occurring at multiple notches.

4.5.2 Study of the interface notches

4.5.2.1 Layer height effect

To investigate the evolution of interface notches under varying print conditions, layers with heights ranging from 3 to 6 mm were printed, and their cross-sections were analyzed to characterize the resulting notches. As shown in Figure 4.10, the results indicate that notch depth increases while notch angle decreases with layer height, suggesting that notches become more severe as layer height increases. Since a and θ are dependent variables, an increase in a for a

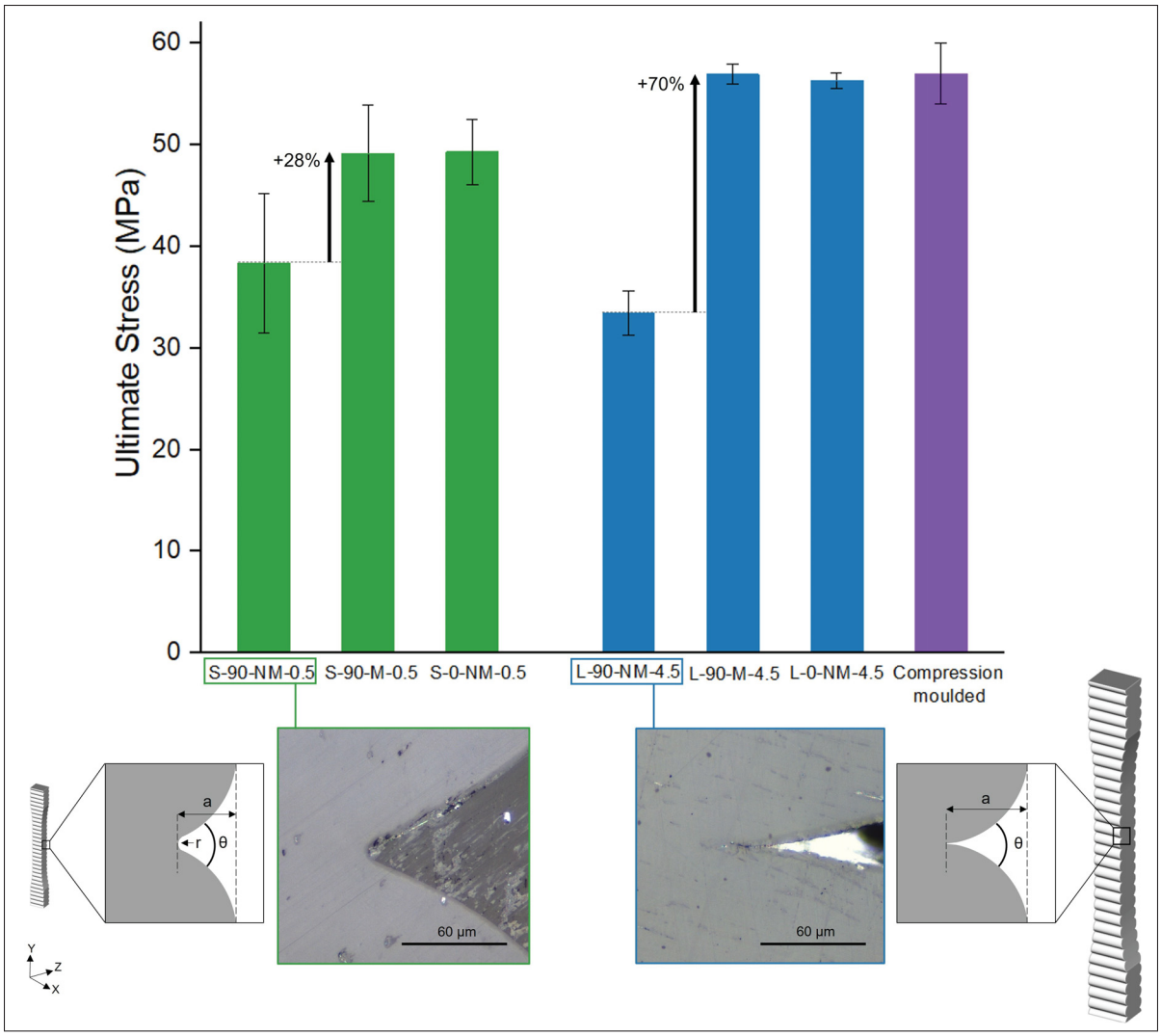

Figure 4.8 The ultimate stress values for small- and large-scale prints, as well as compression moulded ones. Strength recovery after surface machining at both scales highlights the strain concentration effect of the interface notches. Similar ultimate stress values for S-90-M-0.5 and S-90-NM-0.5, as well as L-90-M-4.5 and L-90-NM-4.5, indicate full-strength bond formation at both scales. Error bars indicate one standard deviation. Cross-sectional views of the interface notches show a rounded notch root for S-90-NM-0.5, while a crack-like root is observed for L-90-NM-4.5

given extrudate width corresponds to a decrease in θ. The relationship between these variables is obtained as: $a = -0.042\theta + 2.5$ up to 5.25. However, this trend does not persist at 6 mm, likely due to excessive material flow caused by a slow cooling rate, preventing the extrudate from retaining its shape during solidification. It can be observed that the notch shape changes

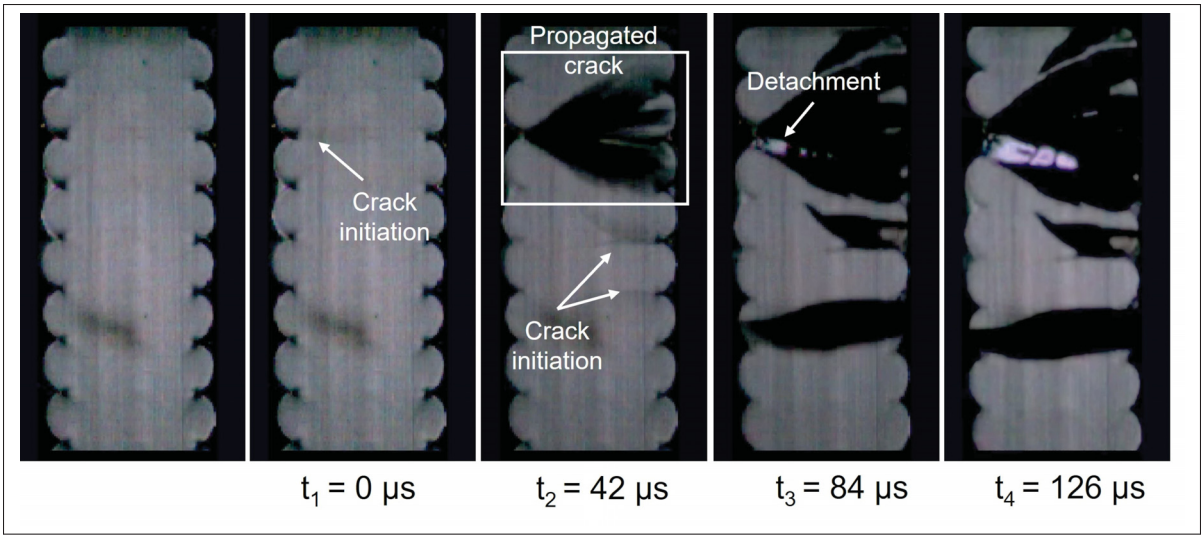

Figure 4.9 High-speed camera images at the fracture moment of L-90-NM-4.5. Cracks initiate at the notches at different locations and propagate along different paths, indicating that the interfaces are not the preferred crack propagation paths

beyond a certain layer height, transitioning from a U-shaped notch with a curved root at 3 and 3.75 mm layers to a V-shaped, crack-like form at higher layer heights.

To analyze strain fields induced by notches at different layer heights, high-resolution DIC was performed on a section of the gauge length from the side view for large-scale samples printed with 3 and 4.5 mm layer heights. This analysis was only feasible for large-scale samples, as the extrudate width in small-scale prints (~1.4 mm) was too narrow for effective measurement. Figure 4.11(a) presents the DIC results at nominal strain just before failure ($\varepsilon_{yy\text{-n-failure}}$), highlighting strain concentration at interface notches. The zoomed-in view further reveals localized strain fields around the notch. The high-strain region takes on a half-oval shape that extends inward from the notch. Angled high-strain bands emerge from the ends of this oval (shown by dashed lines enclosing the region), resembling the typical pattern observed at the crack tip. This pattern is consistently observed across multiple notches. The high-strain regions span several millimetres and connect with similar regions from adjacent notches.

Moreover, a high-strain region at a 21-degree angle is visible (indicated by a dashed line in Figure 4.7), suggesting that the sample would have likely yielded there if there had been no

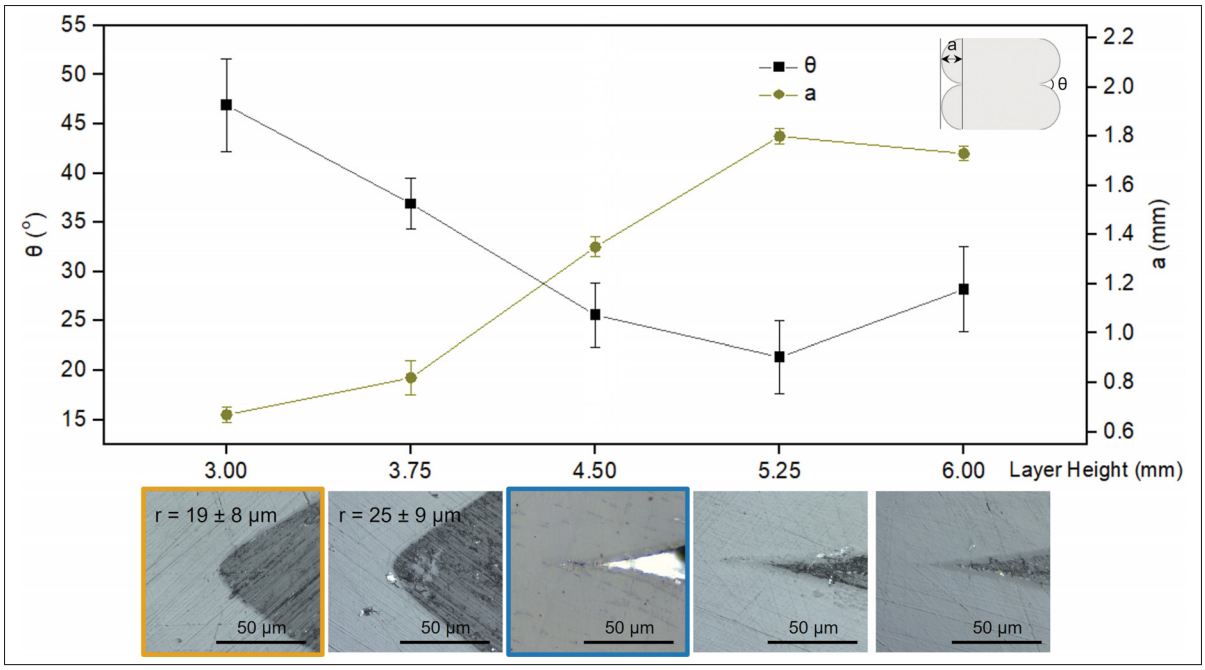

Figure 4.10 Notch characterization parameters at different layer heights. Notch depth (a) increases while notch angle (θ) decreases, both indicating greater severity with increasing layer height. This trend is not observed at 6 mm, likely due to excessive material flow from insufficient cooling, affecting the extrudate shape

strain concentration at the edges. Figure 4.11(b) compares nominal stress and strain at break, showing that L-90-NM-3 fails at higher strain and slightly higher stress, likely due to differences in notch-induced strain fields.

To investigate the linearity of the behaviour, Figure 4.12 shows the strain concentration factor at the notch plotted against the nominal strain for L-90-NM-4.5 and L-90-NM-3. Data points at strains below 0.003 contained too much noise and were therefore omitted from the graph. The graph illustrates that the strain concentration factor remains relatively constant (2.7 ± 0.5) for L-90-NM-3, while it slightly increases with nominal strain for L-90-NM-4.5, indicating the onset of non-linear elastic behaviour.

Figure 4.13(a) presents the strain concentration factor along the Z-axis. Localized strain concentration within a small area (less than 2 mm) is observed, which sharply decreases outside this region. A higher strain concentration factor at the notches in L-90-NM-4.5 compared to

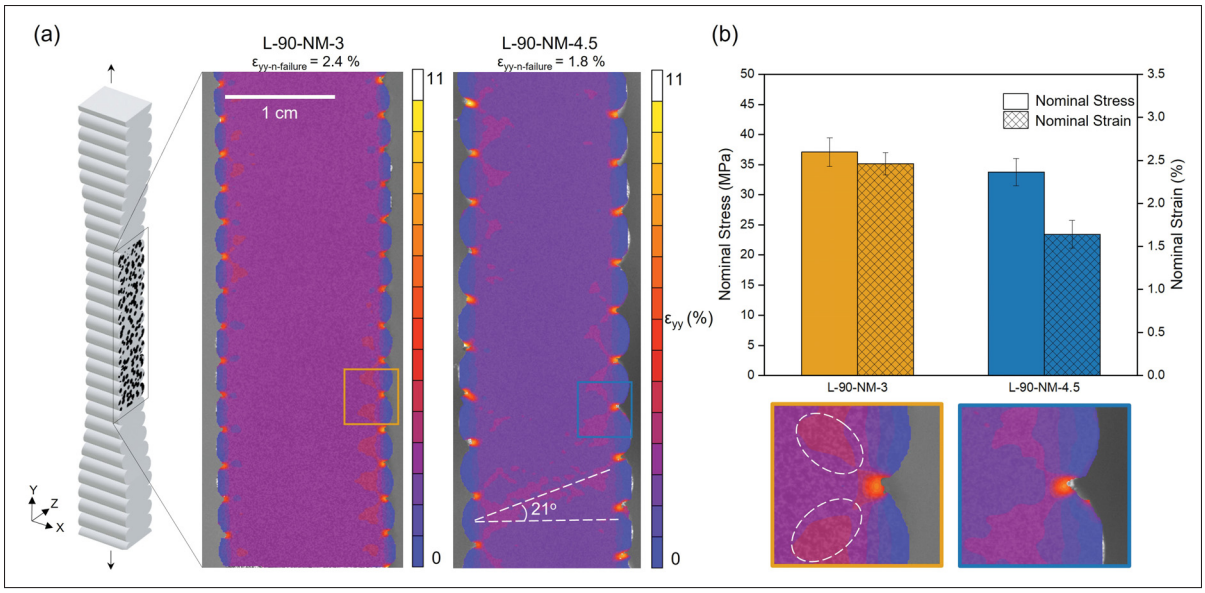

Figure 4.11 (a) High-resolution DIC analysis of the side view of L-90-NM-4.5 and L-90-NM-3 at nominal strain before failure, showing strain fields induced by interface notches. These strain fields are localized, with no visible effect beyond this region. The angled high-strain region may indicate the potential yielding location in the absence of strain concentration features. (b) Nominal stress and strain at break, showing that L-90-NM-3 fails at a higher strain and slightly higher stress

L-90-NM-3 confirms increased notch severity with larger layer heights. Figure 4.13(b) presents the strain concentration factor distribution for 20 different notches at $\varepsilon_{yy\text{-n-failure}}$, obtained by dividing the strain values at the notches by the nominal strain value (solid line represents the normal distribution). The results highlight the variability in notch characteristics within the sample, as reflected in the standard deviation values reported in Figure 4.10.

4.5.2.2 FEA of interface notches

Figure 4.14 shows the strain concentration factor obtained via FEA for the notch geometry corresponding to L-90-NM-3. It is important to note that such a model is not feasible for L-90-NM-4.5, as the notch root resembles a crack, with a continuous approach, as this involves a singularity in the stress field (Weißgraeber, Leguillon & Becker, 2016). The higher strain concentration value observed with FEA (approximately twice as high) is attributed to the finer

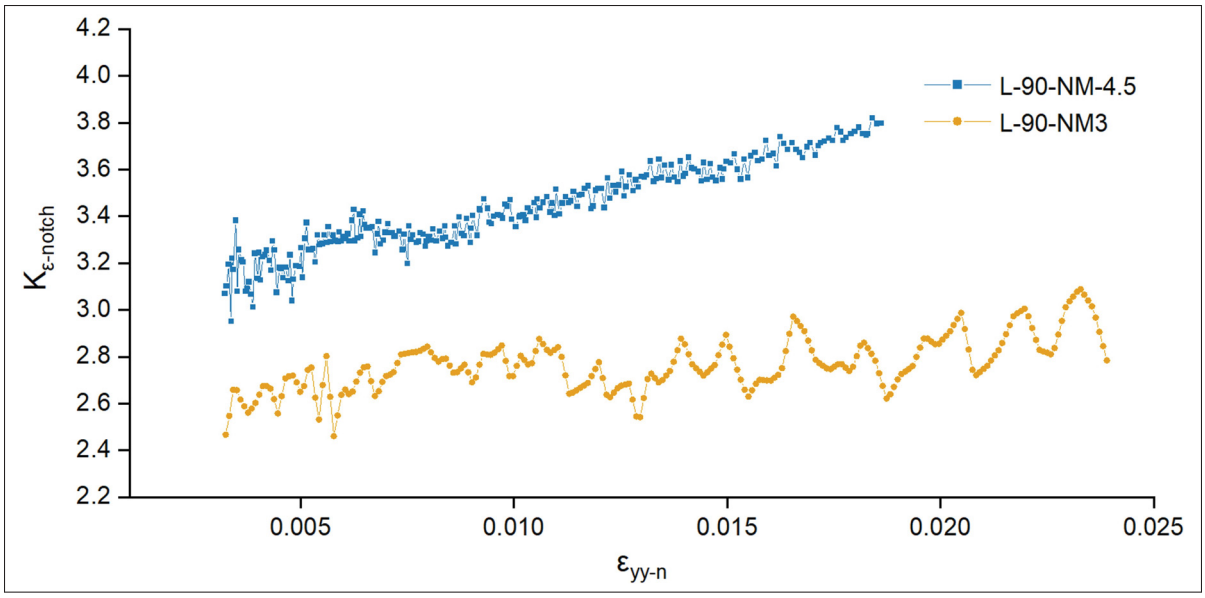

Figure 4.12 Effect of nominal strain on $K_{\varepsilon\text{-notch}}$. The factor remains relatively constant for L-90-NM-3, while it slightly increases with nominal strain for L-90-NM-4.5

spatial resolution in FEA compared to DIC (0.5 mm). A coarser mesh cannot achieve a similar resolution, as it fails to capture the geometric features of the notch root. Additionally, at the considered frame ($\varepsilon_{yy\text{-n-failure}}$) for DIC, plasticity likely occurred at the notch tip, which is not accounted for in the elastic FEA model. However, the average strain calculated in the area marked by the dashed circle is very close between FEA and DIC (2.12% and 2.21%, respectively), suggesting that the model is valid and aligns closely with the experimental data.

It was observed that curved-root notches form under certain printing conditions. To investigate the potential impact of root radius on the strain concentration factor at the notch, the concentration factor was evaluated for different r values. Figure 4.15 presents the strain concentration factor obtained from FEA, along with analytical stress concentration values from the literature (Schijve, 2009), for different notch geometries observed in the experiment across various layer heights. Since a and θ are dependent variables, only θ is presented here. The stress concentration factor values obtained from FEA closely matched the strain concentration factor values, which can be attributed to the assumption of an elastic, isotropic, and homogeneous material, as well as the minimal influence of Poisson's ratio in this case.

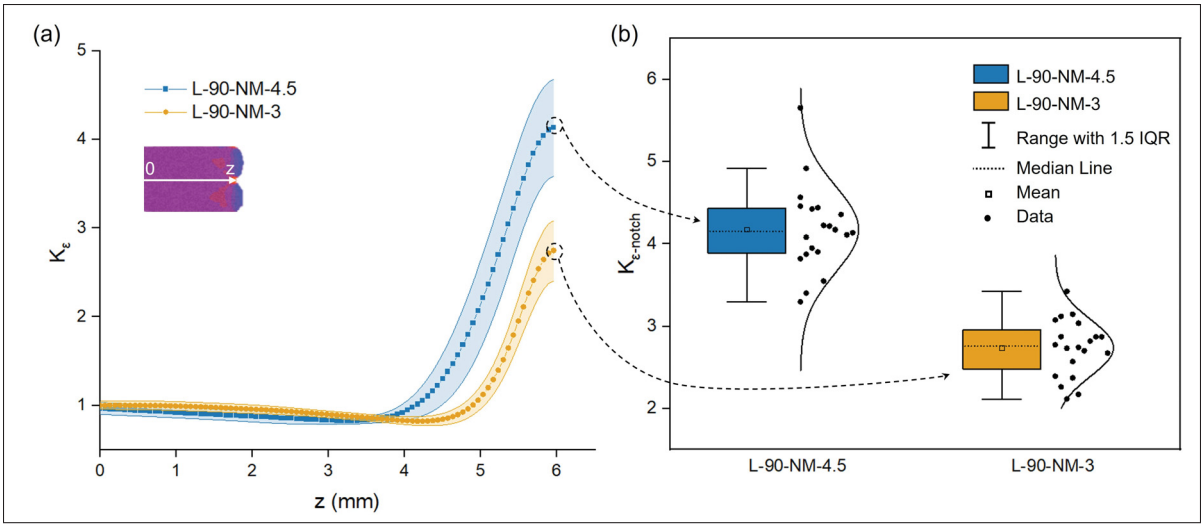

Figure 4.13 (a) Strain concentration factor (K_ε) values along the x-axis (white arrow) show localized strain at the notch root, with values sharply decreasing near the region and approaching 1 as the distance increases. K_ε is higher at the notches and their vicinity for L-90-NM-4.5 compared to L-90-NM-3. (b) Strain concentration factor values at the notch ($K_{\varepsilon\text{-notch}}$) for L-90-NM-4.5 and L-90-NM-3 at $\varepsilon_{yy\text{-n-failure}}$. The distribution shows significant variability in strain concentration values among the notches within a single sample

The results indicate that for a given value of r, the concentration factor increases with layer height. Additionally, a decrease in r leads to an increase in K_{notch}. These findings confirm that notch severity intensifies with layer height, while r emerges as a potentially significant factor influencing K_{notch}, possibly compensating for the severity introduced by a or θ.

4.6 Discussion

4.6.1 Strength recovery upon interface notch removal

Tensile testing revealed that surface machining led to a strength recovery in both small and large-scale samples, elevating the strength to values equivalent to those of the 0° samples. The identical ultimate stress values for 90-M and 0-NM for both large and small-scale samples strongly suggest that full interface healing is achieved in FFF and FGF printing. These findings provide compelling evidence that challenges the commonly held view that insufficient polymer

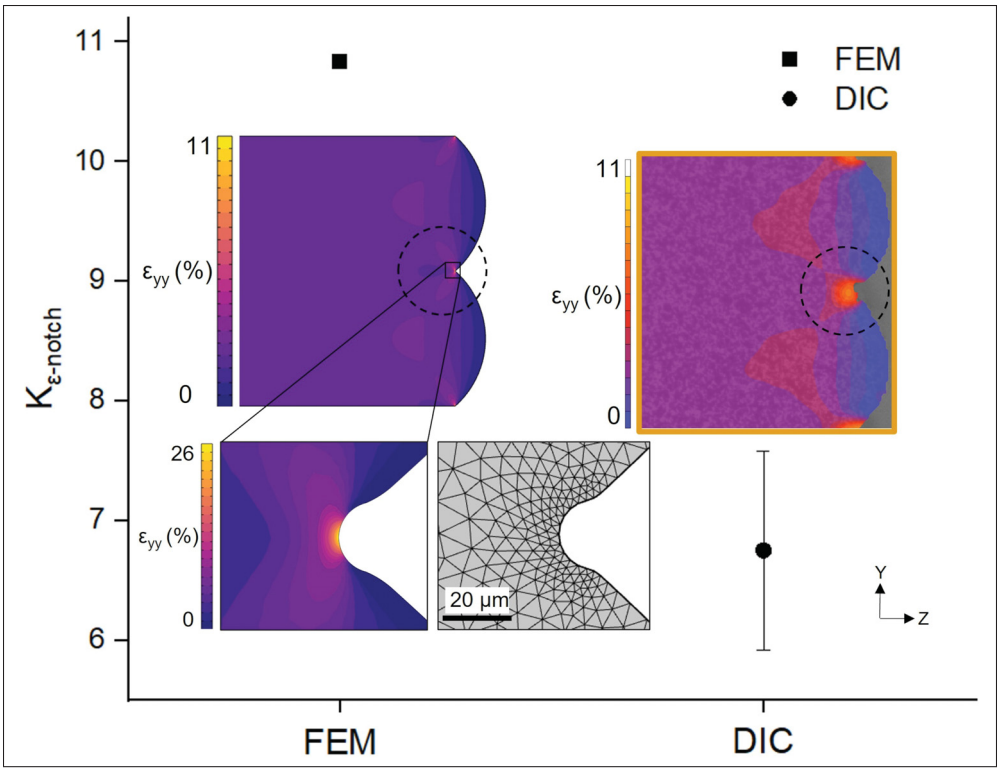

Figure 4.14 Strain concentration values obtained by FEA and DIC. The higher values in FEA are due to its finer spatial resolution compared to DIC. The average strain value in the dashed circle area is similar for both methods, suggesting that the model is valid

chain interdiffusion is the primary cause of interfacial weakness in printed parts. In our case, the thermal environment appears to have allowed sufficient interdiffusion and entanglement of polymer chains, resulting in complete healing. There is strong support for the argument that interdiffusion is often complete in many studies and that conclusions about its insufficiency should not be drawn until its effects are clearly separated from those of notch geometries. While prior literature often highlights the limited time window (0.1 to 100 ms) for effective chain diffusion during FFF as insufficient (Gao *et al.*, 2021; Vaes *et al.*, 2021), the results suggest that this constraint could be overcome and confirm other existing work (Allum *et al.*, 2021; Moetazedian *et al.*, 2023). In large-scale samples, the suitable interface temperature profile is likely achieved by the substantial amount of extruded polymer, while in small-scale samples, the heated chamber helped reduce the cooling rate, providing an optimal temperature profile for

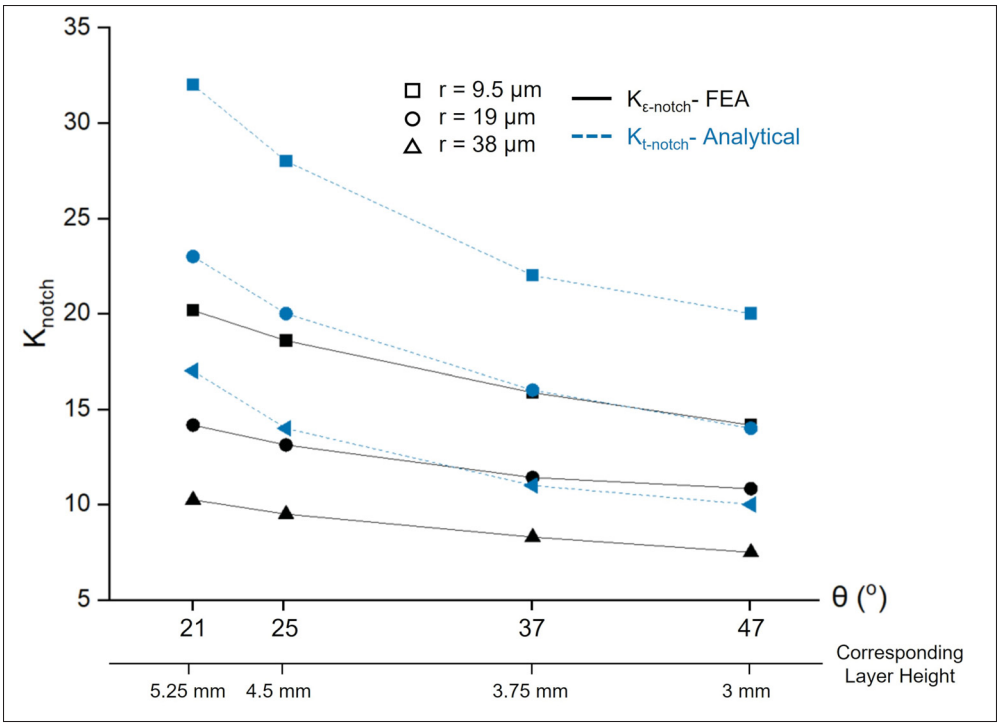

Figure 4.15 Effect of notch geometry on the strain concentration factor obtained by FEA, along with analytical stress concentration factor values from the literature. The results show that K_{notch} increases with layer height for a given r value, and decreases as r reduces. This suggests that notch severity intensifies with layer height, while r plays a significant role in influencing K_{notch}, potentially offsetting the effects of other notch geometric parameters

full bond strength formation. Together, these findings point to process-controlled pathways for achieving full interface bonding.

Comparing fully bonded samples with bulk material properties in terms of mechanical performance and fracture behaviour could offer valuable insights. This comparison may reveal other factors contributing to the reduced performance of 3D-printed parts, such as residual stresses. Achieving full bond strength in semi-crystalline polymers might present additional challenges, as crystal formation at the interface can impede chain diffusion, limiting effective bonding (Awaja, 2016; Vaes *et al.*, 2021). Additionally, isotropic mechanical properties are difficult to attain in fibre-reinforced composites due to fibre alignment along the extrusion direction. Even with

complete bond formation, the mechanical properties will remain higher along the extrusion direction, reflecting the inherent anisotropy introduced by the fibre orientation.

A comparison of the ultimate stress values in Figure 4.8 shows that both large-scale 0° samples and compression-moulded samples exhibit higher strengths than the small-scale 0° samples. This disparity may be attributed to sample size and geometry effects, which can alter the stress distribution and provide different levels of geometric constraint. Additional factors such as batch-to-batch material variability and potential residual stresses in the printed samples—particularly at the small scale—may also contribute to the observed differences. These residual stresses could arise from the high cooling rates of small filaments and unrelaxed molecular orientation induced during extrusion.

4.6.2 Interface notch effect at small- and large scale

Tensile testing results revealed that the strength increase observed after surface machining is significantly more pronounced in large-scale samples, with a 70% enhancement compared to a 28% increase for small-scale samples. According to the values in Table 4.7, the normalized notch depth (defined in (Kundurthi *et al.*, 2023)) as the ratio of notch depth to layer height) is similar in both scales (0.34 for small and 0.3 for large scale). However, the notch angle is smaller in the large-scale sample (26° vs. 36° in small-scale), which may contribute to higher strain concentration at the notch (He *et al.*, 2020; Kundurthi *et al.*, 2023). Moreover, the U-shape notch in the small-scale sample has a curved root while the V-notch in the large-scale samples has a notably sharp root, which could potentially further increase the local strain levels at the notch tip. Given that these naturally formed notches in printed parts are a primary cause of reduced mechanical properties and failure initiation, conducting a notch sensitivity analysis on the print material would be valuable to assess their impact.

Another factor that may mitigate the negative effects of notches in small-scale samples is the variability in extrudate width across layers. This variability, arising from printer limitations, causes a non-uniform cross-section in terms of extrudate width. As a result, the load applied

to the notches is not purely uniaxial, since the notch orientation relative to the applied load is not perfectly perpendicular, as shown in Figure 4.16. This introduces a minor shear stress component, potentially redistributing strain concentration around the notch. To account for these process-induced variations in filament geometry, the uncertainty is quantified. The extrudate width was measured as 1.3 ± 0.2 mm, resulting in the notches being at 77° ± 7° relative to the load direction. These variations in notch orientation contribute to a reduction in the stress concentration factor. The stress intensity factor of mode I at the crack tip can be expressed as $K(\theta) = K(90)\sin^2(\theta)$, where θ is the angle between the crack and loading direction (Li & Guo, 2019; Yang, Xie, Huang, Zhang & Chao, 2020). Applying this principle to the observed variation shows that the reduction in stress concentration factor could range from approximately 0.55% to 11.70% for notches at different orientations relative to the loading direction. This effect may contribute to the varying strain concentration levels across different layers in the small-scale samples, as illustrated in Figure 4.7. These unintended geometric variations highlight the complexity of stress states in printed structures and emphasize the need to account for manufacturing-induced imperfections in both experimental and computational analyses.

4.6.3 Notch root sharpness

The observed differences in notch root sharpness between large-scale and small-scale samples, as well as between the first two layer heights in Figure 4.10, could be attributed to variations in the capillary time (τ_c), defined as $\tau_c = \mu a_0/\gamma$, which quantifies the characteristic time for surface tension to affect the polymer flow. In this equation, μ is the Newtonian dynamic viscosity, a_0 is the initial extrudate radius, and γ is the surface tension (Lepoivre *et al.*, 2021). The value of τ_c evolves rapidly after the extrudate is deposited as temperature decreases.

In large-scale printing at high layer heights, the large filament size (a_0) leads to a higher initial τ_c during extrudate deposition. This higher τ_c persists for a longer period due to the larger thermal mass and slower cooling rate. This indicates an extended period where viscous forces dominate, which resists the smoothing of sharp features. Conversely, smaller filament size results in a lower τ_c. This smaller a_0 means that the coalescence time, driven by surface tension, is inherently

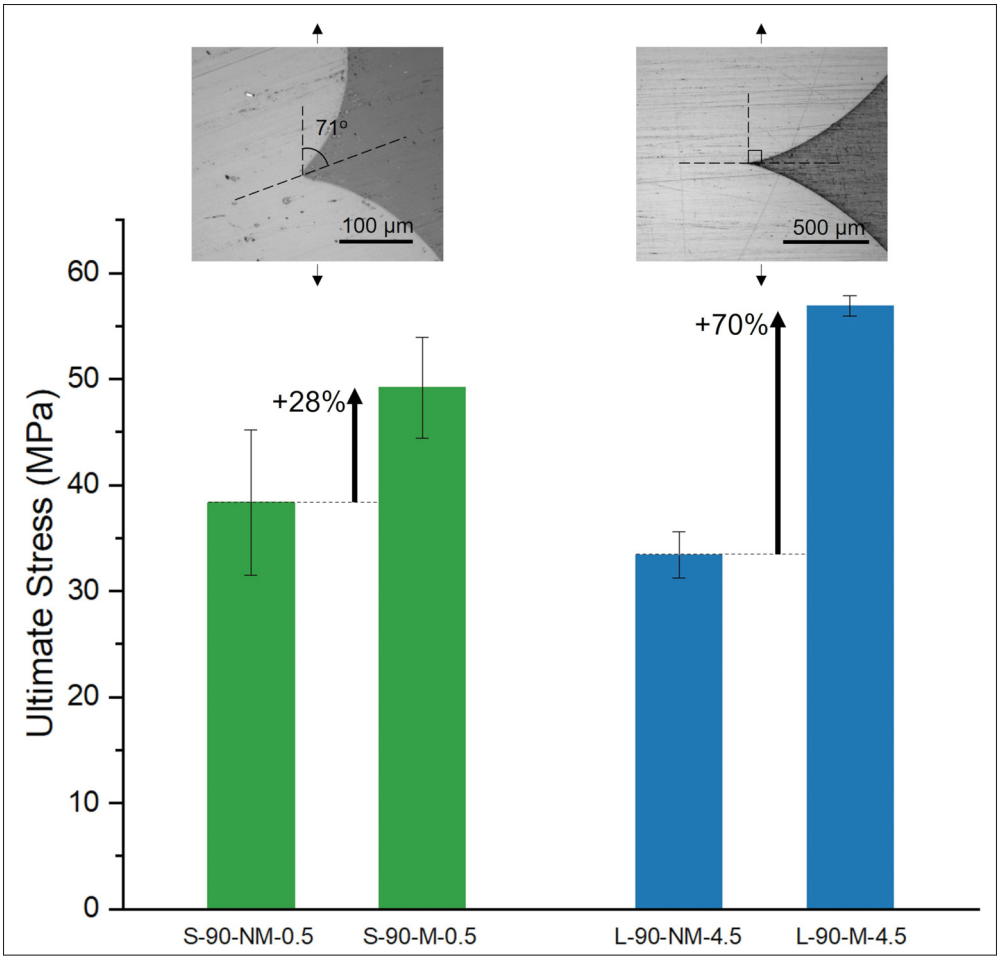

Figure 4.16 Ultimate stress values for machined and non-machined 90° samples in both small and large scales. The more pronounced strength recovery observed in large-scale samples is primarily attributed to the notch characteristics, while the non-perpendicular orientation of the notch relative to the applied load in small-scale samples may also contribute

faster. The faster coalescence for smaller filaments allows surface tension to act more quickly, promoting effective rounding of notch roots.

Understanding these size- and time-dependent variations in τ_c can provide insight into the observed differences in notch root sharpness. Such differences are critical, as sharper notches result in higher stress concentrations, which can accelerate the onset of premature failure. Research into optimizing printing parameters for optimal τ_c evolution over time may be a viable

strategy for mitigating the adverse effects of interface notches on the mechanical performance of printed parts.

4.6.4 Strain field measurement at different layer heights

The high-resolution DIC from the side view of L-90-NM-3 and L-90-NM-4.5 provided experimental measurements for the strain concentration field induced by interface notches in the 3D printed part. As illustrated in Figure 4.11(a), to the best of the author's knowledge, all investigations on strain fields induced by extrudate geometric features in the literature are FEA-based (Allum *et al.*, 2020c; Kundurthi *et al.*, 2023; Ghorbani *et al.*, 2022). This experimental measurement could potentially serve as a benchmark for validating and refining FEA models, helping to identify areas where current models may need improvement.

Although strain concentration is higher for notches in L-90-NM-3, the ultimate nominal stress shows only a slight increase. To explain this, we assessed the principal stress as a failure criterion, assuming it triggers failure. Given that strain in the x- and z-directions is negligible compared to the loading direction (y), the principal stress in the y-direction equals the von Mises stress, expressed as follows:

$$\sigma_1 = \sigma_{\mathrm{VM}} = E \cdot \varepsilon_{yy-\mathrm{notch}}.$$

The values obtained are 145 ± 18 MPa for L-90-NM-3 and 165 ± 21 MPa for L-90-NM-4.5. Given the standard deviations, some notches in L-90-NM-3 may exceed the failure threshold, explaining the limited increase in ultimate nominal stress. However, the strain at break is noticeably higher for L-90-NM-3. Additionally, L-90-NM-4.5 shows greater sensitivity to small fluctuations in applied nominal strain, suggesting that L-90-NM-3 may perform better in real-world applications with complex loading conditions.

FEA results further confirm that notch severity increases with layer height. However, Figure 4.15 shows that the extent of this increase depends on notch root sharpness: a higher r value could allow printing with larger layer heights while maintaining a relatively low strain concentration factor, whereas a low r leads to a high strain concentration factor even at small layer heights.

This is further supported by the analytical stress concentration factor values from the literature. It should be noted that the shift in stress concentration factor values may be attributed to differences in notch geometry and loading conditions between the assumptions in the analytical solution and FEA. These findings highlight the need to understand what governs notch root sharpness, as well as how process parameters can be optimized to mitigate its negative effects.

4.7 Conclusion

In this study, the impact of interface notches induced by the extrudate geometry on tensile properties of FFF and FGF printed pure PETG was investigated. This involved analyzing small- and large-scale samples, subjected to tensile testing in both extrudate and transverse directions, with and without the presence of naturally formed interface notches. It was found that interface notches act as strain concentration regions on the surface of the tensile samples, resulting in a decrease in ultimate stress and inducing brittle behaviour. This effect was significantly more pronounced in large-scale FGF printed samples compared to small-scale FFF samples, as the interface notch featured a sharper root and a smaller angle. Consequently, the strength decreased by 70% in large-scale samples and by 28% in small-scale samples.

Remarkably, similar tensile properties were observed for samples in the absence of these stress concentrators at different extrudate angles, indicating the formation of full bond strength under the chosen printing conditions for both scales. These findings challenge prevailing assumptions regarding the observed anisotropic behaviour of FFF/FGF printed parts, previously attributed to incomplete bond formation (Coogan & Kazmer, 2017b; Gao *et al.*, 2021; Syrlybayev *et al.*, 2021). Instead, it suggests that this behaviour arises from the stress concentrator effect, with this being the primary strength reduction mechanism at play (Allum *et al.*, 2020c; Kundurthi *et al.*, 2023).

The evolution of interface notch characteristics was studied at six layer heights (3 to 6 mm) in large-scale samples. The quantified notch parameters showed an increasing trend in notch severity with layer height. DIC analysis was instrumental in better understanding the strain field

induced by the notches at different layer heights by providing experimental measurements of the strain field specifically for samples printed with 3 and 4.5 mm layer height. The results showed that the strain concentration factor for 3 mm is lower and samples showed an improvement in performance by higher strain at break and slightly higher ultimate stress.

The FEA model was verified by DIC results and was used to further study the strain concentration dependence on the notch geometry. FEA confirms that notch severity increases with layer height, but the effect depends on notch root sharpness. A more rounded notch root reduces strain concentration at larger layer heights, highlighting the need to optimize process parameters to control notch geometry. While this study focused on a single amorphous polymer (pure PETG), similar observations of full or near-full healing have been reported in the literature for other thermoplastics (Allum *et al.*, 2020c; Moetazedian *et al.*, 2023). This suggests a broader applicability of the presented findings, though further research is needed to assess the translatability of notch sensitivity and healing phenomena across different polymers.

Future research should focus on gaining a deeper understanding of how process parameters affect coalescence and interface notch characteristics to mitigate their negative impact on part performance. Crucially, future studies must explicitly decouple the effects of geometry (e.g., interface notches) from molecular bonding mechanisms to avoid misattributing strength loss to incomplete healing when it may stem from geometric stress concentrators. Additionally, post-processing techniques to remove these features could be beneficial for simple geometries. Alternatively, practical in-situ approaches could be explored such as using localized heating (e.g., with a laser or infrared source) or mechanical tools like a heated roller to re-shape or smooth the extrudate geometry in real time.

CHAPTER 5

REVISITING INTIMATE CONTACT DEVELOPMENT IN MATERIAL EXTRUSION ADDITIVE MANUFACTURING

Maryam Shokrollahi[1] , Santiago Restrepo López[1] , Adam W. Smith[1] , Martine Dubé[1,2] , Ilyass Tabiai [1,2]

[1] Department of Mechanical Engineering, École de technologie supérieure, Montréal, Canada

[2] CREPEC, Research Center for High Performance Polymer and Composite Systems, Mechanical Engineering Department, McGill University, Montréal, Canada

Paper submitted to *Additive Manufacturing*, January 2026

5.1 Abstract

Interlayer bonding quality in polymer-based material extrusion additive manufacturing (MEAM) techniques is widely recognized as poor, with previous studies characterizing extrudate bonding through two primary mechanisms: the degree of intimate contact (D_{ic}), which focuses on the width of the contacting area, and healing, which describes the interdiffusion of polymer chains within the contact zone. This study provides direct evidence of microvoids at layer interfaces in printed polyethylene terephthalate glycol (PETG) parts, demonstrating that even apparent contact areas may not achieve complete interfacial contact. The intimate contact quality was investigated by varying layer height, print speed, and temperature. Microvoids were observed and quantified using polarized optical microscopy and micro-computed tomography. A novel, low-cost method was developed to measure contact pressure during printing, revealing an inverse relationship between contact pressure and intimate contact quality across all cases. Print parameters influenced both pressure and contact quality in an interdependent manner, with print speed emerging as the most influential factor, meaning that lower print speeds yielded higher degrees of intimate contact. Experimental validation of conventional composite intimate contact model showed that it fails to predict interfacial microvoid formation in polymer extrusion processes. These findings refine current understanding of bonding theories for MEAM

by showing that idealized assumptions of perfect intimate contact do not hold in practice, highlighting the importance of microvoid quantification for predicting mechanical performance, and offering new insights for optimizing printing parameters to produce stronger, more reliable components.

5.2 Introduction

Material extrusion additive manufacturing (MEAM) is rapidly gaining traction across a range of industries due to its cost-effectiveness, material versatility, and scalability (Grand View Research, 2024). Among MEAM techniques, the polymer-based variants include fused filament fabrication (FFF) and fused granular fabrication (FGF), both of which operate on the common principle of extruding thermoplastic material through a heated nozzle to build components layer by layer. FFF uses pre-formed filaments with strict dimensional tolerances, making it ideal for producing small to medium-sized parts with intricate geometries (Patel & Taufik, 2022; Penumakala *et al.*, 2020; Sun *et al.*, 2008). In contrast, FGF leverages a screw-driven system to directly extrude polymer pellets, enabling higher material throughput and the fabrication of larger-scale structures. While differing in feedstock and hardware, both methods share similar process dynamics and face common challenges inherent to layer-by-layer deposition of the material (Pignatelli & Percoco, 2022; Shaik, Schuster & Shaik, 2021; Woern & Pearce, 2018). The use of these techniques in high-performance applications is limited by the relatively low mechanical performance of FFF/FGF-printed parts compared to those produced by conventional manufacturing methods. This performance gap hinders their ability to fully exploit the potential of high-performance polymers. Improving the structural reliability of FFF/FGF components is therefore a critical step toward expanding their industrial viability. While these techniques are highly material-efficient, reducing waste by as much as 80% compared to subtractive methods (Sustainability Directory, 2025), the mechanical anisotropy of printed parts remains a key challenge. Enhancing performance in this way could position them as a transformative technology, capable of delivering strong, lightweight parts while reducing costs, lead times, and environmental impact in line with modern sustainability goals.

Recent studies have identified extrudate geometry as a key factor contributing to anisotropy in FFF/FGF parts (Allum *et al.*, 2020a,b; Shokrollahi *et al.*, 2025; Kundurthi *et al.*, 2023). As schematically shown in Figure 5.1, Deposited extrudates typically exhibit a rounded rectangular cross-section, resulting in surface ridges and internal macrovoids between them. Sharp grooves at extrudate junctions act as stress concentrators, often causing premature failure under transverse loading. Nevertheless, the literature has predominantly focused on incomplete interlayer bonding as the primary cause of reduced mechanical performance (Barocio *et al.*, 2022; Coasey *et al.*, 2020; Coogan & Kazmer, 2019; Gao *et al.*, 2021; Yan, Zhang, Hong & Yuan, 2000; Yin *et al.*, 2018; Zhou *et al.*, 2021).

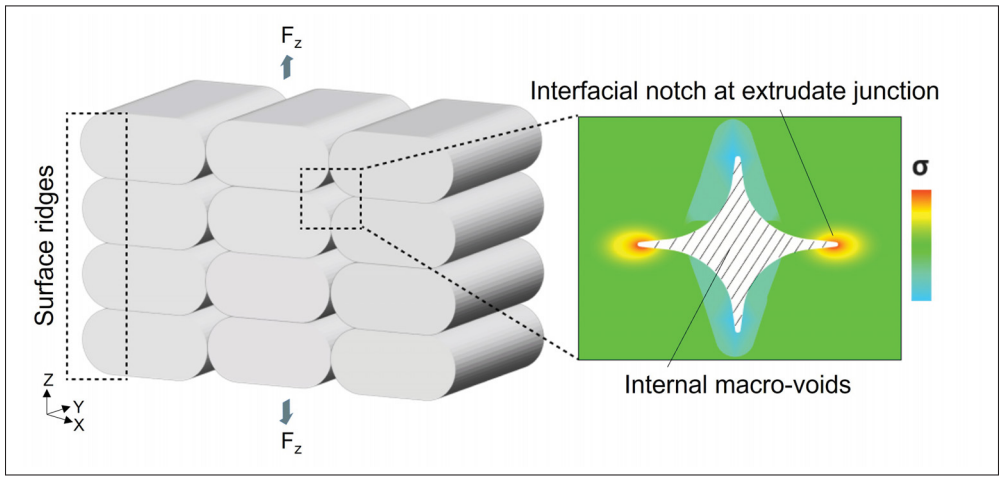

Figure 5.1 Schematic illustrating internal macrovoids and interfacial notches formed due to extrudate geometry. Sharp corners at extrudate junctions act as stress concentrators, leading to premature failure under transverse loading

The interlayer bonding process can be divided into two main stages: initial contact formation between adjacent extrudates, followed by interdiffusion of polymer chains across the interface. Both stages are highly sensitive to temperature, and the rapid cooling of the extrudate during printing often prevents the development of a fully formed bond (Coogan & Kazmer, 2019; Gao *et al.*, 2021; Kishore *et al.*, 2017). Although a few studies have reported the formation of fully developed bonds (Allum *et al.*, 2020a; Shokrollahi *et al.*, 2025; Ghorbani *et al.*, 2022), such bonding is often limited under typical processing conditions.

In many studies, the healing stage—typically modelled using Wool's theory (Wool & O'Connor, 1981) and the reptation model (de Gennes, 1971)—is considered to be the critical step in bond formation. As a result, the final interlayer bond strength is often estimated solely based on the extent of polymer chain interdiffusion, while the initial contact formation is either neglected or used as a refinement/correction of diffusion behaviour in bonding models (Basgul, Thieringer & Kurtz, 2021; Bellehumeur *et al.*, 2004; Han *et al.*, 2019; Hill & Haghi, 2014; McIlroy & Olmsted, 2017; N. Turner *et al.*, 2014). In contrast, some studies have identified interlayer contact formation as the key factor governing ultimate bond strength. In this context, interlayer contact is quantified by the bond width developed between adjacent extrudates, which serves to connect successive layers (Tronvoll *et al.*, 2018; Abbott *et al.*, 2018; Bartolai *et al.*, 2018; Hart *et al.*, 2018; Lepoivre *et al.*, 2021; Gao *et al.*, 2021).

Two main approaches have been used to explain interlayer contact formation during printing. The first is wetting, which describes the contact evolution between consecutive layers as a surface tension–driven process. This idea was initially applied to FFF by Li (Li, Sun, Bellehumeur & Gu, 2002), who employed a sintering-based model, and has since gained traction in the broader polymer extrusion additive manufacturing context (Bellehumeur *et al.*, 2004; Faes *et al.*, 2016; Gurrala & Regalla, 2014; Lepoivre *et al.*, 2021; Yin *et al.*, 2018). However, some more recent studies have shown that the rapid cooling of extrudates, which can reach up to 100 °C/s, leads to a sharp rise in viscosity, limiting wetting (Bechtel *et al.*, 2020; Coogan & Kazmer, 2017b, 2019; D'Amico & Peterson, 2018).

The second approach to interlayer contact formation emphasizes pressure-driven intimate contact as the dominant mechanism (Aliheidari, Christ, Tripuraneni, Nadimpalli & Ameli, 2018; Coogan & Kazmer, 2018; Kim, Kazmer, Colon, Coogan & Peterson, 2020; Xu *et al.*, 2025; Zhang *et al.*, 2025a). This perspective builds on the traditional theory of intimate contact, originally proposed by Dara and Loos (Loos & Dara, 1987). In this model, developed for composite welding, surface asperities deform through viscous flow under applied pressure and elevated temperature, progressively eliminating interfacial gaps. Intimate contact is considered complete when the two surfaces conform fully with no remaining microvoids. This model has

since been adapted for FFF to describe and predict interlayer contact formation by characterizing the development of the contacting area during printing (Coogan & Kazmer, 2018; Xu *et al.*, 2025; Zhang *et al.*, 2025a).

Coogan and Kazmer (Coogan & Kazmer, 2018; Rane & Strano, 2019; Kim *et al.*, 2020) advanced the application of the intimate contact model by incorporating in-situ experimental measurements of melt pressure using an inline rheometer positioned inside the nozzle. Their work highlighted contact pressure as a critical, yet previously overlooked, factor influencing final part strength in FFF. By using measured pressure values in their model, they demonstrated strong agreement between predicted and experimentally observed bond widths, reinforcing the importance of pressure-driven contact formation. For most of their print conditions, they concluded that incomplete interlayer contact, and not insufficient diffusion, was primarily responsible for the weak mechanical performance. More recently, Zhang et al. (Zhang *et al.*, 2025a) applied a similar approach to the printing of continuous fibre-reinforced composites. By placing a force sensor beneath the print bed, they measured the printing pressure in real time and modelled pressure-driven intimate contact along with resin impregnation behaviour. Their results showed that increased printing pressure enhanced bond width and improved impregnation within fibre bundles, leading to superior mechanical properties.

These models provide valuable insight into the role of pressure-driven intimate contact in determining final part strength and underscore the importance of in-situ pressure measurement during printing. However, as shown in Figure 5.2(a), the degree of intimate contact (Dic) is typically defined using a nominal geometry, i.e., the ratio of bond width to extrudate width—a geometric measure that assumes perfect contact quality within the bonded region. In this framework, the extrudate is modelled as a single asperity undergoing squeeze flow, where increased deformation leads to a larger bond width and, consequently, a higher degree of intimate contact (Coogan & Kazmer, 2019; Zhang *et al.*, 2025a). Incomplete bonding, therefore, is attributed either to insufficient chain interdiffusion (healing) or to limited contact area, i.e., a bond width smaller than the extrudate width. This approach does not account for the possible presence of microvoids within the bonded region. In contrast, Figure 5.2(b) illustrates an approach that

considers the actual contacting area within the bonded region and evaluates contact quality by capturing the interfacial microvoid content between bonded layers. While this approach has been experimentally validated in composite welding (Çelik, Peeters, Dransfeld & Teuwen, 2020; Grouve, Warnet, Rietman, Visser & Akkerman, 2013; Levy, Heider, Tierney & Gillespie, 2014; Schaefer *et al.*, 2017), to the best of the authors' knowledge, no prior work has examined whether interfacial microvoids are present in MEAM parts or whether existing models can accurately predict their formation.

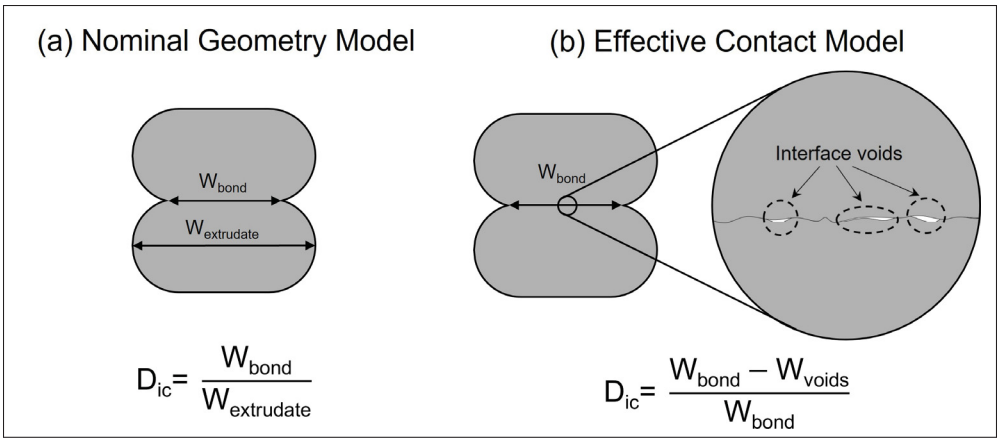

Figure 5.2 Schematic of two modelling approaches for the degree of intimate contact (D_{ic}). In the nominal geometry model (a), D_{ic} is calculated from the extent of extrudate deformation and the resulting bond width. In the effective contact model (b), D_{ic} is determined from the actual contacting area between layers. The first approach is commonly used in MEAM, while the effective contact model has not been previously investigated

This study aims to address the current gaps in understanding interfacial contact quality in MEAM. Virgin polyethylene terephthalate glycol (PETG), an amorphous polymer known for its durability, chemical resistance, and ductility, was selected due to its cost-effectiveness and ease of processing compared to other materials with similar performance (Valvez *et al.*, 2022; Srinivasan *et al.*, 2020). This work investigates the presence of interfacial microvoids at the bonded layers under different printing conditions and provides an experimental quantification of these microvoids. A novel, cost-effective methodology is introduced to measure contact pressure during printing, enabling systematic evaluation across various process parameters. Other key factors influencing

intimate contact formation, such as viscosity evolution and extrudate surface roughness, were also experimentally characterized to validate existing models for predicting contact quality based on interfacial microvoids. The findings offer new insights into an overlooked contributor to the inferior mechanical properties of MEAM parts and assess the ability of current intimate contact models to capture microvoid formation at the interface.

5.3 Material and Methods

5.3.1 Material

Virgin PETG filament (1.75 mm diameter) was obtained from 3DXTech Advanced Materials, featuring a density of 1.24 g/cm^3, a glass transition temperature (Tg) of 80 °C measured by differential scanning calorimetry (DSC) with a heating ramp of 10 °C/min, and a tensile strength of 45 MPa according to ISO 527 (obtained from the material's datasheet).

5.3.2 Printing conditions

Figure 5.3 schematically shows the setup used for printing and contact pressure measurement. The specific methodology for contact pressure measurements is described in Section 2.3. A total of 54 samples were printed by testing all possible combinations of the layer height, nozzle temperature, and print speed values listed in Table 5.1. All other printing parameters were kept constant, including a layer width of 1.2 mm and a bed temperature maintained at room temperature.

Table 5.1 Key printing parameters and their investigated ranges

Parameter	Values
Layer height (mm)	0.3, 0.4, 0.5, 0.6, 0.7, 0.8
Nozzle Temperature (°C)	225, 230, 235
Print speed (mm/s)	5, 10, 15

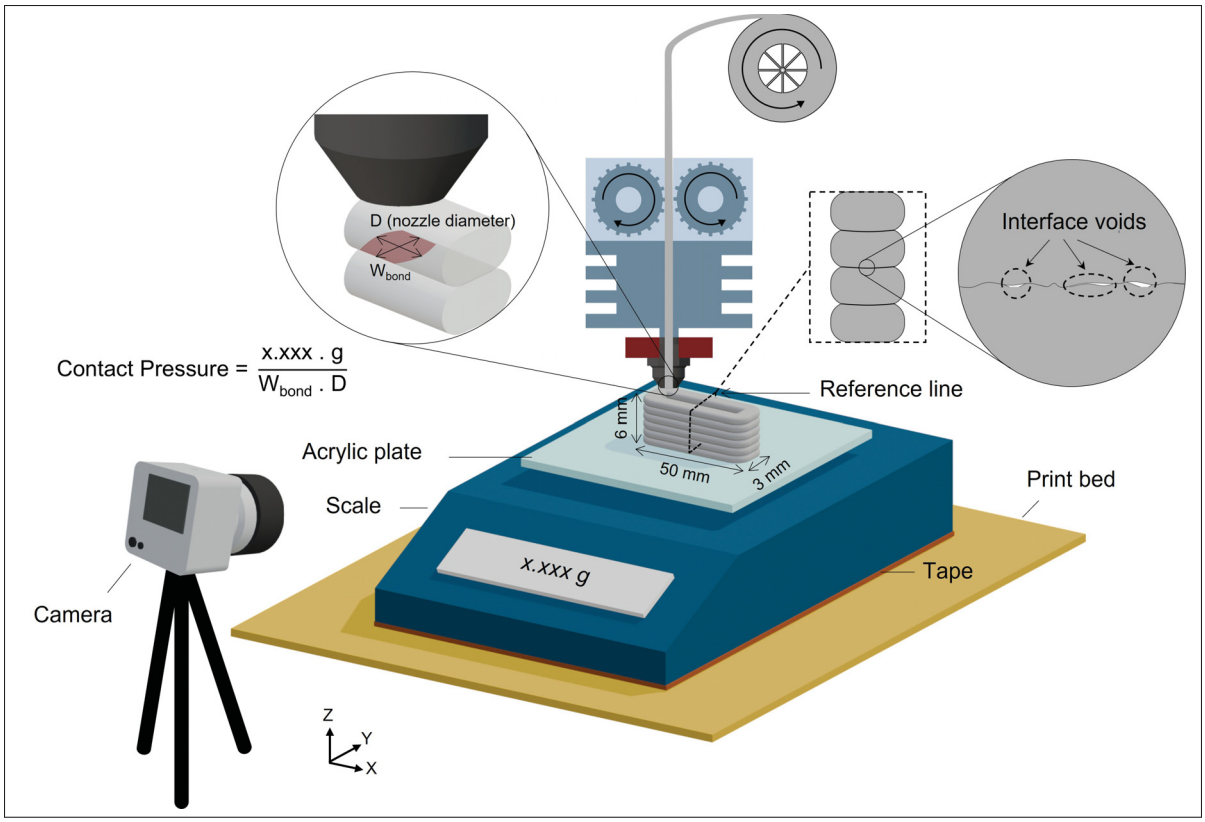

Figure 5.3 Schematic of the contact pressure measurement setup. A scale was placed on the printer bed, with the original scale plate replaced by an acrylic plate to improve measurement accuracy. When the printer reaches the reference point, the nozzle is positioned at the midpoint of the lines, and the corresponding mass is recorded. The printing configuration used two closely spaced straight lines to minimize measurement variation, with two data points recorded per layer

5.3.3 Contact pressure measurements

As depicted in Figure 5.3, a digital scale with an accuracy of ±0.001 g was positioned on the printer to record mass values during printing. The scale was calibrated with a 100 g weight before each measurement, ensuring its precision. All measurements were performed at room temperature. The original metallic plate of the scale was replaced with an acrylic one, as the uneven surface of the metallic base made it challenging to properly level and set up the printer. To ensure accurate mass measurements, several geometries were tested with the goal of minimizing variability in the scale readings. Two main sources of this variability were identified:

the challenge of properly levelling the acrylic plate, and the tendency for parts positioned farther from the scale's sensor to introduce inconsistencies. Ultimately, the geometry depicted in Figure 5.3, featuring two closely spaced straight lines, was selected to effectively reduce these variations. The mass values measured by the scale were recorded once the nozzle reached the midpoint of the lines, as indicated by the reference line. The entire printing process was video recorded, and measurements were taken for the final 5 layers, providing 10 data points for each sample. The initial layers were excluded from the analysis to ensure the print had stabilized, minimizing levelling issues and reducing variability in the measurements. The recorded mass at each measurement point was corrected by subtracting the known mass of the deposited material. Table 5.2 presents the recorded values for a representative sample.

The recorded mass values were first converted to force, and the corresponding contact pressure was determined by dividing this force by the contact area between the deposited extrudate and the underlying extrudate at the moment of deposition. As schematically illustrated in Figure 5.3, this contact area was approximated as a rectangle with dimensions W_{bond} and D, representing the bond width and nozzle diameter, respectively.

Table 5.2 Representative mass measurements during printing (230 °C, 0.5 mm layer height, 10 mm/s print speed)

Mass at Reference Line (g)	Number of Measurements	Total Sample Mass (g)
9.22 ± 0.47	10	0.79

5.3.4 Interfacial microvoid characterization

Two different techniques were employed to observe and quantify the interfacial microvoids: a 2D optical method using polarized optical microscopy (POM) on cross-sectional cuts and a 3D method using high-resolution micro-computed tomography (micro-CT).

5.3.4.1 Polarized optical microscopy

Cross-sections of printed samples were examined under an optical microscope after being polished using sandpapers of 600, 800, 1200, and 2000 grit. Imaging was performed with a Nikon Eclipse MA100 microscope, using polarized light to capture images. The polarization was linear, with the polarizer and analyzer oriented at 90 degrees, employing a halogen light source. The diaphragm aperture was fully open, and the light intensity was set to maximum. Microvoids at the interfaces were identified as darker pixels in the images, allowing their presence and distribution to be assessed.

5.3.4.2 Micro-computed tomography

To verify the reliability of 2D cross-sectional cuts for comparing contact quality across samples, high-resolution micro-CT scans were performed to provide 3D validation. These measurements were conducted on a limited number of samples due to time and cost constraints. Samples with a width of 6 mm and at least 3 layers in height were cut from the printed parts for scanning. The scans were acquired using a Zeiss X-radia 520 micro-CT scanner with the following parameters: X-ray voltage of 50 kV, current of 80 μA, and an exposure time of 2.5 s per projection. A total of 3201 projections were captured over a 360° rotation using a 4× objective, resulting in a voxel size of 1.5 μm. Image reconstruction was performed using DragonFly software. The reconstructed 3D volumes were analyzed to quantify microvoids at the interface. Microvoids were identified using threshold-based segmentation, allowing direct detection and quantitative measurement.

5.3.5 Rheological measurement

A MCR 501 rotational rheometer (Anton Paar) was used to measure the Newtonian viscosity of the material at various temperatures. Initially, the linear elastic region was determined by performing a dynamic strain sweep test (DSST) at 220 °C. A strain of 2% was found to be within the linear elastic region. Subsequently, frequency sweeps were conducted from 500 to 0.1 rad/s,

with three points per decade on a logarithmic scale, at temperatures of 150, 160, 170, 180, 190, 200, 210, 220, and 230 °C. Newtonian viscosity values were obtained when the viscosity versus frequency curves reached a plateau.

5.3.6 Thermal analysis

In-situ thermal measurements were conducted using a FLIR A700 thermal camera to monitor the temperature distribution during the print. The camera was positioned at the front of the printer to capture the *z*–*x* plane, and its position remained fixed throughout all measurements. The emissivity was set to 0.92, based on reported values for PETG (Valvez *et al.*, 2022; Srinivasan *et al.*, 2020; Robles Poblete, Ireland, Slattery, Davids & Lopez-Anido, 2023). Thermal data were processed and analyzed using FLIR Research Studio software to extract temperature profiles and identify thermal gradients across the printed layers. The frame sampling period (FSP) was 0.03 s. To enable finer temporal analysis near the temperature peak, the data were interpolated using the piecewise cubic hermite interpolating polynomial (PCHIP) method, chosen for its ability to preserve monotonic trends without introducing artificial oscillations. Interpolated values were generated at 1 ms intervals. The interpolation accuracy was assessed using a leave-one-out cross-validation approach, yielding a mean absolute error of 0.95 °C.

5.3.7 Surface roughness characterization

Surface characterization was performed at multiple levels. Confocal laser scanning microscopy was used to obtain the 3D profile of the bottom extrudate, capturing its curvature and overall shape. To mitigate optical artifacts and enhance image quality, a thin opaque coating of acrylic paint was applied to the extrudate surface using an airbrush. Imaging was conducted with a LEXT 4100 laser confocal microscope (Olympus) using a 10× objective combined with a 1.2× optical zoom. Surface topography scans were acquired in XYZ fine mode at a resolution of 1024×1024 pixels, with a lateral sampling pitch of 4.81 μm and a Z-range of 400 μm. Image corrections were applied to improve clarity.

To obtain the asperity profiles, tactile profilometry was employed, as the paint coating used for confocal imaging could alter the fine surface roughness features. A Mitutoyo profilometer with a 2 μm stylus tip (applied force: 0.75 mN) was used. Scans were conducted at a speed of 0.05 mm/s over a travel distance of 2.4 mm.

5.3.8 Model description

The original squeeze flow-based intimate contact model proposed by Dara and Loos (Loos & Dara, 1987) represented surface roughness as a series of non-uniform rectangular asperities. Building on this approach, Lee and Springer (Lee & Springer, 1987) proposed an alternative method to characterize surface roughness. They assumed a simplified geometry, where all asperities are identical rectangles with fixed dimensions, as illustrated in Figure 5.4. The applied pressure causes the rectangular asperities to deform, as illustrated by the dashed line. Under this assumption, the degree of intimate contact can be calculated using the following equation:

$$D_{\mathrm{ic}}(t) = \left[\frac{1}{1 + \frac{w_0}{b_0}} \left(1 + 5 \left(1 + \frac{w_0}{b_0} \right) \left(\frac{a_0}{b_0} \right)^2 \int_0^{t_c} \frac{P}{\mu(T)}\, dt \right) \right]^{1/5} \tag{5.1}$$

where a_0, b_0, and w_0 are geometric parameters defining uniform rectangles. The applied pressure is denoted by P, and μ represents the Newtonian viscosity, which is a function of temperature, T.

5.4 Results

5.4.1 Evolution of D_{ic} with print conditions

The contact quality between printed layers was evaluated through cross-sectional microscopy. While interfacial microvoids are not visible in conventional surface microscopy, the material's transparency, combined with polarized light, enabled depth visualization, revealing internal interfacial microvoids. Figure 5.5(a) presents a cross-sectional view of multiple layers from a representative sample (printed at 225 °C, with a 0.4 mm layer height and a print speed of

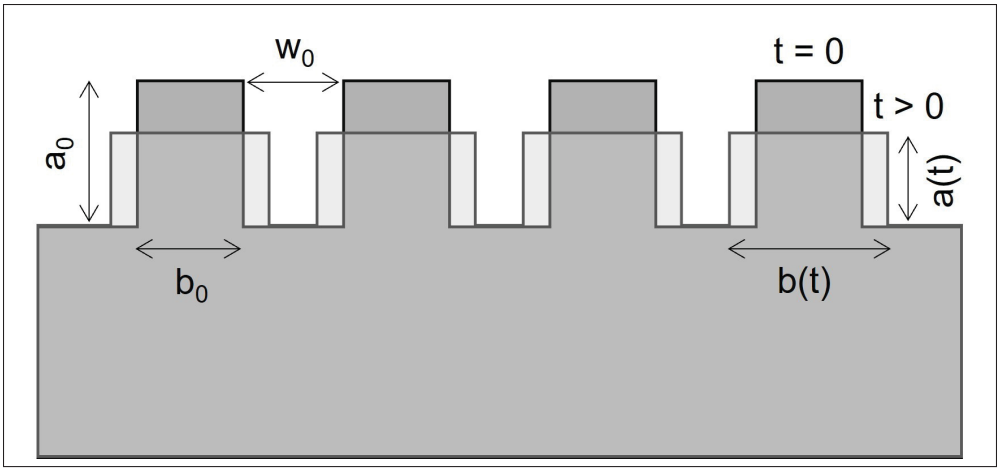

Figure 5.4 Schematic illustration of surface roughness in the Lee–Springer model assuming identical rectangular asperities

15 mm/s), revealing the presence of interfacial microvoids. The microvoids appear consistently distributed across the layers, suggesting a relatively repeatable pattern in their formation. For a more detailed observation, higher-magnification images of individual interfaces from all samples are provided in Figures 5.5(b)–5.5(d). Each matrix illustrates the interfacial microvoids observed under varying temperatures and layer heights at a certain printing speed. The number of microvoids varies across printing conditions, with some samples appearing almost void-free, indicating good contact quality (e.g., 235 °C, 0.5 mm layer height, 5 mm/s), while others show a significant presence of microvoids, reflecting poor contact quality (e.g., 225 °C, 0.8 mm layer height, 15 mm/s). Overall, lower print speeds generally lead to fewer microvoids.

Figure 5.6 presents the micro-CT results for six different layer heights printed at 230 °C and 10 mm/s. The green areas at the interfaces represent microvoids. For comparison, polarized optical microscopy (POM) images are shown below each micro-CT image. Both methods reveal the same microvoid distribution trend. The number of layers visible in the images varies with layer height: smaller layer heights allow three layers to fit within the field of view, whereas larger layer heights capture only two layers. Additionally, the 3D view shows that microvoids form in a repetitive pattern along specific lines, further confirming that cross-sectional POM cuts provide consistent microvoid representation, regardless of the cut position.

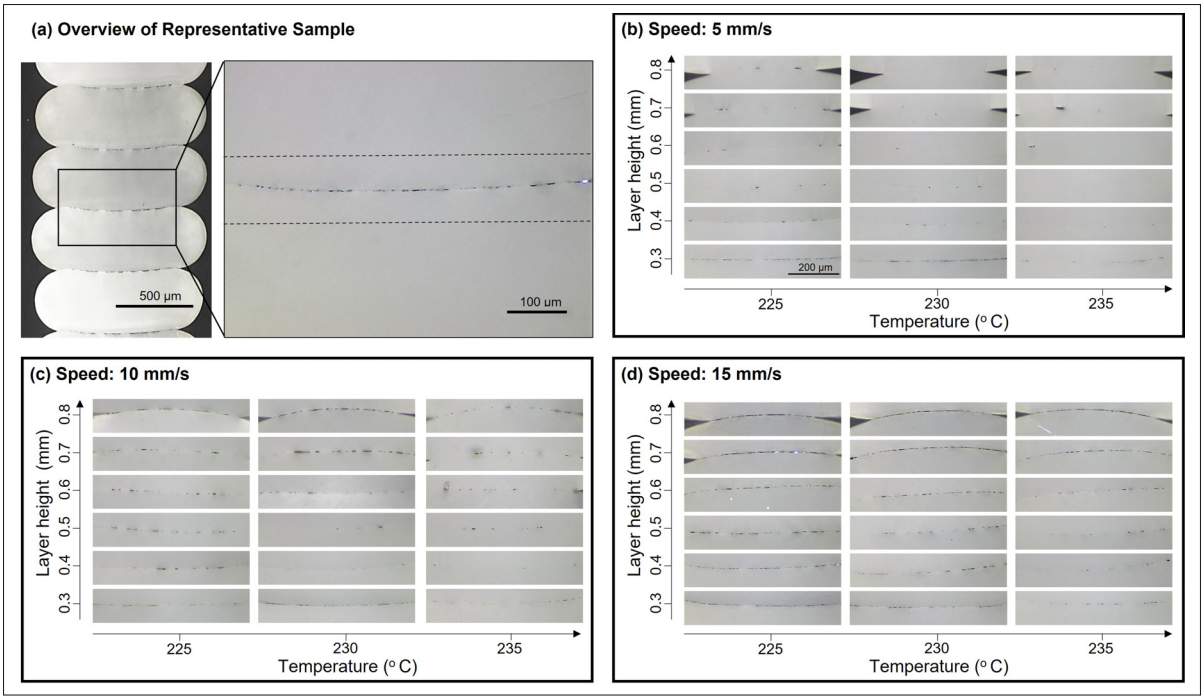

Figure 5.5 Illustration of interface contact quality: a) cross-sectional view of multiple layers in a representative sample (printed at 225 °C, 0.4 mm layer height, 15 mm/s print speed). b–d) higher-magnification images showing interfacial microvoids for different print conditions. Contact quality varies with different print conditions

To further compare the two methods, the degree of intimate contact was quantified for each using the procedure described in the Appendix IV. Figure 5.7 shows the resulting D_{ic} values. In general, POM measurements yield lower values, as the cross-sectional view captures additional microvoids beyond those located strictly along the interface line due to the observation extending through the sample depth. Both methods show a similar overall trend: the D_{ic} is low at 0.3 mm layer height, reaches its maximum at 0.4, 0.5, and 0.6 mm, and then decreases at 0.7 and 0.8 mm. While the POM method cannot distinguish between samples with similar D_{ic} values (e.g., 0.4, 0.5, and 0.6 mm), it proves to be reliable for qualitative comparison purposes.

The D_{ic} values obtained via the POM method for all samples are presented in Figure 5.8 as three contour plots. Each plot shows the results at varying temperatures and layer heights at a certain printing speed. Overall, similar to the POM images, the contact quality decreases with

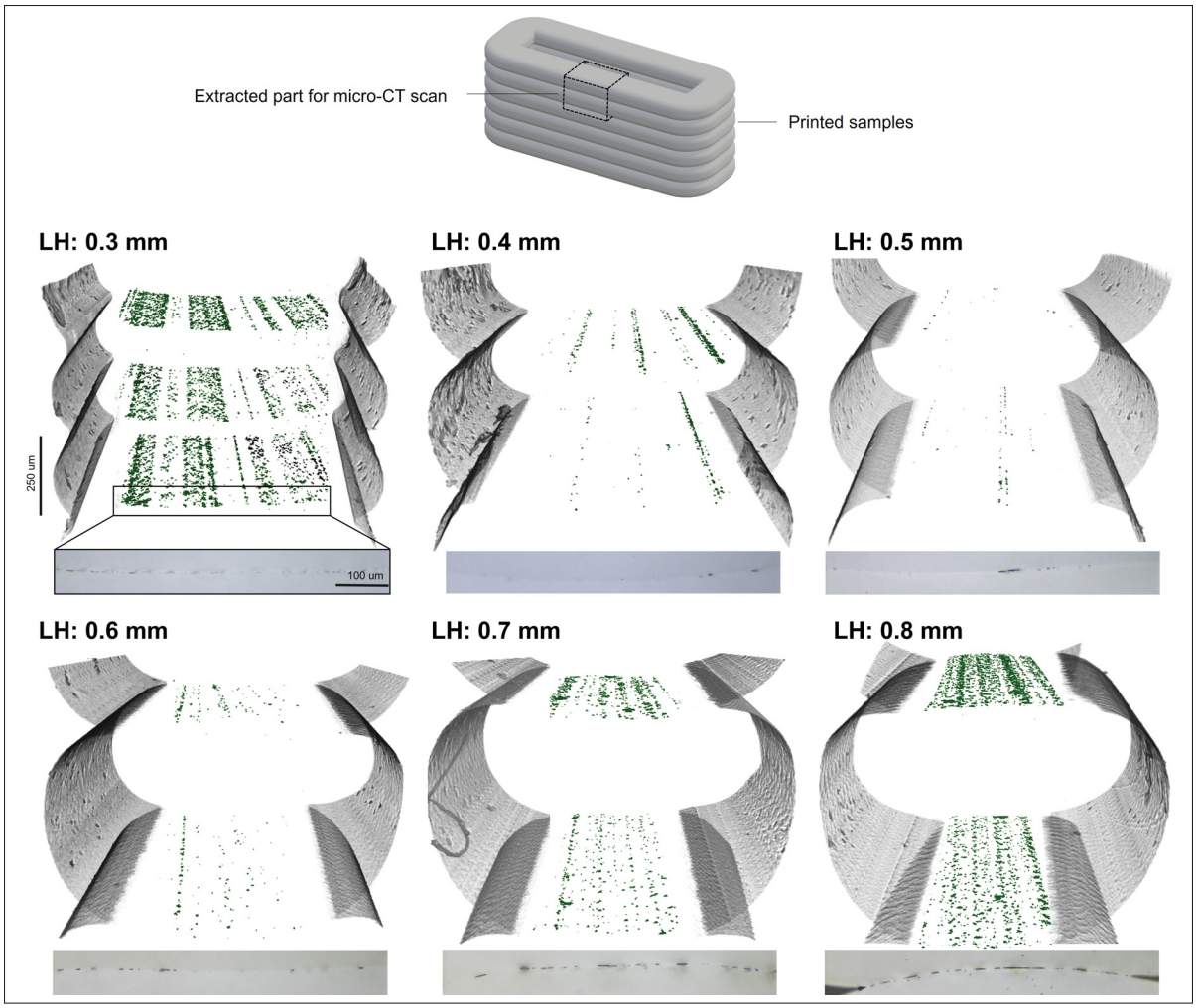

Figure 5.6 Validation of interfacial microvoid observations using high-resolution micro-CT for six samples with varying layer heights, printed at 230 °C and 10 mm/s. Green regions indicate interfacial microvoids. Polarized optical microscopy images are shown for comparison, demonstrating consistent microvoid distribution trends

increasing print speed. The printing parameters appear to influence the D_{ic} in an interdependent manner, as further discussed in the Discussion section.

5.4.2 Contact pressure measurements

Figure 5.8 presents the recorded contact pressure values for each sample, averaged over 10 measurement points. The results show contact pressures ranging from 0.04 MPa to 0.32 MPa,

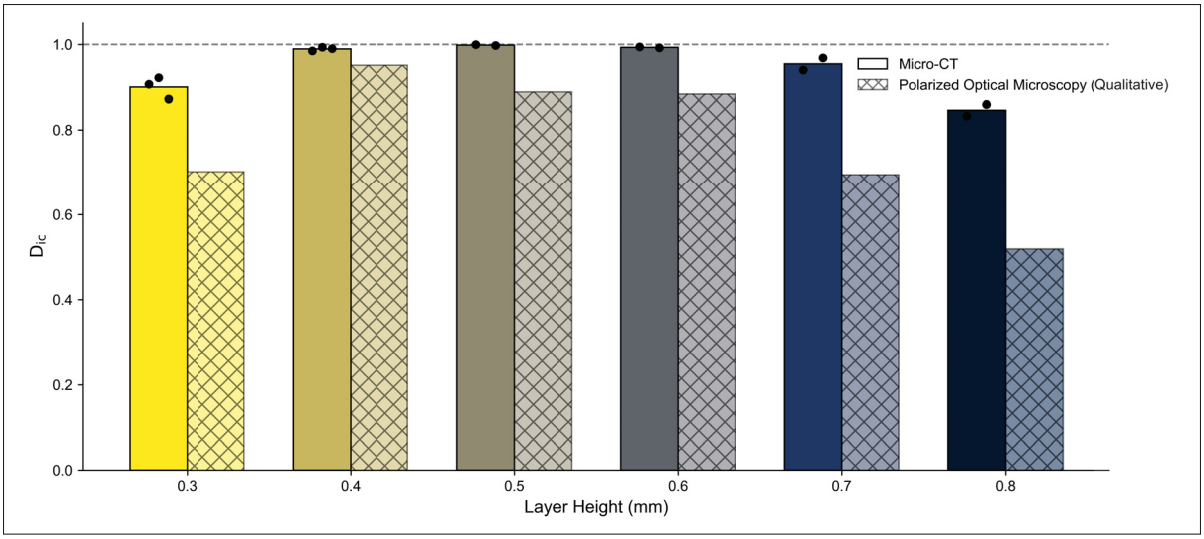

Figure 5.7 D_{ic} values obtained from micro-CT and POM images of samples printed at 230 °C and a print speed of 10 mm/s. Points represent the quantified D_{ic} for each layer from micro-CT. The POM method shows consistent trends with micro-CT, indicating its reliability for general comparisons, although it has limited sensitivity for closely similar D_{ic} values

consistent with the order of magnitude reported in (Anderegg *et al.*, 2019; Coogan & Kazmer, 2018; Kim *et al.*, 2020; Zhang *et al.*, 2025a). Similar to the D_{ic} plots, the contact pressure plots present results at varying temperatures and layer heights for a given printing speed. Lower contact pressure values are predominantly observed at low print speeds. The effects of the printing parameters appear to be interdependent and cannot be readily interpreted from the plots alone. Moreover, a counterintuitive inverse relationship is observed between the D_{ic} and the contact pressure values. A more detailed analysis of this relationship, as well as the effects of printing parameters on contact pressure, is provided in the Discussion section.

5.4.3 Viscosity characterization

To determine the viscosity profile during contact formation between two extrudates in the printing process, two key inputs are required: the temperature-dependent viscosity of the polymer, obtained through rheological measurements, and the temperature evolution near the interface, starting from the moment the extrudate contacts the underlying layer.

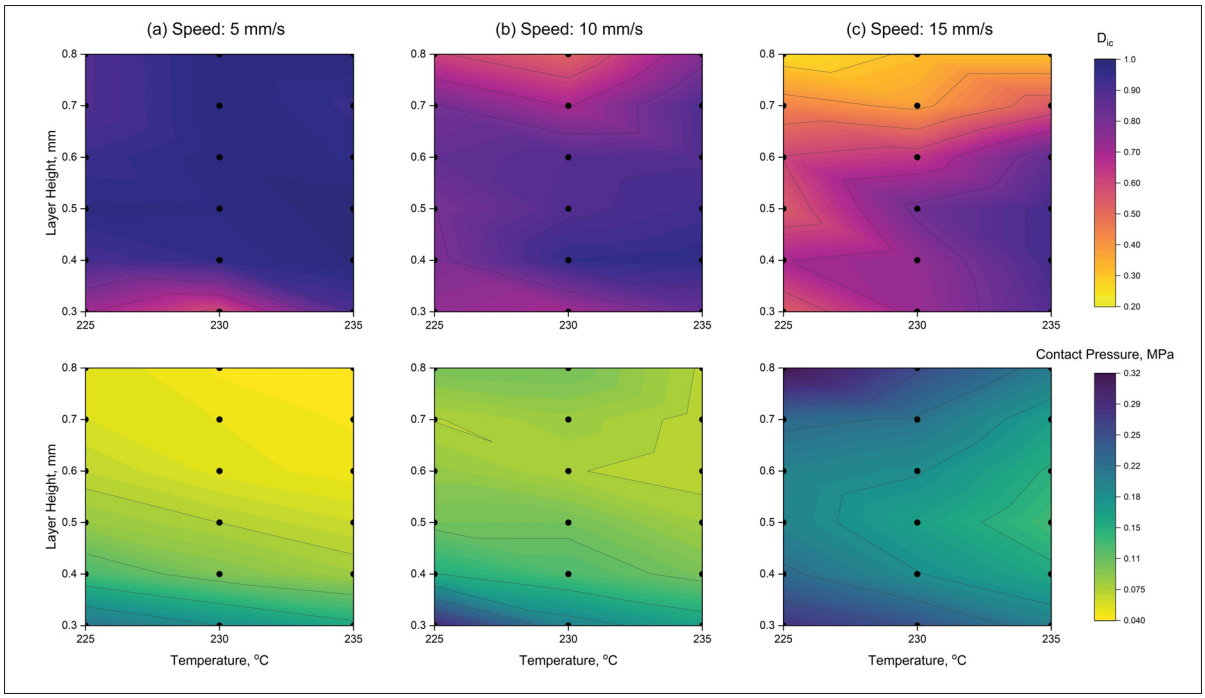

Figure 5.8 a) D_{ic} values obtained from POM images, following the same trend observed in the micrographs. b) Measured intimate contact pressure values under different printing conditions. Contact pressure averages around 0.1 MPa across samples

Rotational rheometry was employed to measure the polymer's temperature-dependent viscosity, with the complex viscosity versus angular frequency curves at different temperatures shown in Figure 5.9(a). For the intimate contact model, the polymer is assumed to exhibit Newtonian or non-shear-dependent behaviour. Accordingly, the Newtonian viscosity was obtained from the plateau region of these curves, where viscosity is independent of frequency. These values were then fitted to the Arrhenius equation (Equation. 2), as shown in Figure 5.9(b). The pre-exponential factor (K) was determined to be 1.244×10^{-6} Pa·s, and the activation energy (E_a) was found to be 108.1 kJ/mol.

$$\mu(T) = K \times \exp\left(\frac{E_a}{R \times T}\right) \tag{5.2}$$

To determine the viscosity evolution as a function of temperature during printing, the temperature profile of the extrudate near the interface was measured using a thermal camera. Direct

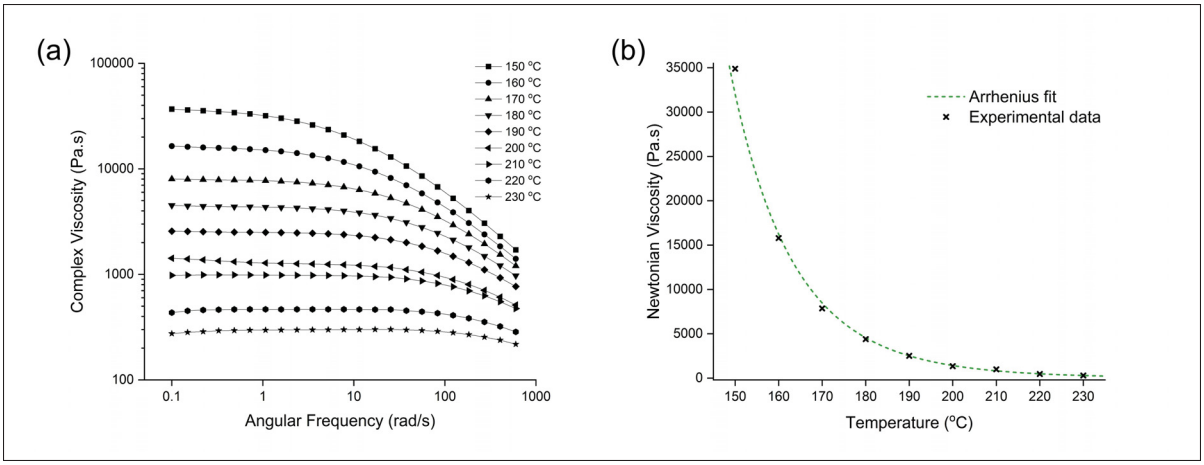

Figure 5.9 Viscosity analysis. (a) Complex viscosity as a function of angular frequency at various temperatures. Newtonian viscosity at each temperature was determined from the plateau region. (b) Arrhenius plot of the extracted Newtonian viscosity values

measurement at the interface is challenging, since the curved interface geometry in most cases makes it difficult to precisely position the measurement cursor. Therefore, all measurements were consistently taken at a location corresponding to 20% of the layer height.

Figure 5.10 presents the temperature profiles of samples printed at 230 °C and 10 mm/s with different layer heights. The results indicate the temperature range increases with layer height, consistent with the larger extrudate size. Across all cases, the temperature evolution can be divided into two distinct phases. The first phase, illustrated by the thermal images for the 0.6 mm layer height, corresponds to the period when the nozzle remains above the deposition point, applying contact pressure and partially shielding the extrudate from ambient cooling. During this stage, the temperature remains within a relatively narrow range. The second phase begins once the nozzle moves past, exposing the extrudate to air and leading to a markedly higher cooling rate.

The initial phase has largely been overlooked in the literature (Vanaei *et al.*, 2021a; van de Werken *et al.*, 2020; Costa, Duarte & Covas, 2017; Prajapati *et al.*, 2021; Rudolph, Chen & Dick, 2019), likely due to its brief duration. However, this phase plays a critical role in bond formation for two main reasons: first, it coincides with the application of pressure, which is essential for

the development of intimate contact; second, interlayer healing has been shown to occur within a narrow time window (0.1 to 100 ms) (Gao *et al.*, 2021; Vaes *et al.*, 2021), emphasizing the need to accurately capture the early thermal conditions at the interface to fully understand the bonding process. Overlooking this phase may therefore lead to an incomplete understanding of the interlayer bonding process.

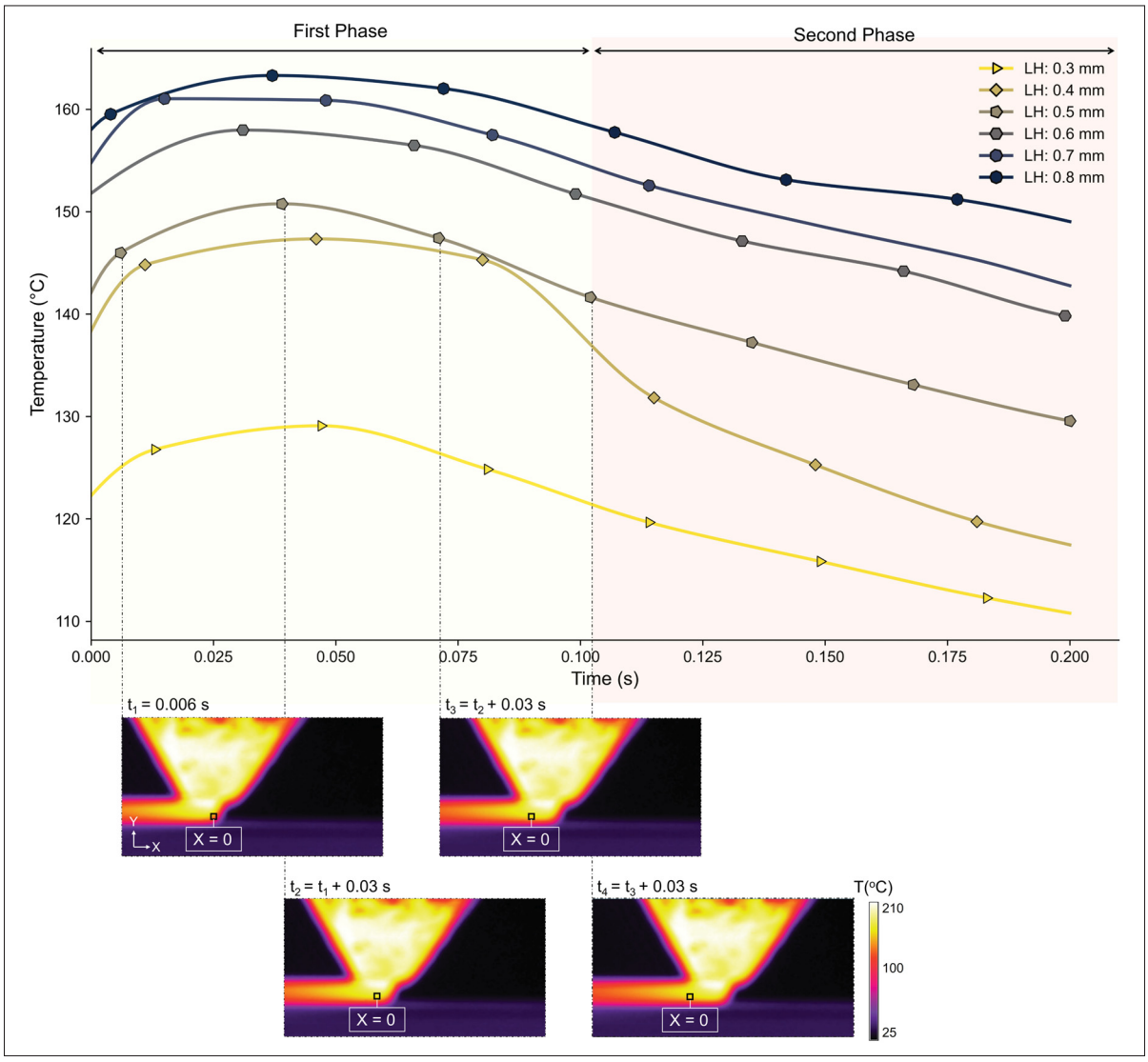

Figure 5.10 Temperature profile at $x = 0$ during printing at 230 °C and 10 mm/s, showing the effect of varying layer heights. Thermal images depict nozzle passage over $x = 0$, a critical period for contact development due to contact pressure. Cooling rate increases after the nozzle passes this point. Higher temperatures are observed at larger layer heights

5.4.4 Surface roughness analysis

The surface roughness of the bonding extrudates influences the quality of contact formation, as described by the composite welding equation in Section 2.8. A rougher surface requires greater squeeze flow to deform the asperities, which can potentially lead to more microvoids at the interface. Therefore, the surface roughness profile of a deposited extrudate is characterized in this study.

Confocal laser microscopy scan results of the extrudate surfaces printed at 230 °C and 10 mm/s with varying layer heights are shown in Figure 5.11(a). The scans reveal that at the lowest layer heights, the extrudate surface is slightly concave; it appears relatively flat at intermediate layer heights, and becomes convex at the highest layer heights. A similar trend is observed in the interfaces captured in the POM images and micro-CT scans, further confirming the variation in surface geometry with layer height. This behaviour is influenced by the confined space between the nozzle and the previous layer: at lower layer heights, the limited space pushes the material downward, whereas at higher layer heights, the increased space allows the extrudates to adopt a more rounded shape.

The corresponding surface roughness profiles along the dashed line in the y-direction, obtained by tactile profilometry, are shown in Figure 5.11(b). To isolate roughness from waviness, the overall curvature was removed and a Gaussian filter with a cutoff wavelength of 0.08 mm was applied. To extract the surface parameters required for the Lee–Springer model from these profiles, the method described in (Schaefer *et al.*, 2017) was employed. Values were averaged over 100 data points, and the resulting parameters are summarized in Table 5.3.

Table 5.3 Summary of Lee–Springer model surface roughness parameters extracted from confocal microscopy profiles

Layer height (mm)	$\mathbf{a_0}$ (μm)	**SD**	$\mathbf{b_0}$ (μm)	**SD**	$\mathbf{w_0}$ (μm)	**SD**
0.3	1.3	0.1	15	6	15	8
0.4	0.7	0.05	9	4	18	8

Layer height (mm)	a_0 (μm)	SD	b_0 (μm)	SD	w_0 (μm)	SD
0.5	0.78	0.04	8	4	21	11
0.6	1	0.2	8	4	23	15
0.7	1.4	0.2	13	7	10	8
0.8	1.84	0.07	37	18	13	7

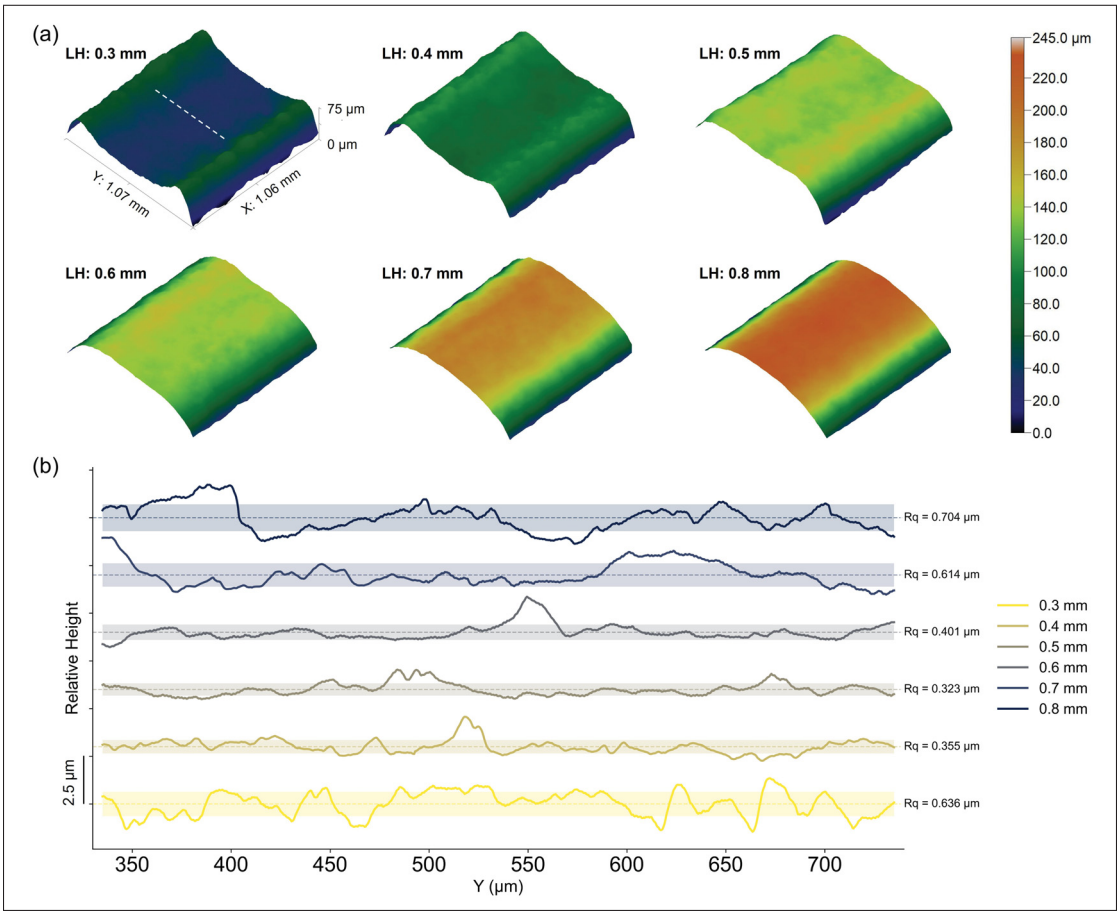

Figure 5.11 (a) Confocal microscopy images of extrudate surfaces printed at 230 °C and 10 mm/s with varying layer heights, showing concave (low layer heights), flat (intermediate layer heights), and convex (high layer heights) morphologies. (b) Surface roughness profiles along the dashed line, obtained by tactile profilometry. A Gaussian filter was applied to remove the overall curvature, highlighting the surface roughness. The standard deviation of the surface profile (R_q) tends to increase with layer height, except for the 0.3 mm layer height

According to Table 5.3, unlike the trends reported in the literature for composite plies (Schaefer *et al.*, 2017; Grouve *et al.*, 2013), the standard deviations of b_0 and w_0 are relatively high for the FFF-printed extrudates, making it difficult to identify consistent patterns from these parameters. For a_0, defined as $2R_q$ where R_q is the standard deviation of the surface profile, the trend appears to increase with layer height, as illustrated in Figure 5.11(b), with the exception of the 0.3 mm layer height.

5.4.5 Model validation

The experimentally obtained values of contact pressure, viscosity evolution, and surface roughness parameters for samples printed at 230 °C and 10 mm/s with varying layer heights were used to evaluate Equation 1 with two different approaches schematically illustrated in Figure 5.2. In the first approach, following methods reported for FFF printing (Coogan & Kazmer, 2019; Zhang *et al.*, 2025a), the extrudate was modelled as a single asperity that deforms during deposition to establish contact. In this case, surface roughness terms were combined into a single parameter, R, and the temperature profiles were taken from the center of the extrudate. The experimental degree of intimate contact was expressed as the ratio of bond width to extrudate width. In the second approach, commonly applied in composite welding literature (Çelik *et al.*, 2020; Grouve *et al.*, 2013; Schaefer *et al.*, 2017), the actual contacting area at the interface was calculated by accounting for interfacial microvoids. The duration for which the interface experiences contact pressure (t_p) corresponds to the time the nozzle remains over a given location and is inversely proportional to the print speed. For example, at a print speed of 10 mm/s and a nozzle diameter of 1 mm, the nozzle requires 0.1 s to pass over a point, representing the available time for pressure-driven intimate contact to occur.

The results of both approaches are summarized in Table 5.4. Regarding the effective contact model, the initial degree of intimate contact (D_{ic0}) is defined as $b_0/(w_0 + b_0)$, and it can be seen that, for all cases, the model predicts no contact development during the process. Compared with data from composite welding, the viscosity values in this study appear significantly lower, likely because measurements were taken near the interface, where cooling rates are high, as shown in

Figure 5.10. This explains why no contact development is predicted by the model. In the case of the nominal geometry approach, the model similarly fails to reproduce the experimental trend for an identical roughness parameter (R_c) across all samples, where R_c is a constant including surface roughness parameters according to (Coogan & Kazmer, 2019). This is likely due to the non-isothermal temperature characterization carried out here, unlike the isothermal assumptions commonly made in the literature; this point will be further discussed in Section 4.3.

Table 5.4 Comparison of experimental measurements with predictions from the Lee–Springer model using two different modelling approaches

Layer height (mm)	**0.3**	**0.4**	**0.5**	**0.6**	**0.7**	**0.8**
D_{ic0} (Effective contact model)	0.50	0.33	0.30	0.25	0.56	0.74
D_{ic} (Effective contact model)	0.50	0.33	0.30	0.26	0.57	0.74
D_{ic} (Effective contact, micro-CT)	0.90	0.98	0.99	0.99	0.95	0.84
D_{ic} (Nominal geometry model)	0.6 R_c	0.75 R_c	0.76 R_c	0.80 R_c	0.86 R_c	0.94 R_c
D_{ic} (Nominal geometry, microscopy)	0.81	0.70	0.64	0.70	0.50	0.40

These results suggest that the Lee–Springer model is applicable for characterizing the interfacial contact quality between printed extrudates, particularly in terms of interfacial microvoids. Unlike its demonstrated effectiveness in composite welding, the model does not adequately capture the interfacial behaviour observed in FFF-printed parts.

5.5 Discussion

5.5.1 Contact pressure and printing parameters

To analyze the trends and effects of different parameters on the measured contact pressure, the plots in Figure 5.12 were generated. Figure 5.12(a) shows contact pressure versus layer height for different print speeds, with each temperature displayed in a separate plot and a second-order polynomial regression applied. At low speeds, contact pressure decreases with increasing layer

height, consistent with the results reported in (Coogan & Kazmer, 2019; Zhang *et al.*, 2025a). This trend is likely due to the increased confinement between the nozzle and the previous layer. At higher print speeds, however, the trend becomes U-shaped, with contact pressure increasing again at the highest layer heights. This behaviour can be attributed to the higher flow rate at larger layer heights: the shorter residence time of the polymer in the hot end may prevent it from fully reaching the set printing temperature, leading to extrusion of a more viscous polymer and, consequently, higher contact pressure.

Figure 5.12(b) presents contact pressure versus print speed for different layer heights, with each temperature shown in a separate plot and linear regression applied. The change in contact pressure (ΔP) is indicated for each regression to compare the relative significance of each parameter. Contact pressure increases with print speed, and this effect is more pronounced at higher layer heights. This trend may be related to the shorter residence time of the polymer in the hot end at higher print speeds, which can reduce its actual temperature and increase viscosity, as well as to the enhanced extrusion force, which pushes the polymer stronger against the previous layer, leading to higher contact pressures.

Figure 5.12(c) shows contact pressure versus temperature for different print speeds, with each layer height displayed in a separate plot and linear regression applied. At higher printing speeds, increasing the temperature reduces the contact pressure, whereas this effect is negligible at lower print speeds. This behaviour can be attributed to the lower viscosity of the polymer at higher temperatures, which allows it to flow more easily, reducing the contact pressure at the interface and the measured pressure on the printing bed.

5.5.2 Intimate contact evolution

Similar to contact pressure, process parameters influence contact quality in an interdependent manner, with print speed being the most influential parameter. Lower print speeds generally result in better contact quality. While the mechanisms governing contact development require further investigation, this behaviour may be related to the longer time during which the nozzle

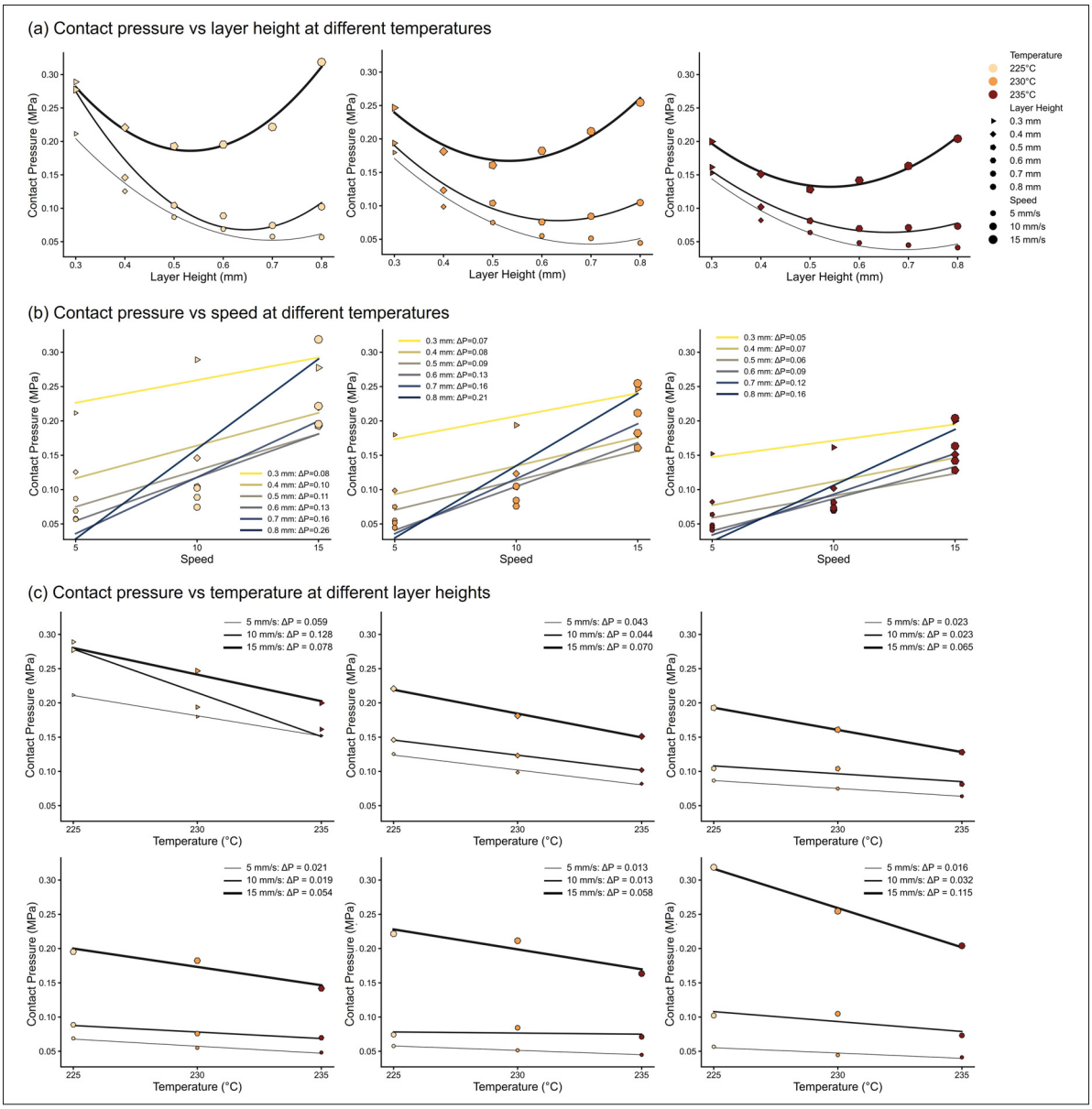

Figure 5.12 Contact pressure under varying printing conditions: (a) as a function of layer height for different print speeds and temperatures, showing a decreasing trend at low print speeds and a U-shaped trend at high print speeds (second-order polynomial regression); (b) as a function of print speed for different layer heights and temperatures, showing an increasing trend, more pronounced at higher layer heights (linear regression); (c) as a function of temperature for different print speeds and layer heights, showing a decrease at high print speeds and little change at low print speeds (linear regression)

remains above the contact area, corresponding to a prolonged first phase, when the nozzle applies contact pressure and partially shields the extrudate from ambient cooling, as described in Section 3.3. It is also observed that, under nearly all conditions, the 0.3 mm layer height exhibits relatively low contact quality. This could be attributed to the smaller extrudate size, which leads to faster cooling rates. In addition, at least for the sample for which surface roughness measurements are available, the relatively rougher surface may further contribute to the reduced contact quality.

Figure 5.13 shows that all experimental data points follow a consistent trend when plotted as contact pressure versus D_{ic}. An inverse relationship between D_{ic} and the measured contact pressure is observed, independent of specific printing parameters. Linear regression confirms a negative correlation, indicating that higher D_{ic} values correspond to lower contact pressure. Although higher measured contact pressure suggests that greater force is applied at the interface—an effect that would intuitively imply more favourable conditions for contact formation and reduced microvoid content—it is important to note that this contact pressure is a process outcome rather than a controlled input. It is influenced by multiple factors, including the geometry of the confined space between the nozzle and the underlying layer, as well as the flow behaviour of the polymer. In this context, lower measured contact pressure reflects better conformability of the newly deposited extrudate, allowing it to adapt more effectively to the surface of the underlying layer and potentially resulting in improved intimate contact at the interface.

Optimizing printing parameters to achieve a desired contact quality is challenging due to the interdependent effects of the process variables, as discussed above. However, the resulting contact pressure appears to provide a reliable estimate of the final contact quality, regardless of the specific printing parameters.

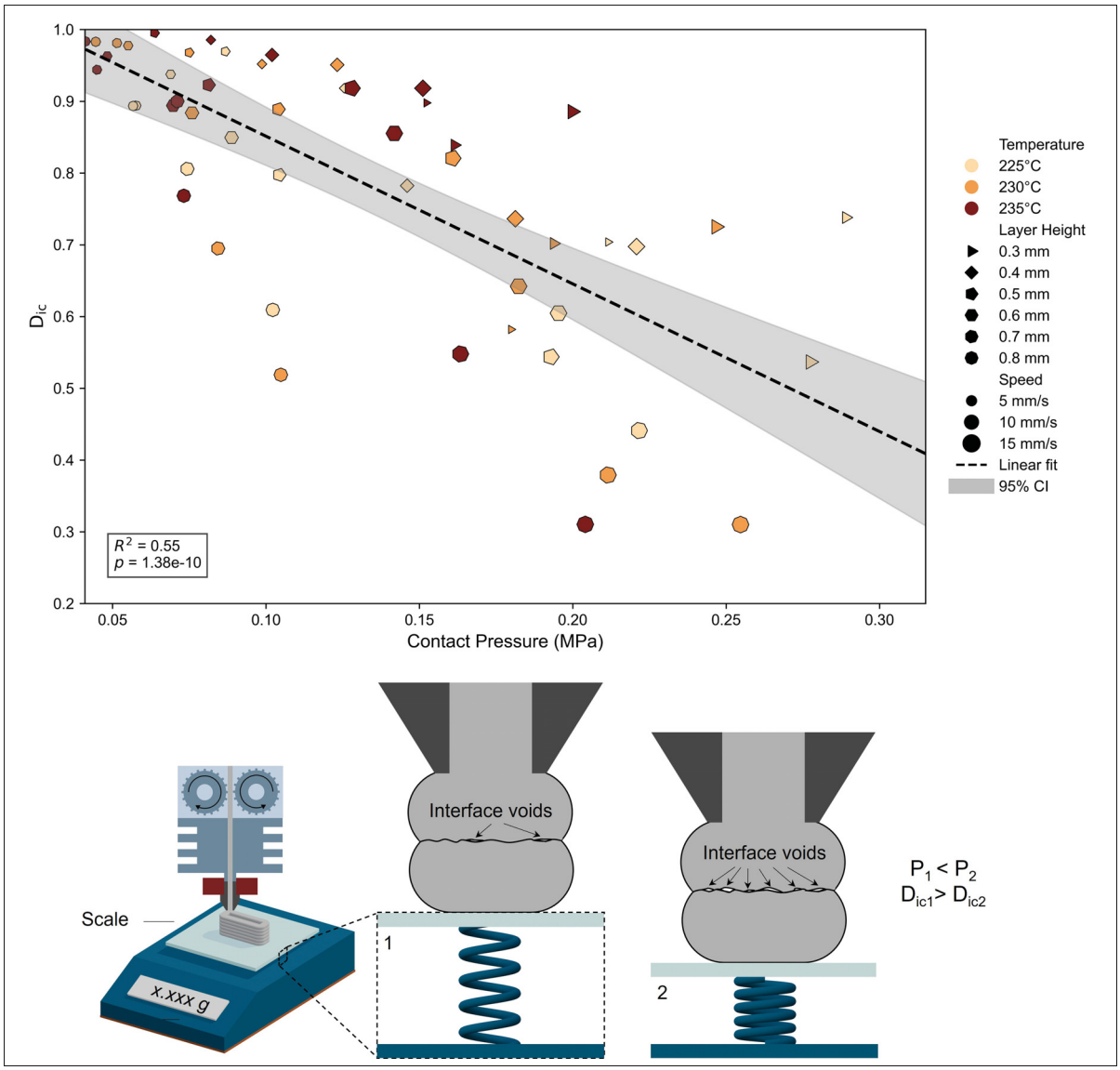

Figure 5.13 Contact pressure plotted against D_{ic} for all experiments, showing an inverse relationship independent of printing parameters. Linear regression indicates that higher D_{ic} values correspond to lower contact pressure. The schematic illustrates that fewer interfacial microvoids are formed when the measured contact pressure is low

5.5.3 Modelling approaches

Previous studies have applied the Lee–Springer model using a nominal geometry approach, where bond width was predicted under various processing conditions to estimate the degree of intimate contact (Coogan & Kazmer, 2019; Zhang *et al.*, 2025a). Both prior studies highlight the

strong influence of layer height on contact pressure, which in turn affects bond width and overall mechanical strength. Lower layer heights consistently resulted in higher contact pressures and improved part performance. In these studies, the increase in bond width contributes to enhanced mechanical properties, primarily due to geometric factors rather than improved bonding quality at the interface. A larger bond width reduces macrovoid content within the bulk material and decreases the severity of interfacial notches, both of which positively impact the overall mechanical performance. While some studies in the literature report contrasting results (Mazlan, Anas, Nor Izmin & Abdullah, 2023; Beníček, Vašina & Hrbáček, 2025; CNC Kitchen, 2019; Bist, Dobriyal, Gwalwanshi & Avikal, 2022)—suggesting that lower layer heights do not always lead to improved performance—this discrepancy may point to the need for a closer examination of the bonding interface itself. The findings here highlight an often-overlooked factor affecting bonding quality: the presence of interfacial microvoids. Additionally, variation in temperature profiles at different layer heights may also influence polymer chain diffusion and the final bond strength. Both the interfacial microvoids and the experimentally validated mass-dependent cooling effect are not considered in conventional bond strength models, and their inclusion is essential for a more complete and accurate understanding of interfacial bonding.

This study accounts for non-isothermal conditions and shows that both the initial temperature and cooling profile of extrudates vary with layer height. Extrudates at higher layer heights cool more slowly due to their increased mass, resulting in higher temperatures and slower cooling rates. Incorporating these experimental inputs may explain why the Lee–Springer model, applied under the same assumptions as in previous studies, fails to predict the observed bond width values in this work.

Regarding viscosity, while Coogan and Kazmer (Coogan & Kazmer, 2019) accounted for non-Newtonian behaviour, the original Newtonian assumption of the model is retained here. However, the polymer experiences shear stress, which is highest at the walls and gradually decreases to zero at the nozzle center (Bakrani Balani *et al.*, 2019; Das, Gilmer, Biria & Bortner, 2021). To estimate whether the printing conditions could induce non-Newtonian behaviour, the

maximum shear rate inside the nozzle was calculated using Equation 5.3 (Bakrani Balani *et al.*, 2019):

$$\dot{\gamma}_w = \frac{8(3n+1)Q}{n\pi D_{\text{Nozzle}}^3} \tag{5.3}$$

Here, Q is the volumetric flow rate, n is the power-law index describing the shear-rate dependence of viscosity, and D_{Nozzle} is the nozzle diameter. The flow rate for each case was calculated by multiplying the extrudate cross-sectional area by the printing speed. Based on these parameters, the shear rate across all samples was estimated to range between 16 and 129 s^{-1}. By applying the Cox–Merz rule (Cox & Merz, 1958), which states that for many polymer melts and solutions the steady shear viscosity at a given shear rate is approximately equal to the complex viscosity measured in oscillatory tests at the same frequency, the results indicate that at the shear rates and temperatures relevant to the printing conditions studied here, the material behaves nearly Newtonian. However, the actual flow within the nozzle is complex, with local variations in shear and extensional deformation that are not captured by this simplified estimate. Accurate characterization of the local rheological behaviour inside the nozzle and during contact development is therefore required to more precisely evaluate predictive models.

The observed failure of the Lee–Springer model may also indicate a limitation in the assumption that contact pressure actively deforms the extrudate: instead of reshaping the extrudate, the measured contact pressure appears to arise from the available space between the nozzle and the previous layer and the material's flow characteristics. What has been interpreted as pressure-driven deformation is more accurately the outcome of how the polymer fills the confined gap between the nozzle and the previous layer, rather than an active compression of the extrudate by pressure. This distinction is critical for improving the accuracy of bonding models in extrusion-based additive manufacturing.

The intimate contact models were originally developed for composite ply welding, where the two plies are already in contact with a known initial degree of intimate contact before heat and

pressure are applied. In such cases, temperature and pressure histories are well-defined and controlled, and the surface roughness of the plies can be accurately characterized. In contrast, conditions in extrusion-based additive manufacturing are markedly different. The top and bottom extrudates come into contact while being at different temperatures, and highly transient heat transfer across the interface makes precise characterization difficult. Furthermore, the roughness of the top (newly deposited) extrudate cannot be directly measured. Instead, what can be measured is the roughness of the bottom extrudate, which, based on thermal imaging results, has not experienced sufficient heating to flow, making it an unreliable input for models that assume pre-existing, flowable surface characteristics. The curvature of the bottom extrudate surface, shown in Figure 5.11, may further complicate flow behaviour during deposition. To better describe contact development in this process, models that capture how a flowing polymer fills gaps under confined conditions, such as squeeze flow or viscous penetration into surface asperities, may be more appropriate.

5.6 Conclusion

In this study, the quality of intimate contact at the bonding interfaces of FFF-printed PETG layers was investigated under various printing conditions, including layer height, print speed, and temperature. The work involved both the observation and quantification of microvoids at the bonding interface. Polarized optical microscopy and micro-CT imaging were employed to provide direct evidence of interfacial microvoids. In addition, a new, low-cost methodology was developed to quantify the contact pressure generated during printing.

An inverse relationship was identified between intimate contact quality and the measured contact pressure during printing, suggesting that contact pressure may serve as an indicator of how effectively the extruded polymer conforms to the underlying extrudate. Among the studied parameters, print speed had the most pronounced influence, with lower print speeds generally associated with improved contact quality. However, the effects of print speed, layer height, and temperature were highly interdependent, highlighting the need for further investigation to fully clarify these relationships. In this context, the applicability of conventional composite

intimate contact models for predicting the extent of interfacial microvoids was experimentally assessed, similar to their use in composite welding. This work also highlights that understanding the interface microstructure and its relationship with printing parameters remains limited, particularly regarding the polymer state at the nozzle exit, such as the actual polymer temperature, which is often assumed to equal the nozzle command temperature but can vary significantly with changes in process parameters. Accounting for these variations is essential for predicting interfacial microstructure and properties. This study represents a first step toward addressing this gap.

It was also found that the degree of intimate contact, determined from the microvoid content at the bonding interface, could not be accurately predicted by conventional composite intimate contact models. The results suggest that the current use of these models to predict bond width may not fully represent the underlying phenomena and should therefore be reconsidered. Further work is needed to incorporate this overlooked factor, interfacial microvoids, into bond-strength models and process-optimization strategies for FFF-printed parts. Alternative approaches, such as capillary flow models, mould-filling models, or modified squeeze-flow models, could be explored to determine whether they more effectively describe intimate contact formation at the bonding interface.

CHAPTER 6

A MULTI-MECHANISM PERSPECTIVE ON INTERLAYER BEHAVIOUR IN MATERIAL EXTRUSION ADDITIVE MANUFACTURING

Maryam Shokrollahi[1] , Adam W. Smith[1] , Martine Dubé[1,2] , Ilyass Tabiai [1,2]

[1] Department of Mechanical Engineering, École de technologie supérieure, Montréal, Canada

[2] CREPEC, Research Center for High Performance Polymer and Composite Systems, Mechanical Engineering Department, McGill University, Montréal, Canada

Paper submitted to *Rapid Prototyping Journal*, January 2026

6.1 Abstract

Purpose - Interlayer weakness limits the mechanical performance of material extrusion additive manufacturing (MEAM) parts. Interlayer behaviour is governed by two mechanisms: the quality of bonding at welded regions and naturally occurring interface notches formed by the extrudate's geometry. This study investigates the interplay between these mechanisms in polyethylene terephthalate glycol parts produced via fused granular fabrication.

Design/Methodology/Approach - Layer height was deliberately varied to generate a spectrum of notch severities and interlayer bonding qualities. Samples were tested in the transverse direction using tensile testing coupled with digital image correlation to quantify strain localization and failure mechanisms.

Findings - Results show that increasing layer height amplifies notch severity while enhancing interlayer bonding. While fracture consistently initiates at interface notches, the resulting strength reduction depends on the interplay between notch geometry and interlayer bonding quality. A less severe notch can cause greater strength loss if the interface bonding is weaker, revealing a competing effect which leads to an optimal condition where notch severity and bonding are balanced. Removal of interface notches largely restores ultimate tensile strength, whereas

recovery of strain at break remains incomplete in samples with weaker bonding, suggesting that conventional strength-based criteria may overestimate full interlayer bonding.

Originality/Value - These findings demonstrate that interface notch geometry and interlayer bonding exert coupled effects on interlayer mechanical behaviour. Recognizing this interplay is essential for accurately interpreting mechanical performance in MEAM parts and for enabling reliable modelling and process optimization.

6.2 Introduction

Polymer-based material extrusion additive manufacturing (MEAM) has experienced rapid growth over the past decade due to its cost-effectiveness, material efficiency, and scalability across a wide range of applications (Zander *et al.*, 2019; Dey *et al.*, 2021; Goh *et al.*, 2024). This technique, including fused filament fabrication (FFF) and fused granular fabrication (FGF), operates by extruding thermoplastic material through a heated nozzle and depositing it layer by layer to build three-dimensional components. While FFF generally uses pre-formed filaments and is optimized for fine-resolution printing of small to medium-sized parts, FGF directly extrudes polymer pellets through a screw-based system, enabling much higher deposition rates and the fabrication of larger components with reduced printing time (Tao *et al.*, 2025; Patel & Taufik, 2022; Penumakala *et al.*, 2020; Pignatelli & Percoco, 2022).

Despite their increasing adoption, MEAM technologies remain underutilized in high-end and load-bearing applications. This limitation is largely attributed to challenges related to geometric accuracy, low mechanical performance of printed components, and the difficulty in accurately predicting their behaviour under service loading (Xu, Agassant & Pigeonneau, 2022; Gilmer *et al.*, 2021; Yu *et al.*, 2023; Bouzaglou *et al.*, 2023). Compared to conventionally manufactured polymers, MEAM parts often exhibit reduced strength, pronounced anisotropy, and large variability in deformation and failure behaviour (Kuznetsov *et al.*, 2018; Cuan-Urquizo *et al.*, 2019; Khan *et al.*, 2022; Popescu *et al.*, 2018; Doshi *et al.*, 2022; Turner & Gold, 2015).

Improving the performance and predictability of MEAM parts requires elucidating the underlying mechanisms responsible for strength reduction. Two primary classes of mechanisms have been identified in the literature. The first relates to interlayer bonding, which involves the formation of intimate contact between adjacent extrudates followed by interdiffusion of polymer chains across the interface (Sun *et al.*, 2008; Krishnanand & Taufik, 2021; Coogan & Kazmer, 2017b; Aliheidari *et al.*, 2018; Vaes *et al.*, 2021).

The second class of mechanisms arises from extrudate-scale geometric features inherent to the deposition process. Owing to the rounded rectangular cross-section of deposited roads, adjacent extrudates do not fully conform to one another, leading to the formation of internal macrovoids between neighbouring extrudates. These macrovoids reduce the effective load-bearing area and have been widely studied in the literature, with numerous process and material strategies proposed to mitigate their formation and associated strength loss (Akhoundi & Behravesh, 2019; Tronvoll *et al.*, 2018; Sun *et al.*, 2023; Ghorbani *et al.*, 2022; Sommacal, Matschinski, Drechsler & Compston, 2021; Eiliat & Urbanic, 2018; Zhang *et al.*, 2025c).

More recently, another mechanism linked to extrudate geometry has been recognized as a contributor to reduced mechanical performance. At the junctions where extrudates meet, their shape creates small notch-like features that can occur at surface ridges or along internal voids. These so-called interface notches act as localized stress concentrators, making these regions more susceptible to the initiation of damage. This mechanism has been shown to play a major role in mechanical anisotropy and early failure in FFF and FGF parts, particularly under transverse loading (Allum *et al.*, 2021, 2020a,c; Kundurthi *et al.*, 2023; Shokrollahi *et al.*, 2025; Park *et al.*, 2022). These notches are characterized by their depth, angle, and root radius, which in turn depend on printing parameters such as layer height, print speed, and deposition conditions (Kundurthi *et al.*, 2023; Shokrollahi *et al.*, 2025; Moetazedian *et al.*, 2023; He *et al.*, 2020).

To explore the mechanical role of these features, studies have employed single-extrudate-thick tensile samples, enabling detailed investigation of local stress and strain fields around notch regions (Allum *et al.*, 2020c; Kundurthi *et al.*, 2023; Shokrollahi *et al.*, 2025). Combined

experimental measurements and finite element analyses have demonstrated that notch geometry governs strain localization and failure initiation, and could reduce the strength by up to 70% (Shokrollahi *et al.*, 2025). Isotropic tensile properties have been observed after eliminating the influence of interface notches, with full recovery of bulk-like properties, suggesting that interface notches, rather than insufficient molecular healing, often govern performance degradation (Shokrollahi *et al.*, 2025; Allum *et al.*, 2020a; Moetazedian *et al.*, 2023).

However, these conclusions must be interpreted in the context of the intrinsic characteristics of the MEAM process. Rapid cooling rates, which can reach up to 100 °C/s (Bechtel *et al.*, 2020), combined with relatively low interlayer contact pressures, can inhibit full bond formation (Coogan & Kazmer, 2017b, 2019; Zhang *et al.*, 2025a). Consequently, mechanical performance in real printed parts is likely governed by an interplay between interface notch severity and interlayer bonding quality. While interlayer bonding has been extensively investigated (Seppala *et al.*, 2017; Popescu *et al.*, 2018; Waly *et al.*, 2023; Wach *et al.*, 2018), interface notches have only recently gained attention. Understanding how these two mechanisms interact is critical, yet their combined effect on deformation and failure has not been studied.

The present study addresses this gap by experimentally investigating the combined effects of interface notch severity and interlayer bonding quality in FGF-printed polyethylene terephthalate glycol (PETG) parts. PETG was selected due to its favourable balance of mechanical strength, ductility, and thermal stability, as well as its good printability and widespread use in material extrusion processes (Valvez *et al.*, 2022; Leśniowski *et al.*, 2025; Srinivasan *et al.*, 2020). By deliberately selecting and modifying processing parameters, single-extrudate-thick samples were produced in which both notch geometry and bonding quality varied in a controlled manner. By decoupling the influence of interface notches from interface bond quality, the study provides a clearer understanding of the role of each mechanism and their combined effect. Full-field digital image correlation was employed to quantify strain localization associated with notch severity, and fractographic analysis was used to elucidate failure mechanisms across different processing conditions. Through this integrated experimental framework, the study provides new insight into the coupled role of geometry and bonding in governing mechanical performance, advancing our

understanding of the mechanisms controlling MEAM part behaviour and supporting improved predictive capability and process optimization for material extrusion additive manufacturing.

6.3 Methodology

6.3.1 Material

Polyethylene terephthalate glycol (PETG) pellets supplied by 3DXTech Advanced Materials were used as the feedstock material. According to the manufacturer's datasheet, the polymer has a density of 1.24 g/cm^3, a glass transition temperature (T_g) of 80 °C measured by differential scanning calorimetry (DSC), and a tensile strength of 45 MPa determined in accordance with ISO 527.

6.3.2 Printing and sample extraction

As shown in Figure 6.1(a), an AM Flexbot printer from the CEAD company was used to fabricate PETG walls with a single extrudate thickness. The objective was to deliberately create processing conditions under which interlayer bonding and notch severity vary. To this end, different printing parameters and wall configurations were investigated. While such conditions could theoretically be achieved using various printing profiles, in practice, a 4 mm nozzle combined with varying layer heights was found to be adequate to accomplish this.

A representative printed wall is shown in Figure 6.1(b). The wall is 40 cm in length and 12 cm in height, dimensions that are suitable for the extraction of ASTM D638 Type IV tensile samples. To prevent warpage and to improve adhesion to the build platform, the bed temperature was increased to 55 °C. Additionally, three raft layers were first printed using a 15 mm nozzle, and the wall was subsequently printed on top of the raft. Two spiral patterns were also added at the ends of the wall to enhance mechanical anchoring and ensure stable attachment to the raft during printing. Printing parameters are listed in Table 6.1.

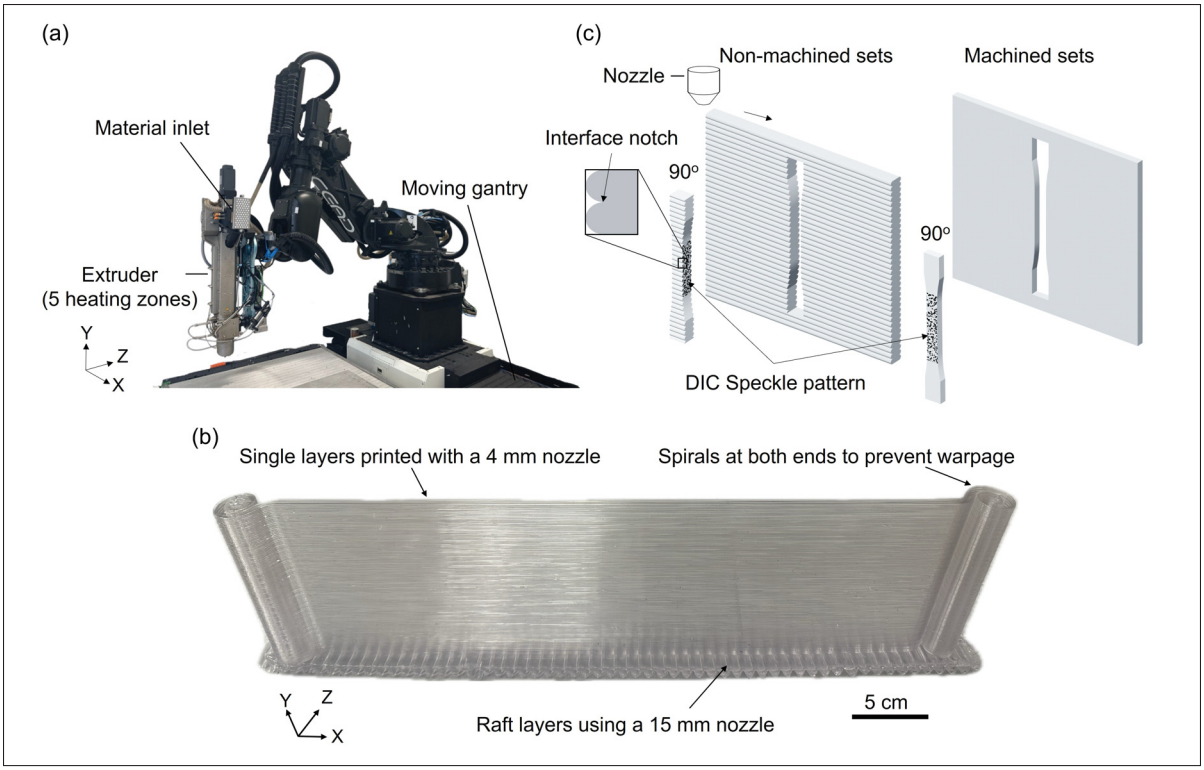

Figure 6.1 (a) Robot-based extruder used for fused granular fabrication (FGF). (b) Printed wall geometry using a 4 mm nozzle, with raft layers and spiral features added to minimize warpage and detachment. (c) Schematic of extrudate sampling in the transverse direction from both as-printed and surface-machined walls

Table 6.1 Printing parameters for walls printed with a 4 mm nozzle

Extrusion temperature (°C)	**Nozzle diameter (mm)**	**Layer time (s)**	**Layer height (mm)**	**Bed temperature (°C)**
190-215	4	125	0.75, 1, 1.25, 1.5	55

Walls were printed at four different layer heights. After printing, the spirals and raft were removed, and each wall was divided into two parts. One part was machined on both surfaces to fully remove the interface notches, with approximately 1 mm removed from each side to ensure complete elimination of the notches. Samples were then extracted in the transverse

direction from both machined and non-machined walls. A continuous flow of coolant was applied during machining to prevent overheating and maintain dimensional accuracy. Previous experiments have shown that this approach keeps the polymer temperature below its glass transition temperature, preventing any heat-induced changes in material properties (Shokrollahi *et al.*, 2025). The machining parameters used for these samples are summarized in Table 6.2. Table 6.3 lists the sample codes along with their corresponding details, providing an overview of the different sample sets prepared for testing.

Table 6.2 Machining parameters for surface removal and sample extraction

Operation	**Tool**	**Feed rate (mm/min)**	**Spindle speed (RPM)**	**Depth of cut (mm)**
Profiling	Endmill, 3/16", Niagara N09892, Finishing, Traverse Tool	1270	12000	1.524
Rough facing	Facemill Walter 2" F4042.UB.051.Z06.11, inserts: ADHT1204PER-G88 WK10	2286	11000	1.524
Finish facing	Facemill Walter 2" F4042.UB.051.Z06.11, inserts: ADHT1204PER-G88 WK10	2286	11000	0.508

Table 6.3 Overview of sample sets and corresponding details

Sample	**Extrudate direction with respect to tensile direction (°)**	**Surface removal**	**Layer height (mm)**
NM-0.75	90	No	0.75
NM-1	90	No	1

Sample	Extrudate direction with respect to tensile direction (°)	Surface removal	Layer height (mm)
NM-1.25	90	No	1.25
NM-1.5	90	No	1.5
M-0.75	90	Yes	0.75
M-1	90	Yes	1
M-1.25	90	Yes	1.25
M-1.5	90	Yes	1.5

6.3.3 Tensile testing and DIC

Tensile testing was performed using an MTS Alliance RF/200 machine equipped with a 1000 N load cell. Prior to testing, all samples were pre-conditioned at 60 °C for 8 hours. The experiments were conducted at a nominal strain rate of 1 %/min under ambient laboratory conditions. A mechanical extensometer was used to measure strain during the tests.

For samples analyzed with Digital Image Correlation (DIC), the virtual extensometer tool in VIC-2D software was employed to calculate the average strain between two selected points within the gauge length; this value is reported as the nominal strain. Five samples were tested for each set. To prepare the samples for DIC, a base layer of white acrylic paint was applied, followed by a speckle pattern of black dots to enable full-field strain tracking. The speckle pattern was generated using an airbrush with a 0.1 mm nozzle. Images were captured using a monochrome Grasshopper 3-51SM5M camera positioned to cover the gauge section during tensile testing. Imaging parameters, including acquisition frequency (frames per second, fps), are summarized in Table 6.4.

For DIC analysis, subset size and step size were selected to ensure at least three independent measurement points per layer, capturing strain distributions within individual extrudates and at inter-extrudate interfaces. Lagrangian strains were computed using a 15-pixel filter. The spatial

resolution of displacement measurements, S^{rd}, defined as the distance between independent displacement points, and the spatial resolution of strain measurements, $S^{r\varepsilon}$, corresponding to the effective strain gauge length, were calculated following (Schreier, Orteu & Sutton, 2009). Speckle pattern and software settings were optimized to minimize displacement error, keeping the standard deviation below 0.03. Table 6.4 summarizes the subset sizes, step sizes, correlation types, and resulting spatial resolutions for each tested condition. The chosen subset size and spatial resolution provide sufficient independent measurement points per layer to resolve strain distributions. With a minimum layer height of 0.75 mm and a spatial resolution of 0.17 mm, approximately four measurement points are obtained per layer, enabling detection of both intra-extrudate strain variations and interfacial strain localization.

Table 6.4 Imaging and DIC analysis parameters

FPS	**Scale (px/ um)**	**Subset (px × px)**	**Step (px)**	**Correlation type**	**S^{rd} (mm)**	**S^{re} (mm)**	**Displacement variation (mm)**	**Strain variation (‰)**
73	15	9	1	Direct	0.156	0.170	6×10^{-3}	0.02

6.4 Results

6.4.1 Tensile testing and DIC

Figure 6.2 shows the stress–strain curves of a representative sample from each non-machined set, along with DIC results at different nominal strain (ε_{yy-n}) levels. The results indicate that the maximum nominal strain before failure is lowest for NM-0.75 and highest for NM-1.25. Strain localization at the notches clearly increases with increasing layer height. Additionally, a slight non-linear behaviour starts to become noticeable in NM-1.25.

Figure 6.3(a) presents the ultimate stress and strain at break for the non-machined sets. Both strength and strain initially increase with layer height, reflecting enhanced mechanical

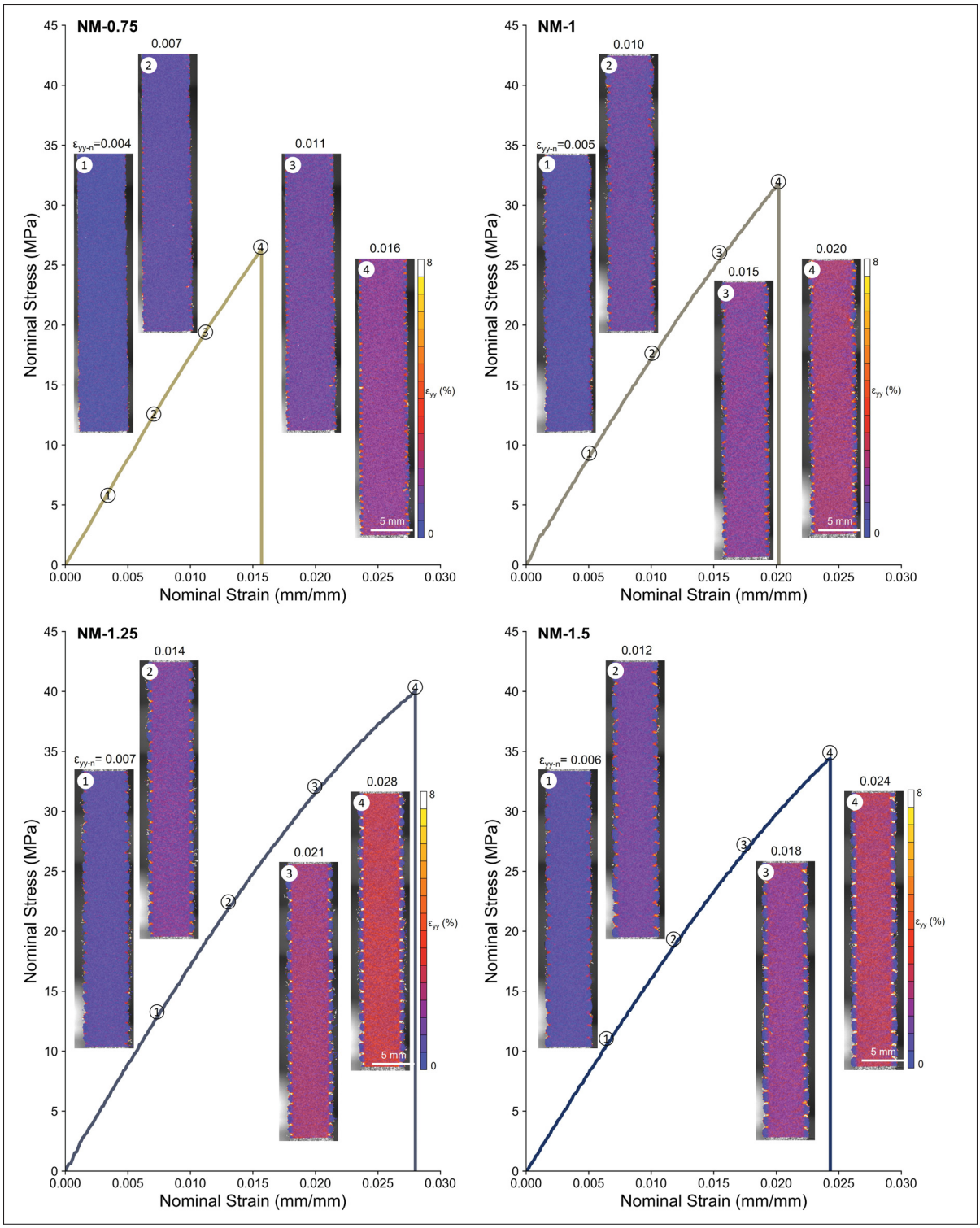

Figure 6.2 Representative stress–strain curves of non-machined samples with DIC results at different nominal strain levels. Strength and maximum strain before failure are lowest for NM-0.75 and highest for NM-1.25. Strain localization at the notches increases with layer height

performance. This upward trend continues up to NM-1.25, after which it reverses: the strength decreases at NM-1.25, and the strain at break shows a corresponding decline at NM-1.5.

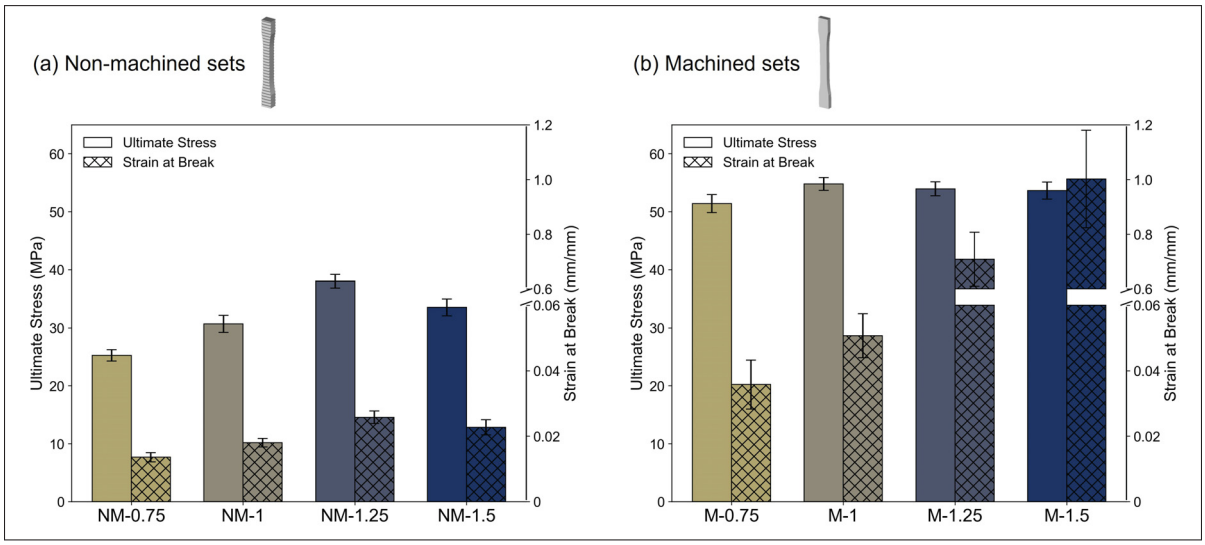

Figure 6.3 Ultimate stress and strain at break for (a) non-machined and (b) machined samples. In non-machined sets, both strength and strain increase with layer height up to NM-1.25 before declining. In machined sets, strength is largely recovered for all samples, while strain at break remains low for M-0.75 and M-1, indicating reduced ductility. The secondary y-axis (strain at break) includes a scale break from 0.06 to 0.6 mm/mm to accommodate the broad range of deformation behaviours observed for M-1.25 and M-1.5

Figure 6.4(a) presents the strain concentration factor, defined as the local strain normalized by the nominal strain, plotted along the z-axis immediately prior to failure. The reported values represent the average over 20 notches, with the shaded band indicating the standard deviation. The strain concentration factor reaches its maximum at the notch and decreases rapidly with increasing distance from the notch. Away from the notches, similar strain concentration levels are observed for all samples, whereas at the notch location, the strain concentration factor increases with increasing layer height. This trend is more clearly illustrated in Figure 6.4(b), which shows box-and-whisker plots of the strain concentration factor at the notch locations. The results confirm that strain concentration at the notches increases with layer height, while more outliers are observed for the lower layer height samples. Outliers were identified using the standard box-and-whisker criterion, defined as values lying more than 1.5 times the interquartile range beyond the first or third quartile.

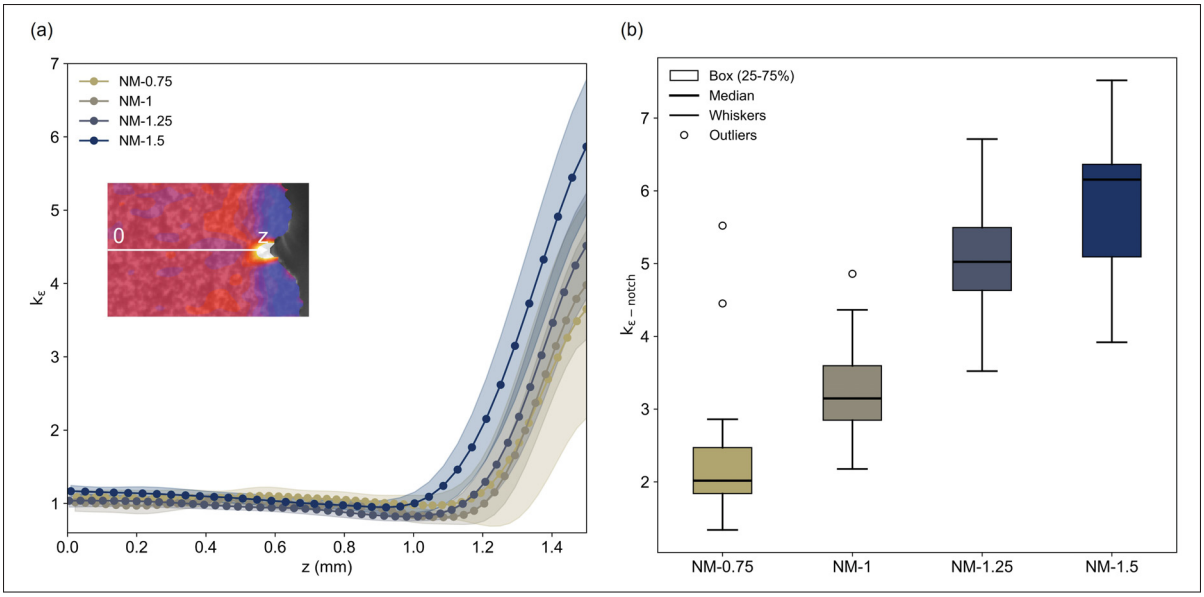

Figure 6.4 (a) Strain concentration factor along the z-axis, averaged over 20 notches with the shaded region indicating the standard deviation. The strain concentration factor is highest at the notch and decreases rapidly with distance from it, with higher values observed at the notch for larger layer heights. (b) Strain concentration factor at the notches, showing an increase in strain concentration factor with layer height and greater variability for lower layer-height samples

Figure 6.5 presents the stress–strain curves for the machined sets, with one representative sample shown for each set. For clarity, the data are truncated at a nominal strain of 0.1. Compared to the non-machined samples, higher ultimate stress values are obtained for all machined cases, and the curves consistently indicate the occurrence of plastic deformation.

For M-0.75 and M-1, failure occurs shortly after reaching the maximum stress, indicating limited post-yield deformation. DIC reveals pronounced strain localization along a horizontal line in both samples, with higher strain values concentrated near the sample edges. These lines, corresponding to strain localization at the interface, are the locations where failure initiates. Additionally, both samples exhibit an X-shaped strain localization pattern with high strain at the center, suggesting the presence of voids.

In contrast, M-1.25 and M-1.5 sustain significantly higher strain levels and exhibit enhanced ductility. Clear yielding behaviour is observed in both cases, although the initiation mechanisms

differ. In M-1.25, yielding initiates along inclined, intersecting bands near the center of the sample, whereas M-1.5 displays the more typical angled yielding pattern. Following yield initiation, deformation progressively spreads throughout the entire gauge section.

Figure 6.3(b) presents the ultimate stress and strain at break for the machined sets. Strength is largely recovered, reaching approximately 90% for M-0.75 and full recovery (100%) for M-1, M-1.25, and M-1.5. In contrast, strain at break is not recovered for M-0.75 and M-1, indicating significantly lower ductility for these samples despite their restored strength. The secondary y-axis for strain at break includes a scale break to accommodate the much higher deformation observed.

6.4.2 Failure analysis

Figure 6.6 illustrates the failure modes of the non-machined samples from different viewing angles. In all cases, the fracture initiates at the interface notches. For NM-0.75 and NM-1, crack propagation predominantly follows the interlayer interface. In NM-1, the fracture surface at the interface appears shiny and smooth, indicative of clear interfacial delamination with no observable damage in the bulk on either fractured side. In contrast, NM-0.75 exhibits a different fracture morphology: while crack growth occurs at the interface, the fracture surface transitions from a relatively smooth region near the initiation site to areas where damage extends slightly into the bulk material.

For NM-1.25, crack propagation increasingly extends into the bulk and creates whitened areas, although the interface remains the primary crack path. In NM-1.5, fracture also initiates at the interface; however, the crack subsequently deviates from the interlayer region and propagates through the bulk, indicating that the interface is no longer the preferred crack path throughout failure.

For the machined samples shown in Figure 6.7, the fracture surfaces of M-0.75 and M-1 closely resemble those of their non-machined counterparts. M-1 exhibits a shiny, smooth fracture surface characteristic of interfacial delamination, whereas M-0.75 shows a relatively flat fracture

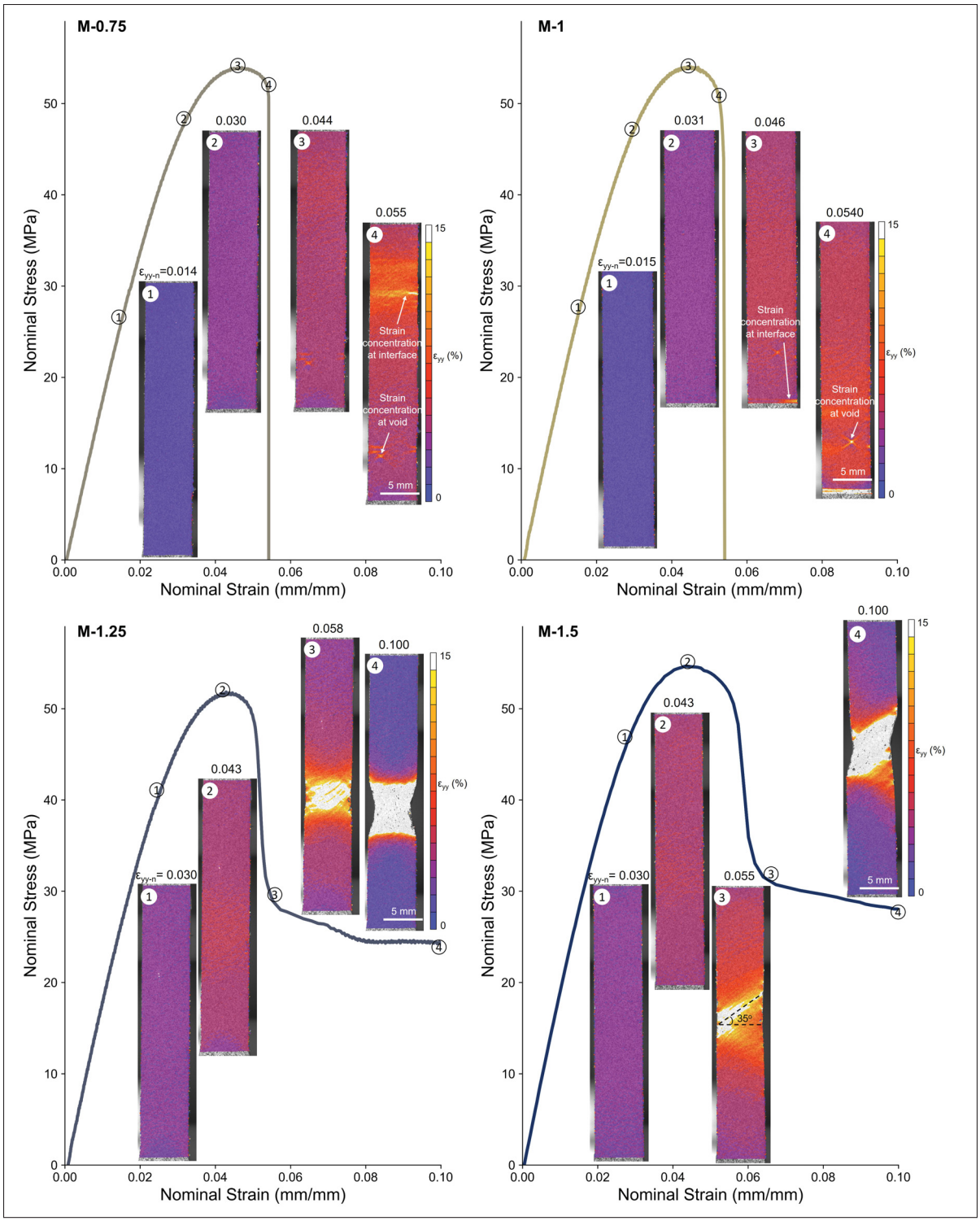

Figure 6.5 Representative stress–strain curves for machined samples (data truncated at 0.1 strain), showing increased ultimate stress and plastic deformation for all cases. Limited post-peak deformation and early failure are observed for M-0.75 and M-1, whereas M-1.25 and M-1.5 exhibit extensive yielding and substantially higher ductility with more distributed deformation

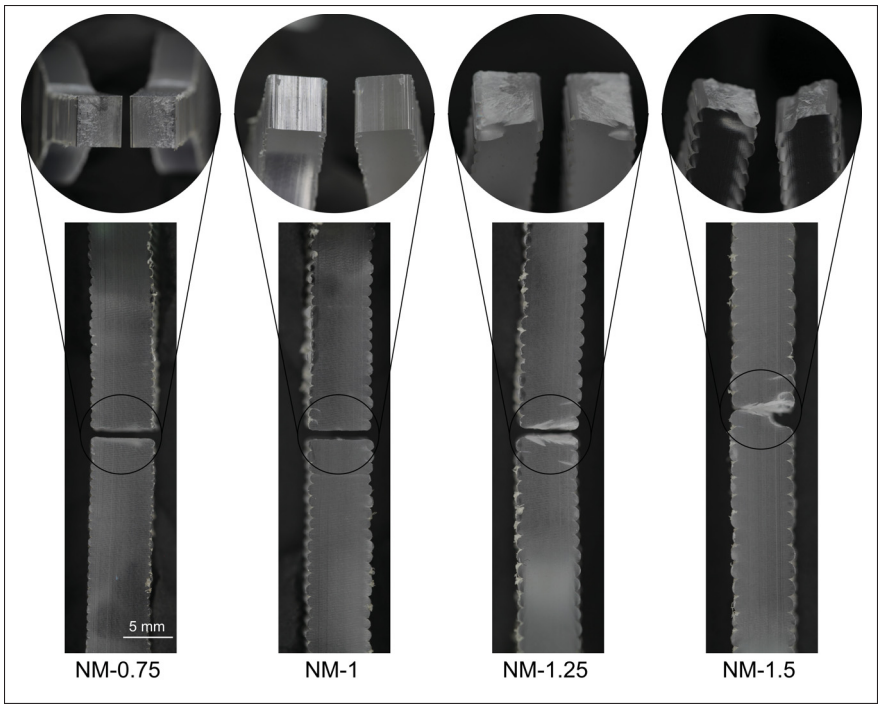

Figure 6.6 Fracture surfaces of non-machined samples. In all cases, the fracture initiates at the interface notches. NM-0.75 and NM-1 predominantly fail by interfacial crack propagation, with NM-1 showing clear interfacial delamination and NM-0.75 exhibiting slightly whitened areas in the bulk. With increasing layer height (NM-1.25 and NM-1.5), crack propagation increasingly extends into the bulk, indicating a reduced preference for interfacial failure

surface accompanied by small whitened regions in the bulk. In contrast, M-1.25 and M-1.5 display extensive plastic deformation prior to failure, suggesting full recovery of strain at break for these samples.

To better understand interfacial fracture, images were captured at a frame rate of 73 fps during the tensile test for M-1, with the results shown in Figure 6.8. As the test progresses, interfaces become visible as horizontal white lines, along with X-shaped damage patterns at several locations along different interfaces. These X-shaped regions correspond to localized damage around the microvoids at the interface that develop under uniaxial loading. Final failure occurs

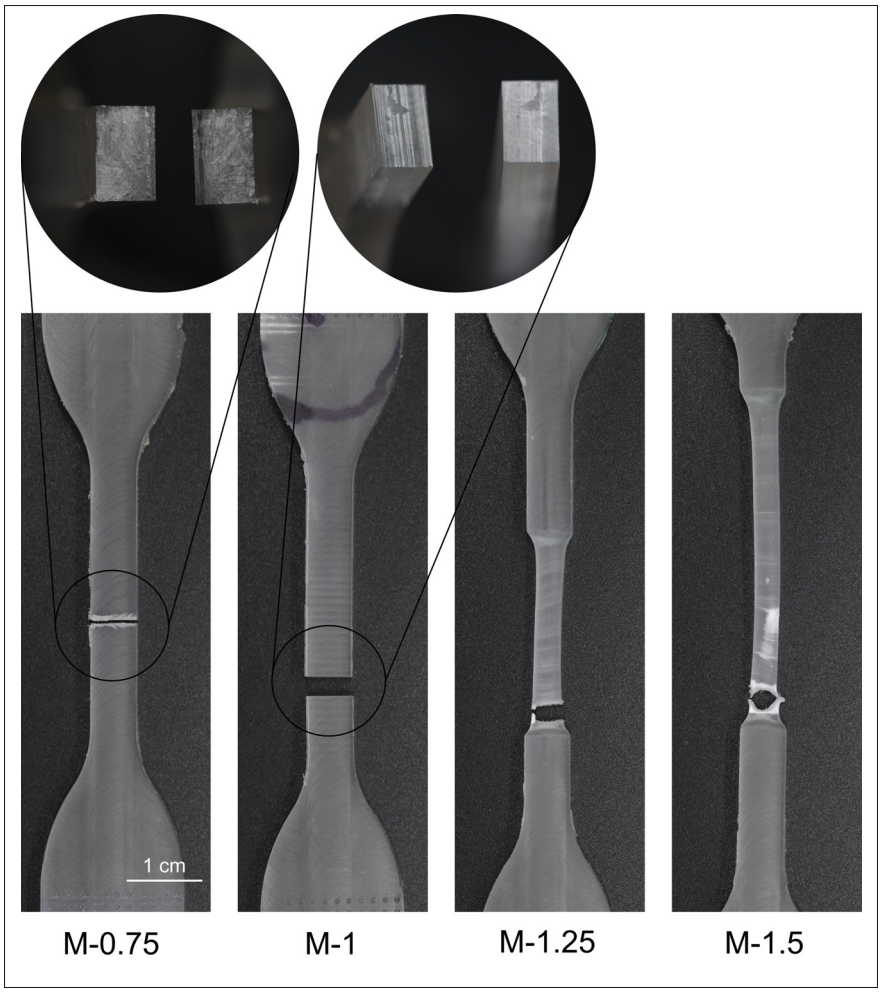

Figure 6.7 Fracture surfaces of machined samples. M-0.75 and M-1 exhibit fracture morphologies similar to their non-machined counterparts, characterized by interfacial failure and limited plastic deformation. In contrast, M-1.25 and M-1.5 show extensive plastic deformation prior to failure, indicating full recovery of ductility

at one of these layers, likely initiated at a microvoid, with half of the X-shaped damage visible on each side of the fractured sample.

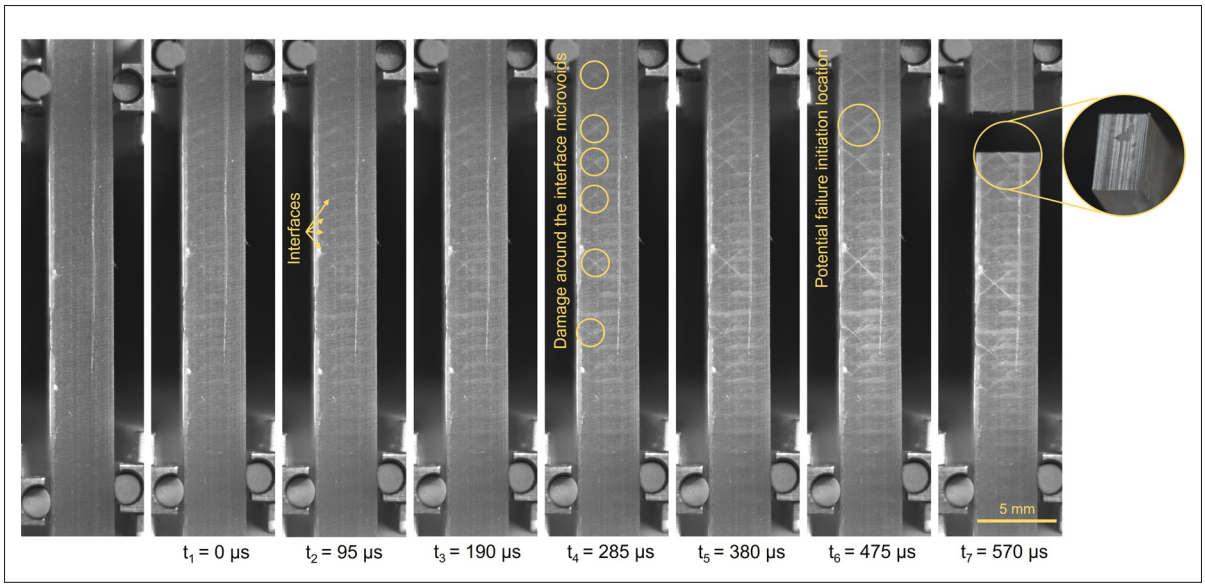

Figure 6.8 High-speed images (73 fps) showing the development of interfacial damage in M-1. Appearing white lines indicate the interfaces, while X-shaped damage patterns form around microvoids under loading. Final fracture occurs at one of these layers, with portions of the X-shaped damage visible on both sides of the fractured sample

6.5 Discussion

Using layer height as the key variable enabled simultaneous variation of both interface notch characteristics and interlayer bonding quality. Previous studies have shown that increasing layer height leads to greater notch depth and larger notch angles, which both theoretically and experimentally increase the strain concentration factor (Shokrollahi *et al.*, 2025; Kundurthi *et al.*, 2023). Consistent with these findings, the present results confirm that notch severity increases with layer height, as evidenced by Figure 6.4, which shows the strain concentration factor measured at the interface notches prior to failure.

The effect of notch severity on performance, however, depends on the interlayer bond strength. The conclusion that lower notch severity improves performance holds when full interlayer bonding is achieved; however, when bonding is incomplete, reduced notch severity does not necessarily lead to better mechanical performance. Instead, optimal performance arises from the combined influence of notch severity and bonding quality.

While interface notches become more severe at higher layer heights, interlayer bonding quality simultaneously improves. This improvement results from larger extrudate size and lower cooling rate at higher layer heights, which enhance intimate contact and promote interlayer healing. These two competing effects—more severe notches versus improved bonding—interact to produce an optimal condition at a 1.25 mm layer height. Notably, the lowest performance occurs for the sample with the least severe notches, highlighting that damage initiation and propagation are not determined solely by notch geometry, but also by the quality of the adjacent bonded area.

Defining a "non-fully bonded" interface in this context is challenging when relying on conventional bond strength metrics, which are typically based on ultimate strength (Lacambra-Andreu *et al.*, 2023; Allum *et al.*, 2020c; Xu *et al.*, 2025; Coogan & Kazmer, 2017b, 2019; Zhang *et al.*, 2025a). While mild notches combined with incomplete bonding lead to the lowest performance for NM-0.75, characterization of the machined sets shows nearly full recovery of ultimate strength. This indicates that, in the absence of local stress concentrators, the load can be effectively distributed, producing strength comparable to the bulk material. However, ductility cannot be fully recovered if the interface is not fully healed, even in the absence of notches. Localized strain at the interface observed by DIC in M-0.75 and M-1 (Figure 6.5) supports this, indicating that strain at break is a more sensitive indicator of interlayer bonding than ultimate strength alone. This represents a novel finding not previously reported for assessing interlayer bonding quality in MEAM.

This decoupling also suggests that incomplete bonding does not substantially limit load transfer at moderate strains, but strongly affects damage evolution and plastic deformation. Sufficient chain interdiffusion and mechanical interlocking allow high stress to be sustained, yet full chain randomization across the interface is likely not achieved. Residual heterogeneities, including partially diffused polymer chains and interfacial microvoids, as shown in Figure 6.8, persist. DIC measurements further confirm this, revealing horizontal bands of elevated strain aligned with the interfaces in M-0.75 and M-1. This indicates that the interface behaves as a mechanically distinct region during loading, preferentially accommodating deformation relative to the bulk material.

Under tensile loading of machined specimens, stress is more uniformly distributed across the interface, allowing interfacial defects to accommodate deformation without limiting load transfer or reducing strength. However, during continued deformation, damage initiation and growth become increasingly sensitive to interfacial quality. Localized void growth, debonding, or excessive stretching of partially diffused chains limit large plastic strains, reducing strain at break.

For M-1.25 and M-1.5, both conditions exhibit high ductility; however, yielding differs markedly. In M-1.25, yielding initiates through cross-band patterns concentrated near the center of the gauge section, whereas M-1.5 shows a typical angled yielding pattern along the maximum shear stress direction. This contrast indicates that, despite its high ductility, M-1.25 does not possess a fully bonded or mechanically homogeneous interface and interfacial heterogeneities continue to influence deformation.

Comparisons between machined and non-machined samples at 0.75 and 1 mm layer heights further support the dominant role of interface notches in damage initiation. Machined samples consistently exhibit higher strain at break despite the presence of residual interfacial voids. This confirms that notch-induced strain concentrations, rather than bonding defects alone, govern premature failure, while interlayer bonding primarily influences the extent of strength reduction.

The coupled influence of notch severity and interlayer bonding underscores the necessity of considering multiple mechanisms when evaluating mechanical performance and developing predictive models for MEAM parts.

6.6 Conclusion

This study demonstrates that the mechanical performance of MEAM parts is governed by the coupled effects of interface notch geometry and interlayer bonding quality. Using single-layer PETG tensile samples printed via FGF, layer height was deliberately varied to systematically modulate both notch severity and bonding quality, enabling a direct investigation of their interplay. DIC analysis revealed that increasing layer height amplifies interface notch severity

while simultaneously enhancing interlayer bonding due to larger extrudate dimensions and reduced cooling rates. While fracture consistently initiates at interface notches, the resulting strength reduction depends on the balance between notch geometry and adjacent bonding quality. Notably, a less severe notch can lead to greater strength loss when interlayer bonding is weaker, highlighting a competing effect and identifying an intermediate layer height as the optimal condition for maximum mechanical performance.

Removal of interface notches largely restored ultimate tensile strength, yet full recovery of strain at break was only achieved in samples with well-developed interlayer bonds. This observation challenges the conventional reliance on ultimate strength as the primary indicator of interlayer bonding, suggesting that strain at break is a more sensitive metric for assessing bonding quality. Crack propagation behaviour further underscores this interdependence: in samples with stronger bonding, cracks extend from the interface into the bulk, whereas in weaker interfaces, failure mainly remains confined to interlayer regions.

By revealing the coupled roles of interface notches and interlayer bonding quality, this work establishes the need for a multi-mechanism framework to understand mechanical performance in MEAM. These findings provide essential guidance for predictive modelling, process optimization, and the design of robust, high-performance polymer extrusion additive manufacturing components.

CONCLUSION

As polymer-based material extrusion additive manufacturing (MEAM) transitions from a prototyping tool to a platform for high-performance, end-use applications, a fundamental understanding of the mechanisms governing mechanical performance becomes increasingly critical. The primary objective of this thesis was to elucidate the underlying mechanisms affected by processing parameters that control the mechanical behaviour of MEAM parts.

To achieve this objective, the mechanical performance of printed parts was investigated using a mechanistically driven framework that explicitly addresses contributions often treated independently or overlooked in the existing literature. This work investigated the influence of processing parameters on individual extrudate properties, as well as multiple contributors to interlayer performance. These included the role of interface notches arising from extrudate geometry, interlayer bonding quality with a particular emphasis on a novel approach to evaluating intimate contact, and, critically, the coupled effects and interplay between interface notch severity and bonding quality. The following sections summarize the key conclusions and original contributions derived from this work.

1. Extrusion rate significantly alters the intrinsic properties of PLA extrudates, particularly impacting ductility and toughness. PLA filaments were extruded at varying rates and characterized independently to assess changes in morphology, microstructure, and mechanical performance. Higher extrusion rates increased die swell, surface roughness, and crystallinity, and resulted in an 85% reduction in toughness and ductility. These effects were non-linear, with a pronounced change observed at the highest extrusion rate. When deposited as printed parts, die swell and surface roughness were largely suppressed; however, a substantial reduction in ductility (65%) persisted, with DIC confirming more uniform strain distribution in printed samples at lower extrusion rates. Relative changes in crystallinity were mirrored in the printed parts, potentially explaining the observed reduction in toughness.

Original contribution: This work provides one of the first investigations of how extrusion rate modifies extrudate properties and how these changes transfer to printed parts. Unlike prior research focused on nozzle temperature or annealing, the role of extrusion rate was explored. Building on independent characterization of extrudate properties, the study establishes a methodology to assess whether and how these properties are transferred to printed-part behaviour. This approach highlights the need to incorporate extrudate-level characteristics into predictive models and process optimization for material extrusion additive manufacturing.

2. Interface notches arising from extrudate geometry are the primary source of strength reduction and anisotropy in both small and large scale additive manufacturing. PETG samples were produced at small and large scales via FFF and FGF and were tested in both extrudate and transverse directions, with and without naturally formed interface notches. Tensile testing and DIC revealed that these notches act as strain concentrators, reducing ultimate stress (up to 70% for large-scale and 40% for small-scale samples) and inducing brittle failure. Removing the notches restored isotropic behaviour and full bond strength across different extrudate orientations, demonstrating that the observed anisotropy is primarily due to geometric stress concentrators rather than incomplete interlayer bonding. The strain field around the notches was experimentally quantified and corroborated with mesoscale FEA validated against DIC, revealing that notch severity increases with layer height and that the magnitude of strain concentration is strongly influenced by the notch root geometry. These findings underscore the critical importance of controlling extrudate geometry during printing to optimize mechanical performance.

Original contribution: A methodology was developed to decouple the effects of extrudate geometry from interlayer bonding in both small- and large-scale PETG parts, which was largely overlooked in previous studies. Performing the study at two scales using FFF and FGF revealed that strength reduction can vary widely for the same material based on extrudate geometry. High-

resolution DIC of single-layer large-scale tensile samples enabled experimental quantification of strain fields around interface notches for the first time. Accurate characterization of notch geometry, including root shape variations (curved vs. crack-like) with processing parameters, highlighted their influence on mechanical performance, which was further demonstrated using FEA to provide design guidance. These findings are broadly applicable to other thermoplastics and offer practical strategies for improving part performance through controlled extrudate shaping.

3. Apparent interlayer contact does not ensure complete intimate contact in MEAM, as interfacial microvoids persist under a wide range of processing conditions. PETG parts were printed under varying temperatures, print speeds, and layer heights. Direct experimental evidence of interfacial microvoids at layer interfaces was obtained using polarized optical microscopy and micro-computed tomography, demonstrating that apparent bonding areas between extrudates do not necessarily correspond to complete intimate contact. The extent of interfacial microvoid content was found to vary significantly with processing conditions. In-situ measurements further showed that the contact pressure generated during deposition also changes markedly as a function of print parameters. A general inverse relationship was observed between the measured contact pressure and the experimentally determined degree of intimate contact, although the exact underlying mechanisms governing this relationship remain unresolved. Experimental evaluation of conventional composite intimate contact models revealed that these models fail to capture the formation and persistence of interfacial microvoids in MEAM, highlighting fundamental limitations in their direct application to material extrusion processes.

Original contribution: This work provides the first direct visualization and quantitative assessment of interfacial microvoids in MEAM parts and demonstrates their systematic dependence on processing conditions. A novel, low-cost methodology was developed to measure contact pressure in situ during printing, enabling direct experimental access to a parameter previously

identified as critical for interlayer bond formation but rarely measured. Furthermore, this study presents a reassessment of widely used intimate contact models by experimentally testing their validity in the context of MEAM, showing that idealized assumptions of complete interfacial contact are not representative of real printing conditions and motivating the need for revised bonding frameworks that explicitly account for the development of intimate contact in material extrusion processes.

4. Interface notches and interlayer bonding quality interact in a coupled manner to govern mechanical performance. Single-layer PETG tensile samples tested in the transverse direction were used to systematically investigate the combined influence of interface notch severity and interlayer bonding quality. By varying the layer height, both notch geometry and bonding quality were deliberately modified. DIC measurements confirmed that increasing layer height leads to more severe interface notches while improving interlayer bonding. Consequently, mechanical performance did not vary monotonically with notch severity; instead, maximum performance was achieved at an intermediate condition where the competing effects of notch severity and bonding quality were optimally balanced. Crack propagation paths depended strongly on bonding quality, proceeding either along the interface or diverting into the bulk material. Removal of interface notches resulted in near-complete recovery of ultimate strength across all processing conditions; however, recovery of strain at break was only achieved when the interlayer bond was fully developed. In non-fully bonded cases, interfacial microvoids were observed, confirming their contribution to incomplete interlayer bonding and reduced ductility.

Original contribution: A deliberately designed experimental methodology was introduced in which layer height was selected as a controlling parameter to vary both interface notch severity and interlayer bonding quality, enabling direct investigation of their coupled effects—an interaction typically treated independently or overlooked in prior studies. This work challenges the conventional use of ultimate strength as the primary experimental metric for assessing

interlayer bonding quality, demonstrating that strain at break may provide a more sensitive indicator of bonding quality. By explicitly revealing the interdependence of geometric and bonding mechanisms, this study establishes the necessity of a multi-mechanism framework for understanding and modelling interlayer behaviour in MEAM, with direct implications for predictive modelling and process optimization strategies.

RECOMMENDATIONS

Based on the findings of this study, the following avenues for future work are suggested.

First, the development of integrated thermal, crystallization, and rheological models of the extrusion and deposition processes would enable more accurate prediction of extrudate property evolution under varying processing conditions, providing stronger links between process parameters and resulting part performance.

Further investigation of extrudate coalescence during deposition is also needed, with particular emphasis on understanding how interface notch formation evolves as a function of processing conditions and deposition history. To capture the strain fields induced by these interface notches with higher fidelity, more precise experimental techniques, such as electronic speckle pattern interferometry (ESPI), should be employed to improve upon the resolution and accuracy of DIC. Furthermore, in-situ or post-processing strategies should be explored to minimize interface notch severity and improve mechanical performance.

Regarding the theoretical modelling of interfacial voids, models such as capillary flow, mould-filling, or modified squeeze-flow should be applied. These theoretical frameworks are essential to predict and explain intimate contact formation in MEAM processes more accurately.

Finally, future work should focus on quantifying interlayer bonding quality and explicitly integrating it with interface notch effects, recognizing that bonding quality alters notch sensitivity and governs the coupled mechanical response of printed interfaces.

APPENDIX I

PUBLICATIONS AND CONFERENCES

Publications

1. Shokrollahi, M., Lampron, O., Dubé, M., & Tabiai, I. (2026). Extrudate-Level Analysis of Thermoplastic Properties in Material Extrusion Additive Manufacturing. *Progress in Additive Manufacturing*. (Submitted)

2. Shokrollahi, M., Restrepo Lopéz, S., Smith, A. W., Dubé, M., & Tabiai, I. (2026). Revisiting Intimate Contact Development in Material Extrusion Additive Manufacturing. *Additive Manufacturing*. (Submitted)

3. Shokrollahi, M., Smith, A. W., Dubé, M., & Tabiai, I. (2026). A Multi-Mechanism Perspective on Interlayer Behaviour in Material Extrusion Additive Manufacturing. *Rapid Prototyping Journal*. (Submitted)

4. Shokrollahi, M., Smith, A. W., Levy, A., Dubé, M., & Tabiai, I. (2025). Reassessing Anisotropy in 3D Printed Structures: The Role of Extrudate Geometry vs Interface Bonding. *Journal of Manufacturing Processes*, 149, 456–472. doi: 10.1016/j.jmapro.2025.05.070

5. Shokrollahi, M., Smith, A. W., Dubé, M., & Tabiai, I. (2025). Influence of interface notch geometry on the tensile behaviour of FGF-printed parts. *Journal of Achievements in Materials and Manufacturing Engineering*, 131, 17–25. doi: 10.5604/01.3001.0055.4368

6. Shokrollahi, M., Smith, A. W., Dubé, M., & Tabiai, I. (2022). Relative Contribution of Different Bonding Mechanisms During the FFF Process. *Proceedings of the Canadian International Conference on Composite Materials (CANCOM 2022)*.

Magazine Article

1. Tabiai, I., (2025). Impression 3D: Optimiser la science derrière la solidité. *Polymères Québec*, 3(2), 38–39.

Conferences

1. CSME-CFDSC-CSR – Canadian Society for Mechanical Engineering (CSME), the Computational Fluid Dynamics Society of Canada (CFDSC) and the Canadian Society of Rheology (CSR), International Congress. Oral presentation, 2025.

2. CASICAM – Casablanca International Conference on Additive Manufacturing. Paper and oral presentation, 2025.

3. CREPEC – Research Center for High Performance Polymer and Composite Systems, Annual and Student Colloquiums. Poster presentations, 2022, 2023, 2024, and 2025.
   (Awarded 1st place best poster presentation in 2022 and 2023)

4. CJWC – 13th Canada-Japan Workshop on Composites. Paper and oral presentation, 2023.

5. CANCOM – Canadian-International Conference on Composites. Paper and oral presentation, 2022.

APPENDIX II

TEMPERATURE CONTROL EXPERIMENT

Type K thermocouples, with a data acquisition frequency of 1 Hz, were embedded within a printed sheet as shown in Figure II-1(a). The sheet was then sanded using the procedure described earlier until the thermocouples were removed by sanding. A similar experiment was conducted during the machining process (Figure II-1(b)) using the parameters mentioned in Table 4.4 and was continued until the thermocouples were removed by the tool.

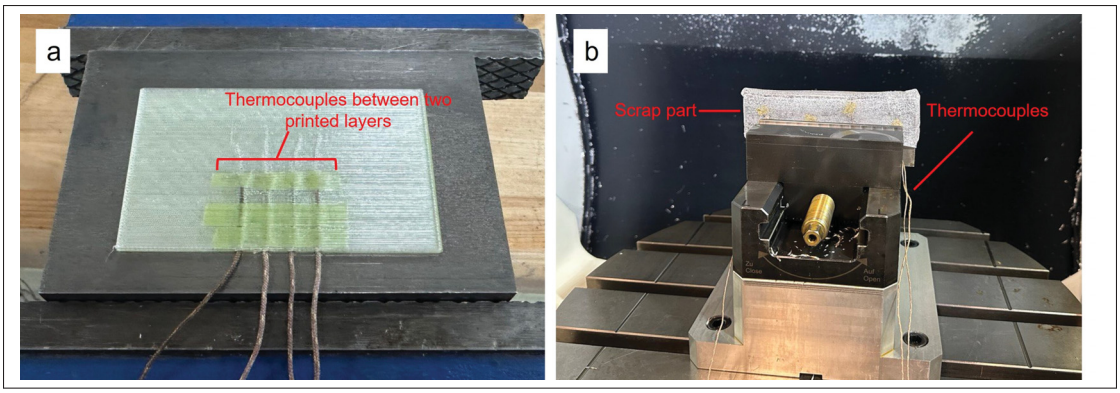

Figure-A II-1 Thermocouples embedded within scrap parts to record the temperature evolution during (a) sanding, (b) machining

The temperature variation observed during sanding ranged between room temperature and 60 °C (Figure II-2(a)), which is below the Tg. Intermittently removing debris and particles using an air compressor effectively prevented a significant increase in temperature during the sanding process. As illustrated in Figure II-2(b)), in the machining process for the large-scale samples, the part remained at room temperature throughout the entire process due to the continuous flow of coolant.

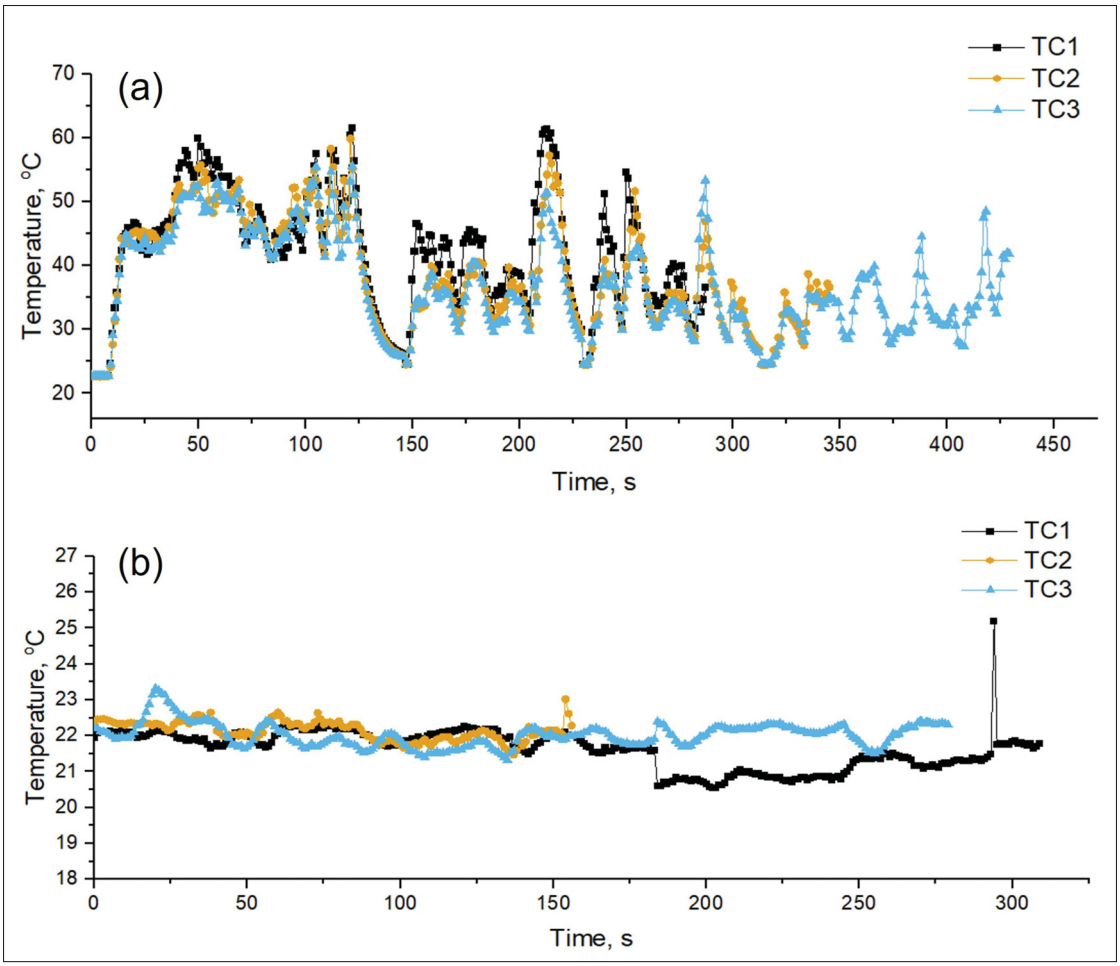

Figure-A II-2 Temperature recorded by the embedded thermocouples in (a) sanded part and (b) machined part. A more stable temperature during machining is due to the continuous use of coolant

APPENDIX III

NOTCH CHARACTERIZATION

In Figure III-1(a), the notch angle measurement procedure for the S-90-NM sample is depicted. Two circles are fitted to the curved openings of the notch angle, and tangents are drawn at their cross-sections. The angle between these tangents is considered as θ.

Figure III-1(b) illustrates the measurement of the notch root radius. A circle is fitted to the curved root of the notch using the Contact Angle plugin in ImageJ, and the radius of this circle represents the notch root radius.

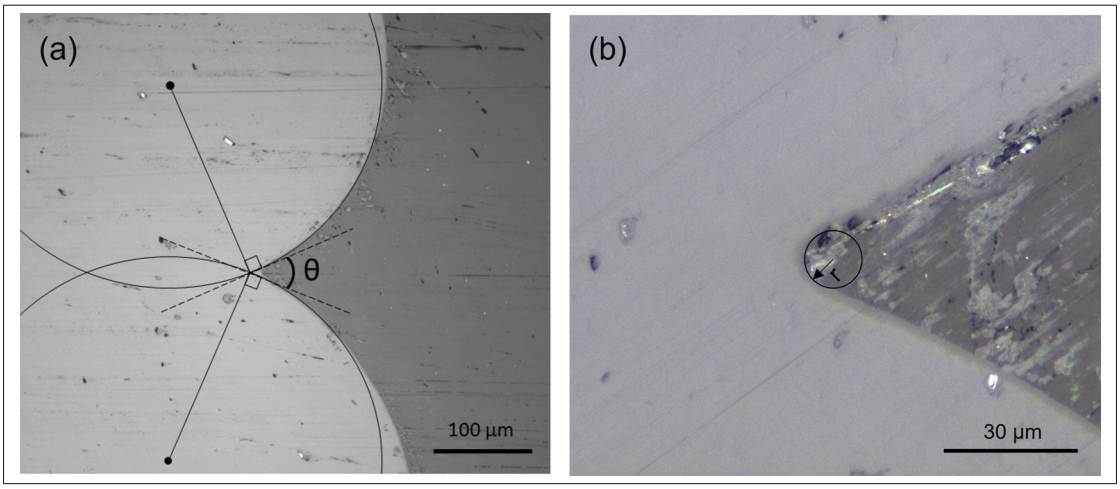

Figure-A III-1 Illustration of the procedure used to measure (a) θ and (b) r

APPENDIX IV

INTIMATE CONTACT CALCULATION

As shown in Figure IV-1(a), in the micro-CT images, microvoids at each layer were projected onto the X–Y plane. The areas of the microvoid regions were measured and subtracted from the total plane area, and dividing the remaining contact area by the total area yielded the D_{ic} value. In the 2D POM images illustrated in Figure IV-1(b), a line was drawn along the interface, and the lengths of the microvoids were subtracted from the total line length. The remaining contact length divided by the total line length was used to calculate D_{ic}.

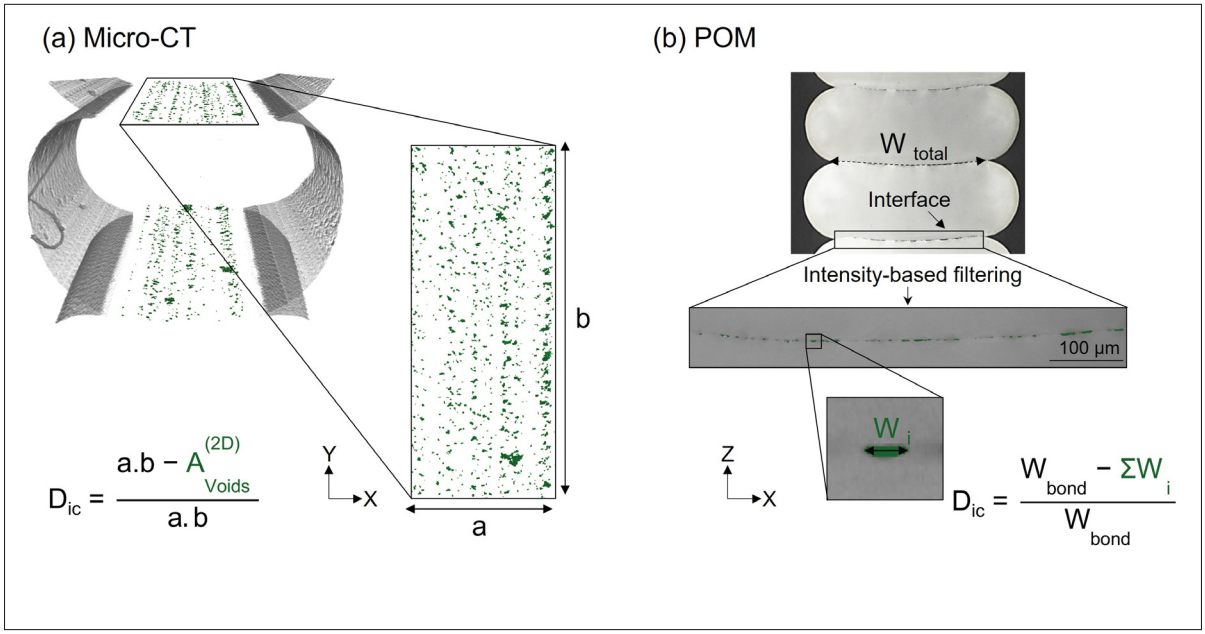

Figure-A IV-1 Methodology to quantify the degree of intimate contact. (a) Micro-CT images: microvoids at each layer are projected onto the X–Y plane, and the remaining contact area (total area minus microvoid regions) is divided by the total area to calculate D_{ic}. (b) 2D POM images: a line is drawn along the interface, microvoid lengths are subtracted, and the remaining contact length divided by the total line length yields D_{ic}

BIBLIOGRAPHY

Abbott, A. C., Tandon, G. P., Bradford, R. L., Koerner, H. & Baur, J. W. (2018). Process-structure-property effects on ABS bond strength in fused filament fabrication. *Additive Manufacturing*, 19, 29–38. doi: 10.1016/j.addma.2017.11.002.

Akhoundi, B. & Behravesh, A. H. (2019). Effect of Filling Pattern on the Tensile and Flexural Mechanical Properties of FDM 3D Printed Products. *Experimental Mechanics*, 59(6), 883–897. doi: 10.1007/s11340-018-00467-y.

Al-Maharma, A. Y., Patil, S. P. & Markert, B. (2020). Effects of porosity on the mechanical properties of additively manufactured components: a critical review. *Materials Research Express*, 7(12), 122001. doi: 10.1088/2053-1591/abcc5d. Publisher: IOP Publishing.

Aliheidari, N., Christ, J., Tripuraneni, R., Nadimpalli, S. & Ameli, A. (2018). Interlayer adhesion and fracture resistance of polymers printed through melt extrusion additive manufacturing process. *Materials & Design*, 156, 351–361. doi: 10.1016/j.matdes.2018.07.001.

Allum, J., Gleadall, A. & Silberschmidt, V. V. (2020a). Fracture of 3D-printed polymers: Crucial role of filament-scale geometric features. *Engineering Fracture Mechanics*, 224, 106818. doi: 10.1016/j.engfracmech.2019.106818.

Allum, J., Gleadall, A. & Silberschmidt, V. V. (2020b). Fracture of 3D-printed micro-tensile specimens: filament-scale geometry-induced anisotropy. *Procedia Structural Integrity*, 28, 591–601. doi: 10.1016/j.prostr.2020.10.069.

Allum, J., Moetazedian, A., Gleadall, A. & Silberschmidt, V. V. (2020c). Interlayer bonding has bulk-material strength in extrusion additive manufacturing: New understanding of anisotropy. *Additive Manufacturing*, 34, 101297. doi: 10.1016/j.addma.2020.101297.

Allum, J., Moetazedian, A., Gleadall, A. & Silberschmidt, V. V. (2021). Discussion on the microscale geometry as the dominant factor for strength anisotropy in material extrusion additive manufacturing. *Additive Manufacturing*, 48, 102390. doi: 10.1016/j.addma.2021.102390.

Allum, J., Moetazedian, A., Gleadall, A., Mitchell, N., Marinopoulos, T., McAdam, I., Li, S. & Silberschmidt, V. V. (2023). Extra-wide deposition in extrusion additive manufacturing: A new convention for improved interlayer mechanical performance. *Additive Manufacturing*, 61, 103334. doi: 10.1016/j.addma.2022.103334.

Anderegg, D. A., Bryant, H. A., Ruffin, D. C., Skrip, S. M., Fallon, J. J., Gilmer, E. L. & Bortner, M. J. (2019). In-situ monitoring of polymer flow temperature and pressure in extrusion based additive manufacturing. *Additive Manufacturing*, 26, 76–83. doi: 10.1016/j.addma.2019.01.002.

Arif, M. F., Alhashmi, H., Varadarajan, K. M., Koo, J. H., Hart, A. J. & Kumar, S. (2020). Multifunctional performance of carbon nanotubes and graphene nanoplatelets reinforced PEEK composites enabled via FFF additive manufacturing. *Composites Part B: Engineering*, 184, 107625. doi: 10.1016/j.compositesb.2019.107625.

ASTM International. (2014). ASTM D638-14: Standard Test Method for Tensile Properties of Plastics. Retrieved from: http://www.astm.org/cgi-bin/resolver.cgi?D638-14.

ASTM International. (2018). ASTM D882-18: Standard Test Method for Tensile Properties of Thin Plastic Sheeting. Retrieved from: https://www.astm.org/d0882-18.html.

Awaja, F. (2016). Autohesion of polymers. *Polymer*, 97, 387–407. doi: 10.1016/j.polymer.2016.05.043.

Bakhtiari, H., Aamir, M. & Tolouei-Rad, M. (2023). Effect of 3D Printing Parameters on the Fatigue Properties of Parts Manufactured by Fused Filament Fabrication: A Review. *Applied Sciences*, 13(2), 904. doi: 10.3390/app13020904. Publisher: Multidisciplinary Digital Publishing Institute.

Bakrani Balani, S., Chabert, F., Nassiet, V. & Cantarel, A. (2019). Influence of printing parameters on the stability of deposited beads in fused filament fabrication of poly(lactic) acid. *Additive Manufacturing*, 25, 112–121. doi: 10.1016/j.addma.2018.10.012.

Balta, E. C. & Altınkaynak, A. (2022). Numerical and experimental analysis of bead cross-sectional geometry in fused filament fabrication. *Rapid Prototyping Journal*, 28(10), 1882–1894. doi: 10.1108/RPJ-09-2021-0255. Publisher: Emerald Publishing Limited.

Barocio, E., Brenken, B., Favaloro, A. & Pipes, R. B. (2022). Interlayer fusion bonding of semi-crystalline polymer composites in extrusion deposition additive manufacturing. *Composites Science and Technology*, 230, 109334. doi: 10.1016/j.compscitech.2022.109334.

Bartolai, J., Simpson, T. W. & Xie, R. (2018). Predicting strength of additively manufactured thermoplastic polymer parts produced using material extrusion. *Rapid Prototyping Journal*, 24(2), 321–332. doi: 10.1108/RPJ-02-2017-0026.

Basgul, C., Thieringer, F. M. & Kurtz, S. M. (2021). Heat transfer-based non-isothermal healing model for the interfacial bonding strength of fused filament fabricated polyetheretherketone. *Additive Manufacturing*, 46, 102097. doi: 10.1016/j.addma.2021.102097.

Bechtel, S., Meisberger, M., Klein, S., Heib, T., Quirin, S. & Herrmann, H.-G. (2020). Estimation of the adhesion interface performance in aluminum-PLA joints by thermographic monitoring of the material extrusion process. *Materials*, 13(15), 3371. doi: 10.3390/ma13153371. Publisher: MDPI.

Bellehumeur, C., Li, L., Sun, Q. & Gu, P. (2004). Modeling of Bond Formation Between Polymer Filaments in the Fused Deposition Modeling Process. *Journal of Manufacturing Processes*, 6(2), 170–178. doi: 10.1016/S1526-6125(04)70071-7.

Beníček, L., Vašina, M. & Hrbáček, P. (2025). Influence of 3D Printing Conditions on Physical–Mechanical Properties of Polymer Materials. *Polymers*, 17(1), 43. doi: 10.3390/polym17010043. Publisher: Multidisciplinary Digital Publishing Institute.

Bernagozzi, G., Battegazzore, D., Arrigo, R. & Frache, A. (2023). Optimizing the Rheological and Thermal Behavior of Polypropylene-Based Composites for Material Extrusion Additive Manufacturing Processes. *Polymers*, 15(10), 2263. doi: 10.3390/polym15102263. Publisher: Multidisciplinary Digital Publishing Institute.

Bhardwaj, N., Henein, H. & Wolfe, T. (2022). Mechanical properties of thermoplastic polymers in fused filament fabrication (FFF). *The Canadian Journal of Chemical Engineering*, 100(11), 3174–3183. doi: 10.1002/cjce.24562. _eprint: https://onlinelibrary.wiley.com/doi/pdf/10.1002/cjce.24562.

Billah, K. M. M., Lorenzana, F. A. R., Martinez, N. L., Wicker, R. B. & Espalin, D. (2020). Thermomechanical characterization of short carbon fiber and short glass fiber-reinforced ABS used in large format additive manufacturing. *Additive Manufacturing*, 35, 101299. doi: 10.1016/j.addma.2020.101299.

Bist, A., Dobriyal, R., Gwalwanshi, M. & Avikal, S. (2022). Influence of layer height and print speed on the mechanical properties of 3D-printed ABS. *AIP Conference Proceedings*, 2481(1), 020012. doi: 10.1063/5.0107304. Publisher: AIP Publishing.

Bond3D. (2025). Bond3D - High Performance 3D Printing Technology. Retrieved from: https://www.bond3d.com/.

Bouzaglou, O., Golan, O. & Lachman, N. (2023). Process Design and Parameters Interaction in Material Extrusion 3D Printing: A Review. *Polymers*, 15(10), 2280. doi: 10.3390/polym15102280. Publisher: Multidisciplinary Digital Publishing Institute.

Brenken, B., Barocio, E., Favaloro, A., Kunc, V. & Pipes, R. B. (2018). Fused filament fabrication of fiber-reinforced polymers: A review. *Additive Manufacturing*, 21, 1–16. doi: 10.1016/j.addma.2018.01.002.

Buj-Corral, I., Tejo-Otero, A. & Fenollosa-Artés, F. (2021). Use of FDM Technology in Healthcare Applications: Recent Advances. In Dave, H. K. & Davim, J. P. (Eds.), *Fused Deposition Modeling Based 3D Printing* (pp. 277–297). Cham: Springer International Publishing. doi: 10.1007/978-3-030-68024-4_15.

Castro-Casado, D. (2021). Chemical treatments to enhance surface quality of FFF manufactured parts: a systematic review. *Progress in Additive Manufacturing*, 6(2), 307–319. doi: 10.1007/s40964-020-00163-1.

Chai, Y., Li, R. W., Perriman, D. M., Chen, S., Qin, Q.-H. & Smith, P. N. (2018). Laser polishing of thermoplastics fabricated using fused deposition modelling. *The International Journal of Advanced Manufacturing Technology*, 96(9), 4295–4302. doi: 10.1007/s00170-018-1901-5.

CNC Kitchen. [Retrieved January 4, 2026]. (2019). The influence of layer height on the strength of FDM 3D prints. Retrieved from: https://www.cnckitchen.com/blog/the-influence-of-layer-height-on-the-strength-of-fdm-3d-prints.

Coasey, K., Hart, K. R., Wetzel, E., Edwards, D. & Mackay, M. E. (2020). Nonisothermal welding in fused filament fabrication. *Additive Manufacturing*, 33, 101140. doi: 10.1016/j.addma.2020.101140.

Colon, A. R., Kazmer, D. O., Peterson, A. M. & Seppala, J. E. (2023). Characterization of die-swell in thermoplastic material extrusion. *Additive Manufacturing*, 73, 103700. doi: 10.1016/j.addma.2023.103700.

Comelli, C. A., Davies, R., van der Pol, H. & Ghita, O. (2022). PEEK filament characteristics before and after extrusion within fused filament fabrication process. *Journal of Materials Science*, 57(1), 766–788. doi: 10.1007/s10853-021-06652-0.

Conway, K. M. & Pataky, G. J. (2019). Crazing in additively manufactured acrylonitrile butadiene styrene. *Engineering Fracture Mechanics*, 211, 114–124. doi: 10.1016/j.engfracmech.2019.02.020. Publisher: Elsevier.

Coogan, T. J. & Kazmer, D. O. (2017a). Healing simulation for bond strength prediction of FDM. *Rapid Prototyping Journal*, 23(3), 551–561. doi: 10.1108/RPJ-03-2016-0051.

Coogan, T. J. & Kazmer, D. O. (2018). In-line rheological monitoring of fused deposition modeling. *Journal of Rheology*, 63(1), 141–155. doi: 10.1122/1.5054648. Publisher: The Society of Rheology.

Coogan, T. J. & Kazmer, D. O. (2019). Modeling of interlayer contact and contact pressure during fused filament fabrication. *Journal of Rheology*, 63(4), 655–672. doi: 10.1122/1.5093033.

Coogan, T. J. & Kazmer, D. O. (2020). Prediction of interlayer strength in material extrusion additive manufacturing. *Additive Manufacturing*, 35, 101368. doi: 10.1016/j.addma.2020.101368.

Coogan, T. J. & Kazmer, D. O. (2017b). Bond and part strength in fused deposition modeling. *Rapid Prototyping Journal*, 23(2), 414–422. doi: 10.1108/RPJ-03-2016-0050.

Coppola, B., Cappetti, N., Di Maio, L., Scarfato, P. & Incarnato, L. (2018). 3D Printing of PLA/clay Nanocomposites: Influence of Printing Temperature on Printed Samples Properties. *Materials*, 11(10), 1947. doi: 10.3390/ma11101947. Publisher: Multidisciplinary Digital Publishing Institute.

Costa, S. F., Duarte, F. M. & Covas, J. A. (2017). Estimation of filament temperature and adhesion development in fused deposition techniques. *Journal of Materials Processing Technology*, 245, 167–179. doi: 10.1016/j.jmatprotec.2017.02.026. Publisher: Elsevier.

Cox, W. P. & Merz, E. H. (1958). Correlation of dynamic and steady flow viscosities. *Journal of Polymer Science*, 28(118), 619–622. doi: 10.1002/pol.1958.1202811812. _eprint: https://onlinelibrary.wiley.com/doi/pdf/10.1002/pol.1958.1202811812.

Cuan-Urquizo, E., Barocio, E., Tejada-Ortigoza, V., Pipes, R. B., Rodriguez, C. A. & Roman-Flores, A. (2019). Characterization of the Mechanical Properties of FFF Structures and Materials: A Review on the Experimental, Computational and Theoretical Approaches. *Materials*, 12(6), 895. doi: 10.3390/ma12060895. Publisher: Multidisciplinary Digital Publishing Institute.

Das, A., Gilmer, E. L., Biria, S. & Bortner, M. J. (2021). Importance of Polymer Rheology on Material Extrusion Additive Manufacturing: Correlating Process Physics to Print Properties. *ACS Applied Polymer Materials*, 3(3), 1218–1249. doi: 10.1021/acsapm.0c01228. Publisher: American Chemical Society.

DataHorizzon Research. [Retrieved November 11, 2025]. (2024). Fused Filament Fabrication (FFF) 3D Printer Market Size, Growth & Analysis Report - 2033. Retrieved from: https://datahorizzonresearch.com/fused-filament-fabricationfff-3d-printer-market-34349.

de Gennes, P. G. (1971). Reptation of a Polymer Chain in the Presence of Fixed Obstacles. *The Journal of Chemical Physics*, 55(2), 572–579. doi: 10.1063/1.1675789.

De Rosa, S., Tammaro, D. & D'Avino, G. (2023). Experimental and Numerical Investigation of the Die Swell in 3D Printing Processes. *Micromachines*, 14(2), 329. doi: 10.3390/mi14020329. Publisher: Multidisciplinary Digital Publishing Institute.

Deshpande, A., Ravi, A., Kusel, S., Churchwell, R. & Hsu, K. (2019). Interlayer thermal history modification for interface strength in fused filament fabricated parts. *Progress in Additive Manufacturing*, 4(1), 63–70. doi: 10.1007/s40964-018-0063-1. Publisher: Springer.

Dey, A., Roan Eagle, I. N. & Yodo, N. (2021). A Review on Filament Materials for Fused Filament Fabrication. *Journal of Manufacturing and Materials Processing*, 5(3), 69. doi: 10.3390/jmmp5030069. Publisher: Multidisciplinary Digital Publishing Institute.

Ding, S., Zou, B., Zhuang, Y., Wang, X., Li, L. & Liu, J. (2023). Hybrid layout and additive manufacturing of continuous carbon/glass fibers reinforced composites, and its effect on mechanical properties. *Composite Structures*, 319, 117133. doi: 10.1016/j.compstruct.2023.117133.

Domenech, T., Ovlaque, P., Trolez, Y., Olivier, D., Bujeau, B., Charlon, S. & Soulestin, J. (2024). Competition between bead boundary fusion and crystallization kinetics in material extrusion-based additive manufacturing. *Additive Manufacturing*, 92, 104395. doi: 10.1016/j.addma.2024.104395.

Domenech, T., Ovlaque, P., Trolez, Y., Olivier, D., Bujeau, B., Charlon, S. & Soulestin, J. (2025). How impactful is die swell in material extrusion-based additive manufacturing of thermoplastic polymers. *Progress in Additive Manufacturing*, 10(12), 11393–11404. doi: 10.1007/s40964-025-01293-0.

Doshi, M., Mahale, A., Kumar Singh, S. & Deshmukh, S. (2022). Printing parameters and materials affecting mechanical properties of FDM-3D printed Parts: Perspective and prospects. *Materials Today: Proceedings*, 50, 2269–2275. doi: 10.1016/j.matpr.2021.10.003.

Doyle, L., García-Molleja, J., Fernández-Blázquez, J. P. & González, C. (2025). Unraveling the Print–Structure–Property Relationships in the FFF of PEEK: A Critical Assessment of Print Parameters. *Polymers*, 17(11), 1444. doi: 10.3390/polym17111444.

D'Amico, A. & Peterson, A. M. (2018). An adaptable FEA simulation of material extrusion additive manufacturing heat transfer in 3D. *Additive Manufacturing*, 21, 422–430. doi: 10.1016/j.addma.2018.02.021.

Eiliat, H. & Urbanic, J. (2018). Visualizing, analyzing, and managing voids in the material extrusion process. *The International Journal of Advanced Manufacturing Technology*, 96(9), 4095–4109. doi: 10.1007/s00170-018-1820-5.

Faes, M., Ferraris, E. & Moens, D. (2016). Influence of Inter-layer Cooling time on the Quasi-static Properties of ABS Components Produced via Fused Deposition Modelling. *Procedia CIRP*, 42, 748–753. doi: 10.1016/j.procir.2016.02.313.

Farahani, M., Bagheri, R. & Marouf, B. (2023). Investigation on the onset and progress of stress whitening in polypropylene using digital image processing. *Polymer Bulletin*, 81, 1–18. doi: 10.1007/s00289-023-05045-4.

Fontana, L., Giubilini, A., Arrigo, R., Malucelli, G. & Minetola, P. (2022). Characterization of 3D Printed Polylactic Acid by Fused Granular Fabrication through Printing Accuracy, Porosity, Thermal and Mechanical Analyses. *Polymers*, 14(17), 3530. doi: 10.3390/polym14173530. Publisher: Multidisciplinary Digital Publishing Institute.

Gao, G., Xu, F., Xu, J., Tang, G. & Liu, Z. (2022). A Survey of the Influence of Process Parameters on Mechanical Properties of Fused Deposition Modeling Parts. *Micromachines*, 13(4), 553. doi: 10.3390/mi13040553. Publisher: Multidisciplinary Digital Publishing Institute.

Gao, X., Qi, S., Kuang, X., Su, Y., Li, J. & Wang, D. (2021). Fused filament fabrication of polymer materials: A review of interlayer bond. *Additive Manufacturing*, 37, 101658. doi: 10.1016/j.addma.2020.101658.

Geng, P., Zhao, J., Wu, W., Ye, W., Wang, Y., Wang, S. & Zhang, S. (2019). Effects of extrusion speed and printing speed on the 3D printing stability of extruded PEEK filament. *Journal of Manufacturing Processes*, 37, 266–273. doi: 10.1016/j.jmapro.2018.11.023.

Ghorbani, J., Koirala, P., Shen, Y.-L. & Tehrani, M. (2022). Eliminating voids and reducing mechanical anisotropy in fused filament fabrication parts by adjusting the filament extrusion rate. *Journal of Manufacturing Processes*, 80, 651–658. doi: 10.1016/j.jmapro.2022.06.026.

Gilmer, E. L., Anderegg, D., Gardner, J. M., Sauti, G., Siochi, E. J., McKnight, S. H., Dillard, D. A., McIlroy, C. & Bortner, M. J. (2021). Temperature, diffusion, and stress modeling in filament extrusion additive manufacturing of polyetherimide: An examination of the influence of processing parameters and importance of modeling assumptions. *Additive Manufacturing*, 48, 102412. doi: 10.1016/j.addma.2021.102412.

Goh, G. D., Wong, K. K., Tan, N., Seet, H. L. & Nai, M. L. S. (2024). Large-format additive manufacturing of polymers: a review of fabrication processes, materials, and design. *Virtual and Physical Prototyping*, 19(1), e2336160. doi: 10.1080/17452759.2024.2336160. Publisher: Taylor & Francis _eprint: https://doi.org/10.1080/17452759.2024.2336160.

Gonabadi, H., Zamani Miandashti, Z. & Oila, A. (2025). Micro-mechanical characterisation of 3D-printed composites via nano-indentation and finite-element homogenization techniques: overcoming challenges in orthotropic property measurement. *Progress in Additive Manufacturing*, 10(10), 8465–8488. doi: 10.1007/s40964-025-01131-3.

Gonzalez-Gutierrez, J., Cano, S., Schuschnigg, S., Kukla, C., Sapkota, J. & Holzer, C. (2018). Additive Manufacturing of Metallic and Ceramic Components by the Material Extrusion of Highly-Filled Polymers: A Review and Future Perspectives. *Materials*, 11(5), 840. doi: 10.3390/ma11050840. Publisher: Multidisciplinary Digital Publishing Institute.

Grand View Research. (2024). Fused Deposition Modeling 3D Printing Market Report, 2030. Retrieved from: https://www.grandviewresearch.com/industry-analysis/fused-deposition-modeling-3d-printing-market-report.

Grouve, W. J. B., Warnet, L. L., Rietman, B., Visser, H. A. & Akkerman, R. (2013). Optimization of the tape placement process parameters for carbon–PPS composites. *Composites Part A: Applied Science and Manufacturing*, 50, 44–53. doi: 10.1016/j.compositesa.2013.03.003.

Gurrala, P. K. & Regalla, S. P. (2014). Part strength evolution with bonding between filaments in fused deposition modelling: This paper studies how coalescence of filaments contributes to the strength of final FDM part. *Virtual and Physical Prototyping*, 9(3), 141–149. doi: 10.1080/17452759.2014.913400. Publisher: Taylor & Francis _eprint: https://doi.org/10.1080/17452759.2014.913400.

G. Rocha, V., Saiz, E., S. Tirichenko, I. & García-Tuñón, E. (2020). Direct ink writing advances in multi-material structures for a sustainable future. *Journal of Materials Chemistry A*, 8(31), 15646–15657. doi: 10.1039/D0TA04181E. Publisher: Royal Society of Chemistry.

Han, P., Tofangchi, A., Deshpande, A., Zhang, S. & Hsu, K. (2019). An approach to improve interface healing in FFF-3D printed Ultem 1010 using laser pre-deposition heating. *Procedia Manufacturing*, 34, 672–677. doi: 10.1016/j.promfg.2019.06.195.

Han, P., Torabnia, S., Riyad, M. F., Thippanna, V., Song, K. & Hsu, K. (2025). In-process laser heating for mechanical strength improvement of FFF-printed PEEK. *Progress in Additive Manufacturing*, 10(5), 3729–3738. doi: 10.1007/s40964-024-00833-4.

Hart, K. R., Dunn, R. M., Sietins, J. M., Hofmeister Mock, C. M., Mackay, M. E. & Wetzel, E. D. (2018). Increased fracture toughness of additively manufactured amorphous thermoplastics via thermal annealing. *Polymer*, 144, 192–204. doi: 10.1016/j.polymer.2018.04.024.

Hart, K. R., Dunn, R. M. & Wetzel, E. D. (2020). Increased fracture toughness of additively manufactured semi-crystalline thermoplastics via thermal annealing. *Polymer*, 211, 123091. doi: 10.1016/j.polymer.2020.123091.

Hassanifard, S. & Behdinan, K. (2024). Impact of Rheology-Based Optimum Parameters on Enhancing the Mechanical Properties and Fatigue of Additively Manufactured Acrylonitrile–Butadiene–Styrene/Graphene Nanoplatelet Composites. *Polymers*, 16(9), 1273. doi: 10.3390/polym16091273.

He, L., Chow, W. T. & Li, H. (2020). Effects of interlayer notch and shear stress on interlayer strength of 3D printed cement paste. *Additive Manufacturing*, 36, 101390. doi: 10.1016/j.addma.2020.101390.

Heidari-Rarani, M., Rafiee-Afarani, M. & Zahedi, A. M. (2019). Mechanical characterization of FDM 3D printing of continuous carbon fiber reinforced PLA composites. *Composites Part B: Engineering*, 175, 107147. doi: 10.1016/j.compositesb.2019.107147.

Heller, B. P., Smith, D. E. & Jack, D. A. (2016). Effects of extrudate swell and nozzle geometry on fiber orientation in Fused Filament Fabrication nozzle flow. *Additive Manufacturing*, 12, 252–264. doi: 10.1016/j.addma.2016.06.005.

Hill, N. & Haghi, M. (2014). Deposition direction-dependent failure criteria for fused deposition modeling polycarbonate. *Rapid Prototyping Journal*, 20(3), 221–227. doi: 10.1108/RPJ-04-2013-0039.

Issametova, M., Martyushev, N. V., Zhastalap, A., Sabirova, L. B., Assemgul, U., Tursynbayeva, A. & Abilezova, G. (2024). Determination of Residual Stresses in 3D-Printed Polymer Parts. *Polymers*, 16(14), 2067. doi: 10.3390/polym16142067.

Jaisingh Sheoran, A. & Kumar, H. (2020). Fused Deposition modeling process parameters optimization and effect on mechanical properties and part quality: Review and reflection on present research. *Materials Today: Proceedings*, 21, 1659–1672. doi: 10.1016/j.matpr.2019.11.296.

Jeon, S., Park, S. J., Moon, S. K. & Yang, D. (2025). Enhanced mechanical properties and reduced anisotropy of material extrusion-manufactured short carbon fibre-reinforced plastic via cold isostatic pressing. *Virtual and Physical Prototyping*, 20(1), e2499934. doi: 10.1080/17452759.2025.2499934. Publisher: Taylor & Francis.

Jin, Y.-a., He, Y., Xue, G.-h. & Fu, J.-z. (2015). A parallel-based path generation method for fused deposition modeling. *The International Journal of Advanced Manufacturing Technology*, 77(5), 927–937. doi: 10.1007/s00170-014-6530-z.

JuggerBot 3D. [Retrieved January 3, 2026]. (2023). Fused Filament Fabrication (FFF) vs. Fused Granulate Fabrication (FGF). Retrieved from: https://juggerbot3d.com/fff-vs-fgf/.

Kantaros, A., Katsantoni, M., Ganetsos, T. & Petrescu, N. (2025). The Evolution of Thermoplastic Raw Materials in High-Speed FFF/FDM 3D Printing Era: Challenges and Opportunities. *Materials*, 18(6), 1220. doi: 10.3390/ma18061220.

Kechagias, J. & Zaoutsos, S. (2024). Effects of 3D-printing processing parameters on FFF parts' porosity: outlook and trends. *Materials and Manufacturing Processes*, 39(13), 1605–1624. doi: 10.1080/10426914.2024.2304843. Publisher: Taylor & Francis.

Khan, S., Joshi, K. & Deshmukh, S. (2022). A comprehensive review on effect of printing parameters on mechanical properties of FDM printed parts. *Materials Today: Proceedings*, 50, 2119–2127. doi: 10.1016/j.matpr.2021.09.433.

Kim, S. K., Kazmer, D. O., Colon, A. R., Coogan, T. J. & Peterson, A. M. (2020). Non-Newtonian modeling of contact pressure in fused filament fabrication. *Journal of Rheology*, 65(1), 27–42. doi: 10.1122/8.0000052. Publisher: The Society of Rheology.

Kishore, V., Ajinjeru, C., Nycz, A., Post, B., Lindahl, J., Kunc, V. & Duty, C. (2017). Infrared preheating to improve interlayer strength of big area additive manufacturing (BAAM) components. *Additive Manufacturing*, 14, 7–12. doi: 10.1016/j.addma.2016.11.008. Publisher: Elsevier.

Krishnanand & Taufik, M. (2021). Fused Filament Fabrication (FFF) Based 3D Printer and Its Design: A Review. *Advanced Manufacturing Systems and Innovative Product Design*, pp. 497–505. doi: 10.1007/978-981-15-9853-1_41.

Krishnanand, Singh, D., Singh, M. P. & Shrivastava, Y. (2025). Surface roughness investigation of 3D printed parts via in-situ pellet-filament co-extrusion process. *Materials and Manufacturing Processes*, 40(8), 1029–1048. doi: 10.1080/10426914.2025.2487275. Publisher: Taylor & Francis.

Kumar, V., Alwekar, S. P., Kunc, V., Cakmak, E., Kishore, V., Smith, T., Lindahl, J., Vaidya, U., Blue, C., Theodore, M., Kim, S. & Hassen, A. A. (2021). High-performance molded composites using additively manufactured preforms with controlled fiber and pore morphology. *Additive Manufacturing*, 37, 101733. doi: 10.1016/j.addma.2020.101733.

Kundurthi, S., Tran, F., Chen, S., Mapkar, J. & Haq, M. (2023). Bead geometry–induced stress concentration factors in material extrusion polymer additive manufacturing. *Rapid Prototyping Journal*, 29(7), 1438–1452. doi: 10.1108/RPJ-11-2022-0404.

Kuznetsov, V. E., Solonin, A. N., Urzhumtsev, O. D., Schilling, R. & Tavitov, A. G. (2018). Strength of PLA Components Fabricated with Fused Deposition Technology Using a Desktop 3D Printer as a Function of Geometrical Parameters of the Process. *Polymers*, 10(3), 313. doi: 10.3390/polym10030313. Publisher: Multidisciplinary Digital Publishing Institute.

Lacambra-Andreu, X., Morelle, X. P., Maazouz, A., Chenal, J.-M. & Lamnawar, K. (2023). Rheological investigation and modeling of healing properties during extrusion-based 3D printing of poly(lactic-acid). *Rheologica Acta*, 62(1), 31–44. doi: 10.1007/s00397-022-01377-6.

Lamnini, S., Elsayed, H., Lakhdar, Y., Baino, F., Smeacetto, F. & Bernardo, E. (2022). Robocasting of advanced ceramics: ink optimization and protocol to predict the printing parameters - A review. *Heliyon*, 8(9), e10651. doi: 10.1016/j.heliyon.2022.e10651.

Lampron, O., Therriault, D. & Lévesque, M. (2023). Phase-field modeling of fracture in fused filament fabricated thermoplastic parts and experimental validation. *Engineering Fracture Mechanics*, 292, 109667. doi: 10.1016/j.engfracmech.2023.109667.

Lee, W. I. & Springer, G. S. (1987). A Model of the Manufacturing Process of Thermoplastic Matrix Composites. *Journal of Composite Materials*, 21(11), 1017–1055. doi: 10.1177/002199838702101103. Publisher: SAGE Publications Ltd STM.

Lendvai, L., Fekete, I., Rigotti, D. & Pegoretti, A. (2025). Experimental study on the effect of filament-extrusion rate on the structural, mechanical and thermal properties of material extrusion 3D-printed polylactic acid (PLA) products. *Progress in Additive Manufacturing*, 10(1), 619–629. doi: 10.1007/s40964-024-00646-5.

Lepoivre, A., Levy, A., Boyard, N., Gaudefroy, V. & Sobotka, V. (2021). Coalescence in fused filament fabrication process: Thermo-dependent characterization of high-performance polymer properties. *Polymer Testing*, 98, 107096. doi: 10.1016/j.polymertesting.2021.107096.

Lepoivre, A., Boyard, N., Levy, A. & Sobotka, V. (2022). Methodology to assess interlayer quality in the material extrusion process: A temperature and adhesion prediction on a high performance polymer. *Additive Manufacturing*, 60, 103167. doi: 10.1016/j.addma.2022.103167.

Levy, A., Heider, D., Tierney, J. & Gillespie, J. W. (2014). Inter-layer thermal contact resistance evolution with the degree of intimate contact in the processing of thermoplastic composite laminates. *Journal of Composite Materials*, 48(4), 491–503. doi: 10.1177/0021998313476318. Publisher: SAGE Publications Ltd STM.

Leśniowski, J., Stawiarski, A. & Barski, M. (2025). Enhancing the Performance of FFF-Printed Parts: A Review of Reinforcement and Modification Strategies for Thermoplastic Polymers. *Materials*, 18(22), 5185. doi: 10.3390/ma18225185. Publisher: Multidisciplinary Digital Publishing Institute.

Li, C. & Cui, W. (2021). 3D bioprinting of cell-laden constructs for regenerative medicine. *Engineered Regeneration*, 2, 195–205. doi: 10.1016/j.engreg.2021.11.005.

Li, G., Zhao, J., Jiang, J., Jiang, H., Wu, W. & Tang, M. (2018). Ultrasonic strengthening improves tensile mechanical performance of fused deposition modeling 3D printing. *The International Journal of Advanced Manufacturing Technology*, 96(5), 2747–2755. doi: 10.1007/s00170-018-1789-0.

Li, L., Sun, Q., Bellehumeur, C. & Gu, P. (2002). Investigation of Bond Formation in FDM Process. doi: 10.26153/TSW/4500.

Li, X.-L. & Guo, J.-G. (2019). Theoretical Investigation on Failure Strength and Fracture Toughness of Precracked Single-Layer Graphene Sheets. *Journal of Nanomaterials*, 2019(1), 9734807. doi: 10.1155/2019/9734807. _eprint: https://onlinelibrary.wiley.com/doi/pdf/10.1155/2019/9734807.

Lin, X., Hao, M., Ying, J., Wang, R., Lu, Y., Gong, M., Zhang, L., Wang, D. & Zhang, L. (2022). An insight into the tensile anisotropy of 3D-printed thermoplastic polyurethane. *Additive Manufacturing*, 60, 103260. doi: 10.1016/j.addma.2022.103260.

Lin, X., Wu, S., Wang, D., Gong, M., Zhang, L., Liu, Y., Zhang, L., Lu, Y. & Wang, R. (2024). Super elastic-plastic behavior of the surface grooves resulting in tensile anisotropy of 3D-printed elastomers. *Additive Manufacturing*, 82, 104030. doi: 10.1016/j.addma.2024.104030.

Lingua, A., Piccirelli, N., Therriault, D. & Lévesque, M. (2022). In-situ full-field measurements for 3D printed polymers during Mode I interface failure. *Engineering Fracture Mechanics*, 269, 108483. doi: 10.1016/j.engfracmech.2022.108483. Publisher: Elsevier.

Loos, A. C. & Dara, P. H. (1987). Processing of Thermoplastic Matrix Composites. *Review of Progress in Quantitative Nondestructive Evaluation*, pp. 1257–1265. doi: 10.1007/978-1-4613-1893-4_143.

Maguire, A., Pottackal, N., Saadi, M. A. S. R., Rahman, M. M. & Ajayan, P. M. (2021). Additive manufacturing of polymer-based structures by extrusion technologies. *Oxford Open Materials Science*, 1(1), itaa004. doi: 10.1093/oxfmat/itaa004.

Matos, B. D. M., Rocha, V., da Silva, E. J., Moro, F. H., Bottene, A. C., Ribeiro, C. A., dos Santos Dias, D., Antonio, S. G., do Amaral, A. C., Cruz, S. A., de Oliveira Barud, H. G. & Silva Barud, H. d. (2019). Evaluation of commercially available polylactic acid (PLA) filaments for 3D printing applications. *Journal of Thermal Analysis and Calorimetry*, 137(2), 555–562. doi: 10.1007/s10973-018-7967-3.

Mazlan, M. A., Anas, M. A., Nor Izmin, N. A. & Abdullah, A. H. (2023). Effects of Infill Density, Wall Perimeter and Layer Height in Fabricating 3D Printing Products. *Materials*, 16(2), 695. doi: 10.3390/ma16020695. Publisher: Multidisciplinary Digital Publishing Institute.

McIlroy, C. & Olmsted, P. D. (2017). Disentanglement effects on welding behaviour of polymer melts during the fused-filament-fabrication method for additive manufacturing. *Polymer*, 123, 376–391. doi: 10.1016/j.polymer.2017.06.051.

Meticulous Market Research Pvt Ltd. [Retrieved December 4, 2025]. (2024). Polymer Additive Manufacturing Market to Reach $36.19 Billion by 2031, Growing at a CAGR of 15.1% from 2024. Retrieved from: https://www.prnewswire.com/news-releases/polymer-additive-manufacturing-market-to-reach-36-19-billion-by-2031--growing-at-a-cagr-of-15-1-from-2024--exclusive-report-by-meticulous-research-302414304.html.

Moetazedian, A., Allum, J., Gleadall, A. & Silberschmidt, V. V. (2023). Bulk-Material Bond Strength Exists in Extrusion Additive Manufacturing for a Wide Range of Temperatures, Speeds, and Layer Times. *3D Printing and Additive Manufacturing*, 10(3), 514–523. doi: 10.1089/3dp.2021.0112. Publisher: Mary Ann Liebert, Inc., publishers.

Mohseni, Y., Suresh, S., Wille, M.-L., Yarlagadda, P. K. D. V. & Little, J. P. (2025). Quantitative Assessment of Voids' Impact on Mechanical Properties of Standard Dogbone Model Versus End-User Component in Non-Linear Geometry. *Polymers*, 17(7), 956. doi: 10.3390/polym17070956.

N. Turner, B., Strong, R. & A. Gold, S. (2014). A review of melt extrusion additive manufacturing processes: I. Process design and modeling. *Rapid Prototyping Journal*, 20(3), 192–204. doi: 10.1108/RPJ-01-2013-0012.

Oleff, A., Küster, B., Stonis, M. & Overmeyer, L. (2021). Process monitoring for material extrusion additive manufacturing: a state-of-the-art review. *Progress in Additive Manufacturing*, 6(4), 705–730. doi: 10.1007/s40964-021-00192-4.

Orellana Barrasa, J., Ferrández-Montero, A., Ferrari, B. & Pastor, J. Y. (2021). Characterisation and Modelling of PLA Filaments and Evolution with Time. *Polymers*, 13(17), 2899. doi: 10.3390/polym13172899. Publisher: Multidisciplinary Digital Publishing Institute.

Orellana-Barrasa, J., Ferrández-Montero, A., Boccaccini, A. R., Ferrari, B. & Pastor, J. Y. (2022a). The Mechanical, Thermal, and Chemical Properties of PLA-Mg Filaments Produced via a Colloidal Route for Fused-Filament Fabrication. *Polymers*, 14(24), 5414. doi: 10.3390/polym14245414. Publisher: Multidisciplinary Digital Publishing Institute.

Orellana-Barrasa, J., Tarancón, S. & Pastor, J. Y. (2022b). Effects of Accelerating the Ageing of 1D PLA Filaments after Fused Filament Fabrication. *Polymers*, 15(1), 69. doi: 10.3390/polym15010069.

Orellana-Barrasa, J., Tarancón, S. & Pastor, J. Y. (2023). Effects of Accelerating the Ageing of 1D PLA Filaments after Fused Filament Fabrication. *Polymers*, 15(1), 69. doi: 10.3390/polym15010069. Publisher: Multidisciplinary Digital Publishing Institute.

Pan, A. Q., Huang, Z. F., Guo, R. J. & Liu, J. (2016). Effect of FDM Process on Adhesive Strength of Polylactic Acid(PLA) Filament. *Key Engineering Materials*, 667, 181–186. doi: 10.4028/www.scientific.net/KEM.667.181. Publisher: Trans Tech Publications Ltd.

Park, S. J., Lee, J. E., Jin, S. C., Lee, N.-K., Choi, K., Park, S.-H. & Son, Y. (2022). Tensile test of additively manufactured specimens with external notch removed via laser cutting in material extrusion. *Polymer Testing*, 110, 107581. doi: 10.1016/j.polymertesting.2022.107581.

Patadiya, N. H., Dave, H. K. & Rajpurohit, S. R. (2020). Effect of build orientation on mechanical strength of FDM printed PLA. In Shunmugam, M. S. & Kanthababu, M. (Eds.), *Advances in Additive Manufacturing and Joining* (pp. 301–307). Springer Singapore. doi: 10.1007/978-981-32-9433-2_26.

Patel, A. & Taufik, M. (2022). Extrusion-Based Technology in Additive Manufacturing: A Comprehensive Review. *Arabian Journal for Science and Engineering*. doi: 10.1007/s13369-022-07539-1.

Patterson, A. E., Chadha, C., Jasiuk, I. M. & Allison, J. T. (2023). Tensile behavior of individual fibers and films made via material extrusion additive manufacturing. *Next Materials*, 1(1), 100002. doi: 10.1016/j.nxmate.2023.100002.

Pedregosa, F., Varoquaux, G., Gramfort, A., Michel, V., Thirion, B., Grisel, O., Blondel, M., Prettenhofer, P., Weiss, R., Dubourg, V., Vanderplas, J., Passos, A., Cournapeau, D., Brucher, M., Perrot, M. & Duchesnay, E. (2011). Scikit-learn: Machine Learning in Python. *Journal of Machine Learning Research*, 12, 2825–2830.

Penumakala, P. K., Santo, J. & Thomas, A. (2020). A critical review on the fused deposition modeling of thermoplastic polymer composites. *Composites Part B: Engineering*, 201, 108336. doi: 10.1016/j.compositesb.2020.108336.

Pignatelli, F. & Percoco, G. (2022). An application- and market-oriented review on large format additive manufacturing, focusing on polymer pellet-based 3D printing. *Progress in Additive Manufacturing*, 7(6), 1363–1377. doi: 10.1007/s40964-022-00309-3.

PlasticsToday Staff. (2015). PEEK aerospace brackets for Bombardier aircraft drive down manufacturing costs. *PlasticsToday*. Retrieved from: https://www.plasticstoday.com/plastics-processing/peek-aerospace-brackets-for-bombardier-aircraft-drive-down-manufacturing-costs.

Pokluda, O., Bellehumeur, C. T. & Vlachopoulos, J. (1997). Modification of Frenkel's model for sintering. *AIChE Journal*, 43(12), 3253–3256. doi: 10.1002/aic.690431213. _eprint: https://aiche.onlinelibrary.wiley.com/doi/pdf/10.1002/aic.690431213.

Popescu, D., Zapciu, A., Amza, C., Baciu, F. & Marinescu, R. (2018). FDM process parameters influence over the mechanical properties of polymer specimens: A review. *Polymer Testing*, 69, 157–166. doi: 10.1016/j.polymertesting.2018.05.020.

Pourali, M. & Peterson, A. M. (2021). Fused filament fabrication of void-free parts using low viscosity hot melt adhesives. *Additive Manufacturing*, 46, 102110. doi: 10.1016/j.addma.2021.102110.

Prajapati, H., Salvi, S. S., Ravoori, D., Qasaimeh, M., Adnan, A. & Jain, A. (2021). Improved print quality in fused filament fabrication through localized dispensing of hot air around the deposited filament. *Additive Manufacturing*, 40, 101917. doi: 10.1016/j.addma.2021.101917. Publisher: Elsevier.

Priyanka, G., Kumar, K., Reddy, V. G. P. & Tadepalli, T. (2021). Mechanical reliability of extruded PLA filaments. *Materialia*, 16, 101075. doi: 10.1016/j.mtla.2021.101075.

Protolabs. [Place: Maple Plain, MN, USA]. (2024). 3D Printing Trend Report 2024. Protolabs. Retrieved from: https://www.protolabs.com/resources/guides-and-trend-reports/3d-printing-trend-report/.

Pulidindi, K. & Ahuja, K. [Report ID: GMI8432. Retrieved November 11, 2025]. (2024, march). 3D Printing Plastics Market - By Type, By Form, By End-user & Forecast, 2024–2032 [Market Report]. Retrieved from: https://www.gminsights.com/industry-analysis/3d-printing-plastics-market.

Qi, S., Gao, X., Su, Y., Dong, X., Cavallo, D. & Wang, D. (2021). Correlation between welding behavior and mechanical anisotropy of long chain polyamide 12 manufactured with fused filament fabrication. *Polymer*, 213, 123318. doi: 10.1016/j.polymer.2020.123318.

Qi, S., Gao, X., Su, Y., Liu, G., Lu, Y., Zhou, Y., Dong, X. & Wang, D. (2023). Characteristic gradient structures in polyamide 12 parts fabricated by material extrusion additive manufacturing. *Additive Manufacturing*, 69, 103528. doi: 10.1016/j.addma.2023.103528.

Rane, K. & Strano, M. (2019). A comprehensive review of extrusion-based additive manufacturing processes for rapid production of metallic and ceramic parts. *Advances in Manufacturing*, 7(2), 155–173. doi: 10.1007/s40436-019-00253-6.

Ravi, A. K., Deshpande, A. & Hsu, K. H. (2016). An in-process laser localized pre-deposition heating approach to inter-layer bond strengthening in extrusion based polymer additive manufacturing. *Journal of Manufacturing Processes*, 24, 179–185. doi: 10.1016/j.jmapro.2016.08.007. Publisher: Elsevier.

Ravoori, D., Salvi, S., Prajapati, H., Qasaimeh, M., Adnan, A. & Jain, A. (2021). Void reduction in fused filament fabrication (FFF) through in situ nozzle-integrated compression rolling of deposited filaments. *Virtual and Physical Prototyping*, 16(2), 146–159. doi: 10.1080/17452759.2021.1890986. Publisher: Taylor & Francis _eprint: https://doi.org/10.1080/17452759.2021.1890986.

Rivet, I., Dialami, N., Cervera, M. & Chiumenti, M. (2024). Mechanism-Based damage and failure of Fused Filament Fabrication components. *Composites Part B: Engineering*, 270, 111119. doi: 10.1016/j.compositesb.2023.111119.

Robles Poblete, F., Ireland, M., Slattery, L., Davids, W. G. & Lopez-Anido, R. A. (2023). In Situ, Real-Time Temperature Mapping and Thermal FE Simulations of Large-Format 3D Printed PETG/CF Vertical Wall. *Materials*, 16(19), 6486. doi: 10.3390/ma16196486. Publisher: Multidisciplinary Digital Publishing Institute.

Rodrigues, S., Miri, S., Cole, R. G., Postigo, A. A., Saleh, M. A., Dondish, A., Melenka, G. W. & Fayazbakhsh, K. (2023). Towards optimization of polymer filament tensile test for material extrusion additive manufacturing process. *Journal of Materials Research and Technology*, 24, 8458–8472. doi: 10.1016/j.jmrt.2023.05.088.

Rodriguez, J. F., Thomas, J. P. & Renaud, J. E. (2000). Characterization of the mesostructure of fused-deposition acrylonitrile-butadiene-styrene materials. *Rapid Prototyping Journal*, 6(3), 175–186. doi: 10.1108/13552540010337056. Publisher: Emerald Publishing Limited.

Rudolph, N., Chen, J. & Dick, T. (2019). Understanding the temperature field in fused filament fabrication for enhanced mechanical part performance. *AIP Conference Proceedings*, 2055(1), 140003. doi: 10.1063/1.5084906. Publisher: AIP Publishing.

Sam-Daliri, O., Ghabezi, P., Steinbach, J., Flanagan, T., Finnegan, W., Mitchell, S. & Harrison, N. (2023). Experimental study on mechanical properties of material extrusion additive manufactured parts from recycled glass fibre-reinforced polypropylene composite. *Composites Science and Technology*, 241, 110125. doi: 10.1016/j.compscitech.2023.110125.

Samal, S. K., Vishwanatha, H. M., Saxena, K. K., Behera, A., Nguyen, T. A., Behera, A., Prakash, C., Dixit, S. & Mohammed, K. A. (2022). 3D-Printed Satellite Brackets: Materials, Manufacturing and Applications. *Crystals*, 12(8), 1148. doi: 10.3390/cryst12081148. Number: 8 Publisher: Multidisciplinary Digital Publishing Institute.

Schaefer, P., Guglhoer, T., Sause, M. & Drechsler, K. (2017). Development of intimate contact during processing of carbon fiber reinforced Polyamide-6 tapes. *Journal of Reinforced Plastics and Composites*, 36(8), 593–607. doi: 10.1177/0731684416687041. Publisher: SAGE Publications Ltd STM.

Schijve, J. (2009). Stress Concentration at Notches. In Schijve, J. (Ed.), *Fatigue of Structures and Materials* (pp. 59–88). Dordrecht: Springer Netherlands. doi: 10.1007/978-1-4020-6808-9_3.

Schreier, H., Orteu, J.-J. & Sutton, M. A. (2009). *Image Correlation for Shape, Motion and Deformation Measurements: Basic Concepts,Theory and Applications*. Boston, MA: Springer US. doi: 10.1007/978-0-387-78747-3.

Senden, D., Peters, G., Govaert, L. & Van Dommelen, J. (2013). Anisotropic yielding of injection molded polyethylene: Experiments and modeling. *Polymer*, 54(21), 5899–5908. doi: 10.1016/j.polymer.2013.08.047.

Seppala, J. E. & Migler, K. D. (2016). Infrared thermography of welding zones produced by polymer extrusion additive manufacturing. *Additive Manufacturing*, 12, 71–76. doi: 10.1016/j.addma.2016.06.007.

Seppala, J. E., Hoon Han, S., Hillgartner, K. E., Davis, C. S. & Migler, K. B. (2017). Weld formation during material extrusion additive manufacturing. *Soft Matter*, 13(38), 6761–6769. doi: 10.1039/C7SM00950J.

Shaik, Y. P., Schuster, J. & Shaik, A. (2021). A scientific review on various pellet extruders used in 3D printing FDM processes. *Open Access Library Journal*, 8(8), 1–19. doi: 10.4236/oalib.1107698. Publisher: Scientific Research Publishing.

Sharafi, S., Santare, M. H., Gerdes, J. & Advani, S. G. (2022). A multiscale modeling approach of the Fused Filament Fabrication process to predict the mechanical response of 3D printed parts. *Additive Manufacturing*, 51, 102597. doi: 10.1016/j.addma.2022.102597.

Sher. [Retrieved November 11, 2025]. (2024a). Additive manufacturing of consumer products is booming. Retrieved from: https://www.voxelmatters.com/additive-manufacturing-of-consumer-products-is-booming/.

Sher, D. (2024b). Additive manufacturing of consumer products is booming. Retrieved on 2025-01-03 from: https://www.voxelmatters.com/additive-manufacturing-of-consumer-products-is-booming/.

Shokrollahi, M., Smith, A. W., Levy, A., Dubé, M. & Tabiai, I. (2025). Reassessing anisotropy in 3D printed structures: The role of extrudate geometry vs interface bonding. *Journal of Manufacturing Processes*, 149, 456–472. doi: 10.1016/j.jmapro.2025.05.070.

Smith, Z. J., Golias, C. J., Vaske, T. J., Young, S. A., Chen, Q., Goodbred, L., Rong, L., Cheng, X., Penumadu, D. & Advincula, R. C. (2024). Correlating viscosity and die swell in 3D printing of polyphenylsulfone: A thermo-mechanical optimization modus operandi. *Reactive and Functional Polymers*, 194, 105795. doi: 10.1016/j.reactfunctpolym.2023.105795.

Sommacal, S., Matschinski, A., Drechsler, K. & Compston, P. (2021). Characterisation of void and fiber distribution in 3D printed carbon-fiber/PEEK using X-ray computed tomography. *Composites Part A: Applied Science and Manufacturing*, 149, 106487. doi: 10.1016/j.compositesa.2021.106487.

Spiller, S., Berto, F. & Razavi, N. (2022). Mechanical behavior of Material Extrusion Additive Manufactured components: an overview. *Procedia Structural Integrity*, 41, 158–174. doi: 10.1016/j.prostr.2022.05.018.

Srinivasan, R., Ruban, W., Deepanraj, A., Bhuvanesh, R. & Bhuvanesh, T. (2020). Effect on infill density on mechanical properties of PETG part fabricated by fused deposition modelling. *Materials Today: Proceedings*, 27, 1838–1842. doi: 10.1016/j.matpr.2020.03.797.

Stokes-Griffin, C. M. & Compston, P. (2016). Investigation of sub-melt temperature bonding of carbon-fibre/PEEK in an automated laser tape placement process. *Composites Part A: Applied Science and Manufacturing*, 84, 17–25. doi: 10.1016/j.compositesa.2015.12.019.

Stratasys. (2020). Looking Forward: Additive Manufacturing in 2020. Stratasys Direct Manufacturing. Retrieved from: https://info.stratasysdirect.com/rs/626-SBR-192/images/SDM_Looking_Ahead_AM_in_2020_NF.pdf.

Sultana, J., Rahman, M. M., Wang, Y., Ahmed, A. & Xiaohu, C. (2024). Influences of 3D printing parameters on the mechanical properties of wood PLA filament: an experimental analysis by Taguchi method. *Progress in Additive Manufacturing*, 9(4), 1239–1251. doi: 10.1007/s40964-023-00516-6.

Sun, Q., Rizvi, G., Bellehumeur, C. & Gu, P. (2008). Effect of processing conditions on the bonding quality of FDM polymer filaments. *Rapid Prototyping Journal*, 14(2), 72–80. doi: 10.1108/13552540810862028.

Sun, X., Mazur, M. & Cheng, C.-T. (2023). A review of void reduction strategies in material extrusion-based additive manufacturing. *Additive Manufacturing*, 67, 103463. doi: 10.1016/j.addma.2023.103463.

Sun, X., Mazur, M. & Cheng, C.-T. (2025). An interlaced toolpath strategy for void reduction in material extrusion additive manufacturing. *Progress in Additive Manufacturing*, 10(7), 4239–4255. doi: 10.1007/s40964-025-01163-9.

Sustainability Directory. (2025). What statistics indicate reduced waste with 3D printing. Retrieved from: https://sustainability-directory.com/question/what-statistics-indicate-reduced-waste-with-3d-printing.

Syrlybayev, D., Zharylkassyn, B., Seisekulova, A., Akhmetov, M., Perveen, A. & Talamona, D. (2021). Optimisation of Strength Properties of FDM Printed Parts—A Critical Review. *Polymers*, 13(10), 1587. doi: 10.3390/polym13101587.

Tagscherer, N., Consul, P., Kottenstedde, I. L., Latiri, H., Zaremba, S. & Drechsler, K. (2021). Investigation of nonisothermal fusion bonding for extrusion additive manufacturing of large structural parts. *Polymer Composites*, 42(10), 5209–5222. doi: 10.1002/pc.26216. _eprint: https://4spepublications.onlinelibrary.wiley.com/doi/pdf/10.1002/pc.26216.

Tao, Q., Fu, B. & Zhong, F. (2025). A Review of Challenges and Future Perspectives for High-Speed Material Extrusion Technology. *Applied Sciences*, 15(22), 12176. doi: 10.3390/app152212176. Publisher: Multidisciplinary Digital Publishing Institute.

Tao, Y., Kong, F., Li, Z., Zhang, J., Zhao, X., Yin, Q., Xing, D. & Li, P. (2021). A review on voids of 3D printed parts by fused filament fabrication. *Journal of Materials Research and Technology*, 15, 4860–4879. doi: 10.1016/j.jmrt.2021.10.108. Publisher: Elsevier.

Thakkar, B. S., Broutman, L. J. & Kalpakjian, S. (1980). Impact strength of polymers 2: The effect of cold working and residual stress in polycarbonates. *Polymer Engineering & Science*, 20(11), 756–762. doi: 10.1002/pen.760201110.

Tientcheu, S. W. T., Djouda, J. M., Bouaziz, M. A. & Lacazedieu, E. (2024). A review on fused deposition modeling materials with analysis of key process parameters influence on mechanical properties. *The International Journal of Advanced Manufacturing Technology*, 130(5), 2119–2158. doi: 10.1007/s00170-023-12823-x.

Tofangchi, A., Han, P., Izquierdo, J., Iyengar, A. & Hsu, K. (2019). Effect of Ultrasonic Vibration on Interlayer Adhesion in Fused Filament Fabrication 3D Printed ABS. *Polymers*, 11(2), 315. doi: 10.3390/polym11020315. Publisher: Multidisciplinary Digital Publishing Institute.

Torres, J., Cotelo, J., Karl, J. & Gordon, A. P. (2015). Mechanical Property Optimization of FDM PLA in Shear with Multiple Objectives. *JOM*, 67(5), 1183–1193. doi: 10.1007/s11837-015-1367-y.

Toth, L., Slezák, E., Bocz, K. & Ronkay, F. (2024). Progress in 3D printing of recycled PET. *Materials Today Sustainability*, 26, 100757. doi: 10.1016/j.mtsust.2024.100757.

Tronvoll, S., Vedvik, N., Elverum, C. & Welo, T. (2019). A new method for assessing anisotropy in fused deposition modeled parts using computed tomography data. *The International Journal of Advanced Manufacturing Technology*, 105, 47–65. doi: 10.1007/s00170-019-04081-7. Publisher: Springer.

Tronvoll, S. A., Welo, T. & Elverum, C. W. (2018). The effects of voids on structural properties of fused deposition modelled parts: a probabilistic approach. *The International Journal of Advanced Manufacturing Technology*, 97(9), 3607–3618. doi: 10.1007/s00170-018-2148-x.

Turner, B. N. & Gold, S. A. (2015). A review of melt extrusion additive manufacturing processes: II. Materials, dimensional accuracy, and surface roughness. *Rapid Prototyping Journal*, 21(3), 250–261. doi: 10.1108/RPJ-02-2013-0017.

Vaes, D., Coppens, M., Goderis, B., Zoetelief, W. & Van Puyvelde, P. (2021). The Extent of Interlayer Bond Strength during Fused Filament Fabrication of Nylon Copolymers: An Interplay between Thermal History and Crystalline Morphology. *Polymers*, 13(16), 2677. doi: 10.3390/polym13162677.

Valvez, S., Silva, A. P. & Reis, P. N. B. (2022). Optimization of Printing Parameters to Maximize the Mechanical Properties of 3D-Printed PETG-Based Parts. *Polymers*, 14(13), 2564. doi: 10.3390/polym14132564. Publisher: Multidisciplinary Digital Publishing Institute.

van de Werken, N., Tekinalp, H., Khanbolouki, P., Ozcan, S., Williams, A. & Tehrani, M. (2020). Additively manufactured carbon fiber-reinforced composites: State of the art and perspective. *Additive Manufacturing*, 31, 100962. doi: 10.1016/j.addma.2019.100962.

Vanaei, H. R., Deligant, M., Shirinbayan, M., Raissi, K., Fitoussi, J., Khelladi, S. & Tcharkhtchi, A. (2021a). A comparative in-process monitoring of temperature profile in fused filament fabrication. *Polymer Engineering & Science*, 61(1), 68–76. doi: 10.1002/pen.25555. Publisher: Wiley.

Vanaei, H. R., Shirinbayan, M., Costa, S. F., Duarte, F. M., Covas, J. A., Deligant, M., Khelladi, S. & Tcharkhtchi, A. (2021b). Experimental study of PLA thermal behavior during fused filament fabrication. *Journal of Applied Polymer Science*, 138(3), 49747. doi: 10.1002/app.49747. Publisher: Wiley.

Verbeeten, W. M. H. & Lorenzo-Bañuelos, M. (2022). Material Extrusion Additive Manufacturing of Poly(Lactic Acid): Influence of infill orientation angle. *Additive Manufacturing*, 59, 103079. doi: 10.1016/j.addma.2022.103079.

Vidakis, N., Petousis, M., Tzounis, L., Velidakis, E., Mountakis, N. & Grammatikos, S. A. (2021a). Polyamide 12/Multiwalled Carbon Nanotube and Carbon Black Nanocomposites Manufactured by 3D Printing Fused Filament Fabrication: A Comparison of the Electrical, Thermoelectric, and Mechanical Properties. *C*, 7(2), 38. doi: 10.3390/c7020038. Publisher: Multidisciplinary Digital Publishing Institute.

Vidakis, N., Petousis, M., Velidakis, E., Mountakis, N., Fischer-Griffiths, P. E., Grammatikos, S. & Tzounis, L. (2021b). Fused Filament Fabrication Three-Dimensional Printing Multi-Functional of Polylactic Acid/Carbon Black Nanocomposites. *C*, 7(3), 52. doi: 10.3390/c7030052. Publisher: Multidisciplinary Digital Publishing Institute.

Vălean, C., Baban, M., Rajak, D. K. & Linul, E. (2024). Effect of multiple process parameters on optimizing tensile properties for material extrusion-based additive manufacturing. *Construction and Building Materials*, 414, 135015. doi: 10.1016/j.conbuildmat.2024.135015.

Wach, R. A., Wolszczak, P. & Adamus-Wlodarczyk, A. (2018). Enhancement of Mechanical Properties of FDM-PLA Parts via Thermal Annealing. *Macromolecular Materials and Engineering*, 303(9). doi: 10.1002/mame.201800169. Publisher: Wiley-VCH Verlag.

Waly, C., Petersmann, S. & Arbeiter, F. (2023). Crack penetration versus deflection in extrusion-based additive manufacturing – Impact of nozzle temperature and morphology. *Theoretical and Applied Fracture Mechanics*, 127, 104032. doi: 10.1016/j.tafmec.2023.104032.

Wang, J., Xie, H., Weng, Z., Senthil, T. & Wu, L. (2016). A novel approach to improve mechanical properties of parts fabricated by fused deposition modeling. *Materials & Design*, 105, 152–159. doi: 10.1016/j.matdes.2016.05.078.

Wang, X., Zhao, L., Fuh, J. Y. H. & Lee, H. P. (2019). Effect of Porosity on Mechanical Properties of 3D Printed Polymers: Experiments and Micromechanical Modeling Based on X-ray Computed Tomography Analysis. *Polymers*, 11(7), 1154. doi: 10.3390/polym11071154. Publisher: Multidisciplinary Digital Publishing Institute.

Webbe Kerekes, T., Lim, H., Joe, W. Y. & Yun, G. J. (2019). Characterization of process–deformation/damage property relationship of fused deposition modeling (FDM) 3D-printed specimens. *Additive Manufacturing*, 25, 532–544. doi: 10.1016/j.addma.2018.11.008. Publisher: Elsevier.

Weißgraeber, P., Leguillon, D. & Becker, W. (2016). A review of Finite Fracture Mechanics: crack initiation at singular and non-singular stress raisers. *Archive of Applied Mechanics*, 86(1), 375–401. doi: 10.1007/s00419-015-1091-7.

Wickramasinghe, S., Do, T. & Tran, P. (2020). FDM-Based 3D Printing of Polymer and Associated Composite: A Review on Mechanical Properties, Defects and Treatments. *Polymers*, 12(7), 1529. doi: 10.3390/polym12071529.

Woern, A. & Pearce, J. (2018). 3-D Printable Polymer Pelletizer Chopper for Fused Granular Fabrication-Based Additive Manufacturing. *Inventions*, 3(4), 78. doi: 10.3390/inventions3040078. Publisher: Multidisciplinary Digital Publishing Institute.

Wool, R. P. & O'Connor, K. M. (1981). A theory crack healing in polymers. *Journal of Applied Physics*, 52(10), 5953–5963. doi: 10.1063/1.328526.

Wu, W., Li, J., Jiang, J., Liu, Q., Zheng, A., Zhang, Z., Zhao, J., Ren, L. & Li, G. (2022). Influence Mechanism of Ultrasonic Vibration Substrate on Strengthening the Mechanical Properties of Fused Deposition Modeling. *Polymers*, 14(5), 904. doi: 10.3390/polym14050904. Publisher: Multidisciplinary Digital Publishing Institute.

Xia, H., Lu, J. & Tryggvason, G. (2019). A numerical study of the effect of viscoelastic stresses in fused filament fabrication. *Computer Methods in Applied Mechanics and Engineering*, 346, 242–259. doi: 10.1016/j.cma.2018.11.031.

Xu, D., Agassant, J. F. & Pigeonneau, F. (2022). Dimensions of the deposited strand in the material extrusion process: Experimental and numerical investigations. *Additive Manufacturing*, 59, 103107. doi: 10.1016/j.addma.2022.103107.

Xu, P., Li, Q., Wang, C., Li, L., Tan, D. & Wu, H. (2025). Interlayer healing mechanism of multipath deposition 3D printing models and interlayer strength regulation method. *Journal of Manufacturing Processes*, 141, 1031–1047. doi: 10.1016/j.jmapro.2025.03.062.

Yan, Y., Zhang, R., Hong, G. & Yuan, X. (2000). Research on the bonding of material paths in melted extrusion modeling. *Materials & Design*, 21(2), 93–99. doi: 10.1016/S0261-3069(99)00058-8. Publisher: Elsevier.

Yang, F. & Pitchumani, R. (2001). A fractal Cantor set based description of interlaminar contact evolution during thermoplastic composites processing. *Journal of Materials Science*, 36(19), 4661–4671. doi: 10.1023/A:1017950215945.

Yang, F. & Pitchumani, R. (2002a). Healing of Thermoplastic Polymers at an Interface under Non-isothermal Conditions. *Macromolecules*, 35(8), 3213–3224. doi: 10.1021/ma010858o. Publisher: American Chemical Society.

Yang, F. & Pitchumani, R. (2002b). Interlaminar contact development during thermoplastic fusion bonding. *Polymer Engineering & Science*, 42(2), 424–438. doi: 10.1002/pen.10960. _eprint: https://4spepublications.onlinelibrary.wiley.com/doi/pdf/10.1002/pen.10960.

Yang, G., Sun, Y., Limin qin, Li, M., Ou, K., Fang, J. & Fu, Q. (2021). Direct-ink-writing (DIW) 3D printing functional composite materials based on supra-molecular interaction. *Composites Science and Technology*, 215, 109013. doi: 10.1016/j.compscitech.2021.109013.

Yang, L., Xie, H., Huang, C., Zhang, D. & Chao, Y. (2020). Experimental Study on Notched Directional Blasting in Tensile Stress Field. *Journal of Engineering Science and Technology Review*, 13, 106–113. doi: 10.25103/jestr.131.14.

Yin, J., Lu, C., Fu, J., Huang, Y. & Zheng, Y. (2018). Interfacial bonding during multi-material fused deposition modeling (FDM) process due to inter-molecular diffusion. *Materials & Design*, 150, 104–112. doi: 10.1016/j.matdes.2018.04.029.

Yu, X., Yao, T.-Y., Xiong, J.-H., Zhao, Y., Zhou, Y.-J. & Jing, Y. (2023). Mesoscopic analysis and intra-layer progressive failure model of fused filament fabrication 3D printing GFRP. *Construction and Building Materials*, 406, 133285. doi: 10.1016/j.conbuildmat.2023.133285.

Yu, Z.-Z., Lei, M., Ou, Y. & Yang, G. (2002). On compatibilization and toughening of a copolyester with a maleated thermoplastic elastomer. *Polymer*, 43(25), 6993–7001. doi: 10.1016/S0032-3861(02)00547-5.

Zander, N. E., Gillan, M., Burckhard, Z. & Gardea, F. (2019). Recycled polypropylene blends as novel 3D printing materials. *Additive Manufacturing*, 25, 122–130. doi: 10.1016/j.addma.2018.11.009.

Zarzoor, A. K., Jaber, A. A. & Shandookh, A. (2024). 3D Printing for wind turbine blade manufacturing: a review of materials, design optimization, and challenges. *Engineering and Technology Journal*, 42(4), 895–911. doi: 10.30684/etj.2024.144841.1646. Publisher: University of Technology-Iraq.

Zerriouh, A., Deghiche, A., Benayache, W., Hashemi, T., Bernardi, A., Liparoti, S., Di Lorenzo, M. L. & Cavallo, D. (2025). Warpage in Material Extrusion Additive Manufacturing of Amorphous and Semicrystalline Polymers. *Macromolecular Materials and Engineering*, 310(12), 202500172. doi: 10.1002/mame.202500172.

Zhang, J., Yang, W., Wang, P., Chen, Y., Mai, Y.-W. & Li, Y. (2025a). A pressure modulation approach to enhance mechanical properties of 3D-printed continuous fiber-reinforced composites. *Composites Science and Technology*, 270, 111277. doi: 10.1016/j.compscitech.2025.111277.

Zhang, J., Yang, W., Wang, P., Chen, Y., Mai, Y.-W. & Li, Y. (2025b). A pressure modulation approach to enhance mechanical properties of 3D-printed continuous fiber-reinforced composites. *Composites Science and Technology*, 270, 111277. doi: 10.1016/j.compscitech.2025.111277.

Zhang, Z., Hu, C. & Qin, Q.-H. (2025c). The improvement of void and interface characteristics in fused filament fabrication-based polymers and continuous carbon fiber-reinforced polymer composites: a comprehensive review. *The International Journal of Advanced Manufacturing Technology*, 137(3), 1047–1087. doi: 10.1007/s00170-025-15240-4.

Zhao, D., Liu, W., Chen, J., Yue, G., Song, Q. & Yang, Y. (2024). Interlaminar bonding of high-performance thermoplastic composites during automated fiber placement in-situ consolidation. *Journal of Composite Materials*, 58(20), 2247–2261. doi: 10.1177/00219983241263808. Publisher: SAGE Publications Ltd STM.

Zhou, M., Zhou, X., Si, L., Chen, P., Li, M., Zhang, Y. & Zhou, H. (2021). Modeling of bonding strength for Fused Filament Fabrication considering bonding interface evolution and molecular diffusion. *Journal of Manufacturing Processes*, 68, 1485–1494. doi: 10.1016/j.jmapro.2021.06.064.

Çelik, O., Peeters, D., Dransfeld, C. & Teuwen, J. (2020). Intimate contact development during laser assisted fiber placement: Microstructure and effect of process parameters. *Composites Part A: Applied Science and Manufacturing*, 134, 105888. doi: 10.1016/j.compositesa.2020.105888.

Özen, A., Abali, B. E., Völlmecke, C., Gerstel, J. & Auhl, D. (2021a). Exploring the Role of Manufacturing Parameters on Microstructure and Mechanical Properties in Fused Deposition Modeling (FDM) Using PETG. *Applied Composite Materials*, 28(6), 1799–1828. doi: 10.1007/s10443-021-09940-9.

Özen, A., Auhl, D., Völlmecke, C., Kiendl, J. & Abali, B. E. (2021b). Optimization of Manufacturing Parameters and Tensile Specimen Geometry for Fused Deposition Modeling (FDM) 3D-Printed PETG. *Materials*, 14(10), 2556. doi: 10.3390/ma14102556. Publisher: Multidisciplinary Digital Publishing Institute.